Local and remote impacts of regional aerosol emissions on climate

Matthew Kasoar

Department of Physics
Imperial College London

Thesis submitted for the degree of Doctor of Philosophy

Copyright declaration:

Declaration of Originality:

This thesis and the work presented herein is my own. Any data or material that have been contributed by others is attributed to those individuals, and any previous work or ideas that I draw upon or reuse are referenced appropriately.

Abstract

Aerosols are short-lived in the atmosphere, and so their distribution and climate forcing is very inhomogeneous. To understand the behaviour of the climate system in response to inhomogeneous forcing, and to inform emission policy choices, we must investigate how emissions from individual geographic regions affect the climate regionally and globally. I present here the results of two interwoven modelling studies. First, I analyse the simulated temperature response to perturbing sulfur dioxide emissions over a specific region – China – in three current generation climate models. Second, I systematically investigate with a single model the temperature and precipitation responses to black carbon and sulfur dioxide emissions from the United States, Europe, East Asia, and India.

These simulations reveal in the first instance that there is very large uncertainty around aerosol-climate interactions in present climate models. Removing SO_2 emissions from China results in a six-fold difference in the optical depth and short-wave flux changes over China between different models, and the resulting surface temperature response is poorly constrained. However, the subsequent systematic perturbations indicate that in the event the regional forcing is large, then there are striking features of the climate response that are consistent across different perturbation locations. Emission changes always result not only in a strong local response around the emission region, but also a strong remote response, the pattern of which is insensitive to the original location of emission changes. There is, however, variation in the efficacy with which emissions from different regions force the climate, with US and European sulphur dioxide emission changes having a larger effect than East Asian emission changes.

The results presented here are relevant for understanding the effect of potential future emission controls, and also for understanding how the climate responds to different localised forcings, which has not been tested in complex coupled climate models previously.

Acknowledgements

First and foremost, I would like to deeply and sincerely thank my supervisor, Dr Apostolos Voulgarakis. For giving me the opportunity to study for my PhD in his group, for his unending support and advice – not just on my work, but all aspects of my development as a researcher and a person. For encouraging me and challenging me, introducing me, and also giving me some fantastic opportunities that I had never envisioned I would get. I would also like to thank NERC, the Natural Environment Research Council, for funding my PhD, again allowing me to carry out this research, present it at conferences, and in general have the great experiences that have resulted from being a PhD student.

Many other people throughout my PhD have also given me variously great advice, critical feedback, new ideas to think about, new data, and have all been invaluable in helping me understand and interpret the work that has gone into this thesis. In particular I would like to thank Professor Bill Collins and Dr Nicolas Bellouin (University of Reading), Prof Drew Shindell (Duke University), Dr Greg Faluvegi and Dr Kostas Tsigaridis (Columbia University and NASA Goddard Institutes for Space Studies), Dr Jean-François Lamarque (National Center for Atmospheric Research), and Dr Arnaud Czaja (Imperial College London), with all of whom I have had very productive discussions which have helped shape my research. I am also indebted to my supervisor and these colleagues for their comments either on this manuscript or on work that has formed part of it, and to my examiners Prof Jim Haywood and Prof Ralf Toumi for their constructive feedback. I would also like to thank the European Commission's Marie Curie Actions International Research Staff Exchange Scheme (IRSES) for funding my placement at NASA GISS and Columbia University as part of the Regional Climate-Air Quality Interactions (REQUA) project, from which some of these interactions and work presented in this thesis arose.

On the practical side, I would like to thank both NERC and the Met Office for providing access to the (considerable) supercomputer resources that I have needed. There is also a whole group of people at the Met Office and at the National Centre for Atmospheric Science who have provided help and support with the model, without which I would have been utterly lost. In particular, from the Met Office I'd like to thank Dr Fiona O'Connor for helping me get set up with the HadGEM3-GA4 model in the first place, and Mohit Dalvi, Dr Jeremy Walton, and Dr Steve Rumbold for all the time and support they've given me in understanding, troubleshooting, customising, and running the model. Additionally, all the staff of the NCAS Computational Modelling Services helpdesk, who have been indispensable when I've run into problems.

On a personal level, I'd like to thank the whole of the Space and Atmospheric Physics Group at Imperial, who have all made my time there very enjoyable. A few people from SPAT I would like to thank especially though: First, my 711b office mates – Dr Benjamin Wong, Dr Sam Phibbs, and Yi Li – who have always been there to talk about anything, either on or completely off topic, and generally offer their opinions, a different perspective, or answers to ridiculous questions. Also the rest of “Team Apostolos”: Dill Shawki, Stéphane Mangeon, and Sunil Varma, who have livened up our meetings, expanded my cultural education, and offered a lot of support and encouragement when I’ve been under pressure, which has been tremendously appreciated.

And finally, I’d like to thank my family; my Mum and Dad, and my brothers Tim and Elliott (and Oscar the cat), for their love and support throughout, which means everything to me.

Matt Kasoar

Contents

List of Figures

List of Tables

List of Abbreviations Used

ACCMIP	Atmospheric Chemistry and Climate Model Intercomparison Project
AERONET	Aerosol Robotic Network
AOD	Aerosol optical depth
BC	Black carbon
CAM5	Community Atmosphere Model version 5
CESM1	Community Earth System Model version 1
CCN	Cloud condensation nuclei
CLASSIC	Coupled Large-scale Aerosol Simulator for Studies In Climate
CICE	The Los Alamos sea-ice model
CMIP	Coupled Model Intercomparison Project
EA	East Asia
ENSO	El Niño/Southern Oscillation
EOF	Empirical orthogonal function
ERF	Effective radiative forcing
EU	Europe
FFBC	Fossil-fuel black carbon
GHG	Greenhouse gas
GISS	Goddard Institute for Space Studies
GISS-E2	Goddard Institute for Space Studies ModelE2
GPCP	Global Precipitation Climatology Project
HadGEM2	Hadley Centre Global Environment Model 2
HadGEM3-GA4	Hadley Centre Global Environment Model 3 (Global Atmosphere 4.0)
HTAP	Hemispheric Transport of Air Pollutants
IMPROVE	Interagency Monitoring of Protected Visual Environments
IND	India
IPCC AR5	Intergovernmental Panel on Climate Change Fifth Assessment Report
ITCZ	Intertropical convergence zone
JULES	Joint UK Land Environment Simulator
LW	Longwave
MAM	Modal Aerosol Module

MIROC	Model for Interdisciplinary Research on Climate
MISR	Multi-angle Imaging SpectroRadiometer
MODIS	Moderate Resolution Imaging Spectroradiometer
NASA	National Aeronautics and Space Administration
NCAR	National Center for Atmospheric Research
NEMO	Nucleus for European Modelling of the Ocean
NHML	Northern Hemisphere mid-latitudes
NICAM	Nonhydrostatic Icosahedral Atmospheric Model
OC	Organic carbon
OMI	Ozone Monitoring Instrument
PDRMIP	Precipitation Driver and Response Model Intercomparison Project
POP	Parallel Ocean Program
SST	Sea-surface temperature
SW	Shortwave
TOA	Top of atmosphere
US	United States
WDCPC	World Data Centre for Precipitation Chemistry

1 Introduction and Background

Humans are affecting the climate in substantive ways by emitting a range of gases and particles into the atmosphere as waste products. Many of these emitted species - or their chemical products - interact with radiation at the wavelengths that we either receive it from the sun (shortwave (SW), or solar radiation) or at the wavelengths that radiation is radiated from the planet (longwave (LW), or thermal radiation), giving them a capacity to alter the balance of radiative energy entering or leaving the earth system if their concentrations in the atmosphere change. This results in a radiative forcing of the climate – either a net surplus or deficiency of energy entering the atmosphere, warming or cooling the planet and having knock-on effects on other components of the climate system such as the hydrological cycle.

Well-mixed greenhouse gases (GHGs) are one group of particularly harmful climate forcers. This group includes CO_2, as well as other long-lived gases that warm the climate by trapping outgoing LW radiation. Well-mixed GHGs such as CO_2 last for a very long time in the atmosphere, and so they tend to become fairly evenly spread around over time, hence 'well-mixed'. As a result, the radiative forcing they impose on the climate system is fairly homogeneous, and the location well-mixed GHGs are emitted from does not make much difference to their final climate effect. However, other significant climate-forcing agents can be quite short-lived. The most important short-lived species for climate are aerosols – small particles or droplets in the atmosphere which scatter or absorb predominantly SW radiation – as well as tropospheric ozone, which is a potent greenhouse gas (e.g. Myhre et al., 2013b). Increases in aerosol emissions over the last century have been shown to contribute significantly to observed global and regional climate changes. For instance, Booth et al. (2012), Hwang et al. (2013), and Wilcox et al. (2013) discussed the importance of historical aerosol cooling in modulating large-scale temperature and precipitation patterns. Other studies such as Bollasina et al. (2011), Dong et al. (2014), and Polson et al. (2014) have looked at the impact of aerosols on regional climate features such as the monsoon systems or Sahelian rainfall.

Short-lived forcing agents such as aerosols are interesting because being short-lived (here meaning that they have lifetimes ranging from a few days to a few months) means that they do not become evenly mixed through the atmosphere. On top of that, different aerosols force the climate in different ways – for instance some scatter SW radiation back to space, cooling the planet (a negative forcing) while others absorb radiation and warm the planet (positive forcing). Unlike long-lived greenhouse gases such as CO_2, the radiative forcing due to aerosols is therefore highly variable – both in space and, for seasonally varying sources like biomass-burning, in time. The resulting climate response can be strongly influenced by the location and type of emission, as well as the prevailing circulation patterns.

This has motivated an effort to begin to investigate how the regionality and type of aerosol forcing is related to the climate response that results. The central question is: how does the location where a particular radiative forcing is applied, or where a particular aerosol is emitted from, influence the sensitivity of the climate to that species? However there have so far been very few studies that have investigated, in a systematic fashion, the climate response to specific aerosols or other short-lived species, simultaneously to exploring the significance of the region in which the emission originates. A seminal example of such a study is that of Shindell and Faluvegi (2009), followed up further in Shindell et al. (2012), which looked systematically at the response of temperature and precipitation to single-species forcings imposed in different broad latitude bands, and showed that the influence of remote forcings on certain regions can often outweigh and even have opposite sign to the influence of local forcings. Occasionally studies have looked also at the climate response to a particular aerosol type from a single region – e.g. Teng et al. (2012), which investigated temperature responses to drastically increasing carbonaceous aerosols from Asia, finding a strong remote effect on US summertime temperatures.

These few studies all have their limitations though, and there is considerable scope for further investigation of climate responses to regional forcings. The only studies to systematically investigate impacts of individual short-lived forcing species over different regions – those by Shindell and Faluvegi (2009) and Shindell et al. (2012) – applied perturbations by directly scaling the atmospheric concentrations of the species they perturbed, and perturbations were only applied over whole latitude bands. Furthermore, most of the studies that have been done have invariably only used a single model at a time. There is also considerable uncertainty in the details of regional climate change, and in the representation of aerosol-cloud interactions, that vary between models. As a result, there is huge potential for the scope of these existing studies to be extended, firstly by performing similar experiments using different and newer models, and also by going further than some of the existing studies – for instance, perturbing the actual source emissions of aerosol species rather than just scaling their present-day atmospheric concentrations, and looking at forcings over more localised regions such as continent- or country-scale as well as latitude bands. This would be more informative for understanding the physical processes translating both emissions to regional forcings, and zonally asymmetric forcings to climate response, and would also be more directly interpretable for policy applications.

In the following sections of this chapter, I firstly give an overview of aerosols, their composition, chemistry, and interactions with clouds and with radiation. Additionally, I will summarise the findings of some key studies described above to set out the current state of understanding of regional aerosol influences on climate, before describing what will be added by the present study.

1.1 Aerosols

1.1.1 Sources and composition

Aerosols are any liquid or solid particles too small to be considered cloud droplets (typically $\lesssim 10\mu m$) that are suspended in the atmosphere, and so there are actually a variety of different types of aerosols, which are very different in their radiative, chemical, and microphysical properties. Figure 1-1 reproduces an overview of aerosol sizes and lifecycles. The finest aerosol

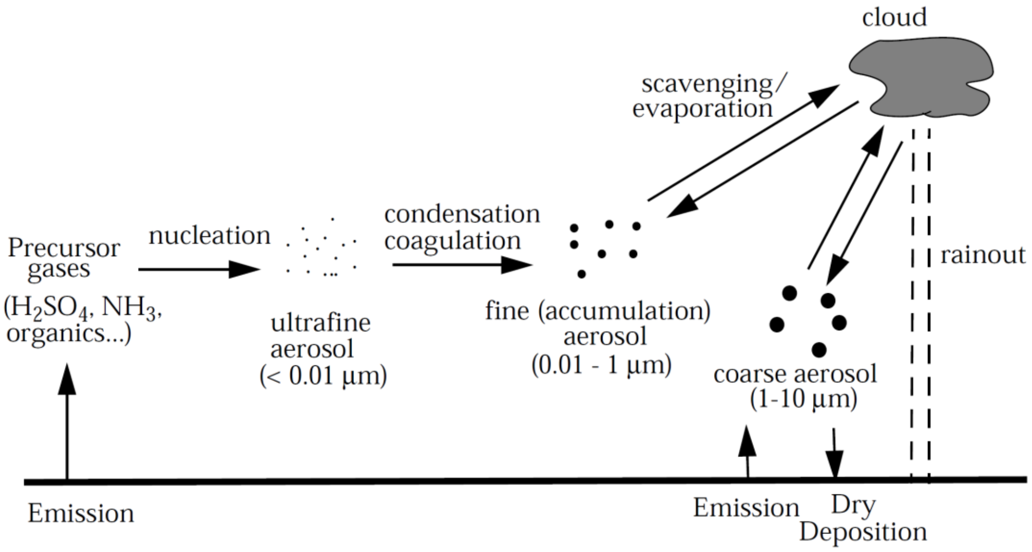

Figure 1-1: *Reproduction of Figure 8-2 in Jacob (1999), showing aerosol emission, growth, and deposition processes.*

particles form from the condensation of precursor gases (nucleation), and then grow by further condensation onto the existing particles, and by coagulation of particles, until they are ultimately removed by being captured in cloud droplets, or by gravitational settling. Other, larger aerosol species such as dust are emitted directly as larger non-gaseous particles.

The most important anthropogenic aerosol species are: black carbon (BC), organic carbon (OC), nitrate, and sulfate. The two carbonaceous aerosols are typically emitted from fossil-fuel and biomass burning, either directly as particulate matter or from combustion products that rapidly condense at atmospheric temperatures; OC can also form from condensation of biogenic gaseous organic compounds (Jacob, 1999; Tsigaridis et al., 2014). BC particles are what might often be characterised as soot; they are dark carbon compounds which are mostly hydrophobic, and in particular highly absorbing of SW radiation. OC particles consist of more complex organic compounds, and are typically hydrophilic (and thus can act as cloud condensation nuclei, as will be discussed below) and generally scatter SW radiation more than they absorb it (Ramanathan et al., 2001). Nitrate aerosol consists mainly of ammonium nitrate (NH_4NO_3) droplets, which form from oxidation and reaction of nitrogen oxides, from fossil-fuel and biogenic sources, with ammonia, mainly from agricultural sources (Bauer et al., 2007). Like OC, nitrate is scattering of incoming SW radiation, and hydrophilic. Its relative abundance to other aerosols like sulfate varies substantially over different regions and seasons, and although globally it has not so far been the most important anthropogenic aerosol species, it may play a dominant role both regionally (Jimenez et al., 2009) and in projections of future emissions changes (Bellouin et al., 2011).

At present, one of the most important anthropogenically-sourced aerosol species is sulfate (SO_4) (e.g. Myhre et al., 2013b). Sulfate aerosol consists principally of aqueous sulfuric acid and ammonium sulfate droplets (Jacob, 1999; Wayne, 2000; Bellouin et al., 2011), and can also form as a sulfate coating on other aerosols such as dust or BC (Haywood and Boucher, 2000). Sulfate particles strongly scatter incoming shortwave (SW) radiation, increasing the planetary albedo and cooling the climate. They are also very hydrophilic, and so easily nucleate cloud droplets. Like nitrate, sulfate droplets are not directly emitted, but are formed by oxidation of sulfur-containing precursor gases, the main anthropogenic source being sulfur dioxide (SO_2) emissions from fossil-fuel burning, while natural sources include volcanic SO_2 and oceanic dimethyl sulfide (DMS) emissions (e.g. Andres and Kasgnoc, 1998; Andreae and Crutzen, 1997). The primary gaseous oxidant in the atmosphere which facilitates the conversion of these precursor gases to sulfate aerosol compounds is the hydroxyl radical OH (Jacob, 1999). However, in the presence of water droplets, sulfur dioxide can also be oxidised in the aqueous phase by dissolved hydrogen peroxide (H_2O_2) or ozone (O_3), which are responsible for most atmospheric oxidation (Jacob, 1999; Bellouin et al., 2011).

As discussed above, historical cooling from sulfate aerosol – predominantly in the more industrialised northern hemisphere – has been implicated by a range of modelling studies in disrupting climate since the mid-20th century. For example Fig 1-2 reproduces Figure 3(a) from Wilcox et al. (2013), showing the long-term historical temperature trends in CMIP5 models with and without aerosol forcing, compared with HadCRUT4 observations. It is clear that there was a significant deviation from GHG-induced global warming from the mid-century, which is consistent only with cooling due to anthropogenic aerosols.

Additional aerosol species that are important for climate include dust, sea salt, and biogenic aerosols, the latter being produced from biological sources such as volatile organic compounds and biological matter released from plants (e.g. Poschl et al., 2010). Though these species all

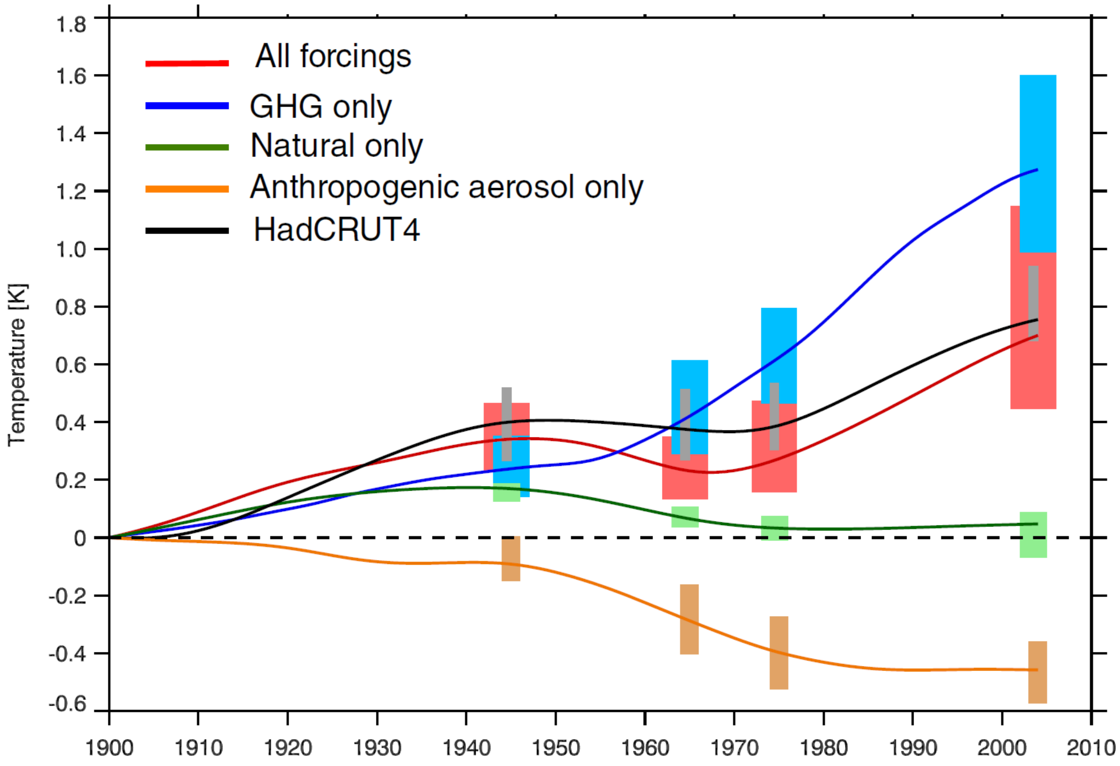

Figure 1-2: *Reproduction of Figure 3a in Wilcox et al. (2013) showing trends in global mean surface temperature in historical CMIP5 simulations with all forcings (red), GHG-only forcing (blue), natural forcing only (green), and anthropogenic-aerosol forcing only (yellow). HadCRUT4 observations are shown in black.*

have very important implications for climate, since they are naturally produced they are not generally considered as important drivers of climate change, unlike anthropogenic emissions. However, changes in their emission and transport due to climate change could potentially act as an important feedback (e.g. Carslaw et al., 2010), and background concentrations of natural aerosols can strongly modulate the aerosol-cloud interactions of anthropogenic aerosols (Carslaw et al., 2013), discussed below.

1.1.2 Aerosol-cloud interactions

Aerosols can have more elaborate effects on climate than greenhouse gases, since in addition to their direct radiative effects due to scattering or absorbing radiation, they can also have indirect effects through their microphysical interactions with clouds.

The capacity of certain aerosol types to affect clouds and precipitation through microphysical interactions has been documented for some time. Warner and Twomey (1967) and Warner (1968) examined changes in cloud droplet properties and precipitation due to smoke from sugar cane burning in Queensland, Australia. They found that downwind of the burning, smoke particles were able to greatly increase the cloud droplet number concentration by acting as cloud condensation nuclei (CCN) – hydrophilic particles on which water vapour can condense to form cloud droplets. However the total liquid water content of the clouds remained unchanged, and so, as the cloud droplet number is increased, correspondingly the average diameter of the cloud droplets must be reduced in the smoke-polluted air. They hypothesised that this reduction in the size of the cloud droplets will have the effect of suppressing precipitation, as droplets take longer to grow large enough to precipitate out. This is supported by an analysis of 60 years of precipitation data over the region, showing that on average during the sugar cane burning season, precipitation has decreased downwind of the burning as sugar cane production has increased, compared with no reduction upwind of the burning. More recently, studies such as those by Rosenfeld (1999), Rosenfeld (2000) and Andreae et al. (2004) have reported similar findings due to forest fires in Indonesia, urban/industrial pollution plumes in South Australia, and forest fires over the Amazon, respectively. Each of these studies suggest that the presence of high levels of aerosol acting as CCN leads to an increase in cloud droplet number and consequently a decrease in cloud droplet size, which suppresses low-level rainfall by delaying the formation of large raindrops.

Clouds are extremely bright, and they have a large influence on the Earth's albedo, on all scales from individual clouds through to the global albedo of the planet. By acting as cloud condensation nuclei and leading to a larger number of smaller cloud droplets forming in supersaturated conditions, hydrophilic aerosols also have the effect of increasing cloud albedo, since the higher concentration of droplets increases the optical thickness of the cloud (Twomey, 1977). This brightening of clouds, along with the previously noted suppression of precipitation which prolongs the lifetime of the cloud, together increase the integrated effect of clouds on planetary albedo. As a result, hydrophilic aerosols within clouds create an additional cooling, separate from the direct scattering of incoming SW by the aerosol itself in cloud-free regions. The cloud-brightening effect is often referred to as the 1st aerosol indirect effect, and the effect on cloud lifetime as the 2nd aerosol indirect effect (Ramanathan et al., 2001). The sensitivity of cloud droplet number concentration to aerosol saturates at high aerosol concentrations, meaning that the indirect radiative forcing of an aerosol species depends also on the background concentrations of other aerosols (Carslaw et al., 2013).

The interaction between hydrophilic aerosols and clouds in the real world is more complex than just a brightening of the cloud and extension of cloud lifetime. For instance, Andreae et al. (2004) found that in addition to delaying precipitation, aerosol pollution can cause invigoration of some cloud systems. They found that in convective clouds, suppressing low-level warm rainout means that the cloud droplets can be transported higher into the cloud, where there is then the potential for them to freeze and release additional latent heat, invigorating the cloud and strengthening updrafts. In their study, clouds grew deeper and, when they did finally precipitate, produced more intense storms and hail. A study on the effect of aerosol pollution on the intensity of tropical cyclones (Rosenfeld et al., 2011), found similarly that by acting as CCN and slowing the conversion of cloud droplets to precipitation, high aerosol concentrations in air ingested by developing tropical cyclones leads to the invigoration of the periphery of the cyclones. Rosenfeld et al. (2008) suggest on conceptual grounds that the effect of aerosol pollution on precipitation depends strongly on the type of cloud system: although they reduce precipitation from shallow clouds, such as observed by Warner (1968) and Rosenfeld (2000), in deep convective clouds aerosol pollution can increase total precipitation. By delaying the formation of precipitation, leading to cloud droplets being carried higher and releasing additional latent heat, this creates more developed deep convective clouds which entrain more moist air from their surroundings, and so when they do then precipitate the quantity of precipitation is much greater. Climate models typically do not include a representation of aerosol microphysical effects in their convective parameterisations, however, and the overall climate impact of these invigoration effects is extremely uncertain (e.g. Fan et al., 2012).

Aside from the indirect effects on clouds that hydrophilic aerosols can have by acting as CCN, absorbing aerosols like black carbon can alternatively affect clouds due to their heating of the atmosphere. Absorption of SW radiation by e.g. black carbon heats up the aerosol and in turn the surrounding layer of the atmosphere – this can have the effect of evaporating clouds in the region, and preventing new clouds from forming by stabilising the atmosphere, thus reducing cloudiness and the local albedo. Because this effect of aerosol heating on clouds is an additional interaction beyond the direct radiative extinction by the aerosol itself, but is more straightforward than the microphysical effects on cloud properties described above, it is sometimes referred to as the semi-direct effect (Boucher et al., 2013).

Aerosol-cloud interactions can also have knock-on effects such as reducing diurnal temperature variations, since increased cloudiness causes daytime SW cooling of the surface by reflecting more sunlight, but night-time warming by trapping LW radiation (Huang et al., 2006; Fan et al., 2012). Clouds will also be affected in a more long-term fashion, by atmospheric temperature and circulation changes as part of the climate response to aerosol forcing (e.g. Allen et al., 2012; Boucher et al., 2013).

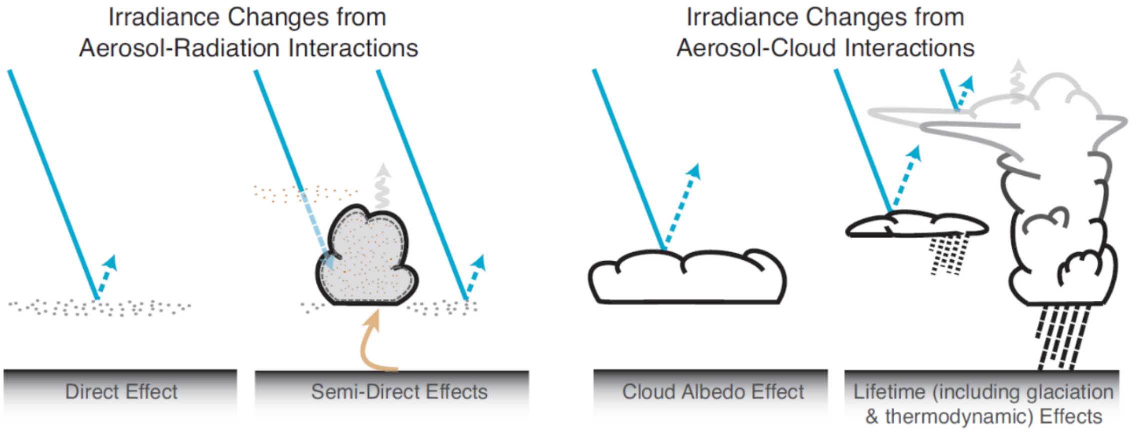

Figure 1-3: *Aerosol effects on radiation, adapted from Boucher et al. (2013) Figure 7.3, illustrating the direct scattering or absorption of solar radiation (leftmost diagram), changing cloud amount due to heating from direct radiative absorption (second from left), increasing cloud albedo by nucleating additional cloud droplets (second from right), and changing cloud lifetime and/or invigorating deep clouds (rightmost diagram).*

1.2 Aerosol-climate interactions

Figure 1-3 reproduces a schematic overview of the different direct and indirect ways aerosols interact with radiation and thereby force the climate. The overall effect of aerosols remains one of the areas of greatest uncertainty in modelling of climate change, however (Myhre et al., 2013b). The dependency on microphysical processes which are too small to resolve in climate models, difficult to measure in the real world, and difficult to generalise because of the huge range of sizes, shapes, and composition of aerosol particles, means that there is a particularly large uncertainty attached to the strength of aerosol indirect effects. Aerosol direct effects are also uncertain, again because of the range of possible compositions, sizes, and shapes that aerosols can come in. Particularly for absorbing or partially absorbing aerosols like BC and OC, the direct forcing is also heavily influenced by the altitude of the aerosol, as well as cloud amount and altitude, and surface albedo, all of which determine the availability of SW radiation to be absorbed (Ramanathan et al., 2001; Samset and Myhre, 2015).

This uncertainty is seen in Figure 1-4 which reproduces the IPCC AR5 estimates, and error bars, for the historical radiative forcing due to all major anthropogenic and natural climate forcers (Myhre et al., 2013b). Although aerosols, and particularly aerosol-cloud interactions, have the largest uncertainties of any major forcing agents, the central estimates nonetheless indicate that they are likely very significant drivers of climate change, with the strongest global mean radiative forcings after CO_2 and methane.

Figure 1-5 shows geographically the simulated surface air temperature changes due to historical forcing from either sulfate, biomass-burning, or BC aerosol, compared with a doubling of pre-industrial CO_2, from Jones et al. (2007). The historical aerosol forcing results in a much more heterogeneous response than the CO_2 forcing, with sulfate and BC temperature responses mostly restricted to the more industrialised northern hemisphere, and dominated by cooling due to sulfate scattering. Even within the same latitude band, there are regions of greater or lesser temperature response, associated with regions with large emissions (e.g. the US and China for SO_4 and BC, central Africa and Siberia for biomass-burning). By contrast, the response to CO_2 forcing is much more hemispherically-symmetric and zonally uniform.

Because of their differing radiative effects and inhomogeneous distributions, short-lived climate forcers such as aerosols can potentially have climate effects that are regionally even more important than those of well-mixed GHGs like CO_2 and methane, even if the latter dominate the global response (Shindell and Faluvegi, 2009; Shindell et al., 2012). A number of studies have

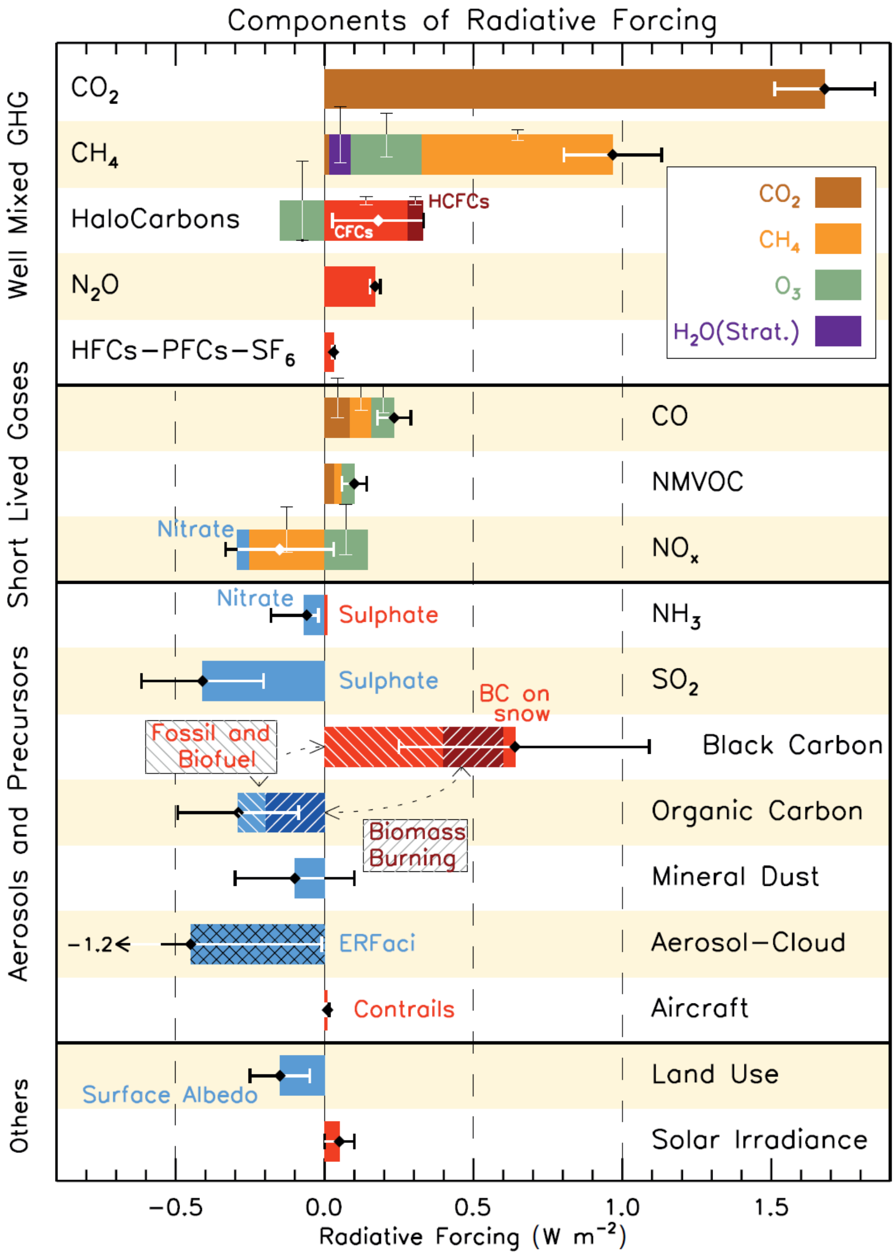

Figure 1-4: *Reproduction of Figure 8.17 in Myhre et al. (2013b), showing historical (1750-2011) radiative forcing estimates for emissions of different forcing agents. Error bars represent 5-95% confidence intervals.*

found evidence that emissions of aerosols and tropospheric ozone precursors have been the dominant drivers of some of the already observed disruption of the climate, particularly on the regional scale.

For example, Booth et al. (2012) argue that historical aerosol emissions – partly from major volcanic eruptions, but mainly from the growth of anthropogenic emissions in the second half of the 20th Century – can explain a large fraction of the observed multi-decadal variability in

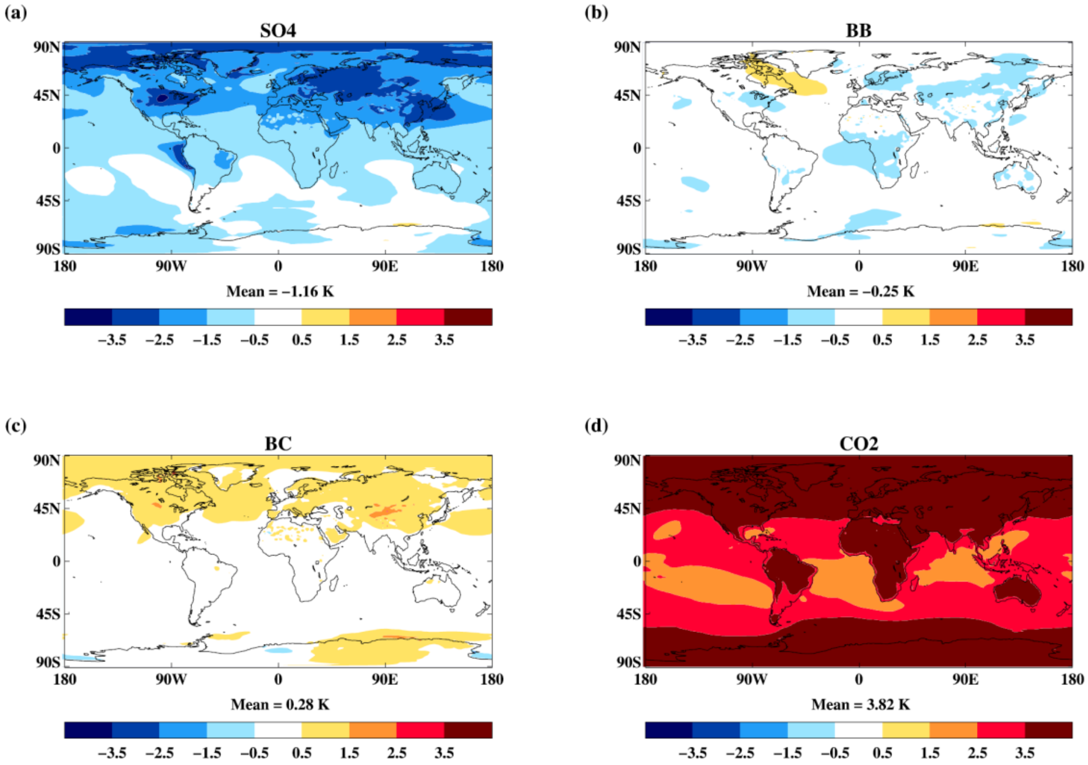

Figure 1-5: *Reproduction of Figure 2 from Jones et al. (2007), showing 1.5m temperature changes in the HadGEM1 model due to historical (1860-2000) changes in emissions of sulfate (a), biomass-burning aerosol (b), and black carbon (c), and due to doubling of 1860* CO_2 *concentrations (d).*

North Atlantic sea-surface temperatures. They suggest that this demonstrates an aerosol influence on major historical climate changes in the North Atlantic region such as changes in hurricane intensity, and the Sahel drought in the second half of the 20th Century.

An aerosol influence on the Sahel drought was also discussed by Haywood et al. (2013) and Hwang et al. (2013), in the context of both volcanic and anthropogenic emissions respectively. They indicate that injection of scattering aerosols into the northern hemisphere causes a widespread southward shift of the tropical rain belt. This appears to be reflected in historical observations and reanalysis, which show that from the late 1960s until the 1990s there was southward shift in the tropical rain belt, with drying on the northern side and wettening on the southern side in the zonal mean (Hwang et al, 2013). The hypothesis is that if there is a heating asymmetry between the two hemispheres, the Hadley cell in the cooler hemisphere will shift towards the warmer hemisphere to keep the tropospheric temperature gradient in the tropics flat, by transporting more heat from the warmer hemisphere polewards in its upper branch. Along with it, this will shift the tropical rain belt, which follows the convergence of moisture in the lower branches of the northern and southern Hadley cells. This is supported by modelling results, which show that there is an increase in the northwards cross-equator energy flux proportional to the magnitude of the southwards precipitation shift (Hwang et al., 2013), and a displacement of the Hadley cell (Haywood et al, 2013). The studies show that peaks in northern hemisphere cooling associated with anthropogenic and volcanic aerosol emissions coincided with particularly large tropical precipitation shifts.

Bollasina et al. (2011) reported similarly an observed decreasing trend in the South Asian summer monsoon precipitation during the latter part of the 20th Century. Their modelling again suggests that only the historical northern hemisphere aerosol forcing can account for the observed weakening of the South Asian monsoon, by weakening the inter-hemispheric temperature gradient during the monsoon season and reducing the meridional circulation. A similar reduction in precipitation due to local aerosol cooling is predicted by Guo et al. (2013) for the East Asian summer monsoon, who find in simulations with the HiGAM model that cooling of the land surface due to historical increases in East Asian aerosols again weakens the summer monsoon circulation, leading to less transport of moisture from the ocean to the land. Polson et al. (2014) show that there has been a detectable decrease across northern hemisphere monsoon systems consistent only with a dominant role for aerosol forcing – GHG forcing is predicted to increase monsoon precipitation due to increases in moisture availability.

In addition to the clearly significant historical role of cooling aerosols like sulfate, some studies have also looked for climate responses to anthropogenic changes in short-lived absorbing species. An analysis of ensemble CMIP3 and CMIP5 model simulations by Allen et al. (2012) suggests that increases in tropospheric heating by BC as well as tropospheric ozone have been responsible for an observed expansion of the tropics in the northern hemisphere in recent decades. Anthropogenic BC and tropospheric ozone have produced additional tropospheric heating predominantly in the northern hemisphere mid-latitudes, as this contains their largest emitting regions (East Asia in particular), and they suggest that this mid-latitude heating reduces the temperature gradient between the equator and mid-latitudes, whilst steepening the gradient between the mid-latitudes and the pole, resulting in an expansion of the northern hemisphere tropical region. (Tropical expansion has also occurred in the Southern Hemisphere where there has not been increasing BC or tropospheric ozone warming, but this has separately been attributed to stratospheric ozone depletion along with well-mixed greenhouse gas forcing (e.g. Polvani et al., 2011)).

Simulations conducted by Kawase et al. (2011) also indicate that carbonaceous aerosols, and BC in particular, have been responsible for a drying trend in austral summer precipitation that has been observed over tropical Africa during the 20th Century. Increases in BC and OC aerosol from biomass burning and fossil-fuel combustion have reduced evaporation over tropical Africa, and they further find that BC atmospheric heating produced circulation changes which induced a descending anomaly over tropical Africa. They argue these two effects together have driven the observed regional reductions in precipitation.

Evan et al. (2011) even find that the intensity of pre-monsoon cyclones in the Arabian Sea has increased between 1979 and 2010 due to the substantial increase in Asian emissions of black carbon and sulfate, which have cooled the sea surface and heated the atmosphere over the northern Indian Ocean, reducing the local circulation and weakening the vertical wind shear. Normally, strong wind shear in the pre-monsoon season limits the growth of tropical cyclones in this region; they find that reduced wind shear in recent decades allowed cyclones to grow larger and more intense.

1.3 Investigating relationships regionally and systematically

The body of work so far on the regional dependency of climate response to short-lived climate forcers has been relatively sporadic and limited in its scope. The studies discussed above typically focused on historical emissions changes, which have been very heterogeneous but equally occurred over many different regions at the same time. Few studies have focused on the climate response to emissions only from a particular region. One example mentioned

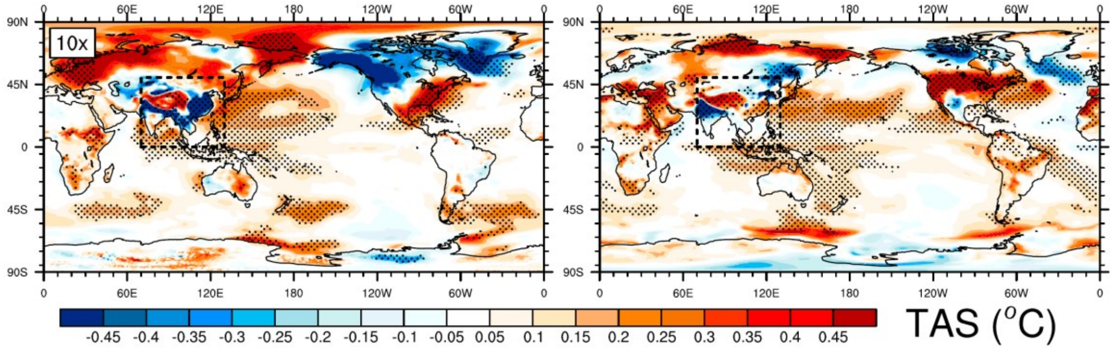

__Figure 1-6:__ Reproduction of the bottom panel from Teng et al. (2012) Figure 2, showing December-January-February (left) and June-July-August (right) surface air temperature responses to scaling up carbonaceous aerosol concentrations by a factor of 10 within the dashed box.

previously is the study of Teng et al. (2012), which simulated scaling up concentrations of carbonaceous aerosols only over Asia, to investigate the global temperature effect that large emissions from this region could have. As well as pronounced changes over Asia itself – mainly a surface cooling from reduced insolation – they also found substantial remote responses across the rest of the world, and particularly a pronounced warming over the US, mainly in the summertime (Figure 1-6). This remote warming over the US is attributed to circulation changes triggered by the additional carbonaceous aerosol heating over Asia.

1.3.1 Mechanisms of remote responses

The results of the Teng et al. (2012) study, along with the various studies of historical aerosol forcing discussed above, demonstrate that the response to a regional or inhomogenous forcing is not restricted to the location of the forcing – rather, there can be remote climate responses that extend far from the original location of the forcing.

Shindell et al. (2010) investigated the spatial extent of the response to inhomogenous forcing by looking at the spatial autocorrelation between forcing and surface temperature response. They find that the influence of inhomogeneous forcings extends much further in the zonal direction than the meridional direction – particularly for mid-latitude forcings, which includes most anthropogenic aerosol forcing – presumably because of heat advection by the atmospheric circulation, which is predominantly in the zonal direction. The exception they find is that the Arctic has a strong sensitivity to most Northern Hemisphere forcing, even though very little of this forcing is located at Arctic latitudes. This is consistent with well-established results that the Arctic appears more sensitive to climate change than other latitudes (Collins et al., 2013).

However, as evidenced by the temperature responses found by Teng et al. (2012) shown in Figure 1-6, the pattern of response to a localised forcing may itself not be all zonally uniform. A number of studies have indicated that localised heating can cause localised remote effects by perturbing circulation patterns, either projecting onto existing modes of variability in the atmosphere, or exciting waves that then propagate through the atmosphere.

Studies such as those of Hoskins and Karoly (1981) and Jin and Hoskins (1995) have used highly idealised dynamical models to investigate the response of atmospheric circulation to spatially localised heating sources, imposed at different latitudes or at different altitudes. They show that such localised heat sources can excite Rossby waves, which are able to propagate large distances both zonally and meridionally, perturbing circulation patterns in an oscillatory fashion and creating a mechanism by which a localised forcing can trigger remote dynamical changes. They find, however, that the dynamical perturbations are sensitive to both the latitude and altitude of the heat source. For instance, upper-tropospheric heat sources are more effective at exciting remote responses, and also tropical heat sources produce wavetrains that propagate more strongly poleward than mid-latitude sources.

This, in particular, results in a strong dynamical connection between the tropics and the extra-tropics, which has been noted in several studies investigating the impact of tropical forcings using more complex climate models. For example, Held et al. (1989) and Lau (1996) demonstrate that there is a connection between tropical SST anomalies (e.g. due to El Niño) and mid-latitude circulation and SST changes, which are mediated via changes to storm-track eddies induced by the tropical temperature anomalies. Aside from naturally-occurring variability, aerosol forcing is a prime mechanism by which localised heat sources can be generated, and Ming et al. (2011) investigate specifically the extra-tropical circulation response to anthropogenic aerosol forcing, and similarly find that anthropogenic aerosol heating in the tropics around South-East Asia produces a remote mid-latitude response by exciting Rossby waves that propagate polewards and eastwards, displacing the Aleutian low in the North Pacific and creating an El Niño-like teleconnection. Outside of the tropics, Ring and Plumb (2007) and Ring and Plumb (2008) find that localised mechanical or thermal forcing in the mid-latitudes instead tends to excite annular mode-like responses. This may help to account for the observations of Shepherd et al. (2014) that the circulation-driven responses to anthropogenic forcings often appear to project onto natural modes of variability.

Although these studies have often highlighted specific teleconnections between localised regions, there are also broader dynamical responses to inhomogenous forcing that can be identified, such as the previously discussed shift in the ITCZ due to any hemispherically asymmetric forcing. In additional to shifting the ITCZ by changing the cross-equatorial temperature gradient, aerosol cooling or heating can also similarly affect the position of the tropospheric jet streams and associated storm tracks by altering the temperature gradients between tropics, mid-latitudes, and polar latitudes (e.g. Lorenz and DeWeaver, 2007). Although for anthropogenic aerosols, effects on the jet streams might be expected to be restricted mainly to the northern hemisphere, in fact Ceppi et al. (2013) and Rotstayn et al. (2013) have shown that northern hemisphere aerosol forcing also impacts the southern hemisphere tropospheric jets via the induced shift in the ITCZ. The southward shift of the ITCZ in response to northern hemisphere aerosol cooling also weakens the subtropical jet in the southern hemisphere due to a weaker southern Hadley cell. This in turn affects the propagation of extra-tropical waves and reduces the transient eddies that support the mid-latitude jet, resulting in a dynamical influence of northern hemisphere forcing which is very remote indeed.

1.3.2 Studies of multiple regions

The Teng et al. (2012) study only looked at the effect of forcing over a single region. The first attempts to systematically quantify how different regions are sensitive to forcings both from different species and different locations are the studies by Shindell and Faluvegi (2009) and Shindell et al. (2012). Their work remains the principal effort in the current literature to evaluate systematically the dependence of regional climate response on the location and type of forcing applied in a global model.

In these two studies, the first examining temperature response and the second precipitation, the authors performed a series of model simulations with the GISS-ER model, in which forcings due to each of several different species (CO_2, BC, sulfate, and tropospheric ozone – each representative of a broader category of climate forcers, i.e. CO_2 the WMGHs, tropospheric ozone the short-lived GHGs, sulphate the scattering aerosols, and BC the absorbing aerosols) were applied individually and only in a single latitude band at a time. They were then able to quantify the responses as the change in temperature or precipitation per unit radiative forcing due to each individual species acting in each latitude band. Their results showing the temperature responses within a latitude band to each of the forcings imposed in each different latitude band are reproduced in Figure 1-7.

As the plots reveal, the magnitude – and in some cases even sign – of the temperature responses depends considerably on the location and type of forcing applied, in this model. For example, the northern hemisphere high latitudes (60°N-90°N) show a negative temperature change per unit forcing due to a local BC forcing, but a positive temperature change per unit forcing to BC forcings applied in the northern mid-latitudes (28°N-60°N) or the tropics (28°S-28°N). The northern hemisphere high latitudes are also more sensitive to BC and ozone forcings in the tropics than local or mid-latitude forcings, but they are much more sensitive to a local sulfate forcing than to sulfate forcing in either the mid-latitudes or tropics (per unit forcing).

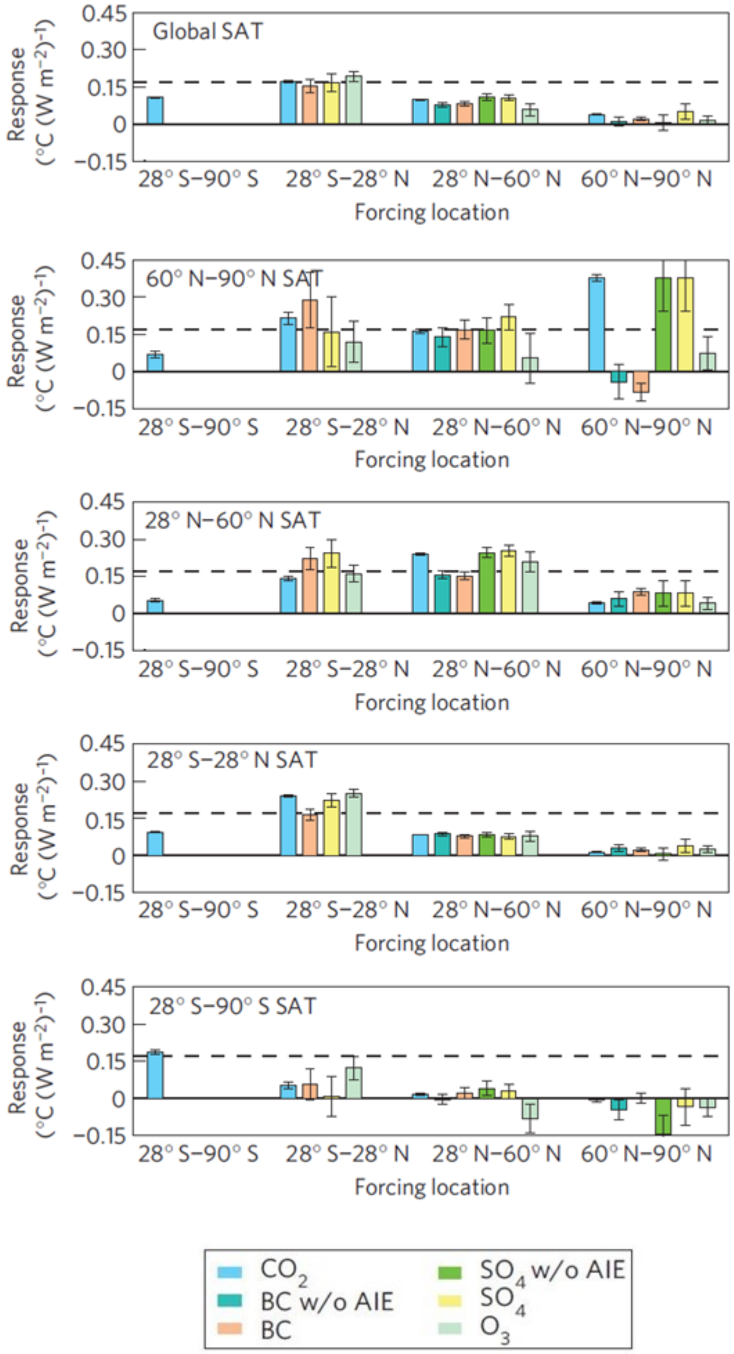

Figure 1-7: *Reproduction of Shindell and Faluvegi (2009) Figures 1. b, d, f, h, j, showing surface air temperature response (°C) in the region indicated in the upper left corner, normalised by the local forcing (W m^{-2}) applied in the latitude bands shown along the x-axes, due to different species (coloured bars). SO$_4$ and BC effects are shown both including and excluding ("w/o AIE") aerosol indirect effects through clouds. Note that latitude bands are not equal in area, so the global energy input per W m^{-2} forcing within a band is not constant.*

A subsection of results from Shindell et al. (2012) showing precipitation responses per unit forcing due to BC and sulfate forcings in the tropics and the northern mid-latitudes is also reproduced in Figure 1-8. The response per unit local forcing is generally stronger for the tropical forcings, which is to be expected since the surface area of the tropics is greater: a 1 W m^{-2} local forcing applied in the tropical band (30°S – 30°N) is a larger total energy input than the same local forcing applied in the mid-latitude band (30°N - 60°N). However, the plots also reveal that some regional precipitation responses again are very dependent on the location as well as the type of forcing applied; for example a positive BC forcing applied in the northern mid-latitudes produces a wettening of the Sahel region, but when applied in the tropics it results in a drying.

A strong sensitivity to mid-latitude SO_4 and BC forcings is generally found in the tropics, and given that historically most aerosol forcing has been in the mid-latitudes, this again suggests that the observed changes in tropical precipitation discussed in Section 1.2 have been dominated by mid-latitude emissions.

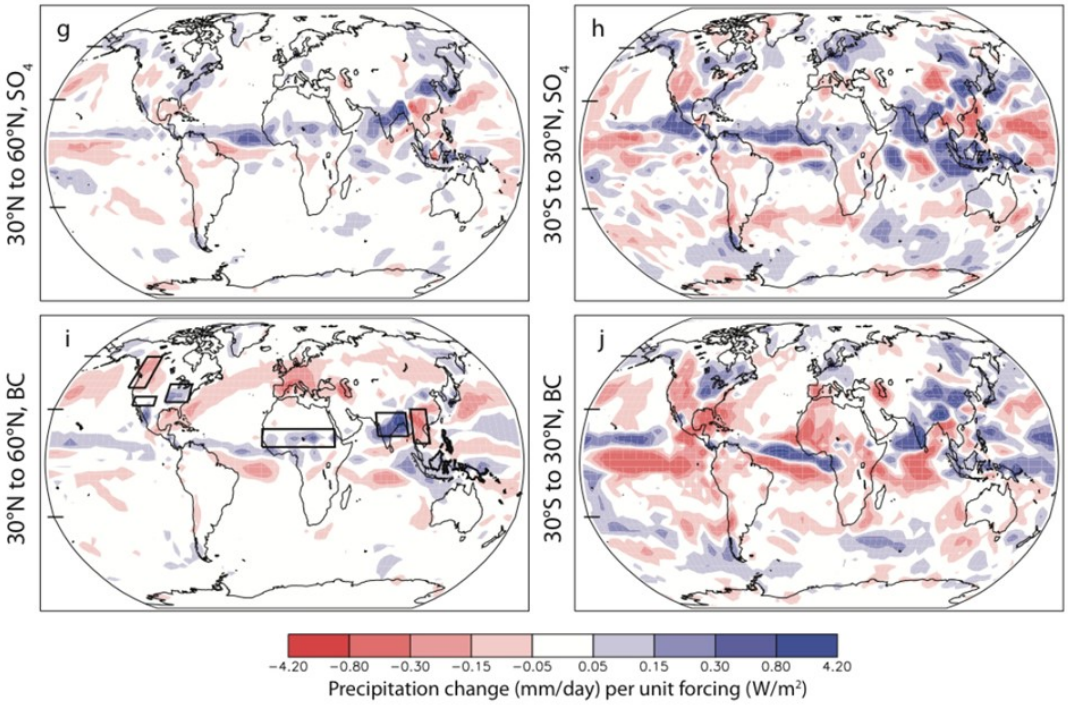

Figure 1-8: *Reproduction of Shindell et al. (2012) Figures 2. g, h, i, j, showing the precipitation change (mm day^{-1}) per unit radiative forcing within the given latitude band (W m^{-2}) due to sulfate (top) and BC (bottom) radiative forcings imposed in the northern mid-latitudes (left) and the tropics (right).*

Although a couple of subsequent studies (Voulgarakis and Shindell, 2010; Collins et al., 2013) have built on the simulations and methodology of Shindell and Faluvegi (2009) to investigate further the temperature sensitivity of different latitude bands, the 2012 study remains the only such systematic investigation of relationships between radiative forcing location and precipitation. As only a single climate model was used in these studies, some of the regional forcing-response relationships may also be highly model dependent, which is a major limitation of the work done so far on this topic.

1.4 Overview of this study

In this manuscript, I seek to extend the understanding of the relationships between regional forcing and climate response, which are particularly relevant for short-lived species such as aerosols where any policy measures will inherently affect emissions, and therefore forcing, in one particular geographic region. I will therefore investigate perturbations to aerosol emissions from more geographically-localised, industrialised northern hemisphere regions, rather than perturbing whole latitude bands as was done in the Shindell et al. (2009, 2012) studies. This will allow an investigation of the effects of localised forcings, rather than the more zonal forcings that were used previously, and means that the sensitivity of the climate response to the longitudinal position of a forcing can also be tested. Since I will perturb aerosol and aerosol precursor emissions, rather than scaling the atmospheric distributions as in the Shindell et al. studies, the full progression from emission to climate response will be included and analysed. This will allow any feedbacks of the climate response to affect aerosol distributions, and is also more relevant insofar as regional emissions are what any climate or air quality policies might actually control. I will also restrict myself to removing emissions rather than other sizes or signs of perturbation, which is more realistic both in terms of the direction of emissions change that future policies are likely to provide, and also in terms of the magnitude of any possible emissions change being no more than a 100% change. Most previous studies of regional forcing discussed above scaled emissions or concentrations up, often, by several hundred percent, to get a large signal. I will instead use very long simulations, to try and avoid the need to have highly unrealistic perturbations to detect a significant response.

To investigate these relationships, I have performed both coupled and atmosphere-only simulations with a state-of-the-art composition-climate model, the UK Met Office HadGEM3-GA4 model. Additionally, with the help of collaborators, some simulations have been performed with the GISS-E2 model (similar to that used in the Shindell et al. 2009 and 2012 studies), and the CESM1 model, the results of which I will also analyse. In the next chapter, I will begin by describing these models and briefly evaluating their simulated present-day climates. Given that I will investigate the responses to aerosol emission perturbations, I then devote Chapter 3 to a more thorough evaluation of the aerosol components of the models. In Chapter 4 I will present the results of simulations with all three models, investigating the surface temperature response to removing SO_2 emissions from the single region featuring the largest aerosol emissions in the present-day: China. In particular, I am interested in comparing and contrasting the responses in these different models to the same regional emissions change. This is important for putting into context the final results chapter, Chapter 5, where I will present the results of systematic black carbon and SO_2 emission perturbations from a series of northern hemisphere industrialised regions using HadGEM3-GA4. Finally, in Chapter 6 I will draw the overall conclusions of the thesis and discuss potential future research directions that could build on this work.

2 Description of climate models used

The principal climate model that I performed simulations with is the Hadley Centre Global Environment Model 3 – Global Atmosphere 4.0 (HadGEM3-GA4). This model and the setup employed is described in detail in Section 2.1 below, along with a comparison of basic climate variables of interest here (temperature, precipitation) against observational datasets, to verify that the model has a satisfactory representation of current climate.

Additionally, in Chapter 4 I make use of data from comparable simulations performed by colleagues with two further current-generation climate models: the Community Earth System Model 1 (CESM1), and the Goddard Institute for Space Studies ModelE2 (GISS-E2). These models are briefly described in Sections 2.2.1 and 2.2.2. Simulations with CESM1 were performed by Dr. Jean-Francois Lamarque at the National Center for Atmospheric Research (NCAR) in Boulder, Colorado, while simulations and data from GISS-E2 were provided by Prof. Drew Shindell (Duke University, North Carolina; formerly at the NASA Goddard Institute for Space Studies (GISS) in New York) and Dr. Greg Faluvegi at NASA GISS.

To allow the climate system to freely respond, all the models were used in a fully coupled atmosphere-ocean configuration. I also performed additional atmosphere-only simulations with the HadGEM3-GA4 model, identical in model version and set-up except that sea-surface temperatures and sea-ice concentrations were prescribed, which will be used primarily to help interpret the responses in the fully-coupled simulations. The three models all feature explicit aerosol modelling, and include both direct and indirect radiative effects of aerosols. For the simulations presented here, all three models will be driven by identical anthropogenic aerosol emissions, using the year 2000 inventory from Lamarque et al. (2010). However, the models vary in the details of the parameterisations used, the dynamical cores, radiation and cloud schemes, model grids and horizontal and vertical resolutions, land surface and ocean components, etc. This lack of common structural features makes these three models well suited to contrast against one another and probe the range of potential model uncertainty.

2.1 HadGEM3-GA4

2.1.1 Model overview

For simulations with HadGEM3, I used the Global Atmosphere 4.0 version of the model in a standard climate configuration with a horizontal resolution of 1.875° longitude x 1.25° latitude in the atmosphere, with 85 vertical levels and the model top at 85 km, dynamically resolving the stratosphere. The atmosphere is coupled to the JULES land surface model, which includes 4 soil layers and 5 plant functional types. Although in principle this can be run in a fully interactive 'Earth-System' mode with dynamic vegetation and a carbon cycle, in my simulations vegetation was prescribed, as were globally-uniform observed mass-mixing ratios for CO_2, CH_4, and other long-lived greenhouse gases, taking their year-2000 values from the CMIP5 historical dataset (Meinshausen et al., 2011). A zonally-uniform present-day ozone climatology is also prescribed in the radiation scheme, derived from the SPARC dataset (Cionni et al., 2011). More detailed description of the atmosphere and land-surface schemes can be found in Walters et al. (2014). The atmospheric model is also coupled to the NEMO dynamical ocean model (Madec, 2008) and CICE sea-ice model (Hunke and Lipscombe, 2008), which are run with a 1° horizontal resolution, and 75 vertical depth levels for the ocean.

Critical to this study is the representation of aerosols; I used the CLASSIC aerosol scheme, which is described in Bellouin et al. (2011). CLASSIC is a mass-based scheme which includes an interactive representation of sulfate in three modes (Aitken, accumulation, and in-cloud), fossil-fuel black carbon, fossil-fuel organic carbon, and biomass-burning aerosol in three modes (fresh, aged, and in-cloud), dust in six size bins, and sea-salt in two modes (jet and film), as well as an offline biogenic aerosol climatology. The scheme can also include a representation of nitrate aerosol, but this option was not used here. All species are considered to be externally mixed.

The sulfate component of the scheme (Jones et al., 2001) includes tracers for two gas-phase precursors: SO_2 from anthropogenic and natural sources, and DMS from natural sources. These are emitted into the atmosphere and can undergo advection, wet and dry deposition, or oxidation using prescribed 4D oxidant fields (Derwent et al., 2003). In CLASSIC, oxidation of SO_2 to SO_4 aerosol can proceed through three possible reaction pathways: in the gas phase by reaction with OH, or in the aqueous phase by reaction with either H_2O_2 or O_3.

The remaining prognostic aerosol species are emitted directly in the particulate phase, and all species can then undergo advection, growth/ageing, wet and dry deposition, and also interact with radiation. The radiative transfer scheme of Edwards and Slingo (1996) is used, with 6 spectral bands in the shortwave. The hygroscopic aerosols (sulfate, organic carbon, biomass-burning aerosol, sea-salt) can also interact with clouds via their role as cloud condensation nuclei. Cloud droplet number concentration and effective radius are determined from the mass concentration of these aerosols, which affects the simulated cloud lifetime (2nd indirect effect) and cloud brightness (1st indirect effect) as described in Bellouin et al. (2011) and Jones et al. (2001).

2.1.2 Validation of basic climate

As the HadGEM3-GA4 model is the principal model I have performed simulations with, I briefly verify here that the model simulates a satisfactory representation of present-day climate. If the model has considerable difficultly in simulating a particular aspect of the climate, this would raise the question of whether its climate response to various forcings, which will be analysed in Chapters 4 and 5, is in fact realistic. The validation is based on a 200-year long coupled control simulation which was forced with repeating year-2000 greenhouse gas (GHG) atmospheric concentrations, and year-2000 aerosol and aerosol precursor emissions from the Atmospheric Chemistry and Climate Model Intercomparison Project (ACCMIP) emissions inventory (Lamarque et al., 2010). This setup formed the base simulation for all the HadGEM3-GA4 coupled experiments discussed in subsequent chapters. An annual mean climatology of surface air temperature (diagnosed at 1.5 m in HadGEM3-GA4) and total precipitation rate was calculated by averaging over all model timesteps from the last 150 years of this simulation.

Figure 2-1 shows the comparison of 1.5m temperature in HadGEM3-GA4 with mean observed 1998-2003 surface air temperatures from the HadCRUT4.0 dataset (Morice et al., 2012). The top panel shows that overall the spatial variation and magnitude of global temperatures are very well captured. The bottom panel shows the difference between the model and the observations and reveals that the most prominent bias in the model is a substantial warm anomaly in the Southern Ocean. This Southern Ocean warm bias is an already well-known feature of the coupled model (Williams et al., 2015), caused by cloud albedos being too low over the Southern Ocean (Bodas-Salcedo et al., 2012), and the Southern Ocean mixed layer being too shallow (Williams et al., 2015). There are also errors of a few degrees in parts of the northern high latitudes, though it is worth noting that the observations in this region are rather patchier, making it difficult to accurately interpolate them to compare with the model in this region. In

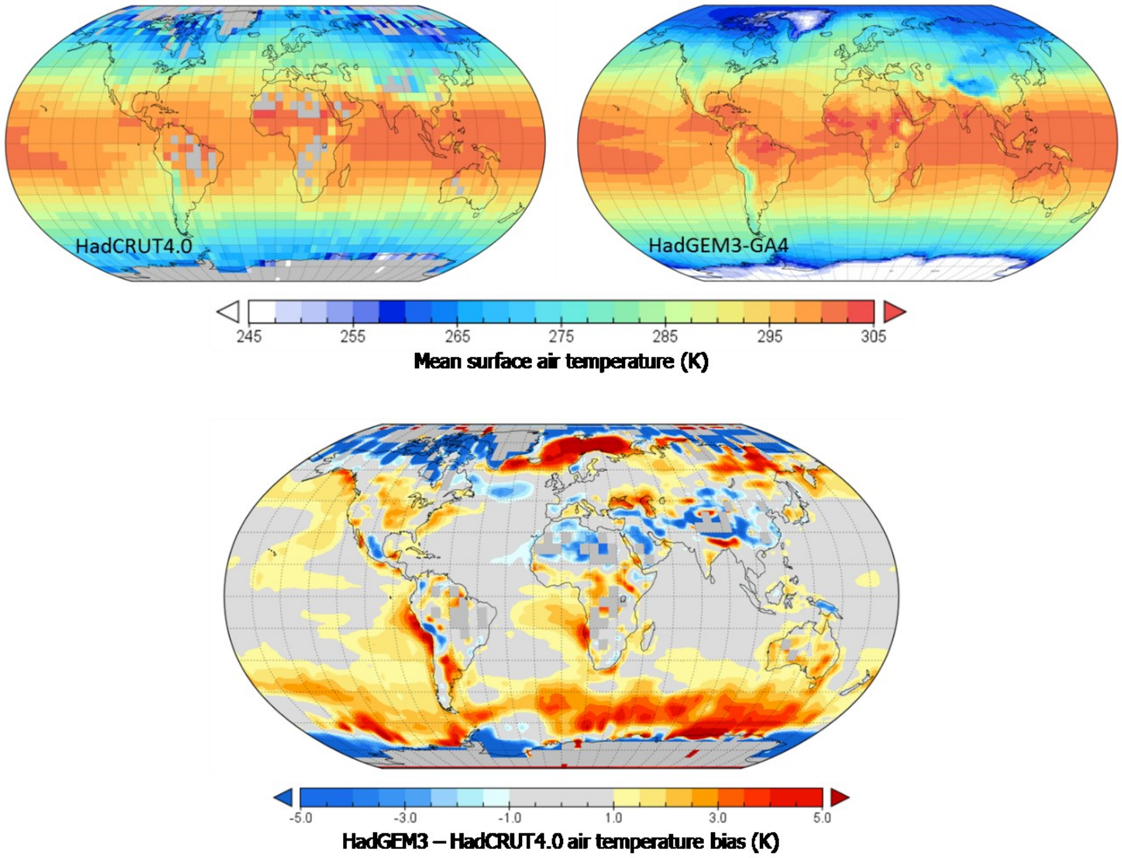

Figure 2-1: *Comparison of HadGEM3-GA4 annual mean surface air temperature with HadCRUT4.0 observations. Top panel shows the HadCRUT4.0 surface air temperature annual mean from 1998-2003 (left) and HadGEM3-GA4 150-year mean 1.5m temperature from a fully coupled control simulation with year-2000 GHG concentrations and aerosol emissions (right). Bottom panel shows the difference between the HadGEM3-GA4 mean and HadCRUT4.0.*

the mid-latitudes and tropics, surface air temperature biases are generally small (< 1K) and there is no consistent large-scale bias as there is in the Southern Ocean. The 6-year average of the HadCRUT4.0 data will also be much noisier than the 150-year average of the model data due to the far shorter averaging period, and so many of the more localised deviations may simply reflect this.

Figure 2-2 shows the comparison of total precipitation rate in HadGEM3-GA4 with observed 1998-2003 precipitation from the Global Precipitation Climatology Project (GPCP) combined satellite and ground station dataset (Adler et al., 2003). Again, the top panel shows that the observed spatial distribution of precipitation is well captured by HadGEM3-GA4, and broadly the magnitude as well, except in some parts of the tropics. This is illustrated in the lower panel, which shows that large precipitation biases are almost entirely restricted to the tropics. Within the tropics, the biases in precipitation in HadGEM3-GA4 are generally characterised by too high

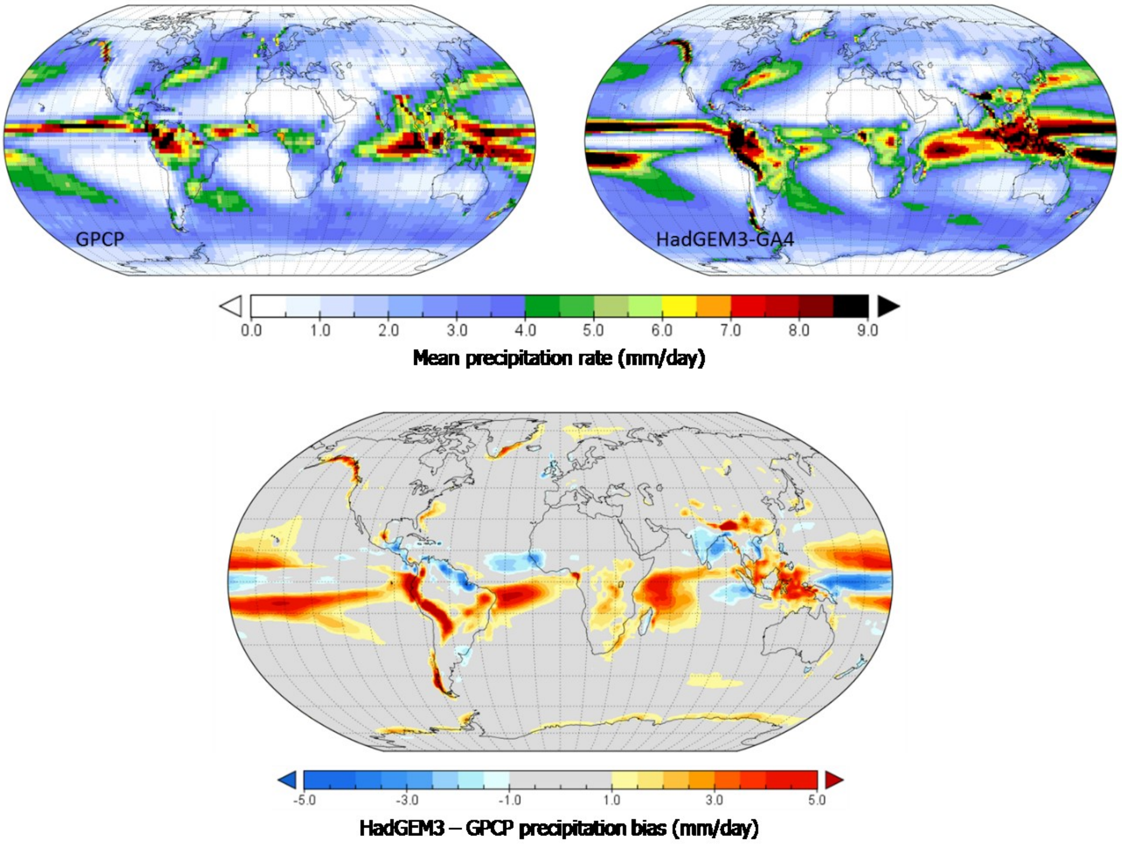

Figure 2-2: *Comparison of HadGEM3-GA4 precipitation with observations from the Global Precipitation Climatology Project (GPCP). Top panels show the annual mean GPCP precipitation rate from 1998-2003 (left), and the HadGEM3-GA4 150-year annual mean precipitation rate from a coupled control simulation with year-2000 GHG concentrations and aerosol emissions (right). Bottom panel shows the difference between the HadGEM3-GA4 mean precipitation and GPCP.*

rainfall rates over ocean regions, and a slightly too southward intertropical convergence zone (ITCZ) leading to a dry bias over northern hemisphere continental regions, and a wet bias over southern hemisphere continental regions.

Regional precipitation is of course highly seasonally varying, and this is true of the tropics as well, where the ITCZ moves north and then south through the year, following the northern hemisphere and then southern hemisphere summer. However, the precipitation biases in the respective summertimes (June-July-August and December-January-February) prove to be almost identical to the bias in annual mean precipitation (Figure 2-3), merely shifted north or south in northern and southern summer seasons respectively. This is encouraging as it indicates that the modelled precipitation is responding correctly to the seasonally-varying insolation, in terms of its seasonal deviation from the annual mean state, and the bias is characterised by a relatively constant offset in the position and strength of the ITCZ. In this case, an overly strong

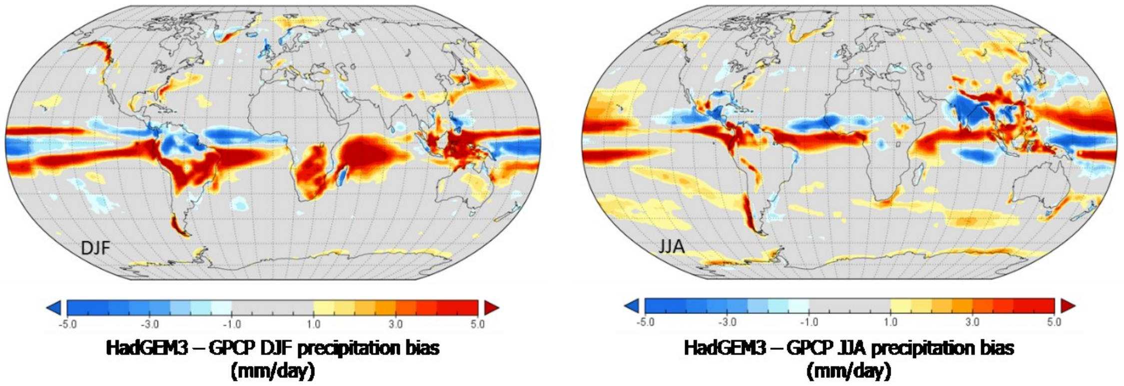

HadGEM3 – GPCP DJF precipitation bias (mm/day)

HadGEM3 – GPCP JJA precipitation bias (mm/day)

Figure 2-3: *Difference between HadGEM3-GA4 precipitation rate and GPCP observations for December-January-February (DJF) (left) and June-July-August (JJA) (right). HadGEM3-GA4 data is a 150-season average from a coupled control simulation with year 2000 conditions. GPCP data is the mean of the respective months from 1998-2003.*

southern flank of the ITCZ is consistent with a slightly too warm southern hemisphere, which is indeed what was suggested by Figure 2-1. It has been shown though that the issue is more subtle than just a surface temperature bias, since fixing the sea-surface temperatures to observed values turns out to only partially improve the tropical rainfall bias – rather, the imbalance in the total energy budgets of the two hemispheres must be corrected (Haywood et al., 2016).

The indication is that overall, HadGEM3-GA4 has a reasonably good representation of surface climate. The notable errors are in Southern Ocean sea-surface temperature, and – potentially related – in location of tropical rainfall. However, there is evidence that this is an error in the mean state which is somewhat independent of the model's response to forcing, in this case through the seasonal cycle and the variation of insolation throughout the year. This is also supported by the results of Haywood et al. (2013), who use the older generation HadGEM2-ES model and find that the response of Sahel precipitation to hemispherically asymmetric aerosol forcing qualitatively agrees with observations despite the model having a notable dry bias over the Sahel in its mean state (although with the absolute magnitude of the response also somewhat underestimated). This gives confidence that I can draw meaningful conclusions about the real climate system from the model's response to perturbed aerosol forcing, as will be presented in Chapters 4 and 5. This is especially true of northern mid-latitude climate, which broadly appears the best represented region.

2.2 Additional models

Data from simulations with two further models – provided by collaborators at NCAR and NASA GISS – are analysed in Chapters 3 and 4. These models are briefly described here, based on text provided by my collaborators. Surface temperature is the principle climate response I will investigate with these additional models, and so I also briefly evaluate climatological surface temperatures in each model.

2.2.1 CESM1

CESM1 was run in its standard CAM5-Chem configuration (Tilmes et al., 2015) with a horizontal resolution of 2.5° longitude x 1.875° latitude, and 30 vertical levels, with the model top at approximately 40 km. The atmosphere is coupled to the Community Land Atmosphere version 4 land surface model (Lawrence et al., 2011). In the present configuration, the vegetation distribution is fixed at its 2005 distribution and the CO_2 concentration is specified. The atmosphere model is coupled to the POP2 ocean and CICE4 sea-ice models, with an equivalent resolution of 1°.

The CAM5-Chem configuration (Tilmes et al., 2015) uses an online representation of tropospheric and stratospheric chemistry so that no chemical constituents are specified, other than specifying the long-lived greenhouse gases' concentrations in the surface layer. CAM5-Chem uses the MAM3 modal aerosol scheme (Liu et al., 2012), which simulates sulfate, black carbon, primary organic matter, secondary organic aerosol, dust, and sea salt aerosol species as an internal mixture in Aitken, accumulation, and coarse modes.

The model includes emissions of natural and anthropogenic SO_2 and natural DMS as sulfate precursors, and the gas-phase chemistry is coupled to the MAM3 aerosol scheme (Liu et al., 2012), so that the rate of formation of sulfate aerosols is dependent on the chemical state of the atmosphere. SO_2 can be converted to SO_4 through three oxidation pathways: by OH in the gas phase, or by either H_2O_2 or O_3 in the aqueous phase. In addition, the surface area of the prognostic tropospheric aerosols is used to compute heterogeneous reaction rates that affect gas-phase chemistry.

Shortwave radiative transfer is based on the RRTM_SW scheme (Clough et al., 2005) with 14 spectral bands, and aerosols interact with climate through both absorption and scattering of

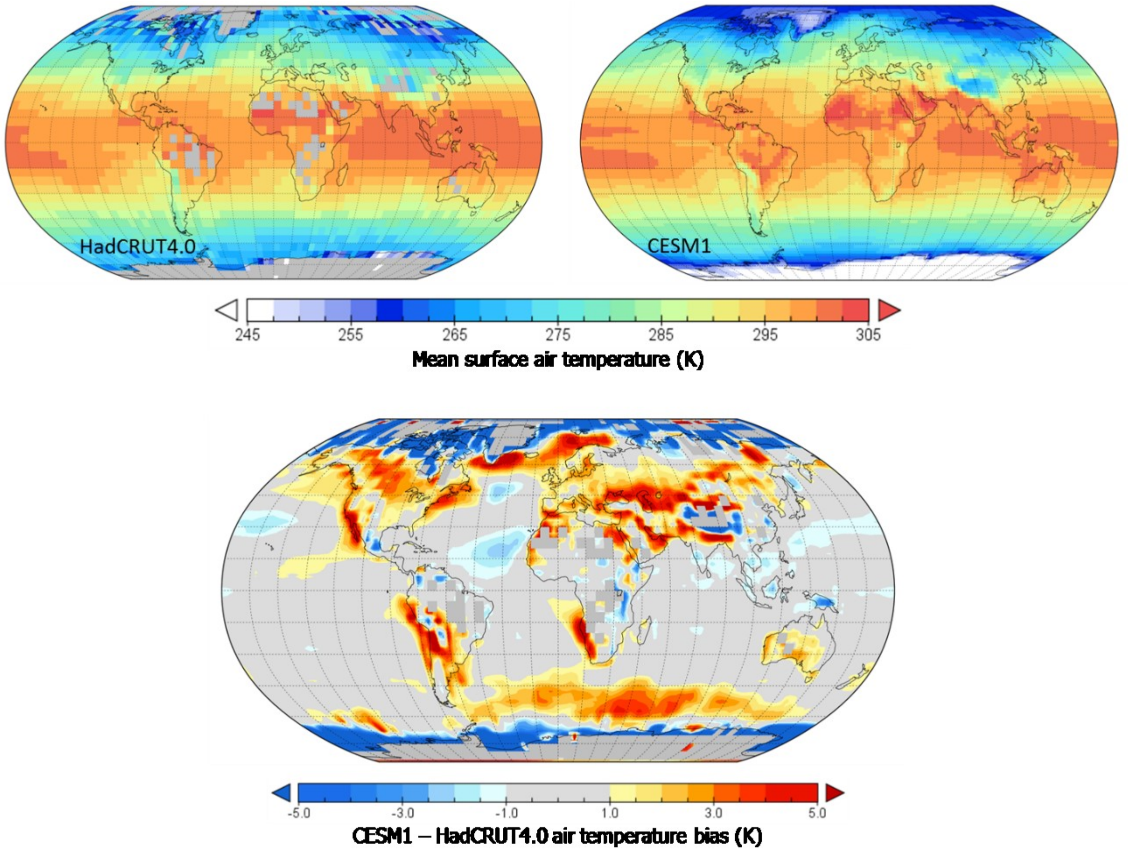

Figure 2-4: Comparison of CESM1 annual mean surface air temperature with HadCRUT4.0 observations. Top panels show the HadCRUT4.0 surface air temperature mean from 1998-2003 (left) and CESM1 150-year mean surface air temperature from a fully coupled control simulation with year-2000 GHG concentrations and aerosol emissions (right). Bottom panel shows the difference between the CESM1 mean and HadCRUT4.0.

radiation. Aerosol-cloud interactions allow for the effect of aerosols on both cloud droplet number and mass concentrations (Tilmes et al., 2015).

Annual mean surface air temperature from CESM1 is compared against HadCRUT4 observations in Figure 2-4. As with HadGEM3-GA4, the model data is from a coupled control simulation with year-2000 conditions, and the observations are a climatology from 1998-2003. The comparison is quite similar to HadGEM3-GA4; overall the global temperature distribution is very well captured, with only small anomalies over most of the world, and is particularly good over the tropics and mid-latitude oceans. There is a notable warm bias over some mid-latitude land regions where HadGEM3-GA4 performed relatively well, though conversely the bias in the Southern Ocean in CESM1 is somewhat less than in HadGEM3-GA4.

2.2.2 GISS-E2

GISS-E2 was run in the configuration used for CMIP5 with a horizontal resolution of 2.5° longitude x 2° latitude, and 40 vertical levels, with the model top at 0.1 hPa (80 km). The atmospheric model is coupled to the dynamic Russell ocean model with horizontal resolution of 1° latitude x 1.25° longitude, and 32 vertical levels as described in Schmidt et al. (2014) and Russell et al. (1995).

Well-mixed greenhouse gases were prescribed as described in Miller et al. (2014), but methane is only prescribed at the surface and is otherwise interactive with the chemistry. The ozone distribution is prognostic throughout the simulated atmosphere, and the chemical mechanism is described in Shindell et al. (2013b). In general, other atmospheric gas and aerosol constituents are also simulated online and interact with each other (via oxidants in both the gas and aqueous phases, heterogeneous chemistry, aerosol-influenced gas photolysis, and aerosol-coating of dust) and with climate (via radiative effects of ozone and methane, water vapour change due to chemistry, and aerosol direct and indirect effects) in a manner consistent with the physics of the rest of the model as described in Sect. 2 of Schmidt et al. (2014).

The aerosol scheme (Koch et al., 2006; Koch et al., 2011) includes sulfate, nitrate, elemental and organic carbon, along with secondary organic aerosols and natural sea-salt and mineral dust. Aerosols are parameterised as an external mixture of dry and dissolved aerosol, with particle size parameterised as a function of relative humidity (Schmidt et al., 2006). The sulfur scheme includes natural emissions of DMS, and natural and anthropogenic emissions of SO_2. SO_2 from these sources can be oxidised to SO_4 aerosol through two reaction pathways: by OH in the gas phase, or by H_2O_2 in the aqueous phase.

Aerosol direct effects are calculated following the Hansen et al. (1983) radiation model, with 6 spectral bands in the shortwave. Aerosol indirect effects are calculated as described in Menon et al. (2010), such that cloud droplet number concentration and autoconversion rate depend on the local concentration of aerosol.

As with CESM1, GISS-E2 surface air temperatures from a year-2000 control simulation are briefly compared here with HadCRUT4 observations in Figure 2-5. The top panels show that broadly GISS-E2 captures global temperature structures well. The bottom panel, showing the difference between model and observations, reveals a notable tropical warm bias, in particular over the eastern sides of the Atlantic and Pacific ocean basins. This is a known deficiency of the model

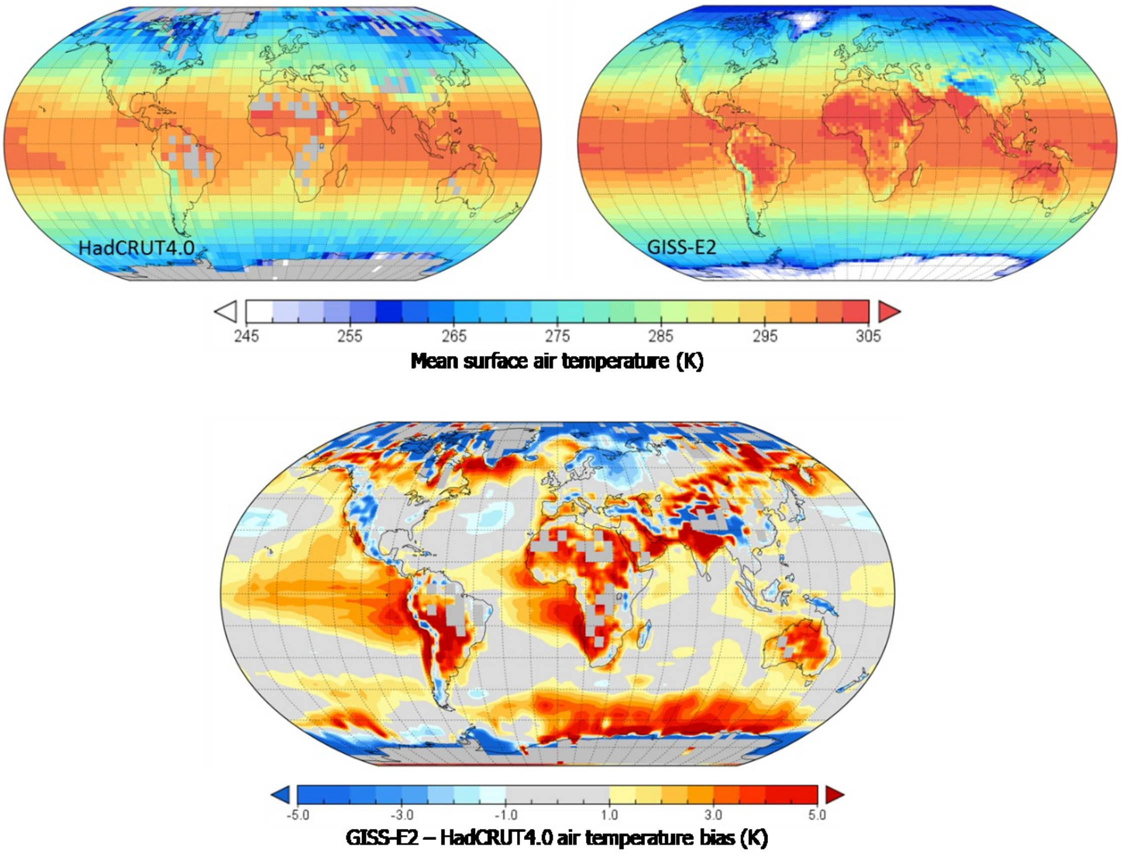

Figure 2-5: *Comparison of GISS-E2 annual mean surface air temperature with HadCRUT4.0 observations. Top panels show the HadCRUT4.0 surface air temperature mean from 1998-2003 (left) and GISS-E2 150-year mean surface air temperature from a fully coupled control simulation with year-2000 GHG concentrations and aerosol emissions (right). Bottom panel shows the difference between the GISS-E2 mean and HadCRUT4.0.*

and has been attributed to insufficient marine stratus cloud in these regions (Schmidt et al., 2014). Elsewhere, the northern mid-latitude regions show some localised anomalies but little in the way of large-scale consistent bias, similar to HadGEM3-GA4. As with both other models, the southern mid-latitudes are again dominated by a warm bias in the Southern Ocean, though the bias in GISS-E2 is not quite as widespread as in HadGEM3-GA4.

2.3 Summary

The key details and references for these three models are collated in Table 2-1. There is a range of complexity represented across different aspects of the models – HadGEM3-GA4 has the best horizontal and vertical resolution, for instance, but CESM1 and GISS-E2 have more detailed interactive chemistry schemes (where this version of HadGEM3-GA4 uses offline aerosol oxidant fields). GISS-E2 neglects oxidation of SO_2 by ozone, a pathway which is included in HadGEM3-GA4 and CESM1, but on the other hand GISS-E2 additionally simulates nitrate, which was not included in the other two models. However all three models are of the latest generation of leading climate models, and all represent present-day climate reasonably well, the most prominent biases being associated with representing clouds over certain ocean regions. The evidence from the HadGEM3-GA4 seasonal precipitation evaluation, and the results of Haywood et al. (2013), suggest however that small errors in the mean state do not prevent the models from responding appropriately to external forcing.

Table 2-1: *Key features and references for the HadGEM3-GA4, CESM1, and GISS-E2 composition-climate models.*

	HadGEM3-GA4	**CESM1**	**GISS-E2**
Primary model reference	Walters et al. (2014)	Tilmes et al. (2015)	Schmidt et al. (2014)
Aerosol scheme references	Bellouin et al. (2011) Jones et al. (2001)	Liu et al. (2012)	Koch et al. (2011) Koch et al. (2006)
Resolution (longitude x latitude)	1.875° x 1.25° 85 vertical levels, model top at 85 km	2.5° x 1.875° 30 vertical levels, model top at 40 km	2.5° x 2° 40 vertical levels, model top at 80km
Aerosol tracers	Sulfate, fossil-fuel black carbon, fossil-fuel organic carbon, biomass-burning, dust, sea salt	Sulfate, black carbon, primary organic matter, secondary organic aerosol, dust, sea salt	Sulfate, nitrate, black carbon, organic carbon, secondary organic aerosol, dust, sea salt
Indirect effects included	Yes (1st and 2nd)	Yes (1st and 2nd)	Yes (1st and 2nd)
SO_2 oxidation reactions included	OH (gas phase) H_2O_2, O_3 (aqueous phase)	OH (gas phase) H_2O_2, O_3 (aqueous phase)	OH (gas phase) H_2O_2 (aqueous phase)
Interactive oxidants	No (prescribed 4D oxidant fields)	Yes – online gas-phase chemistry	Yes – online gas-phase chemistry
Shortwave radiation	Edwards and Slingo (1996) 6 spectral bands	Clough et al. (2005) 14 spectral bands	Hansen et al. (1983) 6 spectral bands

3 Evaluation of modelled aerosol fields

As I investigate here the responses to regional aerosol emissions, it is especially critical to establish that the models employed have a satisfactory representation of regional aerosol distributions, and so I devote particular attention in this Chapter to evaluating the aerosol components of the models.

With HadGEM3-GA4, in later chapters I will investigate perturbations from a number of different regions across the northern hemisphere, and so in Sect. 3.1 I initially compare HadGEM3's simulated aerosol optical depth globally, against satellite datasets and the AERONET network of ground stations, both of which span much of the globe. Data from additional simulations with GISS-E2 and CESM1 is used in the next Chapter to look specifically at the response to sulfur emissions from China, and so in Sect. 3.2 I will validate all three models in further detail against a range of observations over the East Asian region.

3.1 Global AOD in HadGEM3-GA4

Figure 3-1 (top panel) shows the observed aerosol optical depth at 500 nm from 363 ground observation sites in the AERONET radiometer network (Holben et al., 2001). This represents all the sites worldwide able to provide an annual mean estimate for at least one year, averaged over all years for which an annual mean was available (generally ranging between 1994 and 2014 in different stations). This is compared in the lower panel with the 150-year mean AOD at 550nm from my coupled control simulation of HadGEM3-GA4 with year 2000 conditions, masked to the locations of the AERONET sites. The choice of 500nm for the AERONET observations was made as it was the closest wavelength that AERONET observes to 550nm at which HadGEM3, and the other models to be evaluated later, diagnose AOD. The coverage of the AERONET sites is imperfect - largely restricted to continental regions, with far greater numbers of sites in Europe and North America and poorer coverage over Africa and parts of Asia. Nonetheless, the largest anthropogenic aerosol-emitting regions of North America, Europe, northern India, and East and South East Asia, are well sampled.

Broadly, the comparison looks very good. Doing a simple station-by-station comparison, the correlation coefficient (R^2) between HadGEM3-GA4 and the 363 time-averaged AERONET sites

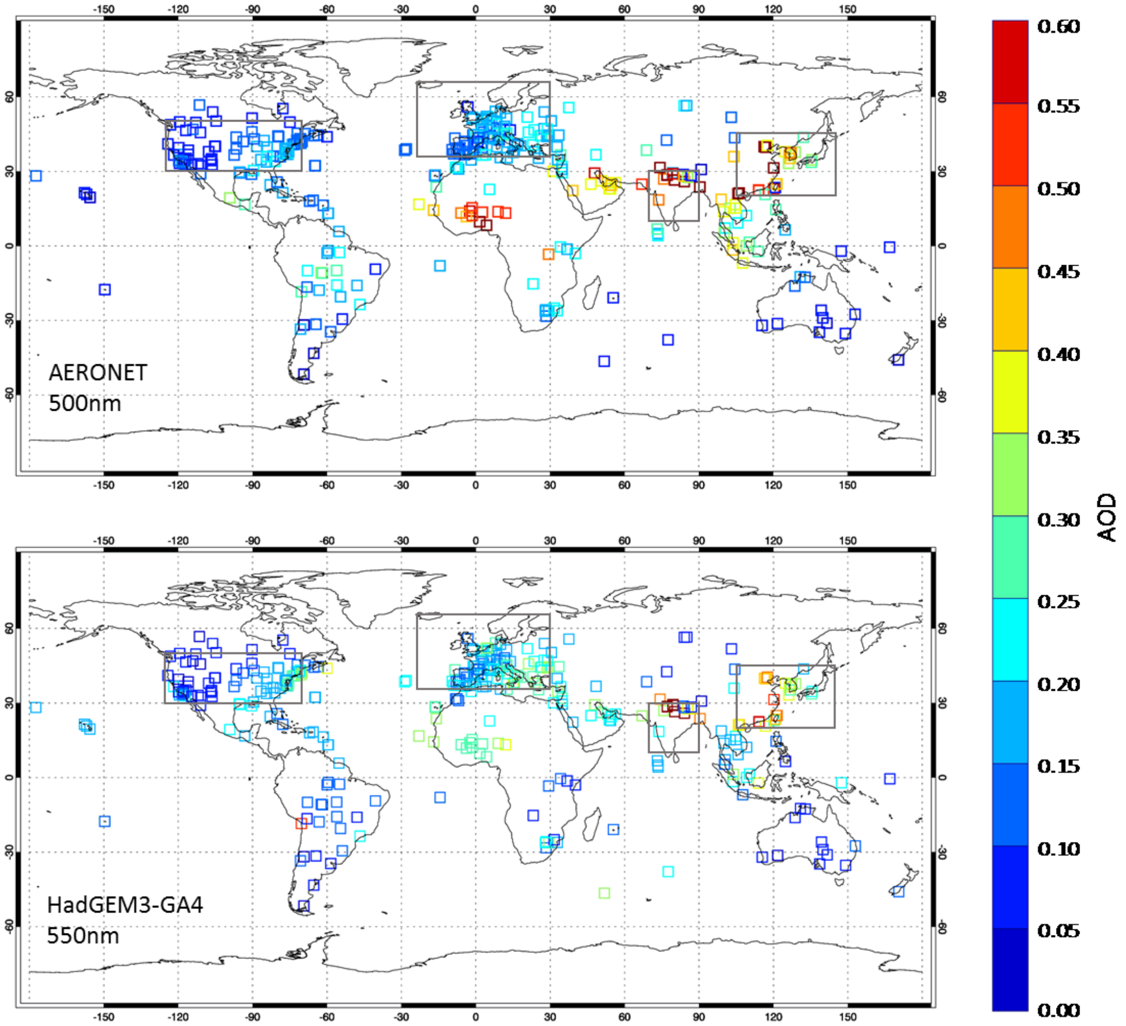

Figure 3-1: *Annual mean aerosol optical depth (AOD) observed by AERONET (top) and simulated in HadGEM3-GA4 (bottom). For AERONET the monthly mean climatology product at 500nm was used, which for each station provides a value averaged over all years that observations for a given month were available. Only stations which could provide a climatological value for all 12 months were then used to calculate an annual mean climatology. For the model, the 150-year mean AOD at 550nm from a year 2000 control simulation is masked to the locations of the qualifying AERONET sites by taking the value in the gridbox that each AERONET station is located in. Grey boxes indicate the regions used in Table 3-1.*

is 0.45, and when compared with each station the model's bias, on average, is +15%. Regionally, over South East Asia the model shows some underestimation, but otherwise all the major anthropogenic source regions compare well, with HadGEM3-GA4 capturing the relatively lower aerosol amounts over North America and Europe, and the much higher amounts over northern India and the east coast of China. Qualitatively, the comparison in Figure 3-1 is similar to the comparison of HadGEM3-GA4's predecessor – HadGEM2 – against a much smaller number of AERONET sites presented in Figure 3 of Bellouin et al. (2011), with the exception of some dust-dominated regions. In particular, the AOD in the Saharan region is much too low in Figure 3-1 whereas it compared more favourably in Bellouin et al. (2011), but conversely in northern Australia the comparison is reasonable in my Figure 3-1, whereas AOD in HadGEM2 was much too high in this region. This suggests that although Bellouin et al. (2011) used the same aerosol scheme (CLASSIC), the change of base model from HadGEM2 to HadGEM3-GA4 has nonetheless resulted in some differences particularly in the interactively-diagnosed dust emissions – improving the previous bias in one region but worsening it in another.

Also highlighted on Figure 3-1 are the four major industrialised regions – the US, Europe, East Asia, and India – which will be investigated subsequently in Chapter 5. Because some regions have a much higher density of AERONET sites, the global mean station bias of +15% is weighted towards regions with more observations. To better assess the model's performance regionally, scatter plots of observed AOD versus modelled AOD for each region separately are plotted in Figure 3-2, and the mean bias for stations within each box is also summarised in Table 3-1. The existing validation of the CLASSIC aerosol scheme in Bellouin et al. (2011), using the earlier HadGEM2 model version, compared against a much smaller number of AERONET sites, and did not provide a breakdown of the scatter plots over these different regions. The larger timespan for qualifying AERONET sites used here is therefore invaluable for extending the comparison against observations, in addition to the fact that I use a newer version of the base climate model than was previously evaluated.

As with the global value, the model tends to be biased slightly high on average within most regions, and very high over India. However, the India and East Asia regions both have relatively small numbers of stations, and the values for these regions are heavily skewed by two stations in India and one in East Asia with very high (>250%) relative biases. Assuming that there are no observational errors, this may be a genuine error in the model, but could also occur as a result of the coarse resolution of the model being unable to capture very localised conditions. If these three anomalous stations are discounted, then the remaining bias over India is close to zero (4.3%), and the bias over East Asia becomes negative (-13.6%), which better reflects the visual comparison between the top and bottom panels in Figure 3-1, where broadly over East Asia the model appears to be underestimating AOD slightly. This is also indicated by the East Asia scatter plot (Figure 3-2, bottom right panel), which shows that for the majority of stations in East Asia the model slightly underestimates the observed value, as the points mostly fall below the y=x line, particularly for high AOD values.

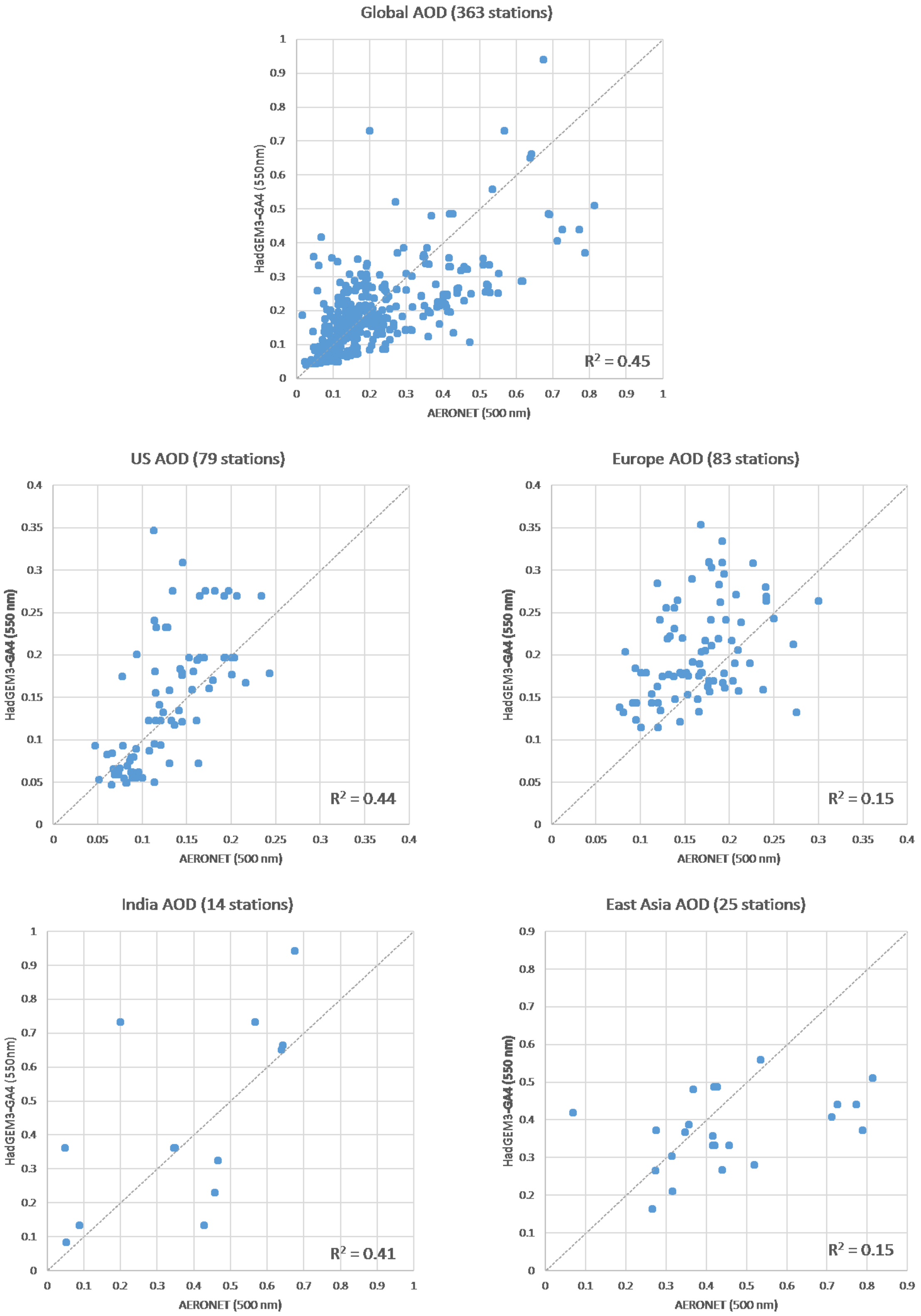

Figure 3-2: *Scatter plots of AERONET observed annual mean AOD at 500 nm against HadGEM3-GA4 total AOD at 550nm from a year-2000 control simulation. Plots are shown for all AERONET stations globally, and those in the US (125°W-70°W, 30°N-50°N), Europe (24°W-30°E, 36°N-66°N), India (70°E-90°E, 10°N-30°N), or East Asia (105°E-145°E, 20°N-45°N) only. Each point corresponds to a single AERONET station for which annual mean data was available. The y=x line, indicating perfect correspondence between model and observations, is shown in dashed grey.*

__Table 3-1:__ Mean bias in HadGEM3-GA4 total AOD when compared to AERONET stations, within each region listed. For AERONET the monthly mean climatology product at 500nm was used, and only stations which could provide a climatological value for all 12 months were then used to calculate an annual mean climatology. For the model, the 150-year annual mean AOD at 550nm from a year 2000 control simulation is masked to the locations of the qualifying AERONET sites by taking the value in the gridbox that each AERONET station is located in. A percentage bias is calculated for each station, and averaged over all stations within the domain specified (see Figure 3-1 for a map of the different regional domains).

REGION	MEAN STATION BIAS
Global **363 stations**	+15.3%
United States (125°W-70°W, 30°N-50°N) **79 stations**	+13.0%
Europe (24°W-30°E, 36°N-66°N) **83 stations**	+29.8%
India (70°E-90°E, 10°N-30°N) **14 stations**	+69.7%*
East Asia (105°E-145°E, 20°N-45°N) **25 stations**	+7.53%**

** For India, two stations out of 14 (Ev-K2-CNR and Nainital, both at high altitude – 5.1 km and 1.9 km respectively) had unusually large biases (+657.9% and +266.2%); discounting these two stations reduces the mean India bias to +4.3%*

*** For East Asia, one station out of 25 (Lulin, again at high altitude – 2.9 km) had an unusually large bias of +514.4%; removing this one station changes the mean East Asia bias to -13.6%*

Figure 3-1 shows that the model also substantially underestimates AOD around the dust-producing regions of the Sahara and Arabian Peninsula, suggesting that dust emissions – which are simulated interactively – may be poorly represented. Dust can also be an important contributor to AOD in major anthropogenic emission regions like India and China as well, and so to better assess the anthropogenic and natural contributions, I also use the AERONET fine and coarse mode products, again averaged between 1994-2014 for all stations with enough data to calculate at least one annual mean (calculated here whenever there is a monthly value reported for at least 9 out of 12 months from a given year). Coarse mode AOD detects larger particle sizes that correspond mainly to uplifted dust, whilst the fine mode corresponds to other aerosol species including both anthropogenic emissions and biomass burning, which result in finer

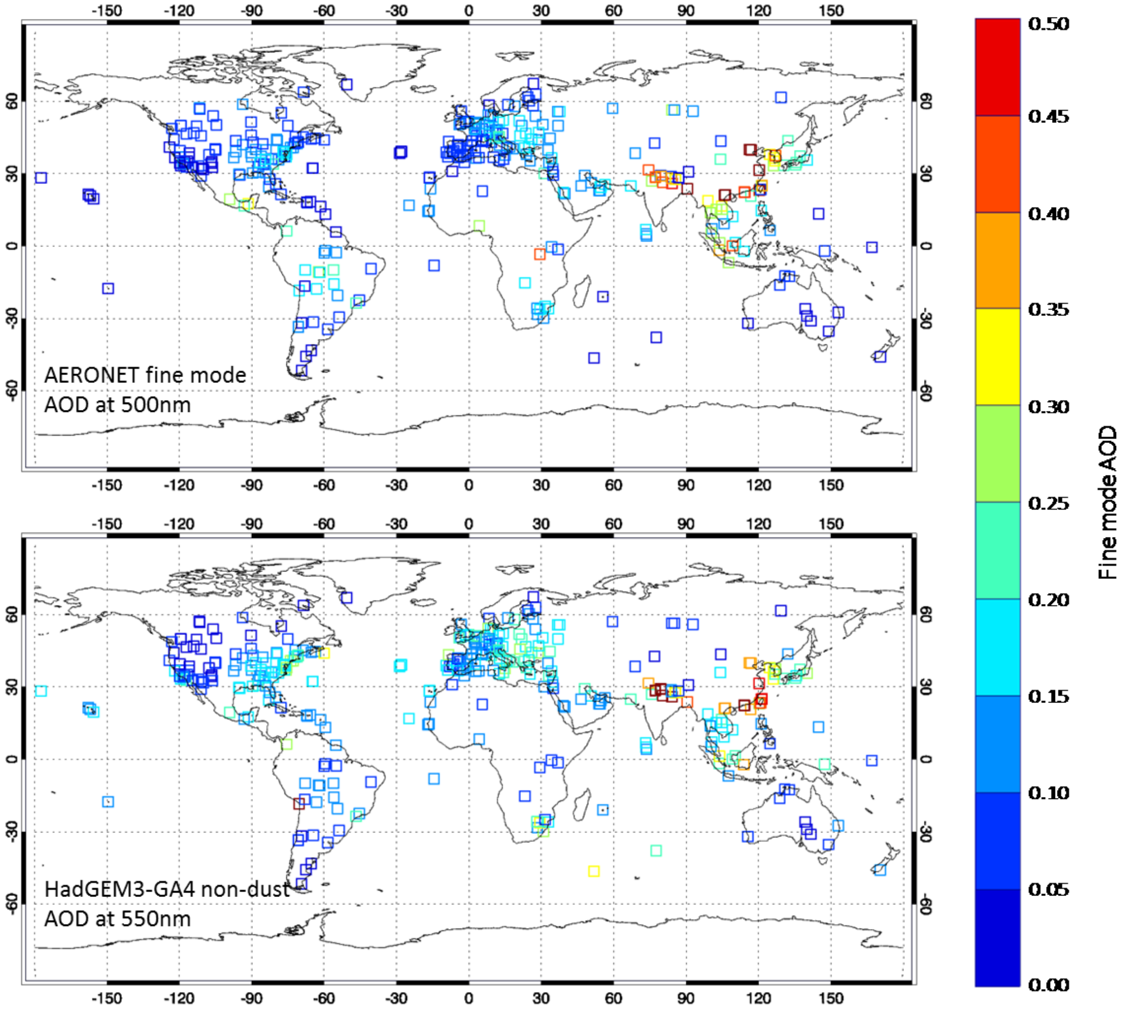

Figure 3-3: *Annual mean fine mode AOD observed by AERONET (top) and non-dust AOD simulated in HadGEM3-GA4 (bottom). For AERONET monthly mean data at 500nm were used, and for each station annual means were calculated for any years that had data for at least 9 out of 12 months, and then averaged over all available years between 1994-2014. For the model, the 150-year mean AOD at 550nm from a year 2000 control simulation is masked to the locations of the qualifying AERONET sites by taking the value in the gridbox that each AERONET station is located in.*

particle sizes. Figure 3-3 compares the AERONET fine mode AOD with HadGEM3-GA4 AOD due to all species except dust, while Figure 3-4 compares the AERONET coarse mode AOD with HadGEM3-GA4 dust AOD.

Figure 3-3 (fine mode AOD) shows largely the same comparison between HadGEM3-GA4 and AERONET within the anthropogenic-dominated regions marked out in Figure 3-1 for the total AOD above – slight overestimation of AOD in Europe and the US, but a slight underestimation in general in East Asia, indicating that this underestimation seen in Figure 3-1 and also the East Asia panel of Figure 3-2 is likely due to underestimating the large anthropogenic contribution in this area. Within India, HadGEM3-GA4 shows a slight overestimation of the fine mode,

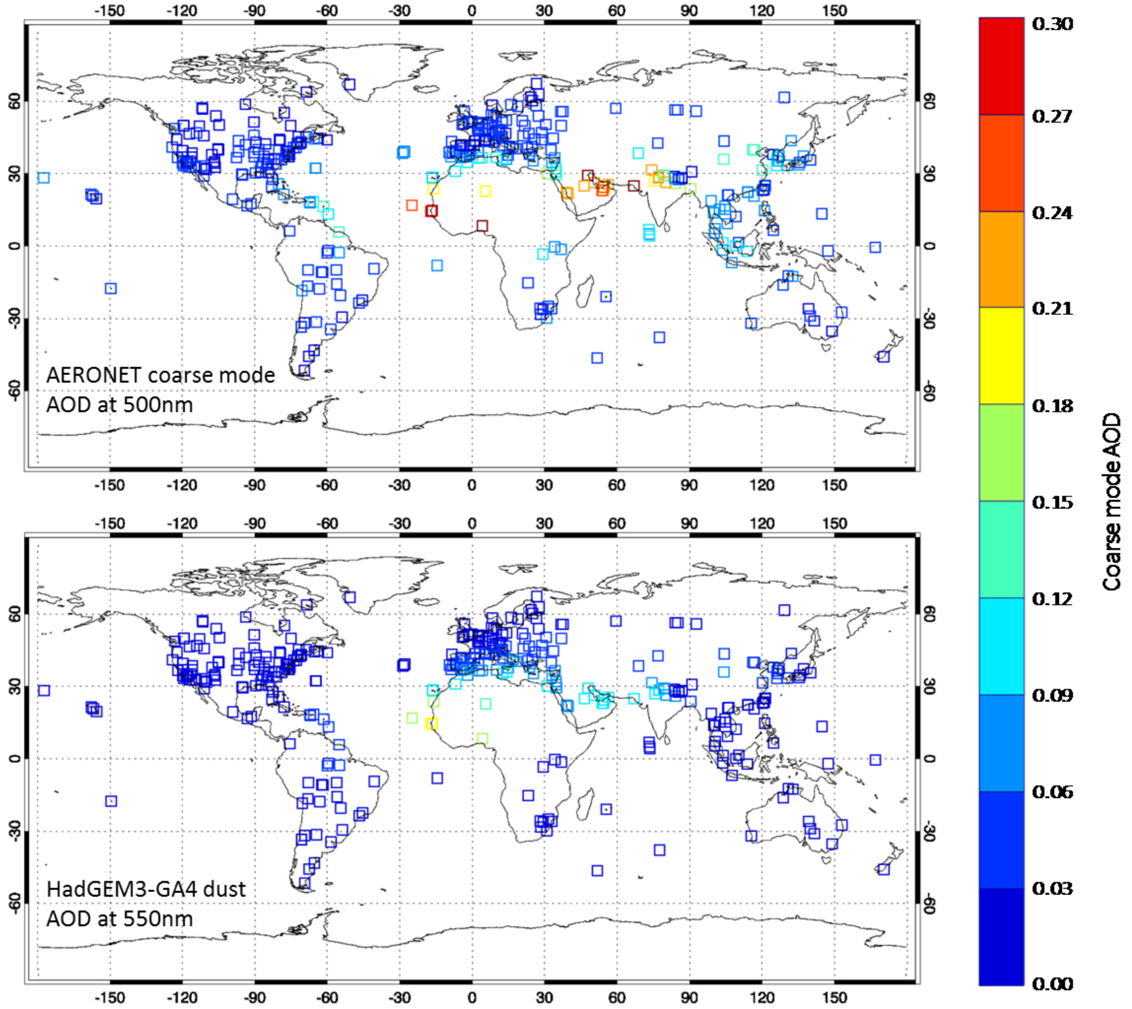

Figure 3-4: Annual mean coarse mode AOD observed by AERONET (top) and dust-only AOD simulated in HadGEM3-GA4 (bottom). For AERONET monthly mean data at 500nm were used, and for each station annual means were calculated for any years that had data for at least 9 out of 12 months, and then averaged over all available years between 1994-2014. For the model, the 150-year mean AOD at 550nm from a year 2000 control simulation is masked to the locations of the qualifying AERONET sites by taking the value in the gridbox that each AERONET station is located in.

suggesting that the relatively good total AOD seen in Figure 3-1 may be due to compensating errors in this region, with a slight overestimation of the anthropogenic aerosol over India, and underestimation of the natural aerosol (Figure 3-4). Overall the errors in fine mode aerosol are still small in all the industrial regions highlighted previously. Although there are extremely few AERONET observations in Central Africa, there is an indication that HadGEM3-GA4 may underestimate the fine-mode AOD in this region, and also over some parts of the Amazon region in South America, both of which are likely dominated by biomass-burning. Poor representation of tropical biomass burning is a known deficiency of the CLASSIC aerosol scheme used here with HadGEM3-GA4 (Johnson et al., 2016), however this is unlikely to substantially affect the perturbations to emissions from Northern Hemisphere industrialised regions investigated in subsequent chapters here.

As suspected from Figure 3-1, the comparison of coarse mode AOD (Figure 3-4) reveals that HadGEM3-GA4 substantially underestimates dust optical depths over the Sahara, Arabian Peninsula, and India. A severe underestimation of natural aerosol could result in an overestimation of anthropogenic aerosol radiative forcing, due to less saturation of aerosol indirect effects (Carslaw et al., 2013). This suggests the model may overestimate anthropogenic forcing over India, however this is the only industrialised region that appears particularly affected by this underestimation of natural aerosol. Coarse mode AOD is also underestimated over East Asia, however the observed values are already much smaller here, and the fine mode (presumably anthropogenic) fraction was also slightly underestimated over the same region.

To get a more complete global coverage, I also compare against satellite observations from the MODIS and MISR instruments. MODIS (Moderate Resolution Imaging Spectroradiometer) is flown on both the Terra and Aqua satellites, whilst MISR (Multi-angle Imaging SpectroRadiometer) is flown on Terra. For MODIS I use the collection 6 combined Deep Blue + Dark Target gridded monthly AOD product at 550 nm (Levy et al., 2013) (available from https://ladsweb.nascom.nasa.gov/), averaged from both Terra and Aqua satellites, and take a 10-year average from 2003-2012 (2003 being the earliest year that data from both satellites is available). For MISR I use the Version 31 gridded monthly AOD product (Kahn et al., 2010) (available from https://eosweb.larc.nasa.gov/) at 555 nm over a 15-year averaging period, from 2000-2014 (2000 being the earliest year MISR data is available). The mean AOD from both instruments is shown in the top panel of Figure 3-5, whilst the 150-year averaged AOD at 550nm from HadGEM3-GA4 is shown in the lower panel, interpolated now across the whole model domain rather than masked to particular grid-points.

Globally over land regions the model again appears to perform well overall, capturing the relatively lower values over North America and Europe and the elevated AOD values over India and East Asia in both spatial extent and magnitude (a more detailed comparison over East Asia follows in Sect. 3.2.2). Again though, the model is seen to be substantially underestimating AOD in dust-dominated areas over West Africa, the Sahara, and Arabia, and also underestimates some biomass-burning dominated regions in Central Africa and South America. The comparison with satellite instruments also reveals what AERONET could not, which is that AOD over some ocean areas, in particular the Southern Ocean and the Atlantic and Pacific storm track regions, is somewhat overestimated in the model – indicating that while levels of dust may be too low, for sea salt aerosol the model may have the opposite issue. This could alternatively be a sampling limitation of the observations however, since sea salt concentrations are likely to be higher in stormy conditions, where high cloud cover would prevent satellite observations. In either case, although one or both of the interactively-simulated natural aerosols are poorly represented, this comparison again suggests that anthropogenic aerosol optical depth – for which the aerosol emissions are prescribed – is reasonably well simulated in distribution and magnitude.

Globally averaged, the area-weighted mean AOD observed by MODIS is 0.17, while for MISR it is 0.15, so both instruments are in reasonable agreement. Globally HadGEM3-GA4 is biased a little high with an area-weighted global mean AOD of 0.22, though from Figure 3-5 it is clear this will be influenced heavily by the biases over the sea-salt dominated ocean regions.

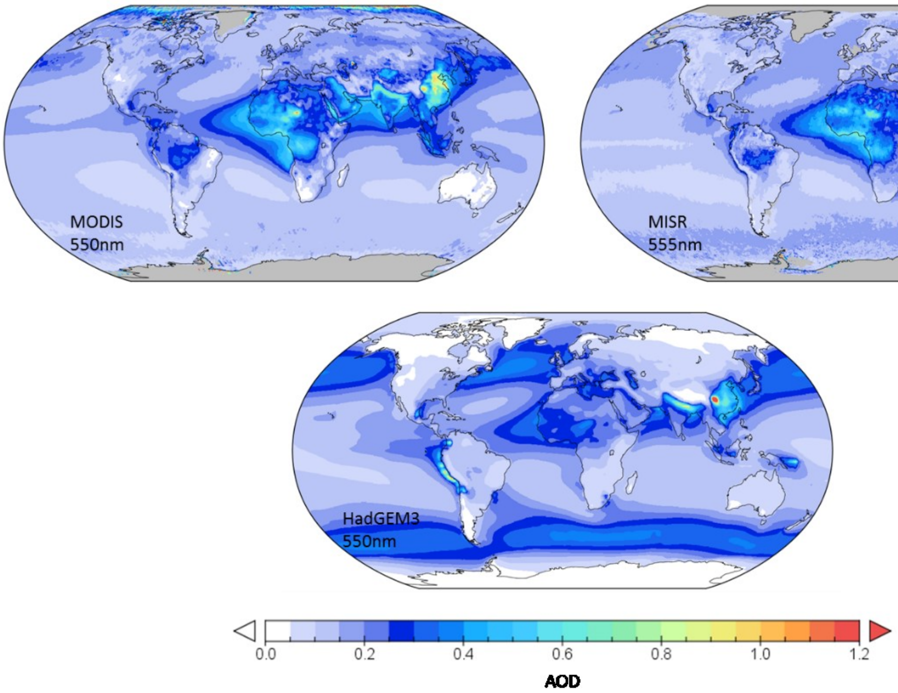

Figure 3-5: *Annual mean AOD observed by MODIS (top left), MISR (top right), and as simulated by HadGEM3-GA4 (bottom). For MODIS, the Collection 6 combined Dark Target + Deep Blue 550nm AOD estimate from both Terra and Aqua platforms is averaged over all months from 2003-2012. For MISR the version 31 555nm AOD best estimate is averaged over all months from 2000 to 2014. For the model, the diagnosed AOD at 550nm is averaged over 150 years from a year 2000 control simulation.*

3.2 Regional sulfate over China in HadGEM3-GA4, GISS-E2, and CESM1

Of arguably greater relevance is the picture over particular anthropogenic emission-dominated regions. In Chapter 4, I will compare and contrast the response of HadGEM3-GA4, GISS-E2, and CESM1 specifically to a perturbation to Chinese SO_2 emissions, and so here I explore in more detail the simulation of aerosols, and particularly sulfate, in all three of these models over the East Asian region.

Unfortunately, the AOD diagnosed by the models is not completely equivalent: HadGEM3-GA4 diagnosed clear-sky AOD, which is done in this model by calculating the relative humidity in the cloud-free portion of each grid-box, and using this adjusted humidity to calculate the size of the aerosol droplets in the optical depth calculation (Bellouin et al., 2007). However CESM1 uses the unadjusted grid-box relative humidity to calculate the droplet sizes in its optical depth calculation, thereby providing an all-sky AOD calculation (Neale et al., 2012). GISS-E2 diagnosed both all-sky and clear-sky AOD, and unless otherwise stated I will use its clear-sky AOD, as it is more directly comparable with satellite retrievals of AOD (Kahn et al., 2010; Levy et al., 2013).

Figure 3-6 shows the modelled AOD over Asia from each of the models. In each case, as with HadGEM3-GA4 above, the data are averaged over the last 150 years from 200-year control simulations, which were driven by the same repeating year 2000 anthropogenic aerosol emissions from the ACCMIP dataset (Lamarque et al., 2010). These anthropogenic emissions correspond to around 104 Tg yr^{-1} of SO_2, and 44 Tg yr^{-1} of carbonaceous aerosol. Emission rates of natural aerosols like dust and sea salt are determined by the individual models, and so these can vary. It is clear that there are distinct differences between the regional AODs in these models – in particular, HadGEM3-GA4 simulates a much higher AOD than either the other two over eastern China, with a particularly intense peak that drops off rapidly with distance from the emission regions. CESM1 and GISS-E2 have much lower peak AOD values over the most industrialised regions, though also with a less steep gradient in AOD spreading out from the region. Comparing the GISS-E2 clear- and all-sky diagnostics (top row of Figure 3-6), it is clear that all-sky AOD is much higher than clear-sky AOD in the region. This would suggest that CESM1, when compared like-for-like, has the lowest AOD of all. However, the size of the difference between clear- and all-sky AODs is likely to be model dependent, since it will depend on the cloud amount and on how hygroscopic growth of aerosol particles is simulated, and so it is possible that GISS-E2 could simply be unusually sensitive to the choice of clear- or all-sky AOD diagnostic.

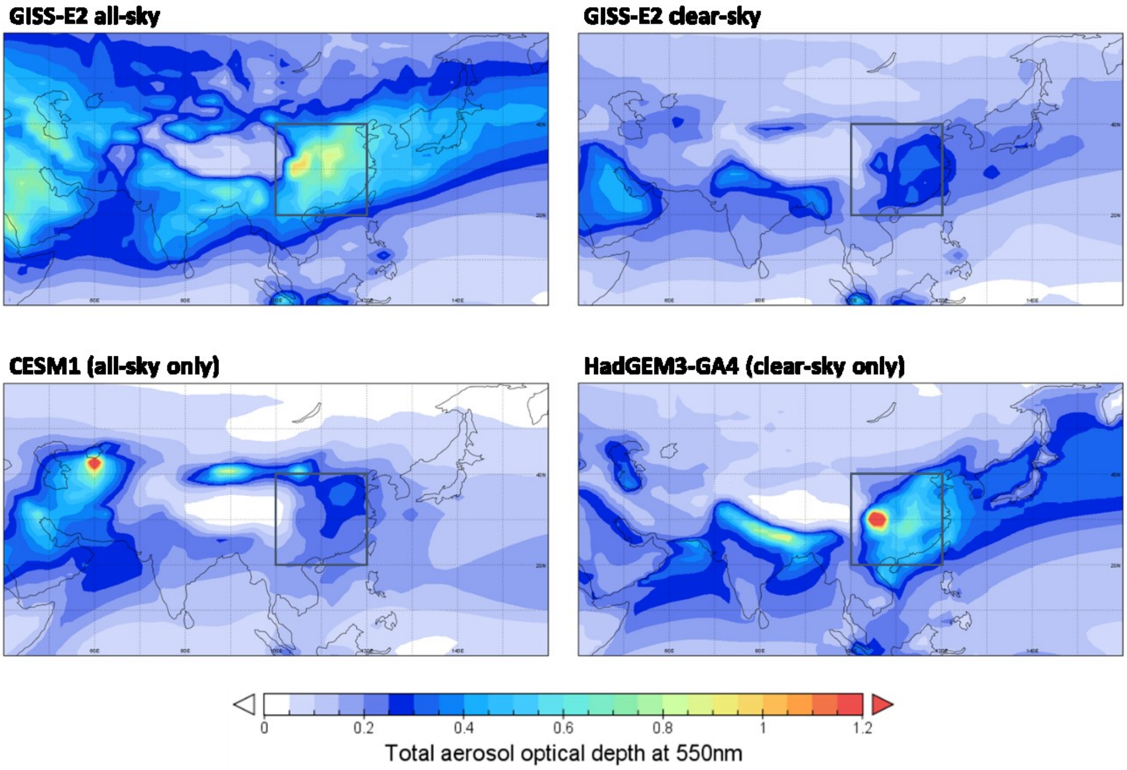

Figure 3-6: *Annual mean total aerosol optical depth at 550nm over Asia in GISS-E2, CESM1, and HadGEM3-GA4. For all models, AOD is a 150-year mean from a control simulation with perpetual year 2000 conditions. AOD is diagnosed for both all-sky and clear-sky conditions in GISS-E2 (top row), for all-sky conditions only in CESM1 (bottom left), and for clear-sky conditions only in HadGEM3-GA4 (bottom right). Grey box shows the E. China region analysed in the text.*

A detailed inter-comparison of AOD around China with this combination of models has not been undertaken previously, and so to get an indication of whether the different model-simulated AODs are realistic in the region of interest, I compare first the mean AOD from each model's control simulation with the AERONET stations in Asia. As before, I use the mean observed AOD at 500 nm from all AERONET stations able to provide an annual mean estimate for one or more years between 1994 and 2014, and compare this with the annual mean AODs at 550 nm from the three models, masked to the locations of the AERONET stations. The comparison is shown in Figure 3-7, where the plot region is zoomed to the Asian region. Focusing on the eight stations in the east China region of 100°-120°E, 20°-40°N (hereafter E. China) which is seen to contain the main concentration of aerosol from China (grey box in Figure 3-6 above), we find that HadGEM3-GA4 compares best with AERONET in this region with a mean station bias of -22%, whilst both GISS-E2 and CESM1 appear to be biased lower in this part of the world, with mean biases of -56% and -60% respectively.

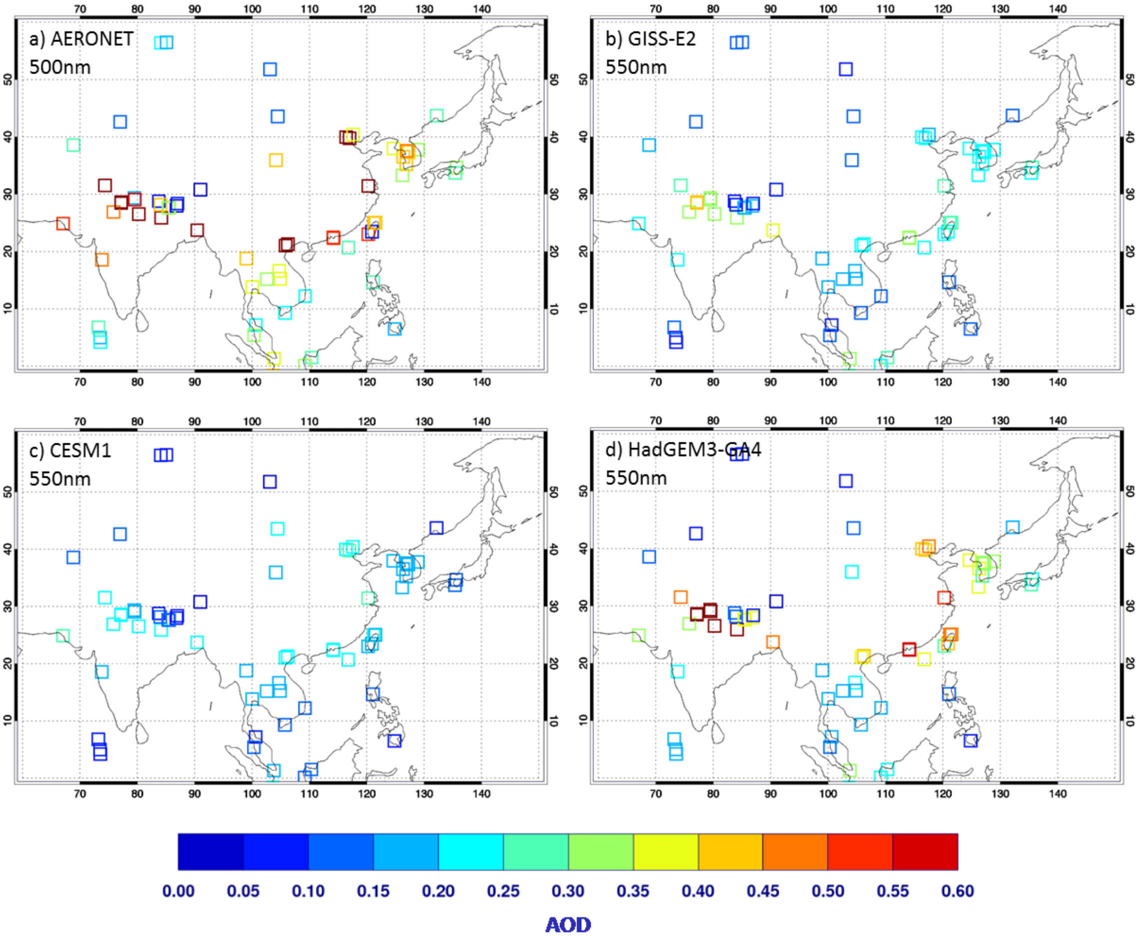

Figure 3-7: *Annual mean AOD observed at 500nm by AERONET (a), and diagnosed at 550nm from GISS-E2 (b), CESM1 (c), and HadGEM3-GA4 (d). For AERONET, the monthly mean climatology product was used, which for each station provides a value for each month averaged from all years that observations for that month were available. Only stations which could provide a climatological value for all 12 months were then used to calculate an annual mean climatology. For the models, the 150-year mean AOD from each model's control (2000) simulation is masked to the locations of the qualifying AERONET sites by taking the value in the gridbox that each AERONET station is located in. For HadGEM3-GA4 and GISS-E2 the AOD is diagnosed for clear-sky conditions, whereas in CESM1 all-sky AOD is diagnosed, which is expected to be higher than the equivalent clear-sky value.*

I also calculate the area-weighted regional mean AOD as observed by the MODIS and MISR satellite instruments. For MODIS the area-weighted E. China mean AOD is 0.51, whilst for MISR it is 0.31, so although the two instruments gave fairly close global mean values, there is a considerable uncertainty regionally between these instruments. HadGEM3-GA4 overestimates the AOD regionally compared with both instruments (though only slightly so when compared to MODIS), with a regional average AOD of 0.58, whilst GISS-E2 and CESM1 underestimate it with regionally-averaged AODs of 0.23 for both models. Globally, GISS-E2 and CESM1 both also underestimate AOD, with 0.13 and 0.12 respectively (compared with 0.17 and 0.15 from MODIS and MISR), however they are either closer than or just as close as HadGEM3-GA4 (with 0.22). Given that CESM1 diagnosed all-sky AOD – whereas satellite retrievals are only possible for clear-sky conditions – the underestimate for this model is likely greater than these numbers suggest, since the effect of greater hygroscopic growth of aerosol particles in clouds means that AOD calculated for clear-sky conditions will be lower than the equivalent all-sky AOD.

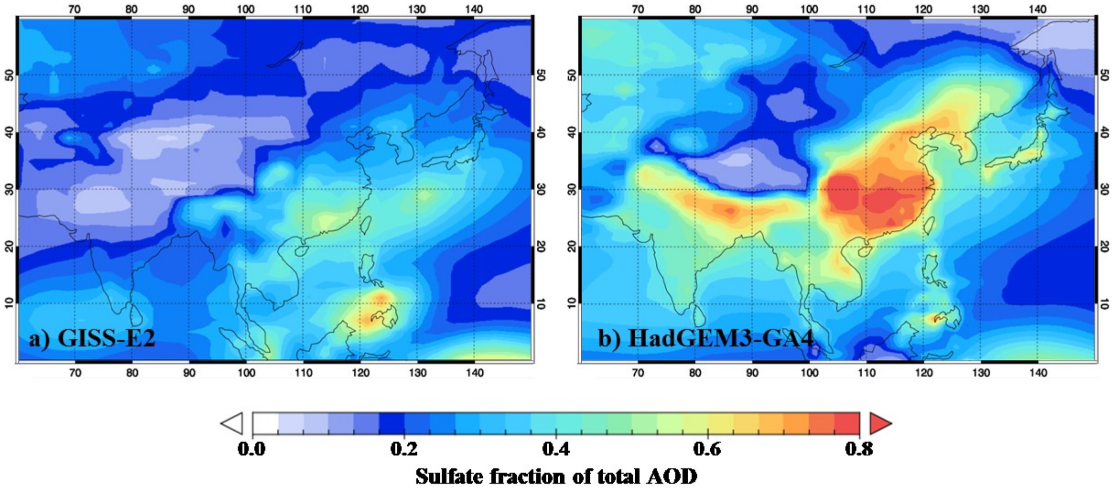

Figure 3-8: *Fraction of total AOD at 550nm made up by sulfate in GISS-E2 (a), and HadGEM3-GA4 (b), over the Asian region. Calculated in each case as the ratio of SO₄ clear-sky optical depth to total clear-sky AOD in the 150-year mean from each model's control simulation.*

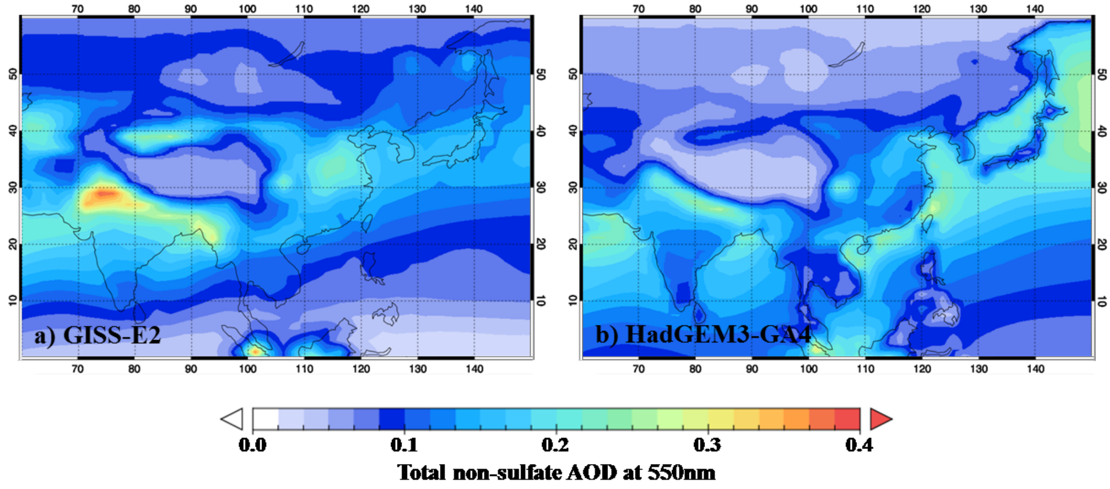

Figure 3-9: *Non-sulfate clear-sky AOD at 550nm over Asia in GISS-E2 (a), and HadGEM3-GA4 (b). Calculated in each case by subtracting the clear-sky sulfate optical depth from total clear-sky AOD in the 150-year mean from each model's control simulation. The average within the E. China region (100°E-120°E, 20°N-40°N, indicated by grey box) is 0.15 for GISS-E2 and 0.19 for HadGEM3-GA4.*

There is evidently considerable variation in the observations as well as the models. Although globally-averaged GISS-E2 is closest to MODIS and MISR, tentatively it is HadGEM3-GA4 that seems to have the more accurate AOD over China, comparing better regionally with both AERONET and MODIS, though poorer against MISR. This suggests that the more concentrated aerosol burden and larger AOD simulated by HadGEM3-GA4 over this region may be more realistic. However, since these observations only measure total AOD and cannot differentiate by species, the comparison cannot show for certain that the sulfate optical depth specifically is more realistic in HadGEM3-GA4, which is what will be of particular relevance for the perturbations to sulfur emissions investigated in Chapters 4 and 5. Based on the reduction in AOD simulated when sulfur dioxide emissions from the region are removed (see Chapter 4), the AOD over E. China due specifically to Chinese SO_2 represents 50% of the regional climatological total AOD in HadGEM3-GA4, compared with 34% in CESM1 and only 20% in GISS-E2. So even if the total AOD in HadGEM3-GA4 is more realistic, there is still considerable variation between the models as to what fraction of that total AOD is due to Chinese SO_2 emissions.

This is illustrated further for the two extreme cases, HadGEM3-GA4 and GISS-E2, in Figure 3-8, which shows that the fraction of climatological AOD made up by sulfate is consistently higher across the east Asian region in HadGEM3-GA4 than in GISS-E2. However, the total non-sulfate AOD is fairly similar across the region in these two models (Figure 3-9), indicating that the stark difference in the fractional contribution of sulfate comes primarily from HadGEM3-GA4 simulating much greater sulfate AOD alone. Given that regionally GISS-E2 appeared to underestimate total AOD, this would then suggest that either the higher sulfate AOD in HadGEM3-GA4 is more realistic, or else both models underestimate the non-sulfate AOD.

Figures 3-10 and 3-11 show the AERONET observed fine and coarse mode AOD over Asia, compared against GISS-E2 and HadGEM3-GA4 non-dust (fine mode) and dust (coarse mode) AOD respectively. From these it is clear that the underestimation of total AOD in GISS-E2 comes mainly from the fine mode (mainly anthropogenic) contribution – the dust AOD in GISS is no worse than in HadGEM3-GA4 over East Asia, and considerably closer to the observations over India. The fine mode aerosol itself contains contributions from multiple different anthropogenic emission species however, which cannot be differentiated by these observations.

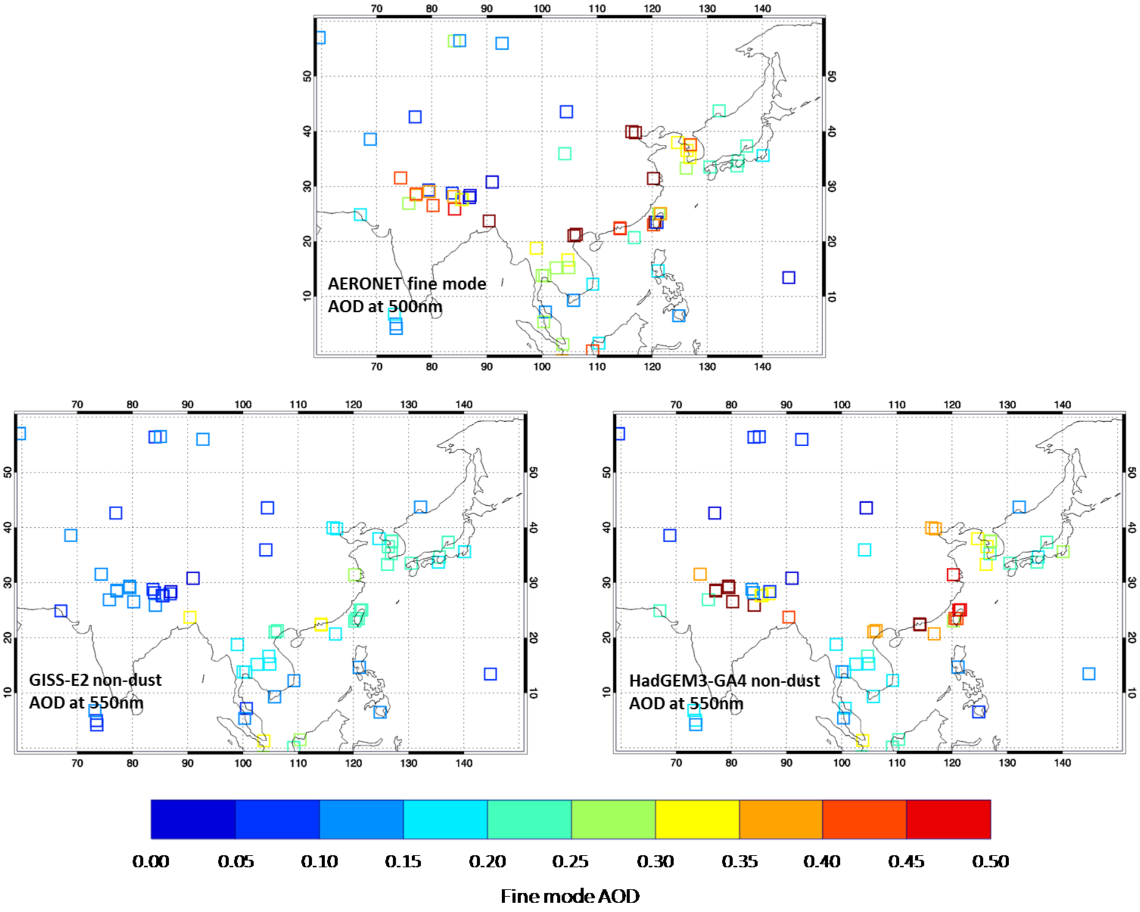

Figure 3-10: *AERONET observed annual mean fine mode AOD at 500 nm (top), compared with GISS-E2 (bottom left) and HadGEM3-GA4 (bottom right) non-dust AOD at 550 nm, masked to the locations of the AERONET observation stations. AERONET observations show stations for which an annual mean (at least 9 out of 12 months) could be calculated for at least one year between 1994 and 2014, averaged over all qualifying years. Model AODs are 150-year averages from simulations with repeated year-2000 aerosol emissions.*

To try and better constrain whether the sulfate content (rather than total aerosol) is correct, I therefore also compare against the surface sulfate observations conducted in China reported by Zhang et al. (2012) for 2006-2007 (Figure 3-12). However, by this measure all three models turn out to perform extremely poorly, with HadGEM3-GA4 having a mean bias of -71% (-66% if urban stations are excluded), CESM1 a mean bias of -71% (unchanged in urban stations are excluded), and GISS-E2 a mean bias of -87% (-86% when urban stations are excluded). Although HadGEM3-GA4 and CESM1 are slightly closer to the observed values, the large underestimation despite the relatively good column AOD comparison in HadGEM3-GA4 suggests that at least this model has difficulty representing the vertical profile of sulfate aerosol, and so this comparison with surface measurements may not be particularly useful in constraining the sulfate optical depth or column-integrated burdens. Large underestimations of surface sulfate concentration over East

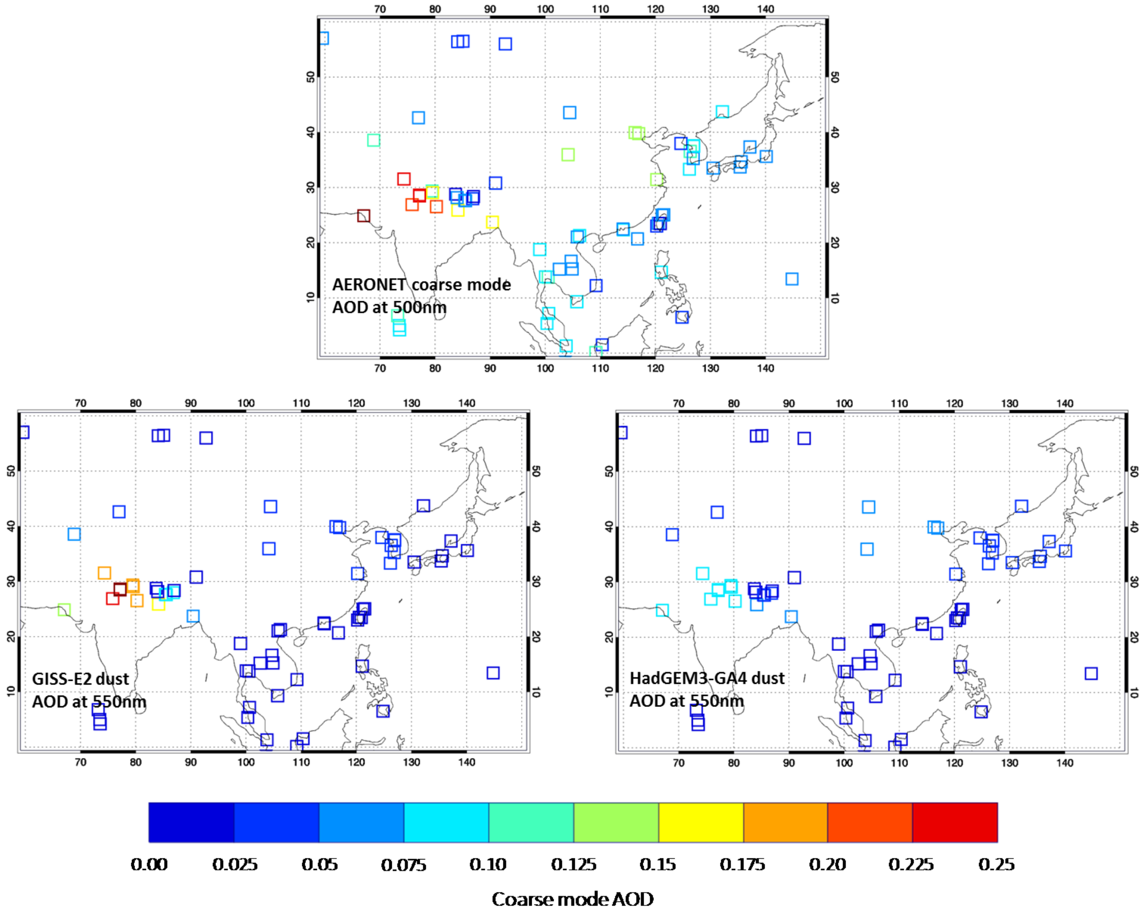

Figure 3-11: *As Figure 3-10, but for coarse mode AERONET observed AOD (top), compared with dust AOD simulated in GISS-E2 (bottom left) and HadGEM3-GA4 (bottom right).*

Asia have been reported previously for two other models, MIROC and NICAM, by Goto et al. (2015), suggesting that this is a problem common to many current generation models.

It seems plausible that any differences in the processing of sulfate aerosol could apply to all polluted regions, and not just over China. Indeed, Figure 3-13 shows that the spatial pattern of the climatological sulfate burden over other major emission regions such as the United States shows a similar characteristic to that over China, with HadGEM3-GA4 and CESM1 having higher burdens close to the emission source regions, whilst GISS-E2 has a more diffuse sulfate distribution. With this in mind, I have also validated the models against surface sulfate observations from the Interagency Monitoring of Protected Visual Environments (IMPROVE) network in the United States (Malm et al., 1994), a dataset with a far more extensive record than the Zhang et al. (2012) dataset for China. Taking 61 IMPROVE stations which have data for at least 6 years between 1995 and 2005, I find that over the United States all three models are

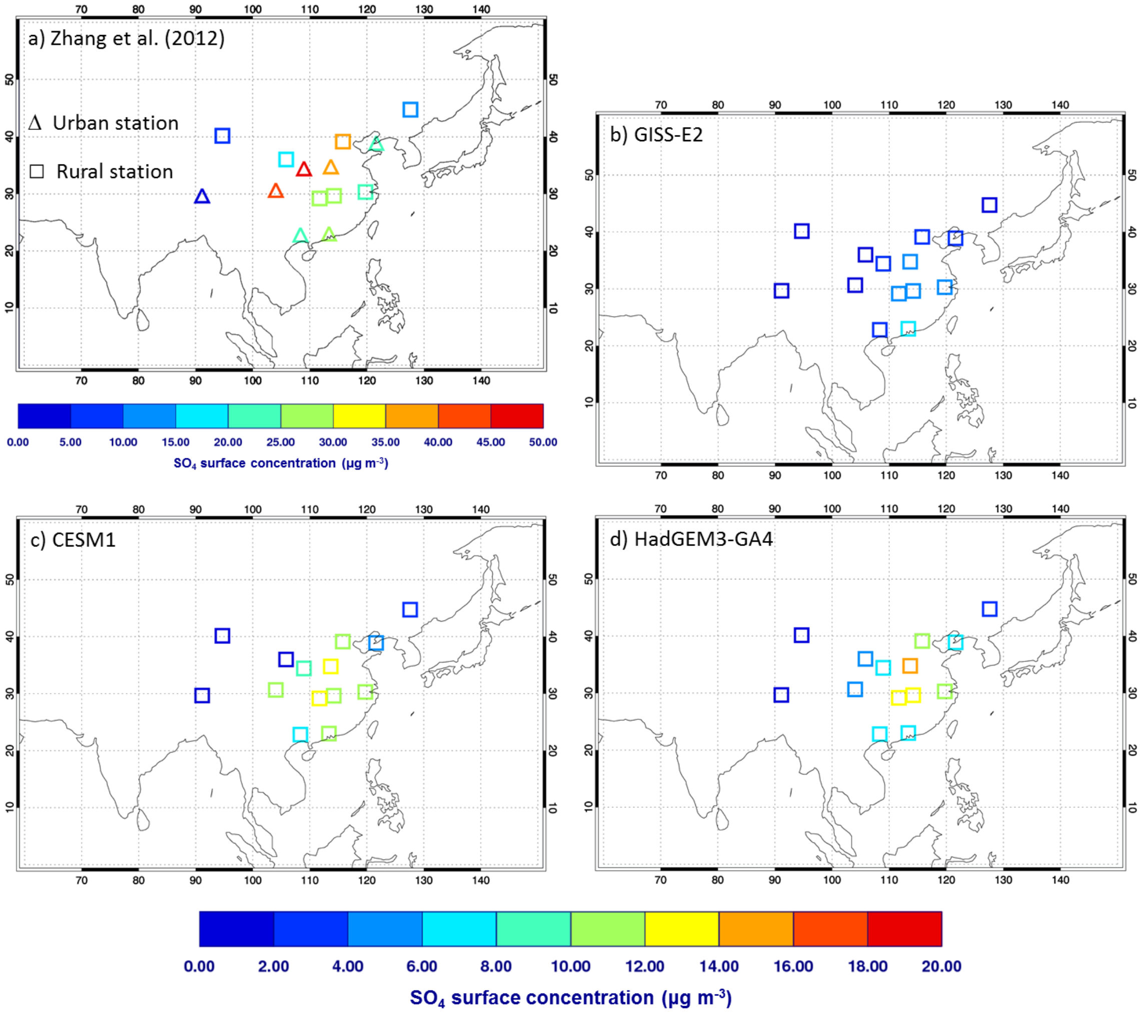

Figure 3-12: *Surface SO$_4$ concentrations in China as reported for 2006-2007 by Zhang et al. (2012) (a), and in GISS-E2 (b), CESM1 (c), and HadGEM3-GA4 (d). For the Zhang et al. dataset, a monthly climatology is calculated by averaging values for each month from both 2006 and 2007 (where available), and then all twelve months are averaged to calculate an annual mean. Stations located in urban areas are denoted by triangles. For the models, the SO$_4$ concentration in the lowest model level of the control (2000) simulation of each model is used, and the data is masked to the locations of the observations by taking the value from the gridbox that each station is located in. For GISS-E2 and HadGEM3-GA4 a 150-year annual mean is used, whilst for CESM1 the mean surface SO4 is taken from a 30-year extension to the original control simulation. For the models, all points are denoted with squares to indicate that the model resolutions are too coarse (~200 km) to make an urban-rural distinction. Note the colour scale for the models is 2.5 times smaller than for the observations.*

in fact biased high, with GISS-E2 performing relatively better with a mean bias of +10.1%, but HadGEM3-GA4 somewhat worse with +44.5%, and CESM1 worse still with +86%.

However, in the case of HadGEM3-GA4 it seems that the larger US bias comes mainly from an incorrect spatial distribution, with a high bias on the relatively less polluted West Coast but a pronounced low bias in surface SO$_4$ on the more industrialised East Coast, as shown in

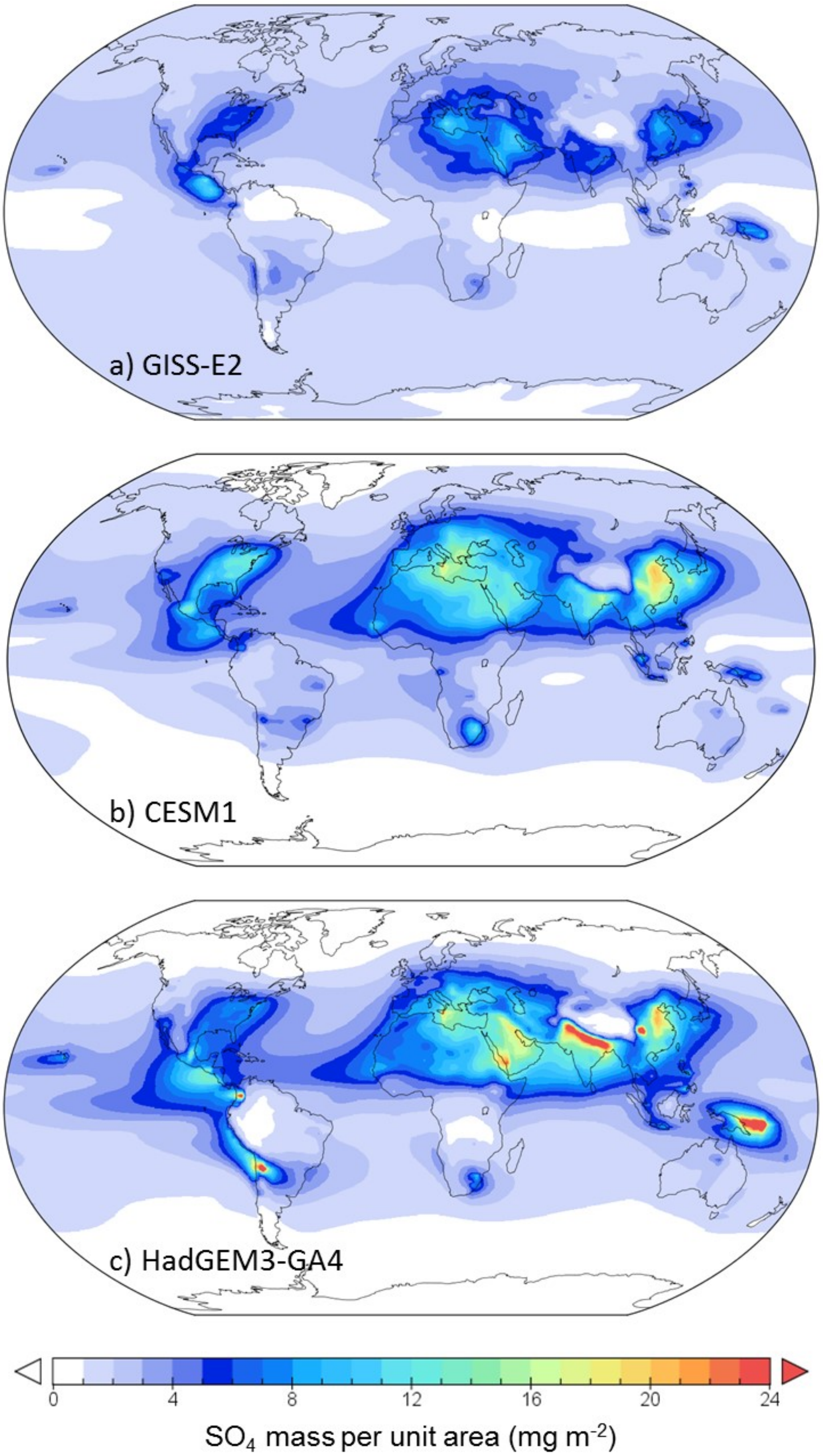

Figure 3-13: *Climatological column-integrated SO$_4$ burden in a) GISS-E2, b) CESM1, and c) HadGEM3-GA4. In each case, a 150-year average is taken from the control simulation of the model.*

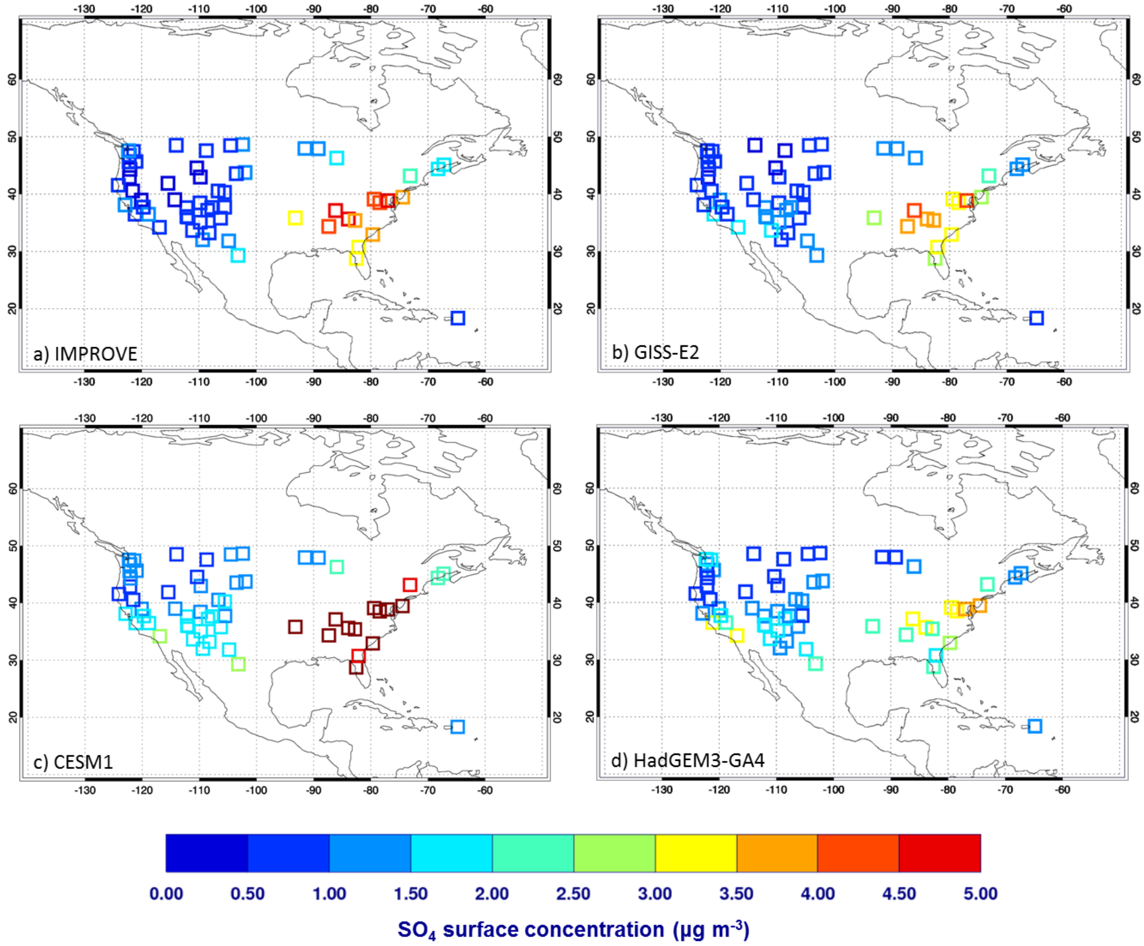

Figure 3-14: *Annual mean surface SO_4 concentrations in over the US as observed by the IMPROVE monitoring network (a), and as diagnosed in GISS-E2 (b), CESM1 (c), and HadGEM3-GA4 (d). For the IMPROVE data I calculate monthly climatologies between 1995-2005 for all stations with data for each month from at least 6 years within this range, and average over months to calculate an annual mean climatology for each station. For the models, the 150-year mean surface SO_4 from each model's control (2000) simulations is masked to the location of the qualifying IMPROVE sites by using the value at the gridbox each site is located in. For GISS-E2 and HadGEM3-GA4 a 150-year annual mean is used, whilst for CESM1 the mean surface SO4 is taken from a 30-year extension to the original control simulation.*

Figure 3-14. Consequently, this comparison would suggest that HadGEM3-GA4 in fact has too little sulfate around the principal US emission regions on the East Coast, even though over that area HadGEM3-GA4 actually has a larger column-integrated sulfate burden (Figure 3-13) and a larger AOD than GISS-E2, as was the case for China. This suggests that HadGEM3-GA4 again fails to capture the vertical profile of sulfate, underestimating surface concentrations over this region despite having a high column-integrated burden. GISS-E2 shows a similar pattern of low bias on the East Coast and high bias on the West, as has previously been reported by Koch et al. (2006), however in either case the biases are somewhat less than in HadGEM3-GA4. CESM1 is biased

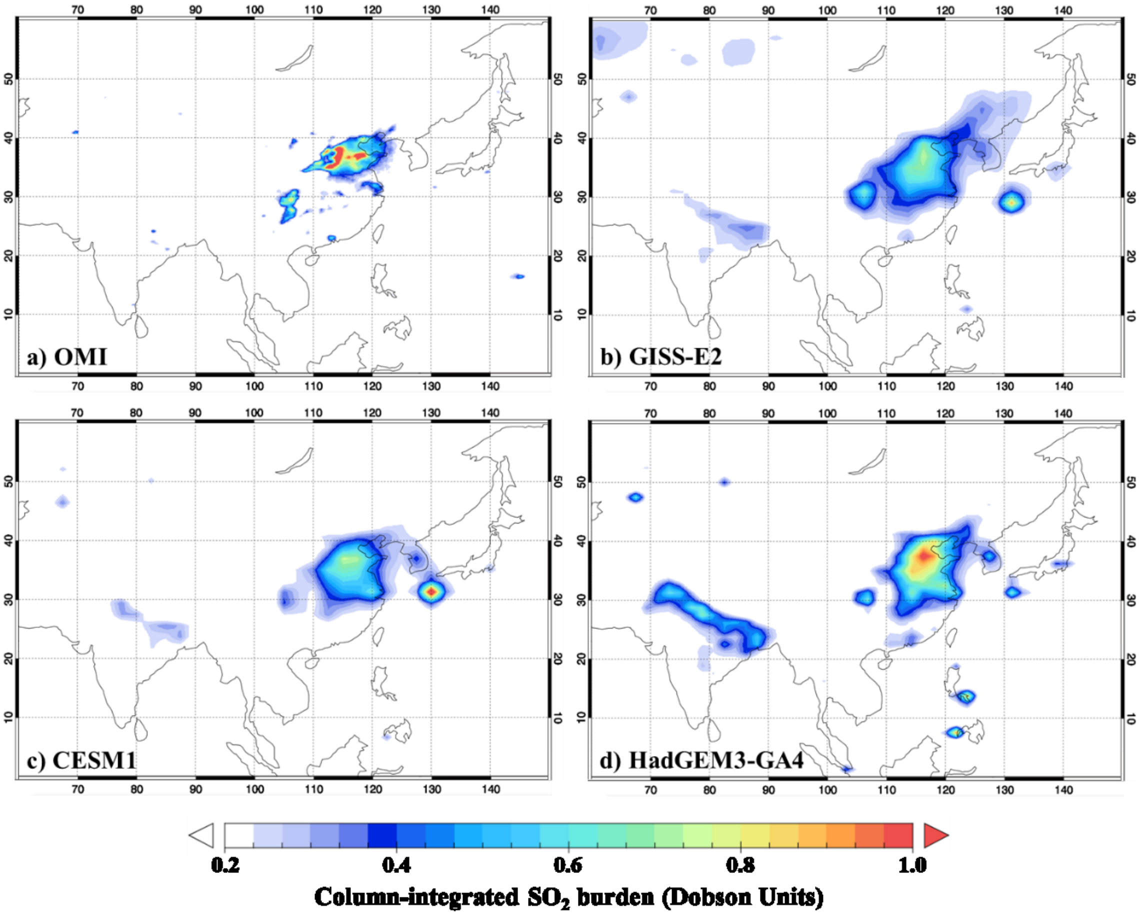

Figure 3-15: *Column-integrated sulphur dioxide burdens over Asia as observed by the OMI satellite instrument (a), and simulated in GISS-E2 (b), CESM1 (c), and HadGEM3-GA4 (d). For OMI SO_2 I calculate a climatology by averaging gridded monthly data to create annual means, and then averaging over all years from 2005-2012. Model data for GISS-E2 and HadGEM3-GA4 are 150-year means from the control simulation of each model, whilst for CESM the data is a 30-year average from an extension to the control simulation. For a fair comparison, only values > 0.2 DU are shown, as this is approximately the annual mean detection limit of the OMI instument (Krotkov et al., 2016).*

high in both regions of the US, though it has been shown in Liu et al. (2012) that the bias is again higher on the West Coast, which appears to be a common problem among the models.

Given the inconsistent comparison between surface concentrations and column-integrated sulfate, validation with surface observations therefore seems insufficient to constrain which model performs better regionally with regard to the more climate-relevant column-integrated quantities of sulfate burden and AOD. Returning to Asia, I have therefore also tried evaluating the model against column sulphur dioxide observations. I use the gridded, monthly mean Level 3 observations from the Ozone Monitoring Instrument (OMI) (Krotkov et al., 2016) (available from http://disc.sci.gsfc.nasa.gov/Aura) which is flown on the Aura satellite, averaged over eight years from 2005 - 2012. Over the E. China region the mean OMI SO_2 is 0.153 Dobson Units (DU), and all three models appear to overestimate this substantially, with very similar regional mean SO_2 columns of 0.282 DU for HadGEM3-GA4, 0.272 DU for GISS-E2, and 0.259 DU for CESM1. However, from Krotkov et al. (2016), the OMI detection limit for annual mean values is estimated at around 0.2 DU. If values below this threshold are assumed to be zero, then the respective E. China regional mean SO_2 columns are instead 0.123 for OMI, 0.224 for HadGEM3-GA4, 0.220 for GISS-E2, and 0.200 for CESM1. The conclusion is the same though: the models all still substantially overestimate the regional mean SO_2 column over E. China. Spatially, all three models also have somewhat more diffuse SO_2 fields than the OMI observations, where the SO_2 burden seems much more concentrated around source regions (Figure 3-15). This may be partly due to the coarse resolution of the models compared with the 0.25° satellite product, but also further suggests that the lifetimes for SO_2 may be too long in all the models, or transport processes too efficient in this region, which could also help account for the consistent underestimation of surface SO_4 in Figure 3-12.

An alternative observational measure which to an extent vertically integrates sulfate is the deposition rate, and for HadGEM3-GA4 and GISS-E2 for which I has this data, I therefore also try comparing against observations of sulfate wet deposition. I use the three-year mean wet deposition data from 2000-2002 described in Vet et al. (2014) and provided by the World Data Centre for Precipitation Chemistry (http://wdcpc.org, 2014), taking the six stations located in China. I exclude the station in Guizhou province in southern China, as for this station's location both models were found to have unusually large biases: +590% in HadGEM3-GA4, and +253% in GISS-E2. This station only provided data for one year and was flagged as having a high uncertainty in the Vet et al. (2014) dataset; it is also located in a mountainous region and so it could equally be that the models cannot resolve the specific local conditions. Removing this station from the analysis we find for the remaining five stations in China that HadGEM3-GA4 performs well with a mean bias of -3.9%, compared with -64.8% for GISS-E2. This gives an indication that HadGEM3-GA4 has more realistic sulfate deposition directly over China (though the sample size is very small), and supports my earlier findings from the comparisons against AERONET and MODIS. If I broaden the analysis to include all stations described as being broadly in Asia (not strictly in China – an additional 32 stations) then the mean bias for HadGEM3-GA4 is worsened (-41.8%), whilst the bias in GISS-E2 is slightly improved (-54.1%). So, HadGEM3-GA4 still performs better over the Asian region as a whole, though less dramatically so (Figure 3-16).

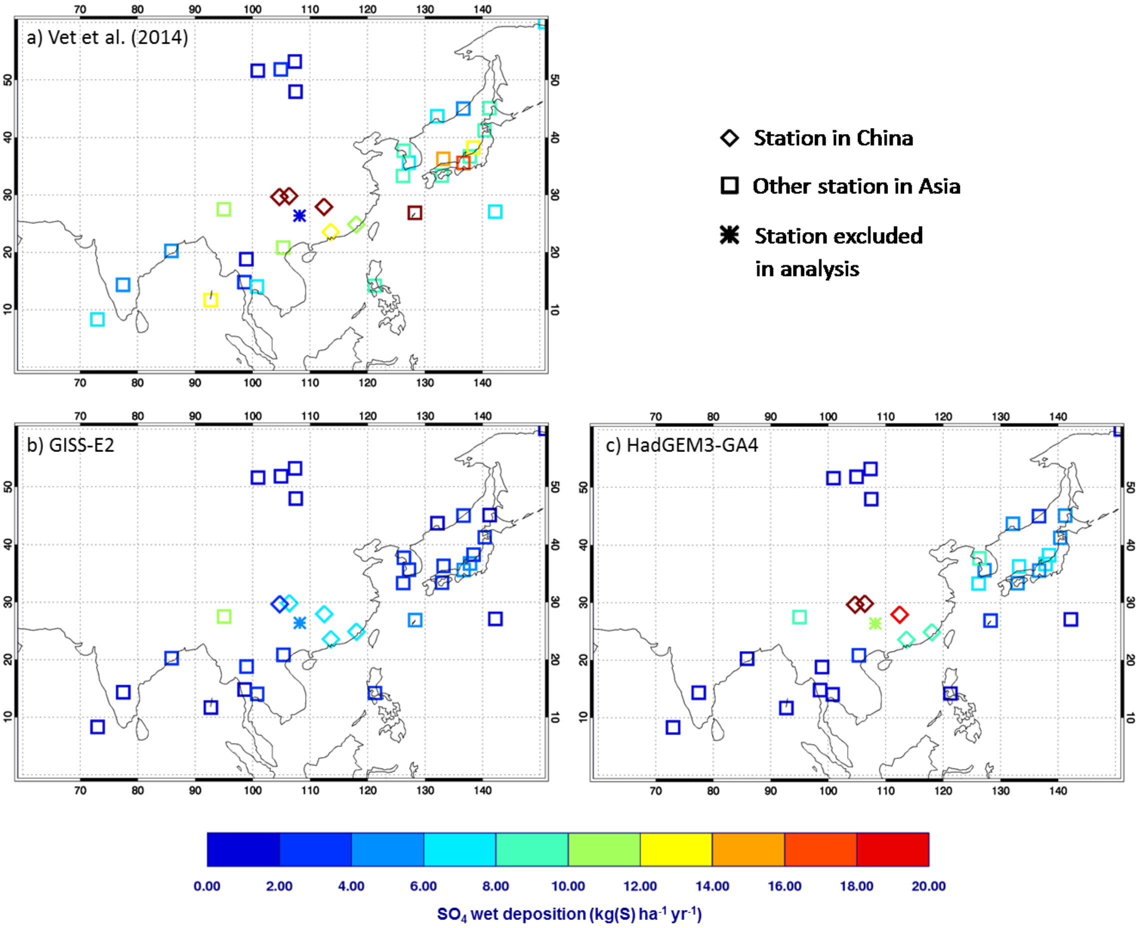

Figure 3-16: *SO_4 wet deposition in Asia, reported for 2000-2002 in Vet et al. (2014) (a), and in GISS-E2 (b) and HadGEM3-GA4 (c). For the Vet et al. (2014) dataset, we use the 3-year mean values provided by the data product. For the models we use the 150-year mean from the models' control (2000) simulations, masked to the location of the observation stations by taking the value from the gridbox each station is located in. Diamonds indicate stations in China, and the asterisk indicates the station that was excluded from the analysis in the main manuscript, as both models had unusually large biases at this one station.*

This overall picture seems consistent with that of the other observational measures looked at here, although it should be noted that wet deposition rates are dependent not just on the column sulfate burden but also on the amount and distribution of precipitation, and so biases in wet deposition could also at least partly be due to different precipitation distributions rather than sulfate.

3.3 Conclusions

For the results of climate responses to regional aerosol perturbations which will be presented in the next two Chapters, it is vital to understand how representative the abundances and distribution of aerosols is in the models employed. I have shown here that globally over land regions, and in particular over the key northern-hemisphere emission regions, HadGEM3-GA4 appears to simulate a fairly accurate distribution of anthropogenic aerosols. The largest errors in this model appear to be associated with natural dust and sea-salt aerosol, the emissions of which are simulated rather than prescribed. However, these are aerosol types that I do not focus on in this thesis.

Regionally over East Asia, HadGEM3-GA4 appears to have the most accurate total AOD out of the three models from which data is used in the following Chapter – GISS-E2, CESM1, and HadGEM3-GA4. GISS-E2 and CESM1 both appear to somewhat underestimate the peak in AOD over E. China compared with AERONET ground-based observations and MODIS satellite measurements, although observations from another satellite instrument, MISR, are somewhat lower and more consistent with the regional values in GISS-E2.

However the experiments to be investigated here will look to isolate responses to emissions of particular emission species, and specifically sulfur dioxide. I have shown that there is large variation between the models in the relevant contributions of different aerosol species to the total AOD regionally. There are no observations though of speciated aerosol optical depth beyond the AERONET apportionment into fine and coarse mode, nor of column-integrated burdens of different aerosol species, which makes it impossible to perform a definitive assessment of whether the distribution and burden of sulfate aerosol, for instance, is represented by the total (all-aerosol) AOD. Subsequent comparison with ground measurements of aerosol concentrations is somewhat inconclusive, though interestingly both HadGEM3-GA4 and especially GISS-E2 perform much better over the US than over China. Kulmala (2015) noted that the unprecedented pollution concentrations over China mean that atmospheric chemistry in this region may diverge from the better understood regimes over the US or Europe, and models may not currently be able to represent this. Validation with surface measurements may also in general be confounded by the coarse resolution of the models, with them potentially failing to accurately capture the vertical profile of aerosol species, to which the column aerosol optical depth would not be strongly sensitive. Trying to compare instead column-integrated quantities, SO_2 burden also proved to be similar across the models and did not differentiate them, while sulfate wet deposition was better for HadGEM3-GA4 than GISS-E2 immediately over China, broadly consistent with the AOD assessment, though wet deposition is not only dependent on the aerosol distribution but also that of precipitation. As a consequence, the best guide to how reasonable the column-integrated aerosol distributions are remains the imperfect comparisons with observed total AOD discussed above.

4 Impact of SO_2 emissions from China in three different climate models

The few studies that have previously investigated specific regional aerosol forcings (e.g. Shindell and Faluvegi, 2009; Shindell et al., 2012; Teng et al., 2012) typically used a single climate model at a time to investigate the climate response to idealised, historical, or projected forcings. However, models vary considerably in their representation of aerosols and their radiative properties, resulting in a large uncertainty in aerosol radiative forcing (e.g. Myhre et al., 2013b; Shindell et al., 2013a). When investigating the climate response to regional aerosol emissions, such uncertainties are likely to be confounded even further by the variability between models in regional climate and circulation patterns (e.g. Hawkins and Sutton, 2009), and variation in the global and regional climate sensitivities, i.e. the amount of simulated warming per unit radiative forcing (e.g. Flato et al., 2013). To best interpret the findings of single-model experiments with regional aerosol forcings – such as those that I will discuss in Chapter 5 – it is therefore critical to understand the range of uncertainty in the global and regional climate response that may arise as a result of structural and parametric differences between climate models.

In this chapter, I investigate the variability that can arise in the translation of a regional emission perturbation to a climate (temperature) response, between three different state-of-the-art global climate models. As a case study, I consider the removal of SO_2 anthropogenic emissions from the region of China, as this experiment was performed in coordination by colleagues at the NASA Goddard Institute for Space Studies (GISS) and the National Center for Atmospheric Research (NCAR) with their respective models along with simulations performed by myself with HadGEM3-GA4, using an identical experimental protocol. Since China is currently the largest anthropogenic source region of sulfur dioxide (Smith et al., 2011) and hence of anthropogenic aerosol, this regional perturbation represents a substantial modification to global aerosol levels, with the additional characteristic of being localised over a particular part of the world. This aspect of our experiment is distinct from many previous model intercomparison studies, which have typically compared the climate response in models forced by global historical trends in aerosols (for example, Wilcox et al., 2013; Shindell et al., 2015), or which have only considered the impact of regional emissions on long-range pollution transport and on radiative forcing (for example the HTAP and AeroCom experiments (HTAP, 2010; Yu et al., 2013; Kinne et al., 2006;

Schulz et al., 2006; Textor et al., 2006; Myhre et al., 2013a), but have not investigated the range of modelled climate responses to a regionally localised emission perturbation. The potential importance of remote climate effects due to the strong zonal asymmetry created by such regional emissions has therefore not yet been explored in multi-model studies. Single-model studies such as Teng et al. (2012) suggest though that regionally localised forcings can produce significant climate teleconnections in at least the longitudinal direction, while the studies by Shindell et al. (2009; 2012) imply that any mid-latitude aerosol forcing could potentially impact areas outside of the mid-latitudes.

The following section describes our experimental setup (Sect. 4.1). I then present the results of the radiative flux changes and surface temperature responses to the removal of Chinese SO_2 (Sect. 4.2), and analyse the possible reasons for the large differences between the model responses (Sect. 4.3). Finally, in Sect. 4.4 I present some conclusions from this comparison.

4.1 Experimental setup

With this study, the aim is to investigate the surface temperature response to an idealised perturbation to realistic regional SO_2 emissions, on a centennial timescale. A control simulation has been performed with each model, initialised from a present-day state, which is forced with the same anthropogenic emissions of aerosols and their precursors following the year-2000 Atmospheric Chemistry and Climate Model Intercomparison Project (ACCMIP) emissions inventory (Lamarque et al., 2010). The control simulations are run for 200 years with continuous year-2000 conditions. For each model, we then run a 200-year perturbation simulation in which SO_2 emissions from energy production, industry, transport, domestic use, and waste, are set to zero over the region of China, defined here to be the rectangular domain 80°-120°E, 20°-50°N (shown in Figure 4-1, along with how this corresponds to regional anthropogenic SO_2 emissions). These emission sectors contribute 98.7% of the anthropogenic SO_2 emitted from this region, so this corresponds to a near complete removal of SO_2 emissions from this highly polluting area of the globe. Quantitatively, this perturbation reduces global anthropogenic SO_2 emissions from around 104 Tg yr^{-1} to 86 Tg yr^{-1}, a reduction of around 17 Tg yr^{-1}, or 16.5%.

Additionally, shorter atmosphere-only simulations were performed with HadGEM3-GA4 (identical in configuration, except with sea-surface temperatures (SSTs) and sea-ice cover prescribed to year-2000 values) to diagnose the effective radiative forcing, as well as the SO_2

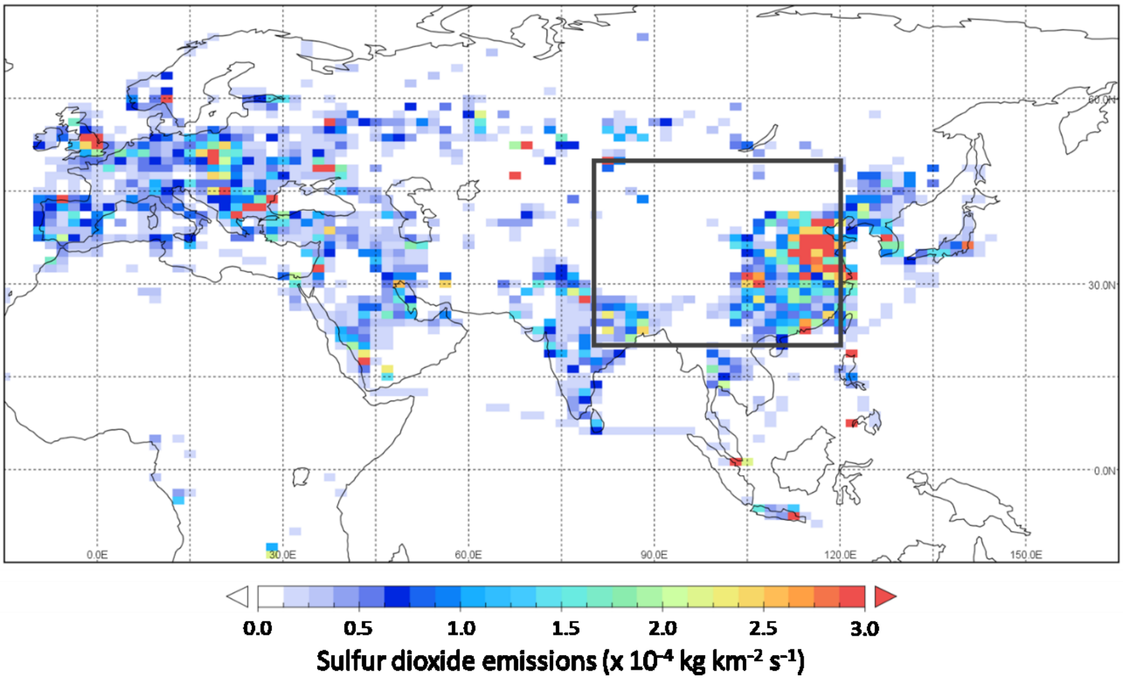

Figure 4-1: *Annual mean SO_2 emissions over the Eurasian continent, with the grey box showing the "China" emission perturbation region (80°E-120°E, 20°N-50°N).*

oxidation rates and SO_4 wet deposition rates for this model, referred to in Section 4.2, Section 4.2.1, and Section 4.3.1. In CESM1, the clear-sky radiative flux and cloud cover referred to in Sections 4.3.2 and 4.3.3, and the SO_2 burden in Table 4-1, were diagnosed from a 30-year extension of the control and perturbation coupled simulations, rather than from the original 200 years.

4.2 Radiative forcing and climate response

I investigate the change in the mean state of the models by taking averages over the last 150 years of the 200-year-long simulations (the first 50 years are discarded to allow the response to the perturbation to establish itself), and taking the difference between the perturbation and control simulations. For each model the changes in SO_2 and sulfate burdens, area-weighted mean temperature, SW radiative flux, and aerosol optical depth, and the ratios of AOD to sulfate burden change and SW flux to AOD change, are tabulated in Table 4-1 both for the globe, and for the east China region (E. China) defined as 100°-120°E, 20°-40°N, as in Chapter 3. This region contains the most intense changes in sulfate aerosol in all three models, and unless otherwise stated is the region used here whenever I quantify the magnitude of "local" changes over China.

Table 4-1: *Changes in area-integrated SO_2 and SO_4 burdens, changes in area-weighted annual mean AOD, net down clear-sky and all-sky TOA SW flux, and surface air temperature, and ratios of the changes in AOD to change in SO_4 burden, and SW flux to change in AOD, for the globe and for the E. China region 100°E - 120°E, 20°N - 40°N, due to removing SO_2 emissions from China in HadGEM3-GA4, GISS-E2, and CESM1. AOD is diagnosed for clear-sky conditions in HadGEM3-GA4 and GISS-E2, and for all-sky conditions in CESM1. Changes are calculated from 150-year means of perturbation and control simulation, except CESM1 SO_2 and clear-sky flux which are 30-year means from an extension to both simulations. For models and variables where data was available, uncertainty ranges indicate ± 2 standard deviations, evaluated in HadGEM3-GA4 from an ensemble of six 150-year control runs with perturbed initial conditions, and in GISS-E2 from twelve 150-year segments of a long pre-industrial control run. Values quoted without error ranges indicate that uncertainty was not evaluated for that model and/or variable.*

		HadGEM3-GA4	GISS-E2	CESM1
Global	Total SO_2 burden change (Tg)	-0.045 ± 0.001	-0.076	-0.050
	Total SO_4 burden change (Tg)	-0.070 ± 0.004	-0.077	-0.136
	Mean AOD (τ) change	-0.0042 ± 0.0004	-0.0003	-0.0013
	Clear-sky SW flux change (W m^{-2})	0.184 ± 0.06	0.052	0.076
	All-sky TOA SW flux change (W m^{-2})	0.279 ± 0.10	-0.034 ± 0.06	0.186
	Mean temperature change (K)	0.115 ± 0.05	-0.028 ± 0.04	0.054
	Δ AOD/Δ SO_4 (τ Tg^{-1})	0.060	0.004	0.009
	Δ Clear-sky SW/Δ AOD (W m^{-2} τ^{-1})	-43.8	-173	-58.5
	Δ All-sky TOA SW/Δ AOD (W m^{-2} τ^{-1})	-66.4	(+)106	-145
E. China (100°E-120°E, 20°N-40°N)	Total SO_2 burden change (Tg)	-0.029 ± 0.0002	-0.028	-0.028
	Total SO_4 burden change (Tg)	-0.035 ± 0.0003	-0.011	-0.039
	Mean AOD (τ) change	-0.287 ± 0.002	-0.047	-0.076
	Clear-sky SW flux change (W m^{-2})	5.06 ± 0.08	4.10	2.16
	All-sky TOA SW flux change (W m^{-2})	5.34 ± 0.3	0.90 ± 0.3	4.20
	Mean temperature change (K)	0.382 ± 0.07	0.049 ± 0.07	0.294
	Δ AOD/ Δ SO_4 (τ Tg^{-1})	8.23	4.12	1.96
	Δ Clear-sky SW/Δ AOD (W m^{-2} τ^{-1})	-17.6	-87.2	-28.4
	Δ All-sky TOA SW/Δ AOD (W m^{-2} τ^{-1})	-18.6	-19.3	-55.0

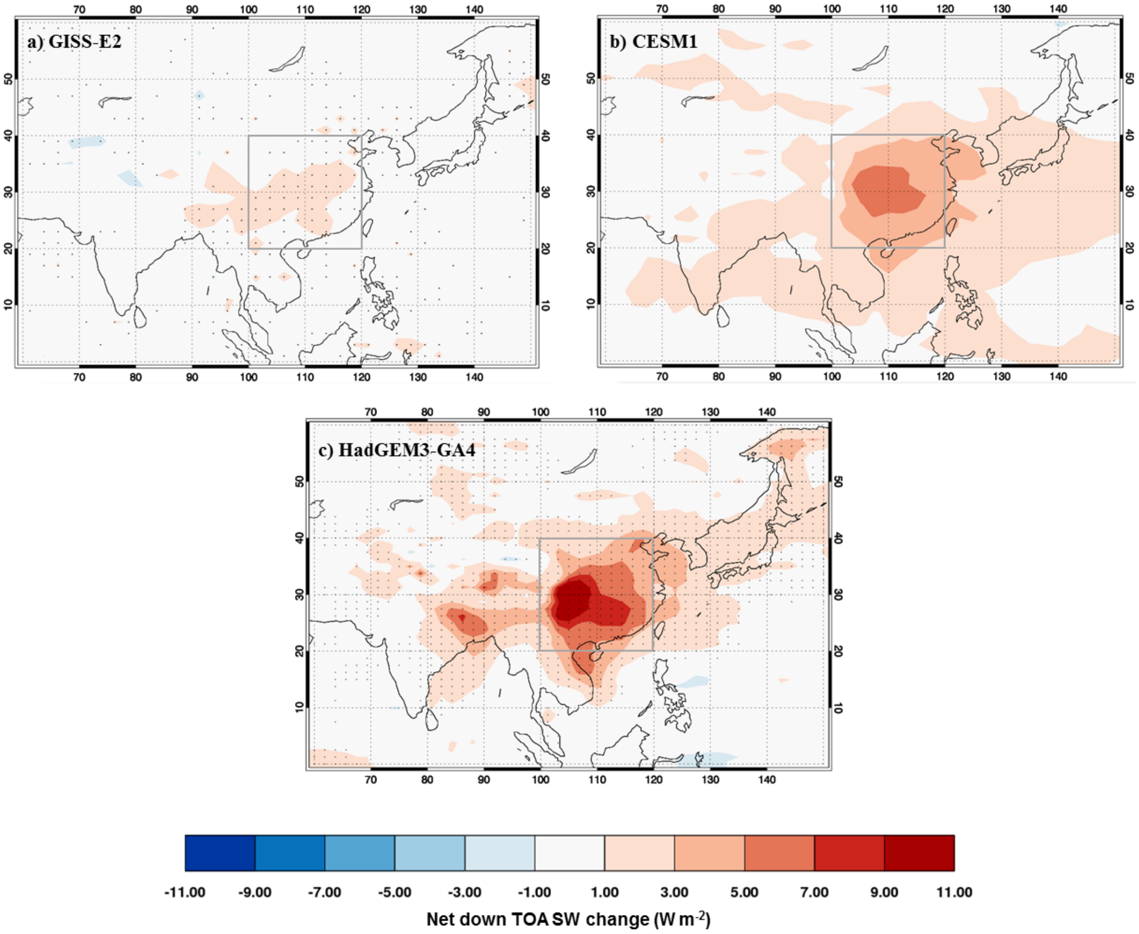

Figure 4-2: *Change in annual mean net downward TOA SW flux due to removal of anthropogenic* SO_2 *emissions over China for a) GISS-E2, b) CESM1, and c) HadGEM3-GA4. Differences are calculated as the 150-year mean of the perturbation simulation minus the 150-year mean of the control simulation. Plots focus on the Asian region as changes outside this domain were found to be minimal. Stippling for GISS-E2 and HadGEM3-GA4 indicates that the change in that grid-box exceeded 2 standard deviations. Significance was not evaluated for CESM1 as multiple 150-year control simulations were not available to assess internal variability for this model. The grey box denotes the E. China (100°E - 120°E, 20°N - 40°N) region which is used in Table 4-1 and throughout the discussion.*

The anticipated immediate consequence of removing SO_2 emissions from China is that there will be a reduction in the amount of sulfate aerosol formed, leading to a positive shortwave (SW) radiative forcing. Figure 4-2 shows the changes in net downward top-of-atmosphere (TOA) SW radiative flux in each of the three models. For reference, Figure 4-2 also shows the outline of the E. China region, which corresponds well to the region of maximum SW flux changes in all three models. For HadGEM3-GA4 and GISS-E2, the Figure 4-2 plots are stippled in locations where the change exceeds two standard deviations, estimated for HadGEM3-GA4 from the grid-point standard deviations from six 150-year long year-2000 control simulations with perturbed atmospheric initial conditions, and for GISS-E2 from 12 non-overlapping 150-year sections of a

1900-year-long pre-industrial control simulation that had reached radiative equilibrium. Such uncertainty analysis has not been performed for CESM1 due to lack of the necessary unforced simulation output for the version of the model used here.

Figure 4-2 reveals that there is a large variation between the models in the intensity of the local radiative flux change over China. GISS-E2 shows a fairly weak increase in net downward SW flux over E. China, with a local increase (from Table 4-1) of 0.91 W m^{-2} and an insignificant global mean change (-0.034 W m^{-2}), whereas HadGEM3-GA4 shows a very pronounced change of 5.3 W m^{-2} locally over E. China, and a global mean value of 0.28 W m^{-2}. CESM1 lies in the middle, with a moderate local SW flux change of 4.2 W m^{-2}, and 0.19 W m^{-2} in the global mean. Between GISS-E2 and HadGEM3-GA4, there is a 6-fold increase in the intensity of the local SW radiative flux change over E. China.

Because these are fully coupled simulations, the change in the TOA SW flux does not provide a measure of the shortwave radiative forcing, since the underlying climate has been allowed to adjust, potentially allowing feedbacks on clouds, and snow and ice cover. A complementary pair of atmosphere-only simulations were performed with HadGEM3-GA4 to diagnose the effective radiative forcing (ERF) – the change in TOA radiative flux when feedbacks due to the slow response of the oceans are prevented (Andrews et al., 2010). Globally, the SW ERF due to removing SO_2 from China in these fixed-SST simulations is 0.18 W m^{-2}, 35% smaller than the 0.28 W m^{-2} SW flux change in the fully coupled case. However, locally over the E. China region, the

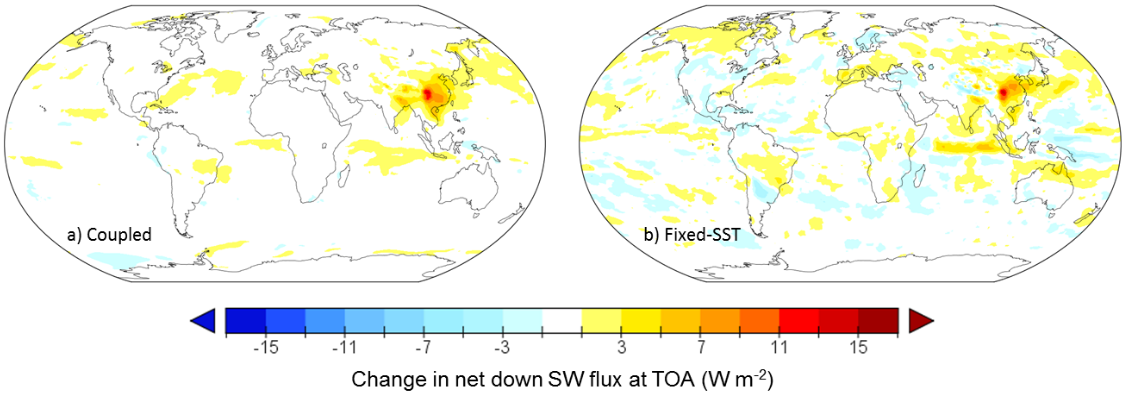

Figure 4-3: Change in annual mean TOA SW flux due to removing anthropogenic SO_2 emissions from China in: a) fully-coupled simulations, and b) fixed-SST simulations, with HadGEM3-GA4. Both panels show the difference between the output of the perturbation simulation minus the control simulation; for the coupled simulations the plot shows an average over 150 years, with the first 50 years of the simulations discarded as spin-up. For the fixed-SST simulations, the model was run for 26 years with prescribed year 2000 SSTs and sea-ice, and the plot shows the average over the last 25 years, discarding the first year as spin-up.

fixed-SST SW ERF was found to be 4.2 W m^{-2}, which is only 21% lower than the 5.3 W m^{-2} SW flux change in the fully coupled experiment. Moreover, the spatial map of the SW flux anomaly over China is very similar between the two experiments (Figure 4-3). At least in HadGEM3-GA4, over E. China the change in sulfate therefore appears to be the dominant driver of the change in TOA SW flux, and the local change in SW flux over this region is reasonably representative of the local radiative effect of the sulfate perturbation even in the fully-coupled simulations with this model. The same is less true of the global-mean values because of positive feedback from ice melt in the Arctic, and also some small but widespread changes in cloud cover, which although too weak to show on the contour scale of Figure 4-3, nonetheless add up to a sizeable effect globally in the coupled simulations.

Based on the fully coupled simulations, the substantial differences in the intensity of SW flux changes over China ultimately translate to very pronounced differences in the strength of the resulting climate response. Figure 4-4 shows the change in surface air temperatures between the perturbation and control simulations for each of the three models, clearly demonstrating

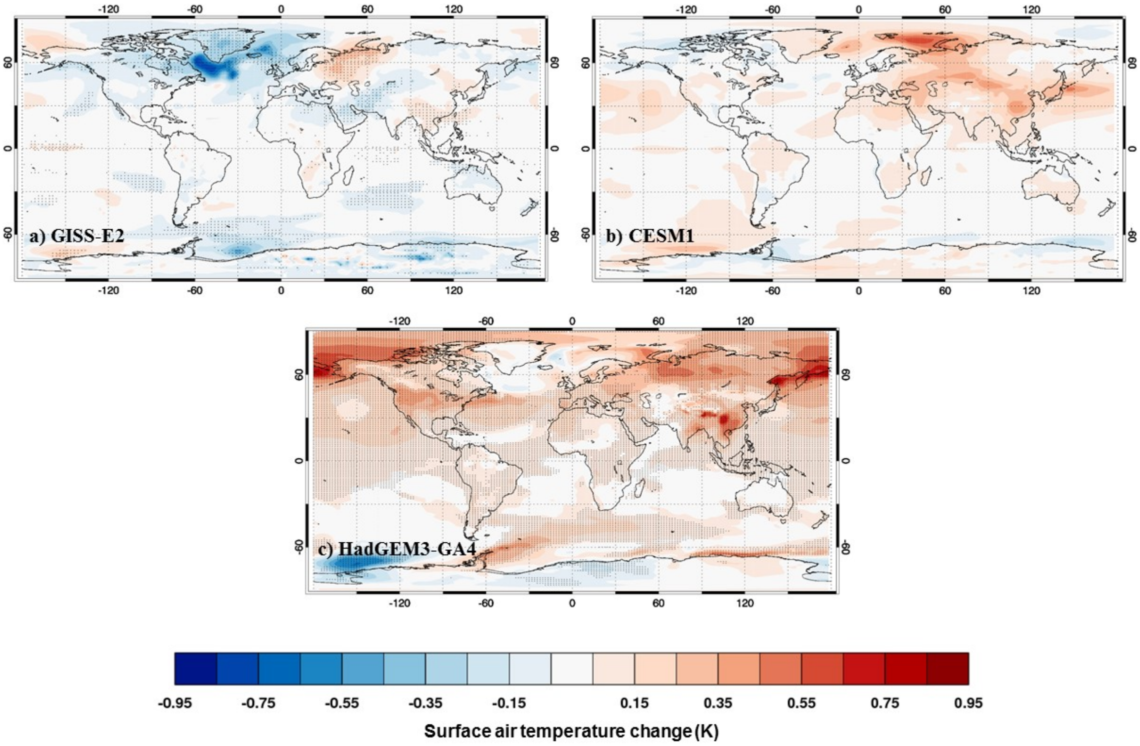

Figure 4-4: Global changes in surface air temperature due to removing anthropogenic SO_2 emissions from China for a) GISS-E2, b) CESM1, and c) HadGEM3. Differences are for 150-year means of perturbation simulation minus control simulation. Stippling for GISS-E2 and HadGEM3-GA4 indicates changes exceeded two standard deviations for that grid box.

that temperature effects extend far beyond the more localised radiative effects. Again stippling indicates that the response exceeds the *2σ* level in HadGEM3-GA4 and GISS-E2. The difference between GISS-E2 and HadGEM3-GA4 is particularly striking. Apart from a small warming in parts of eastern China and north-east Europe by around 0.1-0.3 K, there is virtually no coherent temperature response across the rest of the globe in GISS-E2. The global mean temperature change (Table 4-1) is -0.028 K and is not significant. In contrast, HadGEM3-GA4 displays significant warming across almost all of the northern hemisphere, with much larger increases in temperature between 0.4-1 K in several regions, not only in China but also in much of the US, northern Eurasia, and the Arctic. The global mean temperature response is +0.12 K. CESM1 sits again in the middle, with clear warming responses between 0.2-0.5 K over much of eastern Europe, Asia, and the western Pacific. Overall the warming response is still less strong and less widespread than in HadGEM3-GA4, with a global mean warming of +0.054 K.

The spatial pattern of warming over Europe and Asia in CESM1 bears some qualitative similarity though to the pattern over the same region in HadGEM3-GA4, suggesting that there may be a similar mode of global response excited by heating over eastern China in these models, at least across the Eurasian continent. The dynamical mechanisms through which local aerosol emissions are translated to remote response in HadGEM3-GA4 will be returned to in the next chapter. Whether GISS-E2 would have displayed the same pattern had the radiative forcing over China been stronger is impossible to tell from these results; given the small magnitude of the SW flux change, it seems that most of the spatial pattern in the temperature response in GISS-E2 can be attributed to internal variability – the largest changes in temperature seen in this model are in fact a region of cooling over the north-west Atlantic, which is mostly not significant and appears instead to be the result of particularly large internal variability in this region.

4.3 Exploring drivers of diversity

Given the large diversity found in the climate responses to regional aerosol precursor emissions, and the science and policy importance of quantifying the impact of regional pollutant emission controls, it would be valuable to understand the differences between these models that lead to such a large variation in the predicted temperature response. Therefore, I explore below a number of possible sources of discrepancy.

4.3.1 Differences in simulated aerosol amounts and optical depths

I address first the possibility that differences in the aerosol schemes themselves lead directly to very different aerosol loadings between the models, despite the identical change in SO_2 emissions applied. Figure 4-5 shows the change in column-integrated SO_4 in each model as a result of removing SO_2 emissions from China. The models vary in both the distribution and magnitude of SO_4 reductions. In particular, HadGEM3-GA4 has the reduction in SO_4 burden fairly concentrated over China. CESM1 and GISS-E2 simulate changes in SO_4 which extend further downwind from the source region, giving a larger spatial footprint, although CESM1 still has larger reductions over China as well.

For GISS-E2 and HadGEM3-GA4, more detailed chemistry diagnostics were available for a 5-year period of a HadGEM3-GA4 atmosphere-only control simulation, and a 5-year period of the GISS-E2 coupled control simulation. For these two models, the difference in the spatial extent of the SO_4 field changes due to Chinese SO_2 emissions appears to result from a faster conversion of SO_2 to SO_4 in HadGEM3-GA4, resulting in much more concentrated SO_4 changes close to the source.

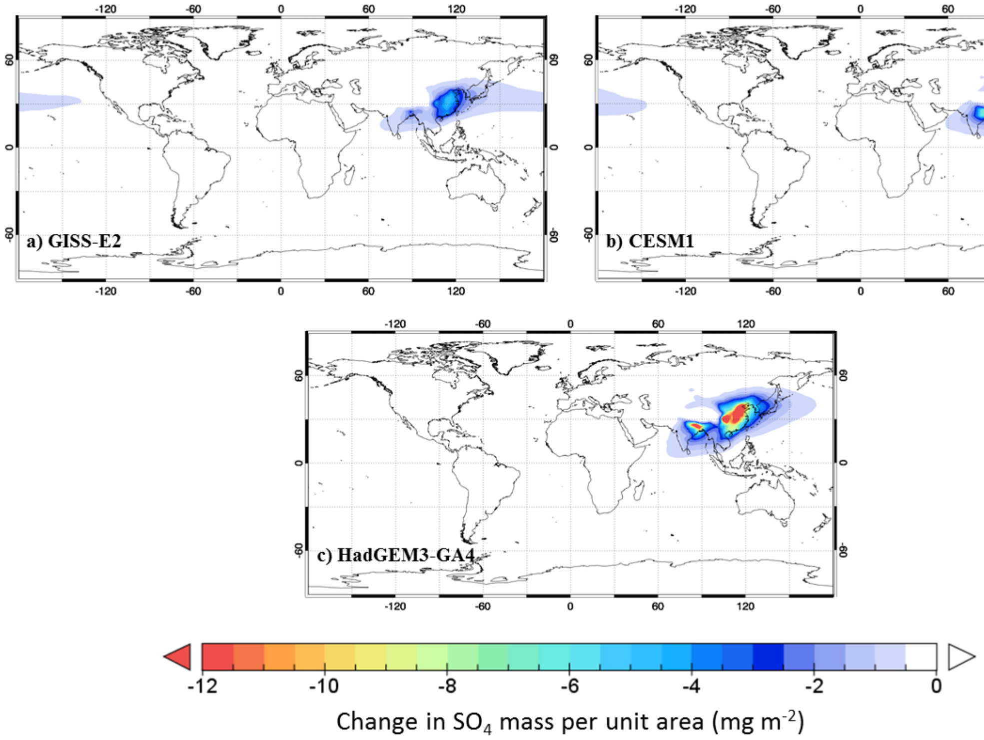

__Figure 4-5:__ Global changes in annual mean column-integrated SO_4 burden due to removing anthropogenic SO_2 emissions from China, for a) GISS-E2, b) CESM1, and c) HadGEM3-GA4. Differences are calculated as perturbation simulation minus control simulation, averaged over 150 years.

The SO_2 lifetime is around 1.8 times shorter in HadGEM3-GA4, and this is found to be associated with around 45% higher wet oxidation rates in this model. This difference is due in part to the inclusion of an additional wet oxidation pathway in HadGEM3-GA4: whereas GISS-E2 only includes wet oxidation of SO_2 by H_2O_2 (around 730 kg(S) s^{-1} globally integrated), HadGEM3-GA4 includes wet oxidation by both H_2O_2 and O_3, each of which contribute similarly in this model (around 540 kg(S) s^{-1} and 520 kg(S) s^{-1} respectively).

Globally integrated, HadGEM3-GA4 and GISS-E2 in fact simulate fairly similar equilibrium reductions in SO_4 burden, at -0.070 Tg and -0.077 Tg respectively (Table 4-1). This, combined with the more concentrated SO_4 field in HadGEM3-GA4, implies that locally over eastern China this model must have a more intense reduction in SO_4 burden, and indeed 50% of the total global reduction turns out to occur locally over E. China in HadGEM3-GA4 (-0.035 Tg), compared with only 21% (-0.016 Tg) in GISS-E2.

CESM1 includes the same oxidation pathways as HadGEM3-GA4, and in fact has a slightly shorter SO_2 lifetime still, and so the differences in SO_4 distribution between these two models have different origins. CESM1 in fact simulates almost double the global change in SO_4 burden as the other two models, with -0.136 Tg. This means that although the SO_4 reduction spreads further from the source in CESM1 than in HadGEM3-GA4, CESM1 still has a similar reduction to HadGEM3-GA4 locally over E. China as well (-0.039 Tg), which is also evident in Figure 4-5.

Given that HadGEM3-GA4 and GISS-E2 simulate a similar global reduction in SO_4, it is surprising that there is such a difference in the magnitude of their climate responses. Also, given that CESM1 simulates a much larger global reduction in SO_4 than the other two models, it is similarly surprising that this model does not have the largest response. A partial explanation may be found by inspecting the change in total aerosol optical depth (AOD), which is a more direct measure of the radiative properties of the aerosol column. Unfortunately, as noted previously in Chapter 3, the AOD diagnosed by the models is not completely equivalent: HadGEM3-GA4 diagnosed clear-sky AOD, whilst CESM1 provided all-sky AOD, and GISS-E2 diagnosed both all-sky and clear-sky AOD. As before, unless otherwise stated I use here the clear-sky AOD from GISS-E2 (as well as being more suited to comparing with observations which are inherently only possible for cloud-free conditions, clear-sky AOD will be less affected by differences in the models' cloud climatologies, and so all else being equal would still be the preferred variable to compare). Figure 4-6 shows these changes in AOD at the 550nm wavelength for the three models.

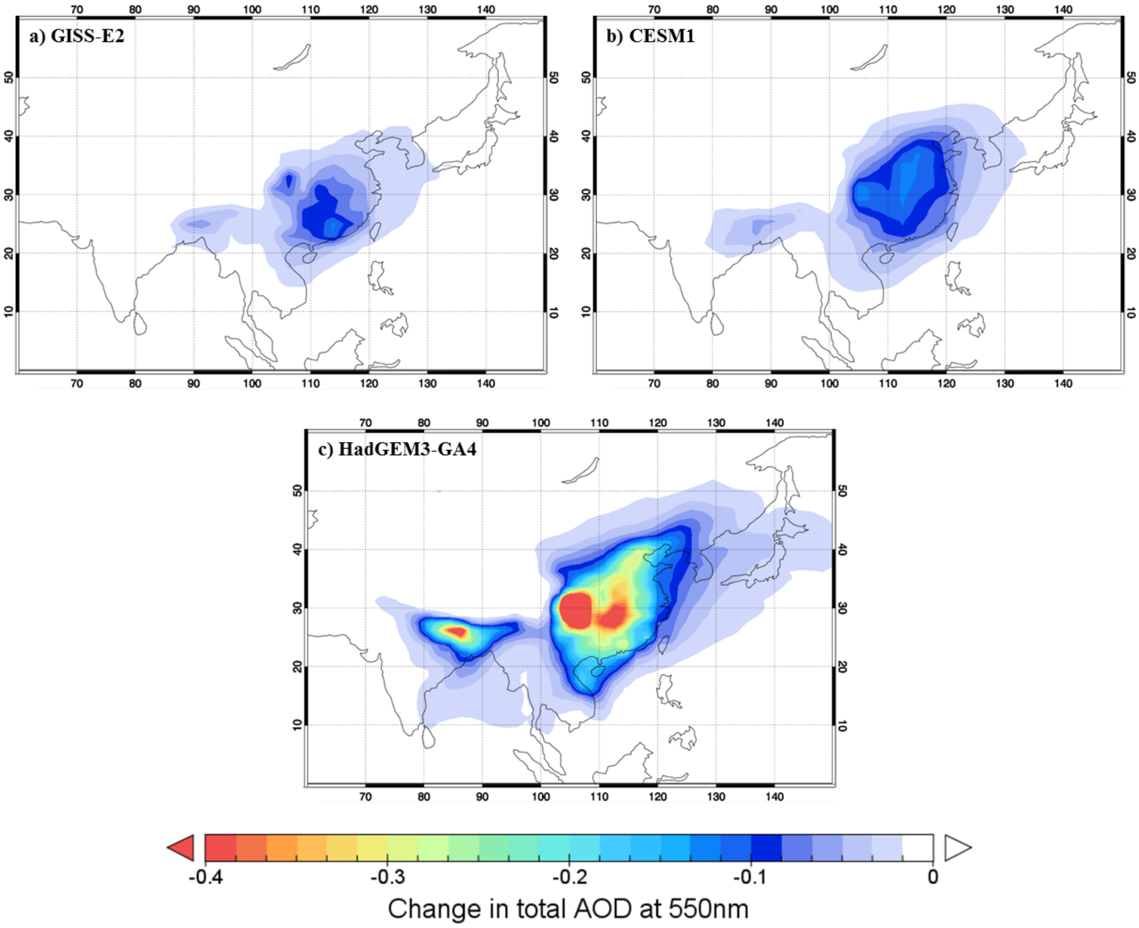

***Figure 4-6:** Change in annual mean AOD at 550nm due to removing anthropogenic SO_2 emissions from China for a) GISS-E2, b) CESM1, and c) HadGEM3-GA4. For HadGEM3-GA4 and GISS-E2, AOD is calculated for clear-sky conditions, whereas for CESM1 AOD is calculated for all-sky conditions, which will generally result in higher values within each simulation. Differences are calculated as perturbation simulation minus control simulation, averaged over 150 years. The plot region focuses on Asia as changes outside of this domain were minimal.*

As with the radiative flux change, there is a large range in the magnitude of local AOD reduction, with E. China AOD reductions ranging from 0.047 in GISS-E2 to 0.287 in HadGEM3-GA4, i.e. about 6 times higher (Table 4-1). This is comparable to the approximately 6-fold range of SW flux change found over this region between the models. Globally averaged, HadGEM3-GA4 also has a much larger AOD reduction than GISS-E2; 0.0042 compared with an almost negligible 0.0003 in GISS-E2, despite these two models having a similar change in global SO_4 burden. The much lower globally-averaged value in GISS-E2 is partly due to a very small but quite zonally-uniform compensating increase in nitrate aerosol (absent in this configuration of HadGEM3-GA4, though see Bellouin et al. (2011) for discussion on the inclusion of nitrate), which occurs across the northern hemisphere in GISS-E2 (Figure 4-7, top panel).

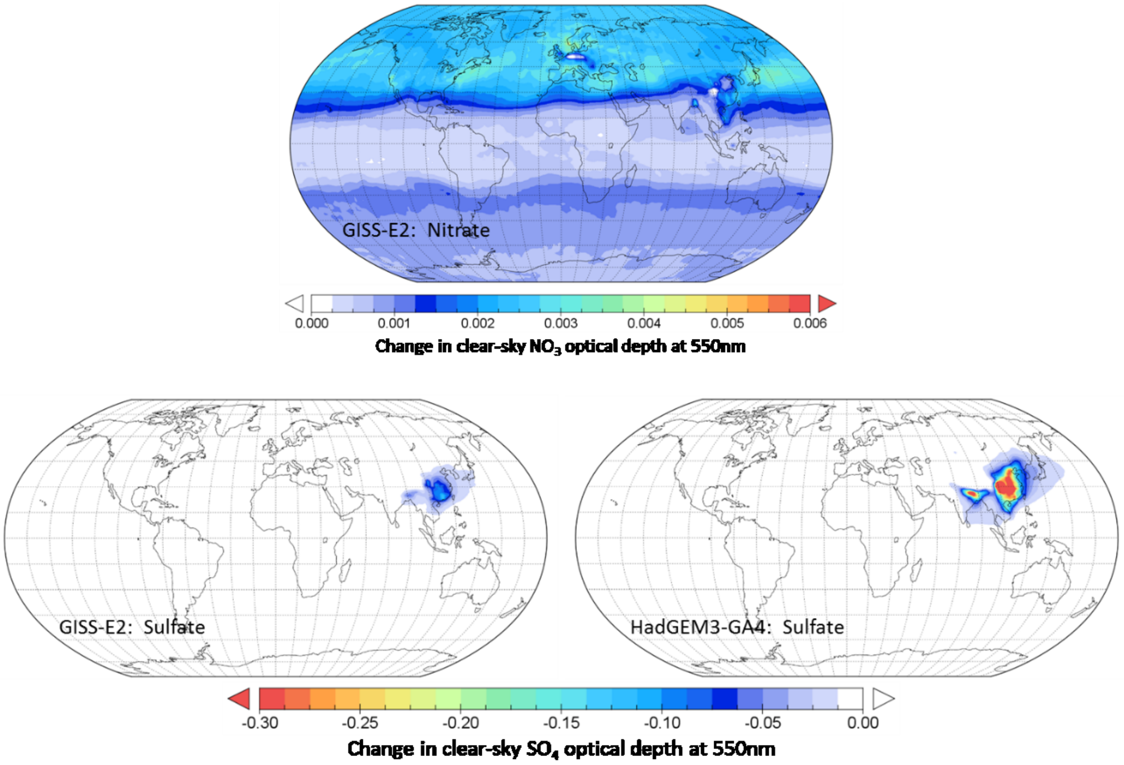

Figure 4-7: *Change in annual mean nitrate optical depth in GISS-E2 (top), and changes in sulfate optical depth in GISS-E2 and HadGEM3-GA4 (bottom), due to removing SO_2 emissions from China. Differences are calculated from the 150-year mean of the perturbation simulation minus the control simulation. Note that the colour scale direction is reversed for nitrate AOD, as this increased almost everywhere, whereas sulfate AOD either decreased or stayed the same everywhere. Also note the scale range for nitrate is a factor of 50 smaller than for sulfate changes.*

However, the global mean change in sulfate-only optical depth in GISS-E2 is still only half that in HadGEM3-GA4, and locally around eastern China the increase in nitrate optical depth in GISS-E2 is found to be at least an order of magnitude smaller than the decrease in sulfate optical depth (Figure 4-7). Hence, nitrate compensation does not substantially contribute to the discrepancy in local AOD changes. It is still the case therefore that HadGEM3-GA4 simulates a considerably larger change in sulfate optical depth per unit change in SO_4 burden at both global and local scales. Having the largest change in AOD per unit change in aerosol burden (Table 4-1) appears to be key for explaining why this model simulates the largest climate response. The exact origin of this discrepancy is not immediately apparent, as both models appear to make similar choices for sulfate dry effective radii and refractive indices (Koch et al., 2007; Bellouin et al., 2011), however these properties are also extremely non-linear with relative humidity, meaning that small variations in the exact choice of values, the parameterised relationship with humidity, and the local humidity in the models, could all play a role.

Comparing the clear-sky and all-sky AOD for GISS-E2 (which diagnosed both), reveals that the simulated reduction in E. China all-sky AOD (-0.183) is much larger than the reduction in clear-sky AOD (-0.047). It can't be known for sure that the same would apply to CESM1, but it suggests that the all-sky values available for CESM1 might be expected to be larger than the equivalent clear-sky values, had these been diagnosed. Given this, it is all the more surprising to find reductions of all-sky AOD in CESM1 for the E. China region of -0.076 and for the global mean of -0.0013 (Table 4-1), which lie in between the clear-sky values of GISS-E2 and HadGEM3-GA4, even though CESM1 had the largest change in SO_4 burden both locally and globally. Consequently, the change in AOD per unit sulfate in CESM1 is again much smaller than in HadGEM3-GA4, as was seen above for GISS-E2, and in fact is locally the smallest of all three models (Table 4-1).

The AOD changes per unit burden change are summarised in Table 4-1, and it is clear that there is a large diversity between all three models. The possible contributors to diversity in the AOD per unit burden are extensive, and a full analysis of them is beyond the scope of this study. Host model effects, such as different cloud climatologies and radiative transfer schemes, are one likely contributor. Stier et al. (2013) suggests that one third of total diversity originates there. Relative humidity, which drives water uptake (hygroscopic growth), is also diverse among models. For example, Pan et al. (2015) find that over India, boundary-layer RH is the main source of diversity. At the more basic level, assumed composition and hygroscopic growth curves also often differ between models – in this case, the aerosol scheme used for HadGEM3-GA4 assumes that all sulfate is in the form of ammonium sulfate, whereas CESM1 and GISS-E2 both assume a mixture of ammonium sulfate and sulfuric acid, and additionally all three models use different sources for their hygroscopic growth parameterisations (Bellouin et al., 2011; Liu et al., 2012; Koch et al., 2011; and references therein).

The changes in SW radiative flux and the final climate response seem to correlate with the change in AOD much better than with the change in SO_4 burden for HadGEM3-GA4 and GISS-E2, where over China there is a 6-fold difference both in AOD and in SW flux change between these two models. For CESM1, the all-sky AOD change over E. China is about 1.6 times larger than the clear-sky change in GISS-E2 (Table 4-1). If I use instead all-sky AOD from GISS-E2 (not shown in Table 4-1) which ought to be more comparable, then the AOD change over E. China is found to be more than 2 times smaller in CESM1 than in GISS-E2. However, in contrast the change in TOA SW flux over the same region is about 4.7 times larger in CESM1, and so it seems that unlike for the discrepancies between HadGEM3-GA4 and GISS-E2, differences in the AOD response cannot explain the difference in the magnitudes of radiative flux change between CESM1 and GISS-E2 (see Sect. 4.3.3 for continuation of the discussion on possible causes).

4.3.2 Differences in cloud effects

Sulfate aerosol exerts indirect radiative effects by modifying cloud properties. The strength of these indirect effects is highly uncertain (e.g. Boucher et al., 2013) and differs substantially between the models, having been shown to contribute substantially to inter-model variation in historical aerosol forcing Wilcox et al., 2015. Differences in the underlying climatologies of the models, particularly with regard to cloud distributions, could also be important. For instance, the radiative effect of sulfate aerosol is modulated by the reflectivity of the underlying surface in the radiation scheme (Chýlek and Coakley, 1974; Chand et al., 2009), which may often be a cloud-top. The low contrast with a highly reflective cloud surface means that sulfate aerosol above a cloud top will have a reduced direct radiative forcing. Blocking of radiation by clouds will also reduce the direct radiative effects of any aerosols within or below them (e.g. Keil and Haywood, 2003). Additionally, aerosol indirect effects can saturate in regions with a high level of background aerosol (e.g. Verheggen et al., 2007; Carslaw et al., 2013), meaning that the potential for indirect radiative forcing can vary with the location of clouds. On top of diversity in indirect effects, and in the climatological distribution of clouds, different dynamical changes in cloud cover could also alter the all-sky flux.

In our case, the good correspondence between higher (clear-sky) AOD change in HadGEM3-GA4 and higher (all-sky) SW flux change in this model might suggest that the cloud effects are not the root cause of the larger radiative response in this model. However, the origin of this good correspondence in fact appears to be somewhat dependent on how clouds modify the radiative effects of sulfate aerosol.

To explore the role of cloud effects, global and regional mean changes in clear-sky TOA SW flux are also given in Table 4-1, and the geographic changes in clear-sky flux are shown alongside the all-sky flux changes in Figure 4-8. For the extreme cases of HadGEM3-GA4 and GISS-E2 (third and first rows), comparing the changes in clear-sky TOA SW flux with the all-sky TOA SW flux changes reveals that for clear-sky conditions, there is in fact a much smaller regional discrepancy between these two models: Over the E. China region GISS-E2 has a 4.1 W m^{-2} clear-sky SW flux

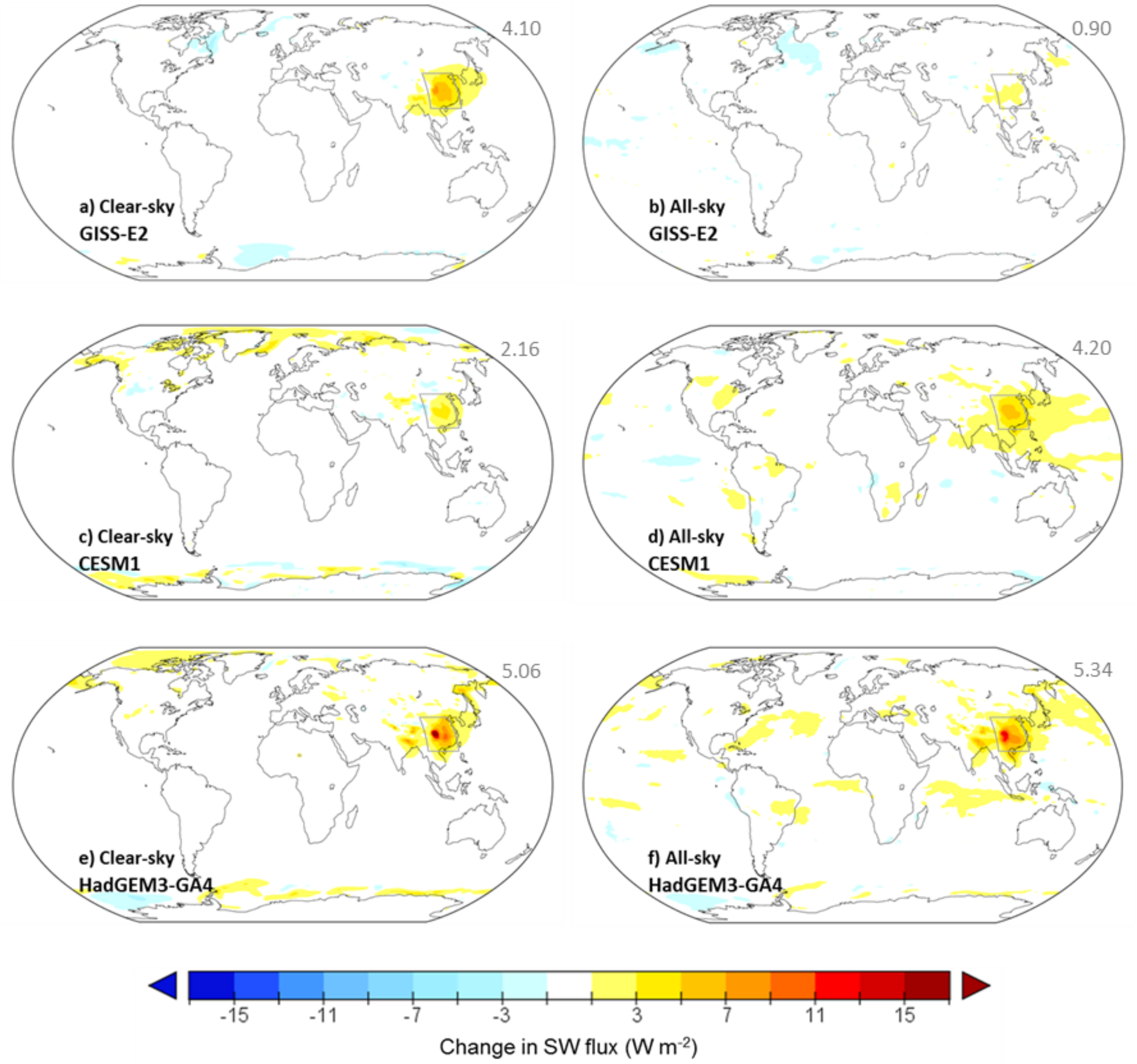

Figure 4-8: *Changes in net TOA clear-sky (a, c, e) and all-sky (b, d, f) SW flux due to removing SO2 emissions from China in GISS-E2 (a, b), CESM1(c, d), and HadGEM3-GA4 (e, f). GISS-E2 and HadGEM3-GA4 plots are calculated from 150-year means of the perturbation minus control simulations. Clear-sky diagnostics were not available for the full 150-year period for CESM1, and so for this model the mean is calculated from a 30-year extension to both perturbation and control simulations. Comparing the left column (clear-sky) with the right (all-sky) over China, GISS-E2 has much larger clear-sky flux changes, HadGEM3-GA4 has very similar clear-sky and all-sky flux changes, and CESM1 has larger all-sky flux changes. Numbers in grey in the top right of each plot indicate the E. China regional mean in W m*$^{-2}$ *(also given in Table 4-1). For reference the E. China region is also denoted with a grey box on each plot.*

change, whereas HadGEM3-GA4 has a 5.1 W m^{-2} flux change. HadGEM3-GA4 still has the larger radiative change, but nowhere near the 6-fold difference that is seen in the all-sky flux (Section 4.2, and Table 4-1). This much reduced difference between GISS-E2 and HadGEM3-GA4 in the clear-sky compared with the all-sky anomaly is hard to apportion quantitatively though, because compared with the clear-sky change, the all-sky response incorporates all the contributing factors described above: the additional radiative forcing due to aerosol indirect effects, the screening of direct radiative effects due to clouds blocking radiation and providing a high albedo background, and also any dynamical changes in cloud cover.

In this case, GISS-E2 simulates a small increase in cloudiness in east China due to dynamical changes when sulfate is removed (Figure 4-9, top panel). Combined with the screening effect of clouds, this appears to almost completely offset the direct forcing of reduced SO_4, resulting in a far smaller all-sky SW flux change than clear-sky SW flux change over E. China (0.9 W m^{-2} all-sky compared with 4.1 W m^{-2} clear-sky). HadGEM3-GA4 by contrast has very little difference between all-sky and clear-sky flux changes (5.3 W m^{-2} and 5.1 W m^{-2} respectively (Figure 4-8)). The changes in cloud amount over east China are somewhat more mixed (Figure 4-9, bottom panel), although area-averaged, the overall cloud change is a small decrease, which should enhance the all-sky flux change. However, spatially as well as in magnitude the HadGEM3-GA4 all-sky flux change is exceptionally similar to the clear-sky flux change, and does not resemble the pattern of cloud changes (comparing Figure 4-8, panels [e] and [f], and Figure 4-9, panel [c]), which suggests that changes in aerosol radiative effects are larger than the effect of the small cloud cover changes, and still dominate the all-sky flux changes. Therefore, the very similar regional all-sky and clear-sky SW flux changes in HadGEM3-GA4 imply that unlike in GISS-E2, aerosol indirect effects in HadGEM3-GA4 probably roughly compensated for the presence of clouds reducing the direct effect, so that the change in all-sky combined direct and indirect forcing is similar to the change in clear-sky direct forcing when sulfate is removed.

The picture is different for CESM1. Comparing the clear-sky and all-sky TOA SW flux changes for this model (Figure 4-8, middle row), we find that the clear-sky changes are much smaller than the all-sky flux changes. In fact, over China the clear-sky SW flux changes in CESM1 are considerably smaller in magnitude than the clear-sky flux changes in GISS-E2 (comparing Figure 4-8 panels [a] and [c]). Averaged over the E. China region, the clear-sky flux change in CESM1 is only 2.2 W m^{-2}, compared with the 4.1 W m^{-2} clear-sky change in GISS-E2. However, whereas in GISS-E2 the all-sky SW flux change (0.9 W m^{-2}) was then more than four times smaller than this clear-sky flux change, in CESM1 the all-sky SW flux change is instead almost two times larger than the clear-sky flux change: 4.2 W m^{-2} regionally averaged.

This is partly again due to cloud changes – in this case CESM1 has predominantly reductions in cloud amount over E. China (Figure 4-9), which will have the effect of increasing the all-sky radiative flux change relative to the clear-sky changes. However, as with HadGEM3-GA4, these

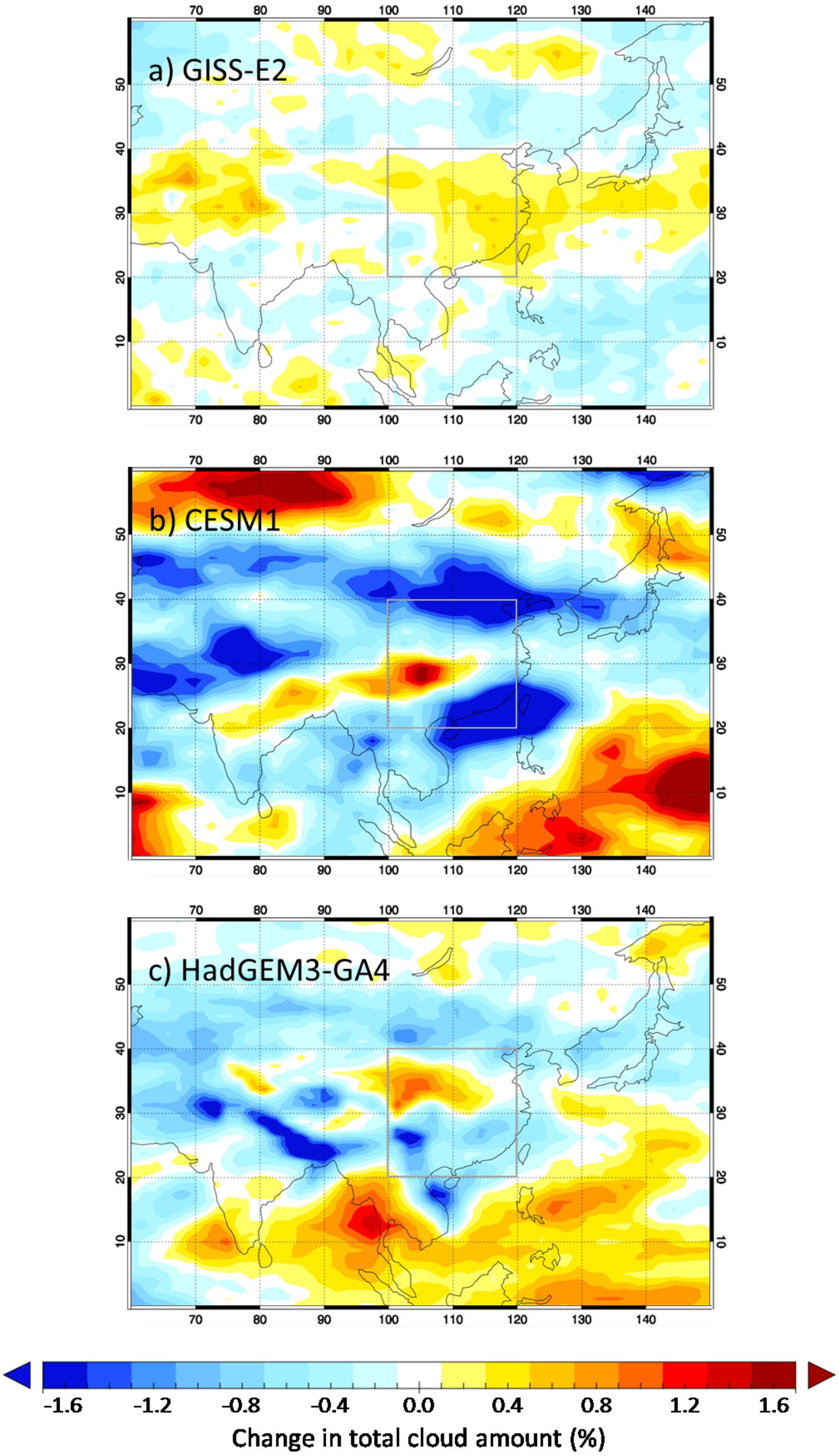

Figure 4-9: *Change in annual mean total cloud cover over Asia in a) GISS-E2, b) CESM1, and c) HadGEM3-GA4, following removal of SO2 emissions from China. GISS-E2 and HadGEM3-GA4 plots are calculated from 150-year means of the perturbation minus control simulations. This diagnostic was not available for the full 150-year period for CESM1, and so for this model the mean is calculated from a 30-year extension to both perturbation and control simulations. Consequently, the apparently larger responses in (b) may be partly the result of the much shorter averaging period, which will result in a poorer signal/noise ratio.*

regional cloud reductions in CESM1 do not match up spatially with the maximum changes in all-sky SW flux seen in Figure 4-2 and Figure 4-8. Instead, the maximum changes in both the all-sky and clear-sky SW flux changes correspond very closely with the reduction in AOD (Figure 4-6[b]). Both all-sky and clear-sky SW flux changes are maximum around where the AOD reduction is maximum, and in this location the all-sky flux change is still substantially greater than the clear-sky change. The good correspondence between the all-sky flux change and AOD change, but poor correspondence between the all-sky flux change and cloud changes, implies that aerosol radiative forcing is the dominant factor in the regional all-sky SW flux changes. The larger all-sky than clear-sky SW flux therefore indicates that in CESM1, a large aerosol indirect effect, and/or effect of clouds increasing aerosol particle size through hygroscopic growth, overall amplifies the radiative effect of aerosols considerably in cloudy conditions, resulting in the much greater regional change in all-sky flux when aerosol is removed.

Between these three models, then, the way that clouds modify the radiative balance is a major source of diversity over the E. China region in the response to removing SO2 emissions from China. In GISS-E2, the inclusion of clouds greatly reduces the radiative effect of a change in sulfate aerosol. In HadGEM3-GA4, the effect of including clouds is small, and does not change the clear-sky forcing substantially. Finally, in CESM1, including clouds considerably amplifies an otherwise weak clear-sky radiative flux change. I note though that clear-sky diagnostics will be influenced by choices within the models of how aerosol water uptake is determined under the artificial assumption of clear-sky conditions. The all-sky SW flux change, which drives the final climate response, is regionally still the most directly comparable quantity, reflecting the total radiative effect of the aerosol change in the different models.

4.3.3 Differences in aerosol radiative forcing efficiency

An additional source of discrepancy between the models lies in differences in the aerosol radiative forcing efficiency – the direct forcing that results from a given aerosol optical depth or burden (e.g. Samset et al., 2013). A previous model intercomparison looking at radiative forcing as part of the AeroCom Phase II study found that, on a global scale, there was a large variation in the radiative forcing due to aerosol-radiation interactions per unit AOD between different participating models (Myhre et al., 2013a). As a result, whether a model simulates AOD changes correctly, for instance, may not particularly constrain the resultant forcing and eventual climate response.

Globally-averaged, the changes in radiative flux and AOD are too small in these experiments to calculate an accurate ratio, but instead I calculate here a regional radiative forcing efficiency by taking the change in clear-sky SW flux over the 100-120E, 20-40N E. China region (from Section 4.4.2), and dividing by the AOD change over the same region (Table 4-1). This is not directly comparable with previous studies like Myhre et al. (2013a) as I use a regionally-averaged number instead of globally-averaged, and for the numerator I use the change in clear-sky TOA SW flux as the best available measure of aerosol direct radiative effect, rather than the direct radiative forcing diagnosed either from double radiation calls or simulations with fixed meteorology. Consequently, I use this metric here mainly to qualitatively highlight differences between the models.

As noted in Sect. 4.4.1 and 4.4.2, over the eastern China region HadGEM3-GA4 has a 6-fold larger mean AOD reduction (-0.29) compared with GISS-E2 (-0.047), but only slightly larger clear-sky SW change (5.1 W m-2 compared with 4.1 W m-2). As a result, the regional radiative forcing efficiency for HadGEM3-GA4 is much smaller than that of GISS-E2: -17.6 W m^{-2} τ^{-1} compared with -87.2 W m^{-2} τ^{-1} (Table 4-1). Normalising by the change in sulfate burden integrated over the same region, instead of the AOD, gives a similar relationship: HadGEM3-GA4 has a smaller regional mean change in clear-sky SW flux per Tg sulfate than GISS-E2: -145 W m^{-2} Tg^{-1} compared with -256 W m^{-2} Tg^{-1}. Proportionally though, the discrepancy is not as great when normalising by change in sulfate burden, due to the much larger AOD per unit mass of sulfate simulated in HadGEM3-GA4. Curiously Myhre et al. (2013a) reported results that were qualitatively the inverse of what I show here, finding that the atmospheric component of GISS ModelE has a smaller sulfate radiative forcing than that of HadGEM2 (HadGEM3's predecessor, with a very similar aerosol scheme) when normalised by AOD, although still larger when normalised by column-integrated sulfate burden. The reason for the discrepancy is not clear, though the aforementioned fact that we calculate our numbers for a specific region means that there may be important local factors. The sulfate-specific radiative efficiencies in Myhre et al. (2013a) are calculated relative to the all-sky direct radiative effect, and regional differences between the models in cloud masking of direct effects or vertical distribution of aerosol may therefore change the relationship. However, they also evaluated the clear-sky forcing normalised by AOD for all aerosol species combined, and still found HadGEM2 to be higher than GISS ModelE.

CESM1 lies in the middle of the range, with a regional radiative forcing efficiency of -28.4 W m^{-2} τ^{-1} (Table 4-1) – though again with the caveat that for CESM1, the AOD is an all-sky quantity, whereas the values given above for HadGEM3-GA4 and GISS-E2 were calculated using clear-sky AOD. GISS-E2 provided both clear-sky and all-sky AOD diagnostics, and using instead the all-sky AOD change from GISS-E2 gives a much smaller value of -22.4 W m^{-2} τ^{-1} for its regional radiative forcing efficiency (c.f. -87.2 W m^{-2} τ^{-1} for clear-sky AOD found in the previous paragraph), suggesting that when compared like-for-like, CESM1 may actually have a somewhat greater radiative efficiency compared to the other models. More directly comparable between all three models is the flux change normalised by regional change in sulfate burden, which for CESM1 is -55.4 W m^{-2} Tg^{-1}. This is considerably lower than either HadGEM3-GA4 or GISS-E2, and indicates that the despite having at least average radiative efficiency per unit AOD, the very weak translation of sulfate burden to AOD in CESM1 is a dominant factor which prevents this model from simulating a larger SW flux change and climate response than it already does. As noted in the previous Section though, this small clear-sky flux change per unit sulfate change is compensated by a large indirect effect as well as favourable regional cloud changes, meaning that the all-sky flux change per unit AOD is by far the largest is CESM1 (Table 4-1), and the all-sky flux change per sulfate burden change is then moderate in CESM1 (not shown, but readily calculated from Table 4-1). Similarly, the exceptional reduction in aerosol radiative effects due to clouds in GISS-E2 means that its all-sky flux change per unit AOD is almost exactly the same as that of HadGEM3-GA4 (Table 2), despite the clear-sky regional radiative efficiency being so much larger.

The Myhre et al. (2013a) AeroCom intercomparison found that globally, the atmospheric component of CESM1 (CAM5.1) had a much higher sulfate radiative forcing efficiency than the atmosphere-only version of GISS-E2. In their case, they found CAM5.1 to have approximately 2.25 times higher all-sky direct radiative forcing per unit AOD than GISS-E2. However, the study also found that, globally, the atmospheric component of HadGEM2 had a slightly larger forcing efficiency to CAM5.1, both for sulfate (all-sky) and all aerosols combined (clear-sky), unlike the somewhat smaller regional efficiency found here for HadGEM3-GA4 compared with CESM1. Given that the regional values here from GISS-E2 and HadGEM3-GA4 also seem to conflict qualitatively with the global values from the AeroCom study, this would suggest that either the global comparison is not relevant on regional scales, or else the radiative efficiency is very sensitive to changes in model configuration and version.

4.3.4 Differences in climate sensitivity

So far I have discussed mainly factors which influence the translation of a change in aerosol precursor emissions to a radiative heating, and these varied strongly between the models. There is a final step in arriving at the climate response, which is the translation of a given radiative heating into a surface temperature change. The climate sensitivity – the amount of warming simulated per unit radiative forcing – is also well known to vary considerably between models, both globally (e.g. Flato et al., 2013) and regionally (e.g. Voulgarakis and Shindell, 2010), and this will additionally impact the strength of the final response. Climate sensitivity is typically estimated from a 2× or 4× global CO_2 simulation, giving a large response and a large forcing from which to calculate the ratio. For GISS-E2, a climate sensitivity value of 0.6 K (W m^{-2})$^{-1}$ was found in the IPCC AR5 report from a 4 × CO_2 simulation (Flato et al., 2013) using the regression method of Gregory et al. (2004) to estimate the effective radiative forcing. This method involves linearly regressing the global annual mean temperature change against the global annual mean TOA radiative imbalance, typically over the first 20 years of the simulation, in order to find the radiative imbalance at the intercept where $\Delta T = 0$. For CESM1, a value of 1.1 K (W m^{-2})$^{-1}$ was obtained from values from a 2 × CO_2 simulation (Meehl et al., 2013), noting that in this case the radiative forcing was calculated using the stratospheric adjustment method (Hansen et al., 2005). For HadGEM3-GA4, I rely on a 100-year 2 × CO_2 simulation that was performed separately as part of the Precipitation Driver and Response Model Intercomparison Project (PDRMIP, Samset et al., 2016), which gave a value of 1.1 K (W m^{-2})$^{-1}$ based on the Gregory method. This is lower than the value found for HadGEM3-GA4's predecessor HadGEM2 in the IPCC AR5 (1.6 K (W m^{-2})$^{-1}$), and means that both HadGEM3-GA4 and CESM1 are very close to the CMIP5 multi-model mean sensitivity of 1.0 K (W m^{-2})$^{-1}$ (Flato et al., 2013).

This indicates that while CESM1 and HadGEM3-GA4 both have very similar climate sensitivities, GISS-E2 has an unusually small sensitivity – in fact, the smallest value of all the CMIP5 models reported in the IPCC AR5 report (Flato et al., 2013). This presumably compounds the fact that GISS-E2 simulates the smallest SW flux change of the three models, ensuring that the resulting surface temperature response is comparatively smaller still. Differences in climate sensitivity do not seem to explain any of the variation in the magnitude of the response between CESM1 and HadGEM3-GA4, at least based on the above values. However, it is worth noting that these climate sensitivity values are derived from global CO_2 forcings, whereas in this case I am looking at the translation of a very regional aerosol forcing into a global response. It is not trivial that the global-mean temperature response to a regionally localised forcing is a function only of the resulting globally-averaged forcing, and in particular it may be that different models are more or less sensitive to forcings in specific regions. Unfortunately, to my knowledge there is no study that has calculated climate sensitivity to regional forcings in single or multi-model frameworks. Jones et al. (2007) found that the climate sensitivity to historical sulfate forcing was statistically the same as to a global 2 × CO_2 simulation in the HadGEM1 climate model, although the historical sulfate forcing is distributed broadly across the northern mid-latitudes, making it a rather less localised forcing than that investigated here. Similarly, Voulgarakis and Shindell (2010) and Shindell (2012) calculated climate sensitivities to forcings imposed in different latitudinal bands for the GISS-E2 model, finding that there is considerable variation relative to the global climate sensitivity. In the Shindell (2012) study, estimates of the response to forcings at different latitudes in three other global climate models, based on the GISS-E2 sensitivities, are found to largely agree to within +/- 20% with the full simulations however, suggesting that regional sensitivities (relative to a model's global sensitivity) may not vary that much between models.

In these experiments we did not diagnose the radiative forcing. However, over the E. Asia region the local temperature changes correlate well with local (all-sky) SW flux changes, and HadGEM3-GA4 and CESM1 both have very similar regional temperature changes per regional SW flux change: 0.07 K (W m^{-2})$^{-1}$ in both models, consistent with their very similar global climate sensitivities discussed above. Also in line with the global sensitivities, GISS-E2 has a slightly smaller regional temperature change per SW flux change, with 0.05 K (W m^{-2})$^{-1}$ – though the values are sufficiently small that within the 2σ uncertainty on SW flux and temperature change, this is not significantly different from HadGEM3-GA4 and CESM1. Globally, the mean temperature change per unit SW flux change is again similar in HadGEM3-GA4 (0.4 K (W m^{-2})$^{-1}$) and CESM1 (0.3 K (W m^{-2})$^{-1}$), with the difference not being significant. These values are somewhat smaller than the 2 × CO_2 values quoted above, likely because the global coupled SW flux change is a poor measure of the actual radiative forcing, and in particular in Section 4.2 was seen to overestimate the actual ERF value in HadGEM3-GA4. Globally GISS-E2 has a negligible temperature change, so no meaningful global result can be compared here for this model.

4.4 Conclusions

By applying an identical regional perturbation to anthropogenic SO_2 emissions in three different climate models, three markedly different resulting climate responses are observed, ranging from virtually no coherent surface air temperature response in one model (GISS-E2), to pronounced surface warming all across most of the northern hemisphere in another (HadGEM3-GA4). The third model (CESM1) sits in the middle in terms of both magnitude and spatial extent of the temperature response. This huge variation in climate response corresponds to a similarly large variation in the SW radiative flux change following the reduction in sulfate aerosol. All three models show a fairly localised increase in net downwards SW radiation over China as a result of reduced SO_2 emissions from this region, however the magnitude of this radiative heating is substantially greater in HadGEM3-GA4 than in CESM1, which is substantially greater still than in GISS-E2. The response in GISS-E2 is so weak that temperature changes are largely not detectable above the internal variability of the model. The stronger heating in CESM1 and HadGEM3-GA4 produces much more pronounced temperature changes, and even though the radiative heating is localised over China, the temperature responses in these two models are much more spread out, particularly in the zonal direction. This is consistent with the findings of Shindell et al. (2010), who found that the temperature response to inhomogeneous aerosol forcings is more uniform and extends much further from the forcing location in the zonal direction than in the meridional direction.

Comparing the models reveals very different changes in the SO_4 mass change due to removing the same amount of SO_2 emissions from China, very different ratios of AOD change per mass of sulfate, and different radiative flux changes per unit AOD. These differences are compounded further by large variations in cloud interactions, as well as variations in climate sensitivity, and feedbacks on other aerosol species such as nitrate, which diversify the response further.

Specifically, CESM1 is found to simulate the largest reduction in sulfate burden both globally and locally. HadGEM3-GA4 has the smallest reduction in sulfate burden globally and the second largest reduction regionally, yet it produces by far the largest reduction in AOD both globally and regionally over E. China. Though GISS-E2 and CESM1 both simulate much smaller changes in AOD than HadGEM3-GA4, still the SW flux changes and temperature responses produced are very different between these two models. An inferred larger aerosol-cloud interaction means that CESM1 simulates a particularly large change in all-sky SW flux relative to its fairly small AOD change, so although having a smaller response than HadGEM3-GA4, it is still much closer to it than GISS-E2. In GISS-E2, the clear-sky radiative forcing efficiency of sulfate is very large, but this is almost perfectly compensated for by large reductions in the direct radiative effect of sulfate when clouds are factored in. The absolute AOD change is also much smaller than HadGEM3-GA4 in the GISS-E2 model. This then combines with compensating increases in nitrate aerosol globally to reduce the radiative response yet further, and finally a smaller global climate sensitivity than the other two models results in this being translated into a largely negligible temperature response.

In addition to differences in the total changes in sulfate and AOD, there are also substantial differences in the spatial distribution of the changes, attributed to differences in the rate of chemical conversion of SO_2 to SO_4, which influences how concentrated the aerosol changes are around the emission region. This implies that even if both the AOD per sulfate burden and the forcing per unit AOD were identical among the three models, they would still have different distributions of radiative forcing.

There are no direct observations of sulfate radiative forcing, nor of sulfate optical depth or vertically-integrated burden, and so in Chapter 3 I have tried validating the aerosol component of the models with a range of surface and satellite-based measurements of total aerosol optical depth, surface sulfate concentration, column SO_2, and sulfate wet deposition. All the models have biases, and no one model performed best against all the observational datasets used. Tentatively, HadGEM3-GA4 seemed to perform best over China against observations of both total AOD and sulfate wet deposition, though over some other parts of the world this model performed slightly poorer, e.g. for global AOD and US surface sulfate concentrations. However, the main conclusion here is that comparison against all existing observational measures is unable to satisfactorily constrain which model response is more realistic, given that the ratios of both AOD change per sulfate burden change and SW flux change per AOD (Table 4-1) are found to vary so substantially between the models. The model with the largest sulfate mass change (CESM1) did not have the largest radiative or climate response, and two models with a similar AOD change (CESM1 and GISS-E2) had markedly different radiative and climate responses. Given the range of discrepancies that I find in all steps along the conversion of SO_2 change to SO_4 change to AOD change to radiative forcing to temperature response, it seems that knowing how accurate a model is with respect to either sulfate concentrations or total AOD is far from sufficient to determine whether the climate response to a regional aerosol precursor emission is similarly accurate.

I have only looked here at surface temperature, which is a particularly direct measure of the climate response. The response of other, less well-constrained, climate variables such as precipitation might be expected to show even greater diversity. These results show that there remains a very large uncertainty in current climate models in the translation of aerosol precursor emissions into a climate response, and imply that care must be taken not to over-interpret studies of aerosol-climate interaction or of climate change in general if the robustness of results across diverse models cannot be demonstrated.

On a more optimistic note, both the models which showed the more substantial change in SW radiative flux (CESM1 and HadGEM3-GA4) also show a remarkably strong remote temperature response to a relatively localised northern mid-latitude heat source, with qualitatively similar temperature change patterns that extend across much of the northern hemisphere, indicating that there may be some agreement on the response to a given regional forcing, if not on the forcing itself. In the next Chapter, I will analyse the patterns of global climate responses to a range of different regional aerosol emission perturbations performed with the HadGEM3-GA4 model, to understand how the climate response might vary with the location of the forcing.

5 Sensitivity of climate response to aerosol emissions from different regions

In Chapter 4, the similar temperature responses seen over Eurasia for HadGEM3-GA4 and CESM1 gave an interesting – albeit very tentative – suggestion that the spatial pattern of response to a regional forcing over China may, in some cases, be qualitatively similar between different models, although there was huge variation in the forcing due to a particular aerosol emissions change. With this possibility in mind, I will turn my attention here to addressing how the climate response varies depending on the region and aerosol species perturbed, though with only a single climate model as this requires a very large number of simulations.

As discussed in Chapter 1, the only previous systematic attempt to investigate the sensitivity of the climate to different forcing locations were the studies of Shindell and Faluvegi (2009) and Shindell et al. (2012). However in these studies they only perturbed forcing within different latitude bands. For aerosol forcing, the northern mid-latitude band they used of 30°N - 60°N already alone contains most of the major industrialised regions contributing to anthropogenic emissions – the US, Europe, and China. Similarly, various studies which have investigated the climate impacts of historical aerosol forcing (eg. Bollasina et al., 2011; Kawase et al., 2011; Hwang et al., 2013; Wilcox et al., 2013) have implicitly diagnosed responses to changes across the northern hemisphere, and especially the northern mid-latitudes, as this is simply where the largest historical changes have been. However, anthropogenic aerosol emissions are far from zonally uniform within the northern hemisphere; there is considerable inhomogeneity in the zonal direction as well. It is therefore pressing to understand how the sensitivity of the climate might depend on the longitudinal as well as latitudinal location of an aerosol forcing, by investigating geographically more localised regions rather than just latitude bands or historical northern hemisphere changes. Such a breakdown of climate response by region driving it also has the potential to be more informative for policy applications, since emission reduction policies are set regionally, and not harmonised across all the hemisphere or indeed within a particular latitude band. Similarly, policy measures cannot directly scale atmospheric forcing or concentration distributions, but instead can target only the actual emissions from that region, and so investigating responses as a function of regional emission changes has again the potential to be more directly informative.

5.1 Experimental setup

To investigate the regional sensitivity of the climate to aerosol emissions, an extensive range of simulations were performed with the HadGEM3-GA4 coupled climate model. Five different northern hemisphere regions were selected in which to perturb emissions: The whole northern hemisphere mid-latitudes (‘NHML’, 30°N - 60°N), the United States (‘US’, 235°E - 290°E, 30°N - 50°N), Europe (‘EU’, defined using the HTAP Phase II definition[1], following country borders), India (‘IND’, 70°E - 90°E, 10°N - 30°N), and East Asia (‘EA’, 105°E - 145°E, 20°N - 45°N). Figure 5-1 shows how these regions correspond geographically. Note the new ‘East Asia’ region is different to the ‘China’ region used in Chapter 4, so as to avoid overlapping with the India region, and also capture some emissions on the very eastern edge of China that fell outside the ‘China’ domain, as well as emissions from Korea and Japan that are significant regionally.

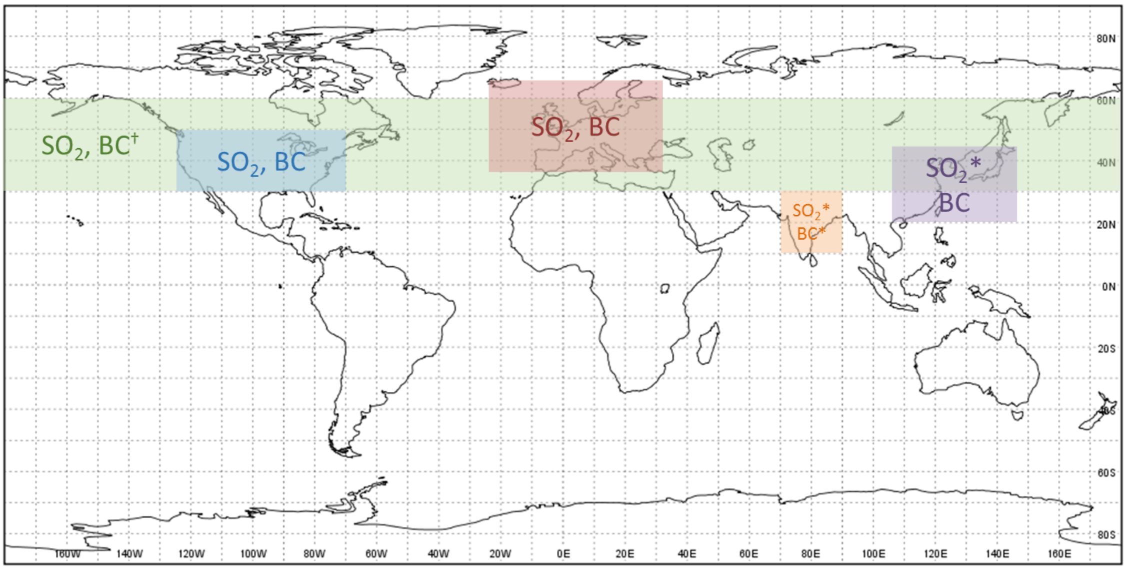

*** Simulations performed partly or wholly by Dilshad Shawki**
† Shorter (100-year) simulation

Figure 5-1: *Map showing the range of regional perturbations investigated with HadGEM3-GA4. Left to right: ‘NHML’ (30°N - 60°N; green box), ‘US’ (235°E - 290°E, 30°N - 50°N; blue box), ‘EU’ (red box is approximate, as European region was defined following the HTAP Phase II definition[1], which follows country borders to define the eastern edge), ‘IND’ (70°E - 90°E, 10°N - 30°N; orange box), and ‘EA’ (105°E - 145°E, 20°N - 45°N; purple box). For each region anthropogenic SO_2 and fossil-fuel BC emission removal experiments were performed separately.*

---

[1] HTAP Phase II region descriptions available at: http://iek8wikis.iek.fz-juelich.de/HTAPWiki/WP2.1

For each region, one simulation was performed in which anthropogenic SO_2 emissions were set to zero ('noSO2') within that region[2], and one simulation was performed with fossil-fuel BC emissions (FFBC) within the region set to zero ('noBC'). Figure 5-2 shows how the regions correspond to the centres of anthropogenic SO_2 and soot emission. In the text, these experiments will be referred to respectively as 'noSO2_REG' and 'noBC_REG', where 'REG' is replaced with the shorthand for the relevant region.

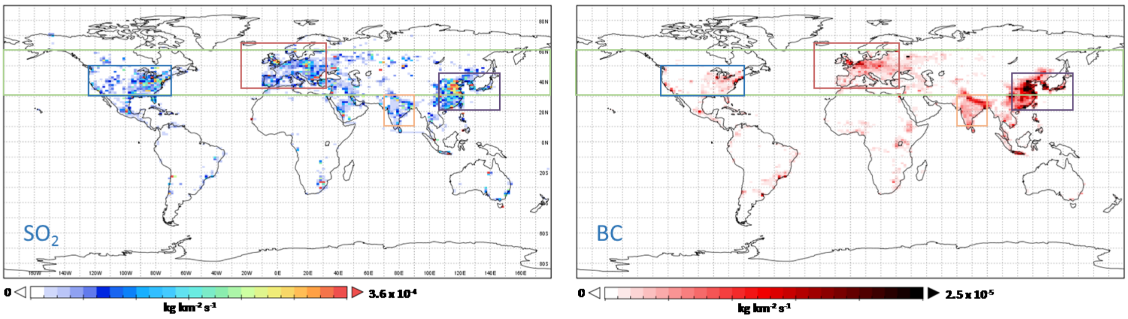

Figure 5-2: Maps showing correspondence of the perturbation regions in Figure 5.1 with the year-2000 distribution of anthropogenic SO_2 emissions (left) and fossil-fuel BC emissions (right) in the Lamarque et al. (2010) ACCMIP emissions inventory that was used to drive HadGEM3-GA4.

These perturbation simulations were complemented by six control simulations that were initialised from different atmospheric initial conditions, the ensemble of control simulations being used to provide an estimate of the internal variability of the modelled climate. With the exception of the noBC_NHML simulation, which was only run for 100 years, all simulations were integrated for 200 years. As in Chapter 4, aerosol emissions were prescribed at year 2000 levels following the ACCMIP emissions inventory (Lamarque et al, 2010) and well-mixed greenhouse concentrations were prescribed globally at the year 2000 concentrations specified in CMIP5 throughout the 200 years. Three of the six control simulations, the noSO2_IND perturbation, and years 101-200 of the noBC_IND and noSO2_EA perturbations, were performed by Mr. Dilshad Shawki (Imperial College London), to whom I am grateful for helping to make possible the full range of simulations presented here.

In all cases, the coupled simulations were branched from a previous control simulation that had already been spun-up for 100 years. Analysis of the control simulation global mean surface

---

[2] For the US region, SO_2 emissions were removed from the same emission sectors as described for China in Chapter 4, corresponding to a near complete (97%) removal

temperature reveals that unfortunately, the ocean model had not yet reached an equilibrium state after this spin-up time, and the control simulation's climate was still drifting. In fact, it took approximately 300 years for the control simulation's global mean temperature to approximately reach equilibrium, and moreover the perturbation simulations should in principle require up to the same length spin up each in order for them to have reached their new equilibrium state, and such long simulations (~500 years each) were computationally unfeasible. However, comparison between the control simulation and perturbation simulation global mean temperatures indicated that after an adjustment period of about 50 years, the perturbation simulations would drift approximately parallel to the control simulations, with an offset interpreted here as the response to the imposed forcing. Previous studies (e.g. Andrews et al., 2012) have indicated that the majority of the response to step-change forcings is indeed realised within the first few decades, and with this in mind, for my analysis below I discard the first 50 years of each simulation and compare averages of years 51-200 on the assumptions that this is sufficient for the majority of the climate response to be realised, and that the climate drift is roughly independent of the response and can be subtracted off, given that both perturbation simulation and control simulation start in a similar state of disequilibrium.

In addition to the coupled atmosphere-ocean simulations, a subset of the perturbations were also performed as 26-year atmosphere-only simulations. Given the availability of atmosphere-only simulations for these regional perturbation experiments, in this chapter I actually present the total (SW + LW) effective radiative forcing resulting from the various perturbations, and not the more indirect measure of aerosol forcing, namely the long-term SW flux anomaly, which was used in Chapter 4. Additionally, atmosphere-only simulations allow me to determine what component of the total responses are due to slow, ocean-mediated temperature changes, compared with faster atmospheric or land-surface changes (adjustments). For these simulations sea-surface temperatures and sea-ice concentrations were prescribed to observed monthly values for year 2000. I discard the first year as spin-up and average over years 2-26 of these simulations when calculating the atmosphere-only responses.

5.2 Climate sensitivity to regional fossil-fuel BC removal

I will look first at the responses to regional FFBC emission removals. A previous study (Baker et al., 2015) has found that global removals of FFBC emissions in multiple different models, including a version of HadGEM3, gave extremely small responses that were largely not significant above internal variability, and so the prospects for finding robust results here from smaller regional perturbations are not high.

Figures 5-3 and 5-4 below show the total (i.e. SW + LW) TOA effective radiative forcing (ERF) diagnosed from the atmosphere-only simulations, where applicable, and the 150-year mean surface temperature and precipitation responses from the coupled experiments, for all the perturbation regions. The temperature and precipitation responses are stippled where the perturbation minus control simulation signal at that gridpoint exceeds two standard deviations of the ensemble of six control simulations.

In all cases, the changes in TOA ERF are seen to be very small, and mostly dominated by patchy variations that are most likely due to internal cloud variability. In the noBC_NHML case, only over eastern China does there appear to be a large enough change in FFBC aerosol to create a noticeable negative forcing which stands out from the patchy changes elsewhere. A similar negative forcing above eastern China can be seen in the noBC_EA perturbation. In both cases, however, the FFBC forcing over eastern China is only slightly larger in magnitude than the patchy changes elsewhere associated with variability. Atmosphere-only simulations were not performed for the noBC_EU or noBC_US perturbations, however no noticeable coherent forcing is seen above Europe or the US in the noBC_NHML plot (which incorporates both these regions in the perturbation), and so it can be surmised that if the relevant atmosphere-only simulations had been performed for the Europe- or US-only experiments they would have revealed nothing substantial.

Unsurprisingly then, the coupled temperature and precipitation responses in all the FFBC cases are weak, patchy, and mostly not significant. Some of the small patches of temperature response which are stippled seem contrary to the expected FFBC TOA forcing – for instance the noBC_US, noBC_EU, noBC_EA, and noBC_IND perturbations all seem to show some warming around the Bering Sea on the eastern tip of Russia (and more broadly across the whole Arctic, though generally not exceeding the 2σ level elsewhere), even though the expected global temperature response due to removing FFBC, a warming agent, would be a net cooling. NoBC_NHML, the largest perturbation, also has changes of opposite sign to the others across much of the Arctic. Similarly, most of the experiments appear to show regions with similar magnitude temperature changes off the coast of Antarctica, but the sign of these temperature changes is not consistent, and their location is exceptionally remote from the location of the FFBC forcings. As a result, these localised temperature changes seem much more likely to be

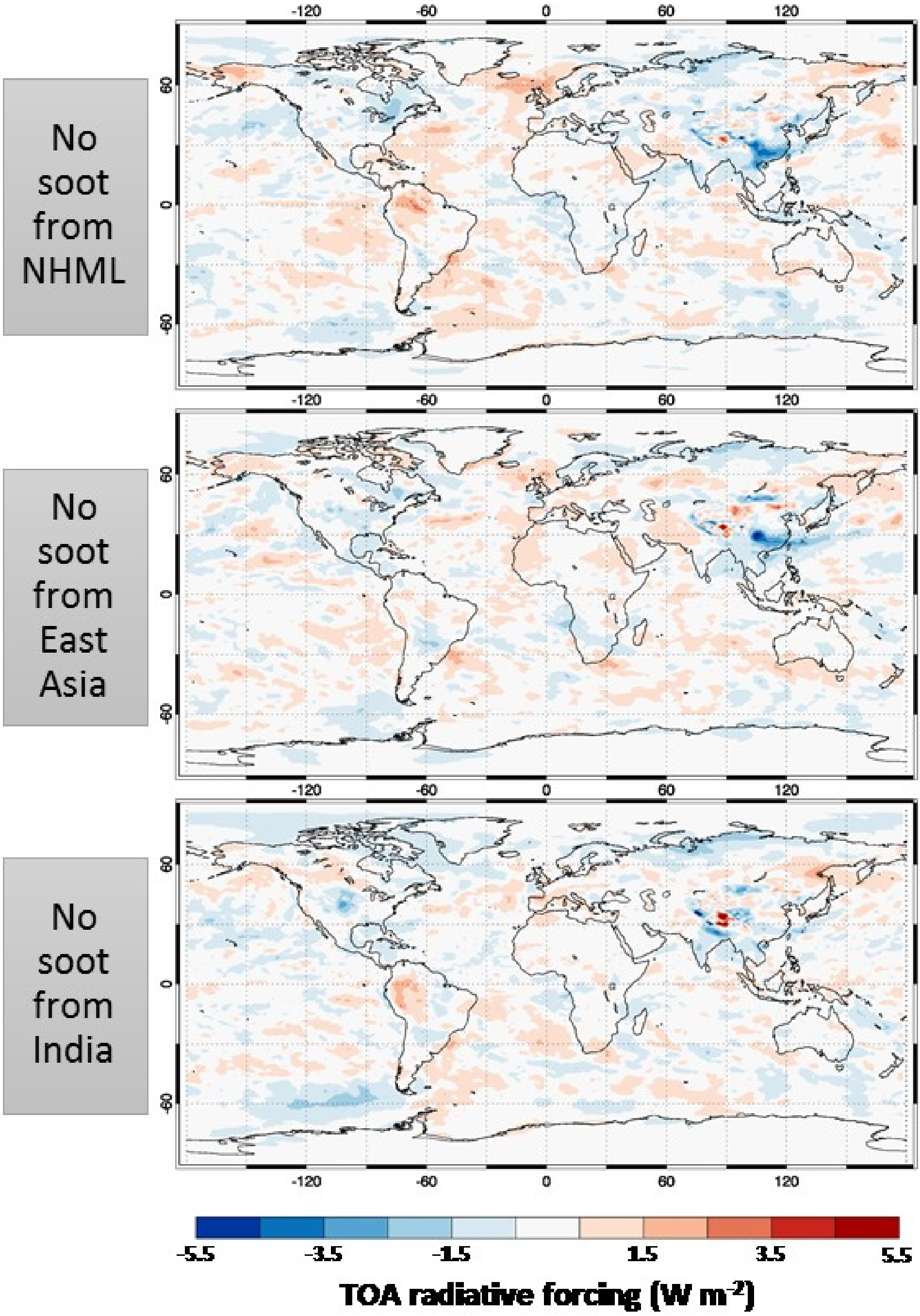

Figure 5-3: *Annual mean TOA effective radiative forcing (ERF) due to removing fossil-fuel black carbon (soot) emissions from the northern hemisphere mid-latitudes (NHML, top row), East Asia (second row), and India (third row), in HadGEM3-GA4. Effective radiative forcing is estimated as the difference in net down TOA radiative flux (both SW + LW components) between 25-year atmosphere-only perturbation and control simulations. Atmosphere-only simulations were not performed for the US or Europe soot removals.*

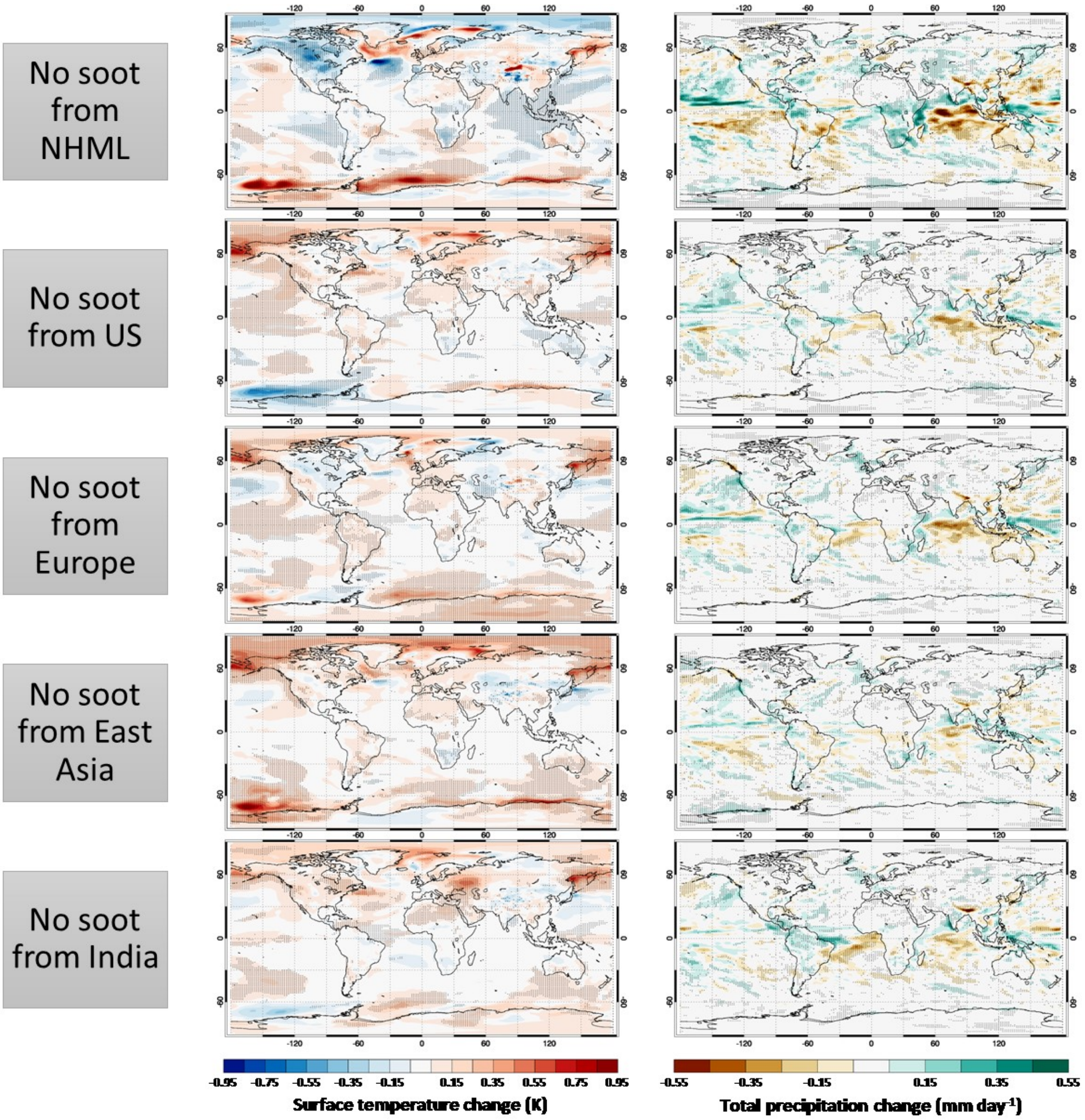

***Figure 5-4:** Annual mean Surface temperature change (left column), and total precipitation change (right column), due to removing fossil-fuel black carbon (soot) emissions from the northern hemisphere mid-latitudes (NHML, top row), the United States (US, second row), Europe (third row), East Asia (fourth row), and India (fifth row), in HadGEM3-GA4. All changes are 150-year-mean differences (perturbation minus control simulation) from coupled simulations, except for noBC_NHML where only 50-year means were used. Changes are stippled where the change at that gridpoint exceeded two standard deviations from an ensemble of six control simulations with perturbed atmospheric initial conditions.*

due to internal variability rather than a true response to the small remote forcings in each case, and this perhaps indicates that six control simulations is insufficient to fully explore the range of unforced variability, or perhaps that the control simulation realisation which was used to create these difference plots was already an outlier in some regions. Still, the fact that we use several control simulations already provides a valuable insight into uncertainty, with the extent of computational resources that are available to us.

The very small and counterintuitive temperature changes contrast with relatively clear and strong responses to black carbon forcing that have been found using previous versions of the HadGEM model. For instance, Figure 5-5 reproduces the radiative forcing and temperature responses due to historical increases in fossil-fuel black carbon that were found for the HadGEM1 model by Jones et al. (2007). Based on this study, my FFBC removal simulations – and in particular the noBC_NHML case, which represents a large fraction of historical FFBC increases, should result in a similarly clear negative temperature response.

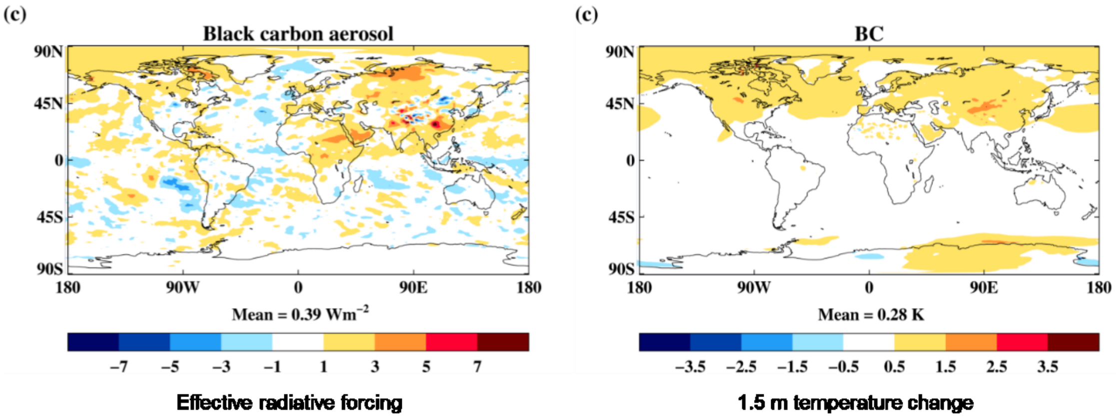

Figure 5-5: *Reproduction of Jones et al. (2007) Figure 1c (left) and Figure 2c (right), showing effective radiative forcing and surface air temperature change to historical (1860-2000) increases in fossil-fuel black carbon emissions in the HadGEM1 climate model. ERF is estimated as the difference between the ten-year means of atmosphere-only simulations with year 2000 and year 1860 emissions, while the temperature response is the difference between twenty-year means of corresponding coupled atmosphere/mixed-layer ocean simulations, after they had reached equilibrium.*

Stronger responses to BC forcing have also been found by other older-generation models, e.g. Hansen et al. (2005) using a previous version of GISS Model E. However, recent multi-model studies by Baker et al. (2015) and Samset et al. (2016) have found much smaller responses to present-day black carbon forcing in a range of newer-generation climate models, although both studies found HadGEM3-GA4 to have among the smallest sensitivities to black carbon. Of particular interest, Baker et al. (2015) performed simulations removing present-day black carbon emissions globally using the same base version of HadGEM3 as in the present study, but coupled to an entirely different aerosol scheme – the more sophisticated GLOMAP modal aerosol scheme (Mann et al., 2010). Their simulated surface temperature responses and TOA SW flux changes for two different ensemble members are reproduced in Figure 5-6.

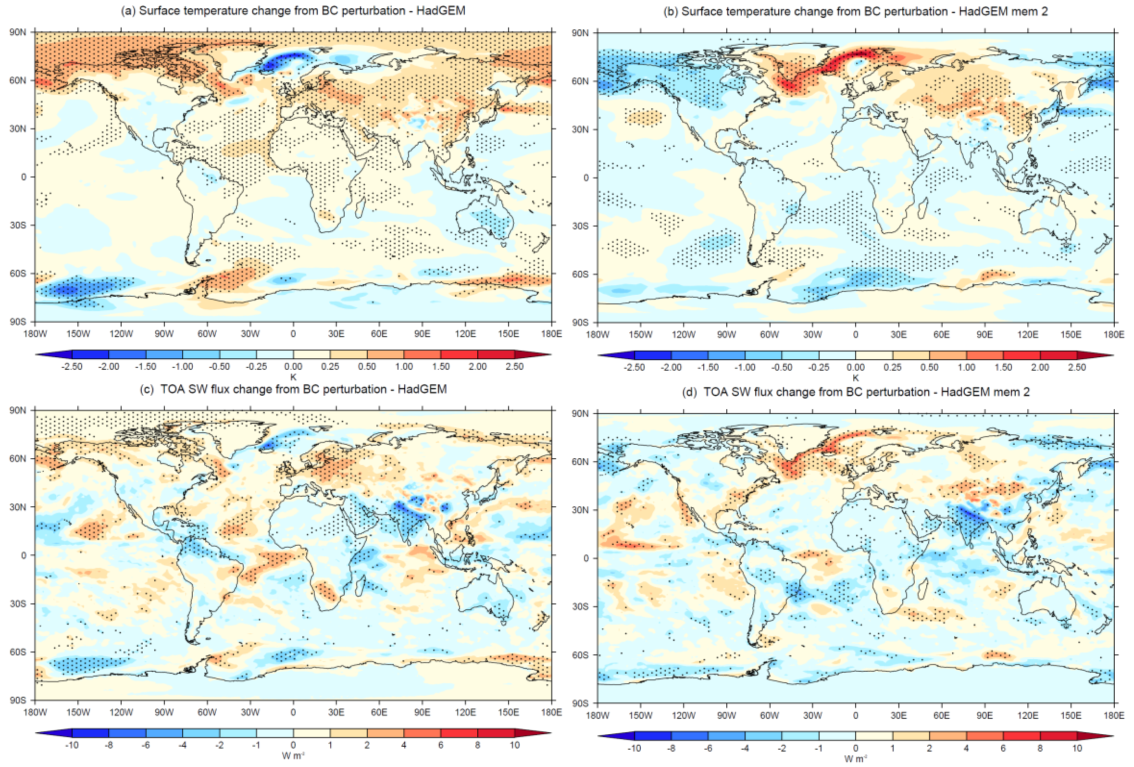

Figure 5-6: *Reproduction of Supplementary Figure S2 a, b, c, and d from Baker et al. (2015), showing the surface temperature change (a, b) and TOA SW flux change (c, d) due to removing anthropogenic black carbon emissions globally in two different ensemble members of HadGEM3-GLOMAP. Plots are 50-year annual mean differences between perturbation and control atmosphere-ocean simulations.*

Remarkably, the temperature differences in the two HadGEM3 ensemble members of Baker et al. (2015) look strikingly similar to the temperature changes seen in the noBC experiments in Figure 5-4. In particular over the northern high latitudes, Figure 5-6 (a) (Baker et al. (2015) member 1) shows the same counterintuitive warming as noBC_US, noBC_EU, noBC_EA, and noBC_IND in Figure 5-4, even showing the same stronger response around the Bering Sea. In contrast, Figure 5-6 (b) (Baker et al. (2015) member 2) shows cooling across the northern high latitudes and North America, very much like the noBC_NHML experiment in Figure 5-4.

The fact that the Baker et al. (2015) study independently obtained such similar temperature responses to present-day BC emissions removal indicates that the small and somewhat counterintuitive results that I obtained here are not just a glitch, but are reproducible in the HadGEM3 model. Moreover, the finding that the CLASSIC and GLOMAP aerosol schemes both produce similar regional responses to BC removal lends further support to my results. Baker et al. (2015) obtained both warming and cooling responses in the northern high latitudes in the 50-year means of different ensemble members, just as I do for different regional emission perturbations in Figure 5-4. This further confirms the conclusion that that the apparently counterintuitive warming response cannot be a genuine signal, but must rather be internal variability of the model which exceeds any forced response in this region, leading to either warming or cooling irrespective of the black carbon emissions changes.

I also calculate the global changes in emissions, radiative forcing, temperature and precipitation, which are summarised in Table 5-1, with error ranges on temperature and precipitation again representing two standard deviations from the ensemble of six control simulations. The noBC_NHML perturbation represents a 52% reduction in global FFBC emissions, but the global surface temperature change is not significantly different from zero. The TOA ERF is actually slightly positive in both the noBC_NHML and noBC_EA experiments, indicating that the small regions of negative forcing seen over eastern China in Figure 5-3 are entirely overwhelmed in the global mean by the internal variability elsewhere. Given that these two experiments have by far the largest reductions in FFBC emissions (52% and 30% of global emissions, respectively), it seems that the global mean TOA ERF is probably not significantly different from zero in any of the experiments. Temperature change appears very marginally significant at the 2σ level in the noBC_EA experiment only, but given how borderline it is and given that the even larger noBC_NHML experiment had no significant global temperature change, it seems unlikely that this can be considered a genuine response.

Global precipitation change also appears to be marginally significant in the noBC_NHML, noBC_EA, and noBC_IND experiments, but is not significant for noBC_US or noBC_EU. BC absorbs downwelling SW radiation before it reaches the surface, and so its presence in the atmosphere tends to radiatively cool the surface even while warming the climate system as a whole through atmospheric absorption of both incoming and reflected radiation (e.g. Ramanathan et al., 2001). Consequently, the atmospheric absorption of BC is larger than its net TOA forcing, and this atmospheric heating acts to stabilise the atmosphere against convection when BC is present (e.g. Ming et al., 2010). It is plausible therefore that FFBC changes could result in a significant precipitation response even if there is no significant change in global mean temperature. It has indeed been found previously by Andrews et al. (2010) and Samset et al. (2016) that the ‘fast’ atmospheric response of precipitation to BC through increasing the stability of the atmosphere, which scales with atmospheric absorption, can typically outweigh the ‘slow’ response mediated by global temperature changes, which scales with TOA forcing.

Table 5-1: *Global, annual mean changes in emissions, TOA effective radiative forcing, surface effective radiative forcing, surface temperature ('Temp'), and total precipitation ('Precip') due to removing fossil-fuel BC emissions from the northern mid-latitudes, the US, Europe, East Asia, or India, in HadGEM3-GA4. Effective radiative forcing is calculated as the difference in net down all-sky radiative flux (both SW + LW components) between a 25-year averaged fixed-SST perturbation simulation and a control simulation (not available for the noBC_US or noBC_EU perturbations). Other values are 150-year mean differences between a coupled perturbation simulation and the control simulation, except for the NHML case where 50-year means were used. Emissions changes are given both as an absolute value, and as a percentage reduction relative to total global emissions. Surface temperature and precipitation changes are quoted with an error range, calculated as two standard deviations from an ensemble of six control simulations with perturbed atmospheric initial conditions.*

	ΔBC emissions ($Tg\ yr^{-1}$)	TOA ERF ($W\ m^{-2}$)	Surface ERF ($W\ m^{-2}$)	ΔTemp (K)	ΔPrecip (mm/day)
NHML	-2.69 (-52.3%)	0.030	0.137	0.003 ± 0.051	0.0052 ± 0.0035
US	-0.36 (-7.0 %)	-	-	0.039 ± 0.052	0.0038 ± 0.0040
Europe	-0.57 (-11.1%)	-	-	0.041 ± 0.052	0.0035 ± 0.0040
East Asia	-1.53 (-29.8%)	0.054	0.090	0.053 ± 0.052	0.0052 ± 0.0040
India	-0.51 (-9.9%)	-0.011	0.026	0.040 ± 0.052	0.0045 ± 0.0040

In my experiments, FFBC is being removed, which should result in less atmospheric heating and therefore decreased stability and increased precipitation, which is indeed what is found in the noBC_NHML, noBC_EA, and noBC_IND experiments, although the global mean changes are very small (Table 5-1). The radiative forcing at the surface is larger (more positive) than the TOA forcing in all these three experiments, which implies a negative atmospheric forcing (defined as TOA forcing minus surface forcing) as would be expected from the theory – although as has already been noted above, the TOA forcing is small enough in all cases that it appears to have been overwhelmed by internal variability in the global mean, and so it is not clear that the larger global mean surface forcings are genuinely reflecting the reduced atmospheric absorption of FFBC, rather than just being coincidental.

Even if this small reduction in atmospheric absorption is indeed due to the FFBC removals, it is still not clear that the small increases in precipitation are genuinely caused by this, rather than just being internal variability which happened to fall very marginally outside the estimated *2σ* uncertainty range. If the precipitation change is dominated by fast precipitation responses due to reduced atmospheric absorption, the same precipitation signal ought to also be present in the atmosphere-only simulations. There is, however, no consistent precipitation response at all in the atmosphere-only simulations, with global mean precipitation changes of 0.0003 mm day^{-1}, -0.0015 mm day^{-1}, and 0.0002 mm day^{-1}, in the noBC_NHML, noBC_EA, and noBC_IND atmosphere-only simulations respectively. Since the atmosphere-only simulations are only averaged over 25 years, it is likely that the internal variability completely dominates these values. It is therefore possible that the longer averaging period of the coupled simulations reveals a signal of a very small fast precipitation response that cannot be detected in the atmosphere-only simulations, but this is only conjecture.

Because FFBC removal results in such a small ERF, and consequently small and very uncertain temperature and precipitation changes, for the rest of this chapter I will focus on understanding the responses to the SO_2 emission removals.

5.3 Climate sensitivity to regional anthropogenic SO_2 removal

SO_2 emissions in the ACCMIP dataset used here are more than an order of magnitude larger than FFBC emissions (103.7 Tg/yr globally, compared with 5.1 Tg/yr), and global sulfate radiative forcing and resulting climate responses have correspondingly been established in many previous studies as being far larger than for BC (e.g. Andrews et al., 2010; Baker et al., 2015; Samset et al., 2016). As shown in Chapter 4, HadGEM3-GA4 in fact has a particularly strong response to changes in SO_2 emissions from China, so it is expected that possibly the signals from other regional perturbations will be large as well. Whether this is realistic or not is a matter of discussion; I argued that HadGEM3-GA4 may actually be one of the more skilful models when it comes to capturing AOD, at least over East Asia, although the resultant forcing per unit AOD is harder to constrain. However what is certainly true is that such strong forcings from regional emission perturbations are ideal for studying responses to zonally (and meridionally) inhomogeneous forcings (and emissions).

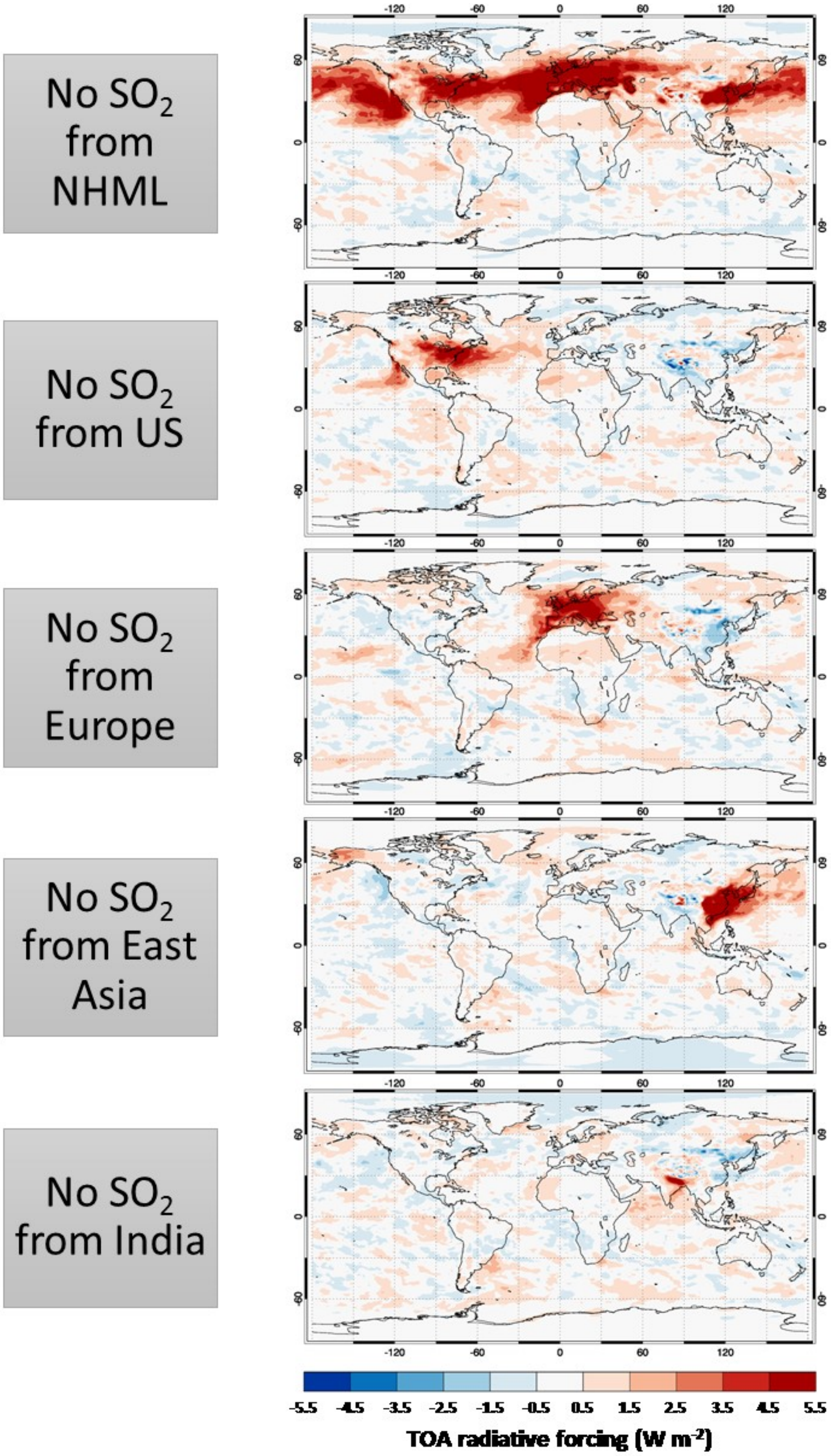

Figure 5-7: *Annual mean TOA effective radiative forcing (ERF) due to removing SO_2 emissions from the northern mid-latitudes (NHML), the US, Europe, East Asia, and India, in HadGEM3-GA4. Effective radiative forcing is calculated as the difference in net down all-sky radiative flux (both SW + LW components) between 25-year averaged annual mean results from the perturbation and the control fixed-SST simulations.*

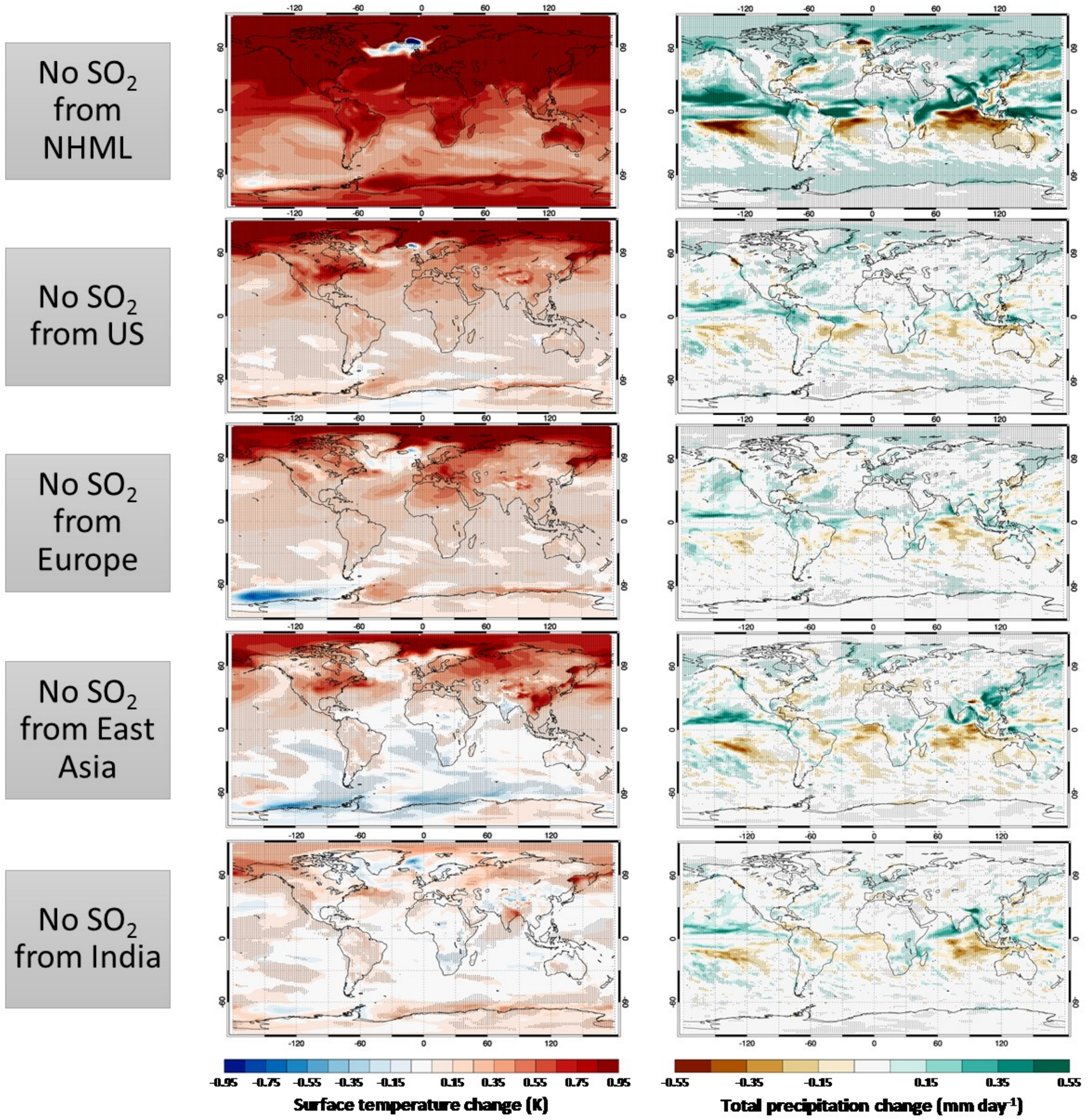

Figure 5-8: *Changes in annual mean surface temperature and precipitation due to SO_2 emission removals from each of the five different regions, in HadGEM3-GA4. Changes are calculated as 150-year averages of the perturbed simulation minus the control simulation. Stippling denotes the magnitude of the change in a given grid-box exceeds 2 standard deviations, calculated from six control simulations with perturbed atmospheric initial conditions.*

Figure 5-7 shows the total (SW + LW) TOA ERF for each of the regional SO_2 emission removals. As expected, they all show much clearer and stronger forcings than FFBC, though localised around the regions of perturbation. The fact that the forcing is quite localised around the region where emissions were perturbed is an indication that the SO_2 and resulting sulfate aerosol does not typically get transported very far from the original source in large quantities, as was also noted in Chapters 3 and 4.

Figure 5-8 shows the corresponding surface temperature and precipitation responses from the 150-year means of the coupled simulations. In all cases, there are widespread significant changes in surface temperature, and in tropical precipitation, though the geographical pattern of response for those two key variables is very different. Removing SO_2 from the whole northern mid-latitudes, representing a 62% reduction in global SO_2 emissions, results in a particularly strong response, with temperature changes saturating the contour colour scale (>0.95K) across almost the entire northern hemisphere. This is also the only experiment to have widespread significant precipitation changes outside of the tropics. The temperature and precipitation responses are discussed separately in detail in the following two sub-sections.

5.3.1 Temperature responses to regional SO_2 removals

Removing SO_2 emissions resulted in a positive radiative forcing, and all the experiments show widespread warming, though particularly the noSO2_NHML, noSO2_US, noSO2_EU, and noSO2_EA perturbations, which are all larger perturbations than noSO2_IND. In all cases, the radiative forcing is located in the northern hemisphere (Figure 5-7), and the experiments all show the warming response to be located preferentially in the northern mid- and high-latitudes (Figure 5-8). The noSO2_NHML, noSO2_US, and noSO2_EU cases show some warming in the southern hemisphere as well, but with a far smaller magnitude than that in the northern hemisphere. The noSO2_EA and noSO2_IND experiments show very little significant warming in the southern hemisphere.

The noSO2_NHML experiment results in positive forcing across the northern mid-latitudes, but in all the other cases, the forcing was very localised around the region where emissions were perturbed (Figure 5-7). Despite this, warming is consistently seen in locations right across the northern hemisphere, often far from the location of the forcing. In the noSO2_US case, the mid-latitude warming is strongest over the US itself, as might be expected from the location of the forcing, but there is warming across the whole latitude band with stronger warming over northern Russia and central Asia. In the noSO2_EU case, the mid-latitude warming response is strongest over Europe, but again with warming across the whole latitude band and stronger warming over the US and central Asia. In the noSO2_EA case the mid-latitude warming is again strongest in East Asia, where the forcing is greatest, but there is almost as strong a remote response over the US and northern Russia. In the noSO2_IND case there is less warming, but a clear response over India itself and also over the US and northern Russia again. In all cases the strongest temperature responses though are in the Arctic, indicating that this region is very sensitive to forcings located anywhere in the hemisphere. Warming in the Arctic is known to be amplified by atmospheric and surface albedo feedbacks (e.g. Graversen and Wang, 2009; Screen and Simmonds, 2010) – in particular, less vertical transport at high-latitudes favours relatively more surface warming (Pithan and Mauritsen, 2014), and additionally Artic warming can result in sea-ice melting, which reduces the surface albedo and in turn results in more warming (Curry et al., 1995). In all cases, it is clear from the widespread remote warming responses that heat is efficiently transported from the location of the radiative forcing through to the rest of the hemisphere, and so once some of this heating reaches the Arctic the positive feedback presumably then results in the particularly strong remote response consistently seen in this region.

5.3.2 Precipitation responses to regional SO_2 removals

All SO_2 experiments result in significant precipitation changes in the tropics. Consistently across the experiments the tropical precipitation response takes the form of a region of wettening just north of the equator, and a region of drying just south of the equator, and can be interpreted as a shift in the intertropical convergence zone (ITCZ). The shift is predominantly seen over the tropical ocean regions with fewer consistent changes over land, although all experiments show some increased precipitation on the western coast of India and over central India, resulting from an intensification of the South Asian monsoon. These changes around India and the Arabian Sea are strongest for the noSO2_NHML, noSO2_EA, and noSO2_IND experiments, which have the largest temperature changes around Asia in general – although the noSO2_EA experiment results in very little temperature change actually over India, suggesting that it is this temperature change around the broader region which is important, through impacting the continental-scale land-sea thermal contrast.

As with temperature, this shift in the tropical precipitation band is not localised to the longitudinal position of the radiative forcing, but is instead seen across all tropical ocean basins. The ITCZ forms at the boundary between the northern and southern hemisphere Hadley cells, which transport heat polewards from the equatorial regions. The position of the ITCZ is consequently set by the temperature contrast between the northern and southern hemispheres. Previous modelling studies, e.g. Haywood et al. (2013) and Hwang et al. (2013), have noted that if one hemisphere is warmed preferentially (for instance by asymmetric anthropogenic aerosol forcing), then the latitude where tropical convection is greatest will shift towards the warmer hemisphere, corresponding to an expansion of the colder Hadley cell into the warmer hemisphere in order to transport excess heat down the temperature gradient. This is further backed up by historical records of river flows, which show reduced rainfall over the Sahel region in response to very large northern hemisphere volcanic eruptions (e.g. Oman et al, 2006), and suggests that the models are reproducing the correct response to hemispheric aerosol cooling. In my noSO2 simulations, the shift in the ITCZ across the tropics seen here is consistent with the widespread temperature responses characterised by preferential warming across the northern hemisphere, due to the removal of a cooling aerosol species. With the whole northern hemisphere being relatively warmer than the southern hemisphere regardless of the perturbation region, tropical precipitation shifts ubiquitously north towards the warmer hemisphere. As with the discussion of seasonal precipitation shifts in Chapter 2, the character of the tropical precipitation anomaly is not particularly seasonally dependant (not shown), and is largely captured by these annual mean plots.

The noSO2_NHML experiment, which has by far the largest temperature change, also shows widespread significant precipitation changes outside of the tropical regions. It broadly reveals increases in precipitation in both the northern and southern hemisphere mid-latitudes, consistent with the substantial global mean warming in this experiment which results in a warmer atmosphere which holds more moisture and has increased radiative cooling, thereby permitting increased latent heating and greater precipitation (e.g. Held and Soden, 2006). The exception to this pattern in the mid-latitudes is a band of drying around the storm track regions in both the north-west Atlantic and north-west Pacific. Both these bands of drying have a region of wettening to the north, and so this may be indicative of a northward shift in the storm tracks, which has been previously reported as a robust response in global warming simulations (e.g. Chang et al., 2012), including due to declining anthropogenic aerosols (Rotstayn et al., 2014). The neighbouring land also warms more than the ocean, weakening the temperature contrast between the land and the warm Gulf Stream and Kuroshio currents, and this could weaken storm activity over the western boundary currents as well (e.g. as in Cione et al., 1993), which when superimposed on the broad mid-latitude wettening may also contribute to this signal.

5.3.3 Fast versus slow responses to regional SO_2 removals

As noted in Section 5.2, the use of atmosphere-only simulations along with coupled atmosphere-ocean simulations allows investigation of the responses that occur on short timescales, before the ocean has been able to respond, as well as long timescales. Figure 5-9 shows the patterns of temperature and precipitation changes that occur in the atmosphere-only versions of the SO_2 removal experiments.

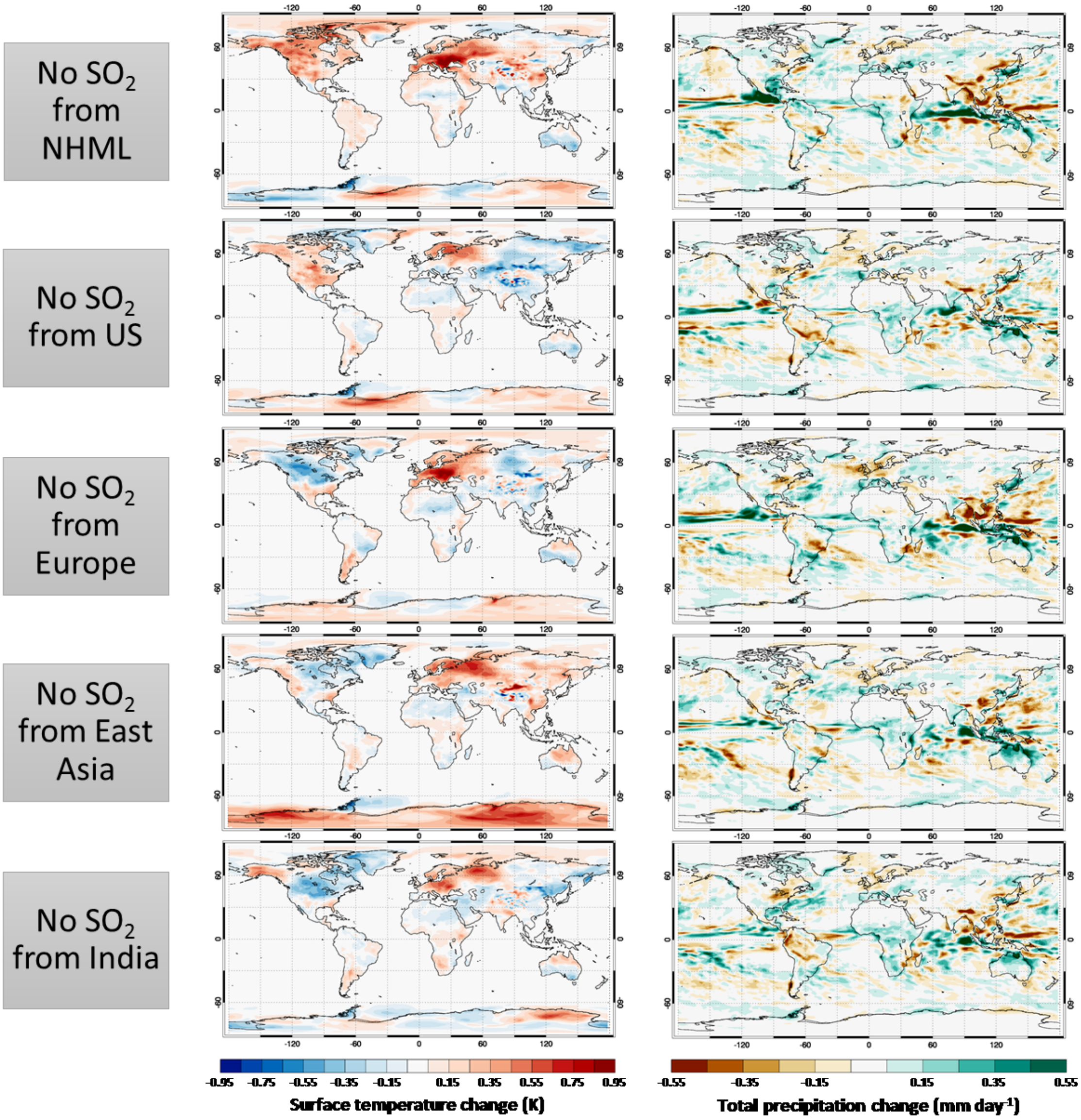

Figure 5-9: Annual mean changes in surface temperature and precipitation when removing SO_2 emissions from the northern mid-latitudes (NHML), the US, Europe, East Asia, and India in the atmosphere-only simulations with HadGEM3-GA4. Differences are calculated from 25-year averages from a perturbation simulation and a control simulation with sea-surface temperatures and sea-ice cover prescribed to observed year-2000 conditions.

In surface temperature, the responses are far patchier in the atmosphere-only simulations than in those that were fully coupled, and do not show the consistent warming across the whole hemisphere (except in the noSO2_NHML case, where the forcing is itself spread across the whole mid-latitudes). In all cases there is some warming directly underneath the location of the radiative forcing, however the surface temperature changes away from the location of the forcing are typically just as large but not consistent in sign, with the exception of a warming feature over north-east Europe that does appear in all the simulations. The other inconsistent remote temperature responses are likely due to internal variability, which is clearly much larger regionally for these 25-year averages in the atmosphere-only simulations than for the 150-year averages in the coupled simulations.

Although the standard deviation is not estimated for these atmosphere-only simulations, to give a qualitative indication of the internal variability the atmosphere-only control simulation was extended, and Figure 5-10 shows the change in surface temperature between the next 25 years and the first 25-year section. From this it is clear that the surface temperature changes in Fig 5-9 are indeed dominated by internal variability, and that even the consistent warming seen over north-east Europe is probably also unforced, as it appears again in Figure 5-10. Indeed, in any one experiment, the warming that is co-located with the radiative forcing would also not be distinguishable from internal variability. It is only the consistency with which warming is always seen around the region of the perturbation across the different experiments that suggests that

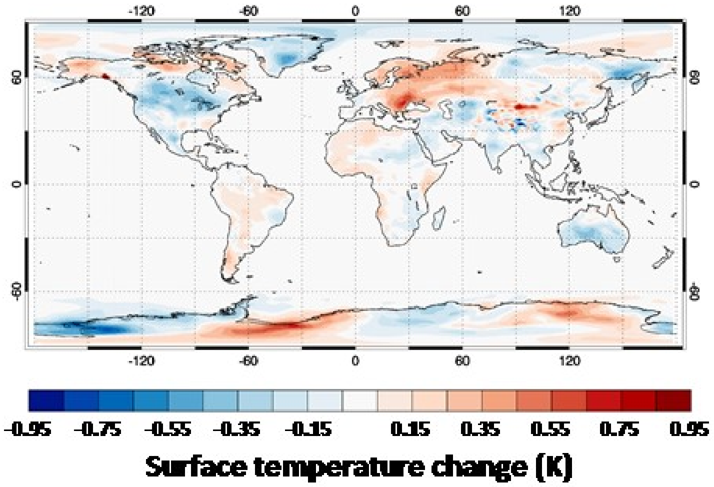

Figure 5-10: *Difference in 25-year annual average surface temperature between years 27-52 and years 2-26 of an atmosphere-only control simulation of HadGEM3-GA4.*

this local warming is in fact a response to the forcing. A large ensemble of 25-year atmosphere-only simulations would hopefully establish this clearly, but with only one realisation of control and perturbation climates this aspect of the response can only be inferred here through comparing the different cases.

The precipitation responses in Figure 5-9 are similarly very patchy and not consistent. Given the very regionally variable temperature changes, these are undoubtedly also dominated by internal variability. As a result, it seems that long-term ocean warming is critical to allowing the radiative heating due to a sulfate reduction to effectively spread to and warm up regions away from the immediate perturbed region, and therefore set up the consistent large-scale shifts in tropical precipitation that are seen in the coupled response.

Unsurprisingly, given that SSTs are fixed, the global mean atmosphere-only changes in both temperature and precipitation prove to be very small for all cases (not shown), and almost all would be insignificant even based on the (presumably smaller) 150-year-average standard deviation range from the coupled simulations. Unlike BC, sulfate is an almost entirely scattering type of aerosol and has very little atmospheric absorption, and so there is also no mechanism for global precipitation to change while global mean temperatures remain fixed. For example, observed hydrological slowdowns due to SO_2 emitted during very large volcanic eruptions are always linked to cooling of the climate system, and hence are observed a few months after an eruption (e.g. Trenberth and Dai, 2007).

5.3.4 Sensitivity to different regions

The global mean changes in SO_2 emissions, TOA ERF, and surface temperature precipitation changes, are summarised in Table 5-2. In contrast to the FFBC removals, global temperature and precipitation changes are significant at the *2σ* level in all experiments, although only very marginally so for the India perturbation, which is also the experiment featuring by far the smallest emissions change. Sulfate aerosol has minimal atmospheric absorption, and so as expected from theoretical arguments and from other modelling studies (e.g. Held and Soden, 2006; Andrews et al., 2010; Samset et al., 2016), global mean precipitation appears to scale closely with global mean surface temperature. The ratio of total precipitation change to temperature change is consistently around 0.07 – 0.08 mm day^{-1} K^{-1} for all SO_2 perturbations. This equates to around 2.2 – 2.5 % K^{-1}, and corresponds very well with the hydrological

Table 5-2: *Global changes in emissions, TOA effective radiative forcing (ERF), surface temperature ('Temp'), and total precipitation ('Precip') due to removing anthropogenic SO2 emissions from the northern mid-latitudes (NHML), the US, Europe, East Asia, and India, in HadGEM3-GA4. Effective radiative forcing is calculated as the annual mean difference in net down all-sky radiative flux (SW + LW components) between a 25-year averaged fixed-SST perturbation simulation and a control simulation. Other values are 150-year annual mean differences between the coupled perturbation simulations and the control simulation. Emissions changes are given both as an absolute value and as a percentage reduction relative to total global emissions. Surface temperature and precipitation changes are quoted with an error range, calculated as 2 standard deviations from an ensemble of six control simulations with perturbed atmospheric initial conditions.*

	ΔSO_2 emissions ($Tg\ yr^{-1}$)	TOA ERF ($W\ m^{-2}$)	ΔTemp (K)	ΔPrecip ($mm\ day^{-1}$)
NHML	-64.0 (-61.7%)	0.906	0.821 ± 0.052	0.0624 ± 0.0040
US	-14.2 (-13.7%)	0.232	0.233 ± 0.052	0.0174 ± 0.0040
Europe	-15.0 (-14.5%)	0.275	0.195 ± 0.052	0.0159 ± 0.0040
East Asia	-20.6 (-19.9%)	0.166	0.119 ± 0.052	0.0080 ± 0.0040
India	-5.5 (-5.3%)	0.101	0.060 ± 0.052	0.0041 ± 0.0040

sensitivities to global temperature changes that have been established in previous multi-model studies (e.g. Held and Soden, 2006; Samset et al., 2016), and in particular falls exactly in the range of the 'slow' precipitation responses identified as being due to long-term, ocean-mediated temperature change in Table 2 of Andrews et al. (2010), which reported 2.1 – 3.1 % K^{-1}.

The magnitudes of the global changes vary considerably with region, however. Of particular interest is the comparison between the noSO2_US, noSO2_EU, and noSO2_EA perturbations. Removing East Asian SO_2 emissions (noSO2_EA) corresponds to a substantially larger emissions reduction than either noSO2_US or noSO2_EU – a 20% reduction in global emissions compared with 14% or 15% reductions. Despite this, both global temperature and precipitation changes are significantly larger in the noSO2_US and noSO2_EU experiments. Figure 5-11 explores this

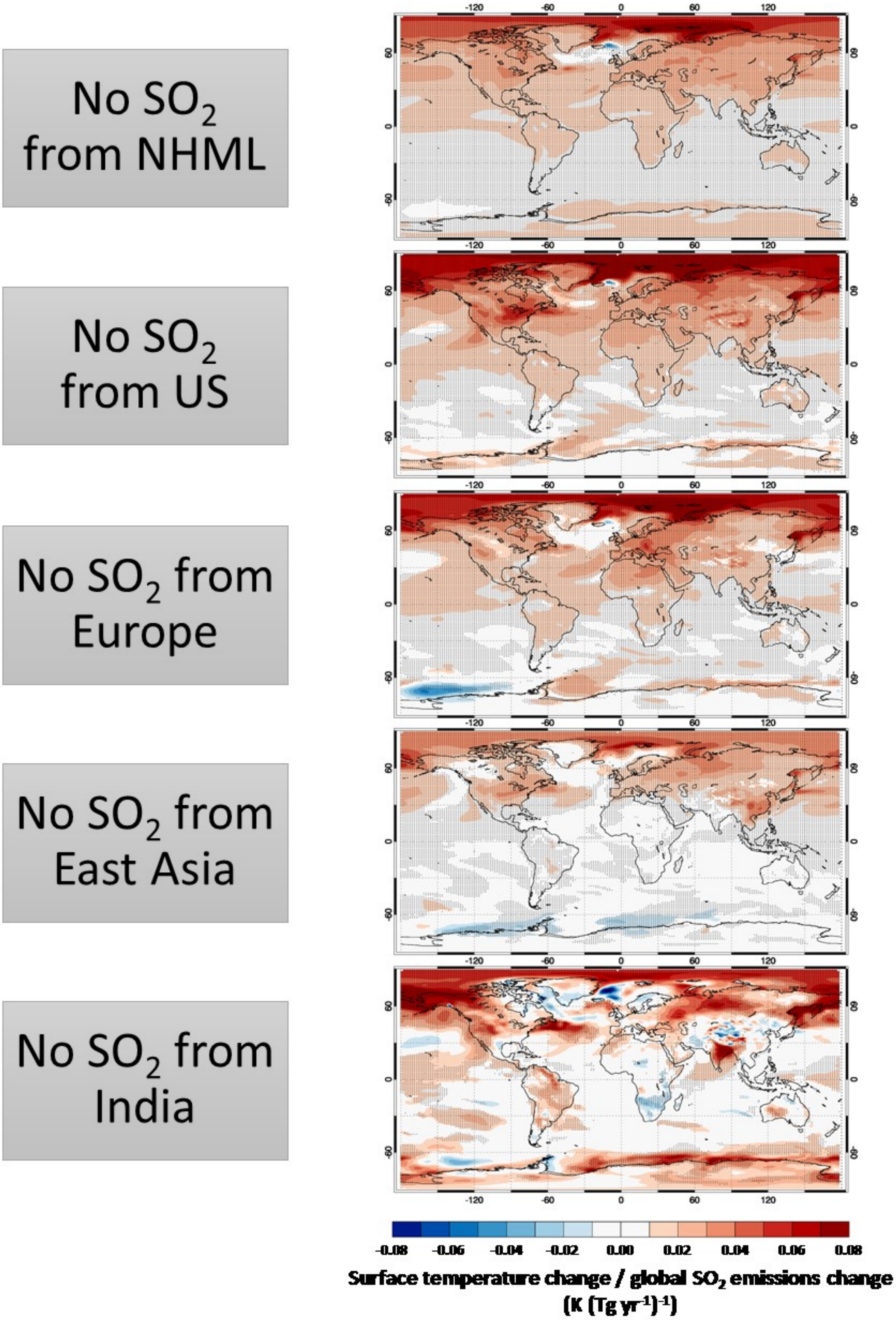

Figure 5-11: *Annual mean surface temperature change per unit global SO_2 emission change, due to removing SO_2 emissions from the northern hemisphere mid-latitudes (NMHL), the US, Europe, East Asia, or India, in HadGEM3-GA4. Temperature changes are 150-year means from the coupled simulations, and the plots are stippled as in Figure 5.5, i.e. where the temperature change exceeds 2 standard deviations calculated at each gridpoint from an ensemble of six control simulations.*

further by showing the geographical temperature change in all the different SO_2 perturbations, normalised by the reduction in global emissions. In most regions across the northern hemisphere, the temperature response per unit emission change is greater for noSO2_US and noSO2_EU than for noSO2_EA or noSO2_NHML. The noSO2_US experiment, in particular, shows particularly large and widespread temperature changes per unit emission change compared to the other regions. These results indicate therefore that the climate, at least in this model (see Sect. 5.5 for discussion of behaviour in a different model), is more sensitive to SO_2 emissions from the US or Europe than from East Asia, and that for a given change in emissions, most parts of the northern hemisphere will see a larger climate response if the emissions change occurs in the US or Europe. The exception to this is the temperature response in East Asia itself, and in particular central and eastern China. This region still shows the largest temperature response per unit emission change when the emission change occurs in East Asia, presumably because in this case, the aerosol radiative forcing is located directly over that region. In fact, for all the regions (US, Europe, East Asia, or India), the largest sensitivity per unit forcing within the region is found when the emissions removal takes place within that same region. At least within these mid-latitude regions, the sensitivity to local emissions therefore still always outweighs the sensitivity to remote emissions, even though the emissions from some regions are consistently more effective at forcing the global climate than others.

The noSO2_IND experiment shows some particularly large temperature responses regionally when normalised by SO_2 emissions (Figure 5-11), for instance over the US and the Arctic, as well as over India itself, however the responses are somewhat patchier across the hemisphere as a whole than in the other experiments. NoSO2_IND has the smallest emission change as well as the smallest responses in absolute terms – globally, the temperature change is only just significant. It is therefore possible that the large regional sensitivities per unit emission seen in this case in Figure 5-11 are simply due to dividing a relatively small response by a small emissions change, in which case it is difficult to conclude whether the sensitivity to Indian emissions really is larger in the areas that it appears to be.

The global temperature changes per unit emissions change are summarised in Table 5-3, and separated into the change in TOA forcing per unit SO_2 emission change, and the change in surface temperature per unit forcing. The surprising larger temperature changes in noSO2_US and noSO2_EU compared with noSO2_EA appear to be foremost due to a greater radiative forcing per unit emission removal in these cases – both noSO2_US and noSO2_EU result in a

Table 5-3: *Change in global mean surface temperature in HadGEM3-GA4 normalised by global change in SO2 emissions (left column). Middle and right column show the global TOA ERF (SW + LW) normalised by change in SO2 emissions, and the global change in surface temperature normalised by global TOA ERF (climate sensitivity), the product of which gives the temperature response per unit emission change. Surface temperature changes are diagnosed from 150-year annual averages of coupled simulations, while ERF is diagnosed from 25-year annual averages of atmosphere-only simulations.*

	ΔTemp / ΔSO_2 (K (Tg $yr^{-1})^{-1}$)	TOA ERF / ΔSO_2 (W m^{-2} (Tg $yr^{-1})^{-1}$)	ΔTemp / TOA RF (K ($Wm^{-2})^{-1}$)
NHML	-0.0128	-0.0142	0.906
US	-0.0164	-0.0163	1.00
Europe	-0.0130	-0.0183	0.709
East Asia	-0.0058	-0.0081	0.717
India	-0.0109	-0.0184	0.594

larger TOA forcing than noSO2_EA, despite being only around ¾ as large an emission change, and Table 5-3 reveals that the forcing per unit emission change is approximately twice as large for noSO2_US and noSO2_EU as it is for noSO2_EA. In addition to the noSO2_US and noSO2_EU experiments, the forcing per unit emissions change is also similarly large for noSO2_IND – however, as previously discussed, in this case the division by a fairly small emissions change will result in greater uncertainty in this value. Strikingly, the noSO2_NHML forcing per unit emissions change turns out to be almost exactly the arithmetic mean of the forcing per unit emissions change for noSO2_US, noSO2_EU, and noSO2_EA – the three regions which combined make up most of the NHML emissions.

To account for the large variation in forcing per unit emission change seen in Table 5-3, the role of clouds and indirect aerosol effects appears to be important here: Table 5-4 compares the clear-sky and all-sky effective radiative forcing, separated by SW and LW components. The longwave forcing in all cases is small, as would be expected given that sulfate particles interact predominantly with SW radiation. Focusing on the SW component, the clear-sky forcing – the

Table 5-4: *Clear-sky and all-sky SW and LW effective radiative forcings (ERFs), due to removing SO2 emissions from the northern hemisphere mid-latitudes (NHML), the US, Europe, East Asia, and India, in HadGEM3-GA4. In all cases, ERF is calculated as the annual mean difference in net down TOA flux between a 25-year atmosphere-only perturbation simulation and the control simulation. Total TOA forcing is the sum of SW and LW components. [As an interesting side note: the global mean change in clear-sky SW flux in the coupled simulations (not shown in table) turns out to be remarkably close to the all-sky SW forcing shown here (from the atmosphere-only simulations), for all the regions. Whether this is coincidence or not, I presently have no hypothesis].*

		SW TOA forcing ($\mathrm{W\ m^{-2}}$)	**LW TOA forcing ($\mathrm{W\ m^{-2}}$)**	**Total forcing ($\mathrm{W\ m^{-2}}$)**
Clear-sky	**NHML**	0.383	-0.117	0.266
	US	0.079	-0.020	0.059
	Europe	0.103	0.013	0.116
	East Asia	0.104	-0.059	0.045
	India	0.022	0.009	0.031
All-sky	**NHML**	1.10	-0.194	0.906
	US	0.276	-0.044	0.232
	Europe	0.272	0.003	0.275
	East Asia	0.240	-0.075	0.166
	India	0.103	-0.002	0.101

aerosol direct effect – is rather modest in all cases, and is actually slightly larger for noSO2_EA than for the noSO2_US or noSO2_EU, consistent with the larger change in aerosol burden in noSO2_EA. The all-sky SW forcing – i.e. the direct and indirect effects collectively – is much greater in all experiments, but ranges from roughly doubling (in noSO2_EA) to more than quadrupling (in noSO2_IND) the clear-sky SW forcing. The indirect radiative forcing due to the response of clouds therefore makes a very substantial difference to the final forcing of the climate system – in particular, it appears to make a rather bigger difference to the noSO2_US and noSO2_EU forcings than to the noSO2_EA forcing, with the noSO2_US and noSO2_EU all-sky SW forcing being greater than their clear-sky SW forcings by a much larger factor.

It has previously been noted by Wilcox et al. (2015) that the predecessor of HadGEM3, HadGEM2, has a relatively strong sulfate indirect effect among models that participated in CMIP5, and so the all-sky results here may also be on the upper end of what present-day models would simulate. Of particular relevance here though, Wilcox et al. (2015) also noted that across CMIP5 models, the cloud albedo sensitivity to a given sulfate load change is greater for smaller sulfate loadings. More generally, it is understood that aerosol indirect effects saturate at higher particle number concentrations (e.g. Carslaw et al., 2013). This could potentially explain why the all-sky forcing in the noSO2_US and noSO2_EU cases is greater than that for noSO2_EA, even though the clear-sky direct effect is smaller. East Asia has much higher emissions of all aerosol species, not just sulfate, and as a result the total aerosol loading above East Asia after SO_2 emissions are removed is considerably higher than that over the US or Europe, where the total aerosol burden becomes very small once regional SO_2 emissions are removed. Consequently, the sensitivity of indirect effects to an SO_2 reduction would presumably be greater over the US and Europe. Additionally, in these simulations it is climatologically cloudier over East Asia in general (not shown), and this would also help to mask the aerosol in this region and further reduce its direct radiative effect. From these data it is hard to determine which of these effects, if either, is the dominant factor, though it could be tested in future work with additional simulations (e.g. turning off indirect effects (to see importance of cloud masking only), or removing all other aerosol species except sulfate (to see the importance of the cloud albedo effect saturating in high background aerosol conditions)).

Between noSO2_US, noSO2_EU, and noSO2_EA, it is the European emissions change that produces the largest TOA forcing. NoSO2_EU produces a larger TOA forcing than the noSO2_US as a consequence of slightly higher total emissions, and also slightly higher forcing per unit emission. However, it is the noSO2_US experiment that simulates the largest global temperature response, and this is due to higher climate sensitivity – the global temperature change per unit global TOA forcing – which is seen in Table 5-3 to be substantially larger for forcing over the US than over either Europe or East Asia, which are found to have very similar values. This indicates a possible additional source of regional diversity – as well as a given emissions change resulting in more or less radiative forcing depending on the region of emission, additionally the efficacy of a given forcing varies depending on the region over which the forcing is located.

Here, it seems that the efficacy of forcings over the US is particularly large. However, it is worth noting that the difference in global mean temperature change between the noSO2_US and noSO2_EU cases is not large enough to be significant at the 2σ level, and consequently the difference between the climate sensitivities, though relatively large (~30%), may also not be significant at this level. Robust conclusions are therefore confounded by the relatively small values of both the numerator and denominator, compared with experiments such as 2x or 4x CO_2 perturbations which are more typically employed to calculate climate sensitivities in global models. Tentatively, however, it seems that the climate sensitivity to the noSO2_US forcing (1.0 K $(W\ m^{-2})^{-1}$) is similar to that found for a global 2x CO_2 perturbation in this model (Chapter 4, Section 4.4.4, and Samset et al., 2016) of 1.1 K $(W\ m^{-2})^{-1}$, whereas the sensitivity in the other regional aerosol perturbations is somewhat lower (0.6-0.7 K $(W\ m^{-2})^{-1}$), suggesting that in general the global sensitivity to a unit of regional forcing may be lower than the sensitivity to a unit of global forcing, except perhaps in the US case. Shindell (2014) found that in transient simulations driven by historical forcing, the global sensitivity to aerosols was in fact greater than to CO_2 forcing in CMIP5 models, however this is attributed to faster land responses in the northern hemisphere, and so the transient nature of the experiments was critical to that result.

5.4 Understanding spatial patterns of climate response

One of the most striking and notable features of the geographical temperature and precipitation responses to the SO_2 removals (Figure 5-8) is the considerable similarity in the spatial pattern of response in many different regions, despite the forcings being mostly quite localised and occurring in very different regions. The precipitation responses were discussed as being driven by the large-scale thermodynamics of one hemisphere being warmed preferentially than the other. This would be the case even if the hemispheric heating was distributed evenly and zonally

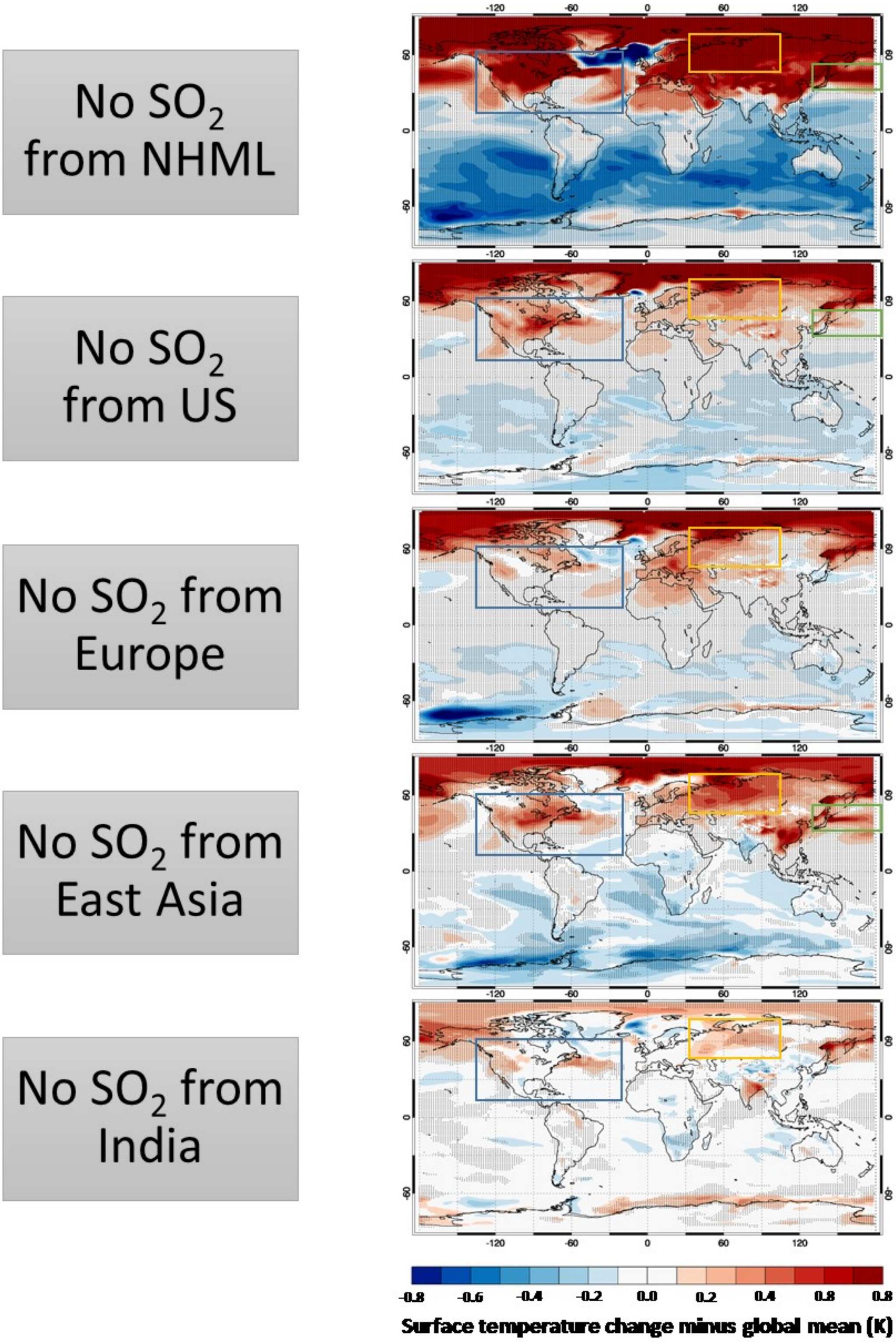

Figure 5-12: *Surface temperature deviations from the global mean response due to removing* SO_2 *emissions from the northern hemisphere mid-latitudes (NHML), the US, Europe, East Asia, and India, in HadGEM3-GA4. Temperature changes are calculated from the 150-year annual means of the coupled perturbation simulation minus a control simulation, and the area-weighted global mean change is subtracted off. Stippling indicates that the temperature change at that gridpoint exceeded two standard deviations, calculated from an ensemble of six control simulations. Coloured boxes highlight particular regions discussed in the text.*

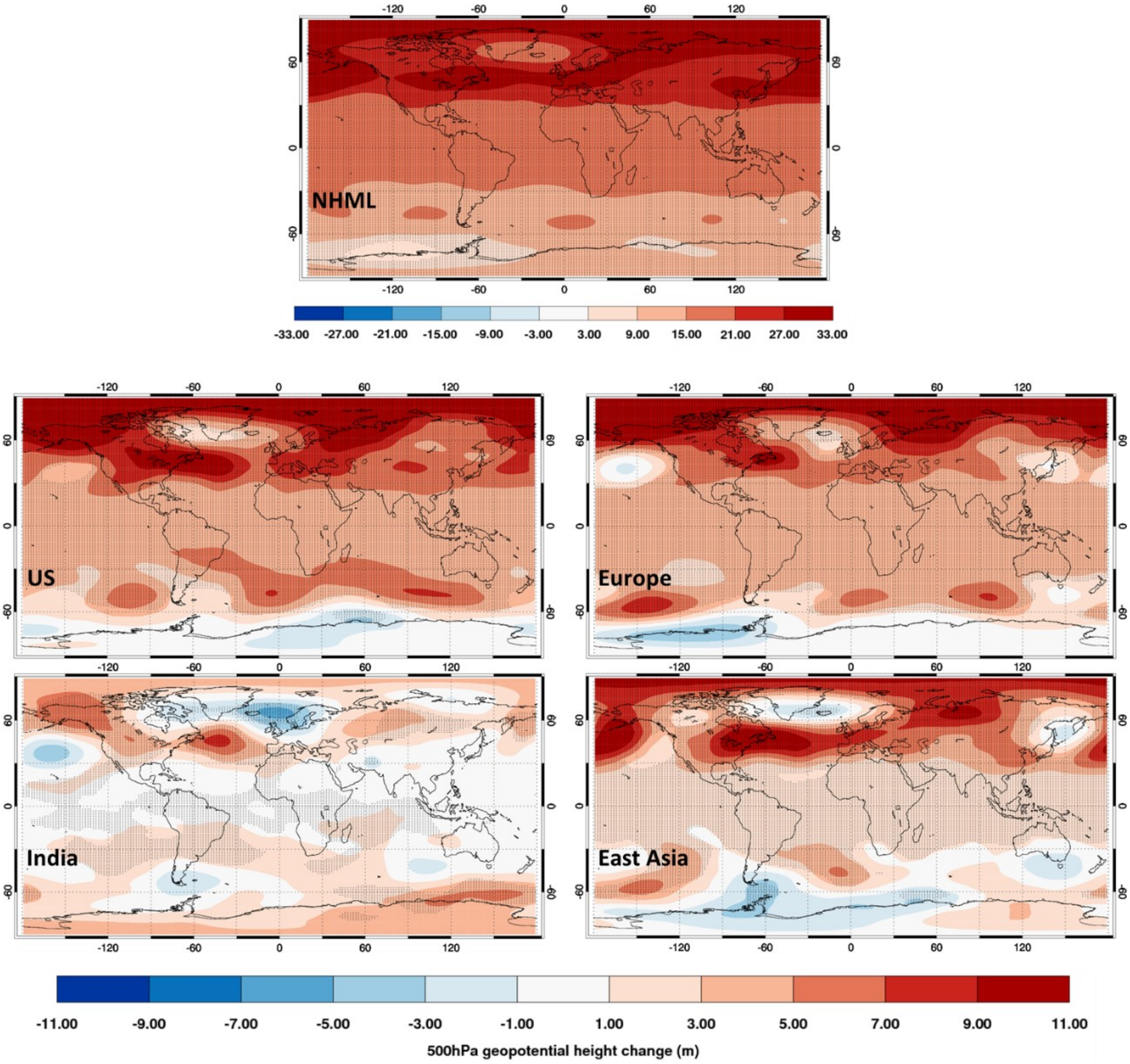

Figure 5-13: *Annual mean changes in 500hPa geopotential height due to removing* SO_2 *emissions from the northern mid-latitudes (NHML), the US, Europe, India, or East Asia, in HadGEM3-GA4. Geopotential height anomalies are calculated as the difference between the 150-year mean coupled perturbation simulations and a control simulation, and stippling indicates the difference exceeds two standard deviations, calculated at each gridpoint from an ensemble of six control simulations. Note the scale is three times larger for the NHML case, as the responses were much stronger for this perturbation.*

around the hemisphere by the large-scale circulation, but instead the temperature responses seem to show a distinct and consistent regionality, with areas of greater or less warming. This is made clearer in Figure 5-12, which shows the surface temperature responses with the global mean temperature change subtracted off, to highlight the regional deviations from the global mean response, and the similarity in the pattern between the different experiments.

All SO_2 experiments show a fairly distinctive pattern of northern hemisphere temperature anomalies, with elevated warming over North America and a “tongue” of warming extending into the western Atlantic (blue box in Figure 5-12), elevated warming over parts of central Russia

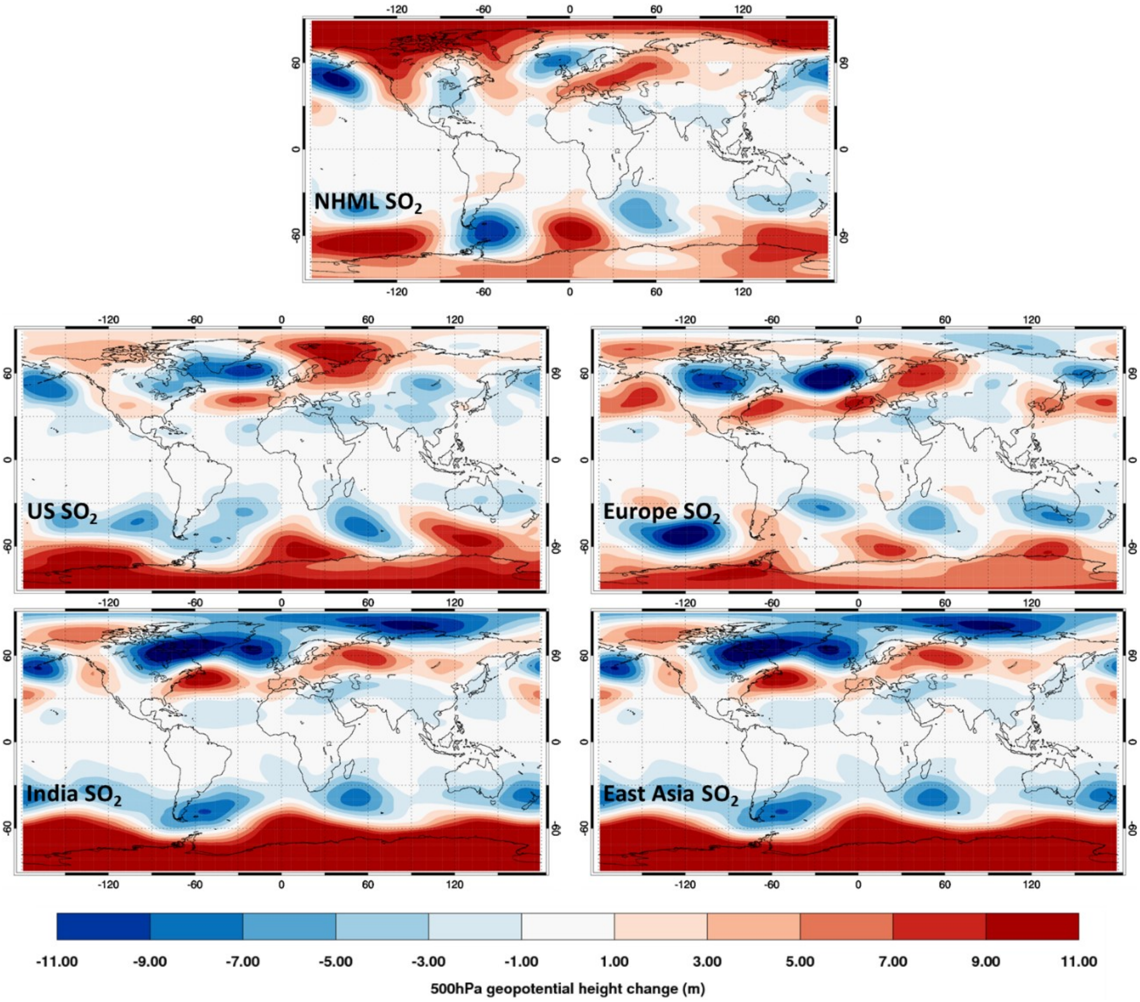

Figure 5-14: *Annual mean changes in 500hPa geopotential height when removing SO_2 emissions from the northern-hemisphere mid-latitudes (NHML), the US, Europe, India, and East Asia in atmosphere-only simulations with HadGEM3-GA4. Changes are calculated as the 25-year mean difference between perturbation simulations and a control simulation, with sea-surface temperatures and sea-ice concentrations prescribed to observed year-2000 values.*

(yellow box), and, in the noSO2_NHML, noSO2_US, and noSO2_EA experiments, a tongue of warming extending from Japan into the western Pacific (green box). This is in addition to the consistent stronger warming all across the Arctic region in all experiments, which has already been discussed.

These similar spatial patterns of stronger northern mid-latitude response are not restricted just to the surface temperature, but are also found in associated dynamical responses. For instance, Figure 5-13 shows the change in 500hPa geopotential height in each of the SO_2 emissions removal experiments. This again shows a remarkably similar spatial pattern of changes in the northern hemisphere across the experiments. In particular, they all show a very similar positive geopotential height anomaly over eastern North America and the west Atlantic, associated with

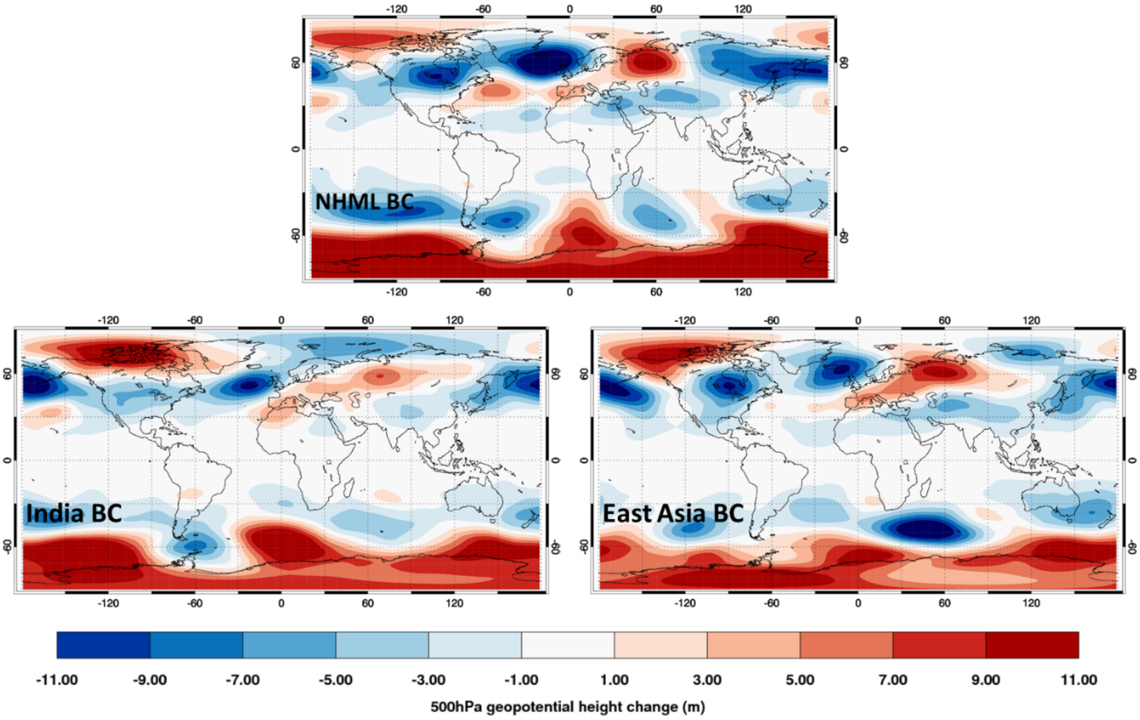

Figure 5-15: *Annual mean changes in 500hPa geopotential height when removing fossil-fuel BC emissions from the northern-hemisphere mid-latitudes (NHML), India, and East Asia in atmosphere-only simulations with HadGEM3-GA4. Calculated as the 25-year mean difference between perturbation simulations and a control simulation, with sea-surface temperatures and sea-ice concentrations prescribed to observed year-2000 values.*

the blue box in Figure 5-12, and almost all also show a distinct positive anomaly over central or northern Russia, associated with the yellow box in Figure 5-12.

Curiously, there is a hint of a similar pattern of 500hPa geopotential height changes in the equivalent atmosphere-only SO_2 removal simulations, which are shown in Figure 5-14, even though the surface temperature responses proved to be extremely noisy in these simulations (Section 5.3.3). The pattern is also somewhat less consistent in the noSO2_NHML and noSO2_US atmosphere-only cases, even though these had among the largest forcings. Geopotential height shows much larger anomalies in the atmosphere-only simulations in general, including in remote parts of the world such as Antarctica and the Southern Ocean, and so these anomalies may just reflect the much larger internal variability in the atmosphere-only experiments due to the far shorter averaging period. Nonetheless, the northern hemisphere pattern in the majority of SO_2 atmosphere-only experiments is surprisingly similar to that seen in the coupled case. For comparison, Figure 5-15 shows instead the 500hPa geopotential height changes in the three FFBC removal cases that had atmosphere-only versions (noBC_NHML, noBC_EA, and noBC_IND), on the basis that these experiments had fairly negligible forcing.

Although the noBC_NHML experiment shows something a bit similar (though weaker) to what is found here for the noSO2 experiments, the other noBC cases show different patterns over the Atlantic and Europe. This suggests that the recurrence of this dynamical pattern in the atmosphere-only response to the SO_2 removals may not be coincidental, and possibly the localised sulfate forcing in these cases is tending to favour a particular wave pattern in the mid-troposphere, even though at the surface the fixed sea-surface temperature boundary prevents any remote responses being realised in the surface temperature.

To investigate further why the temperature and dynamical changes so consistently seem to follow these patterns, apparently regardless of the longitudinal position of the forcing, I have plotted in Figure 5-16 the three leading empirical orthogonal functions (EOFs) of annual surface temperature and geopotential height, calculated from the full 200-year timeseries of one of the control simulations (the pattern was not very sensitive to the particular choice of which control simulation I used). The EOFs decompose the timeseries of these variables into orthogonal spatial patterns, the (time-varying) superposition of which can reconstruct the complete timeseries. In principle, this can expose the leading spatial modes of variability in the climate system – or in this case the simulated climate – although it is more commonly performed for a limited region, such as the tropical Pacific to find the pattern of the El Niño/Southern Oscillation (ENSO), or over the Southern Ocean to find the Southern Annular Mode, rather than for global fields as I have done here.

The three leading modes for surface temperature and 500hPa geopotential height between them explain 35-40% of the total variability in the simulated climate system, and in particular the leading two modes explain very similar fractions of the variance for the two fields, with the first mode explaining just over 20%, and the second just over 10%, in each case. As a result of performing the EOF calculation globally, an ENSO-like pattern in the tropical Pacific is seen to be convolved with all the leading surface temperature EOFs, rather than appearing as a single mode of variability itself. Aside from this, the leading temperature EOF is characterised by a fairly global pattern of the same sign almost everywhere. Inspection of the corresponding principle component timeseries for this mode (not shown) reveals that rather than oscillating, this mode increases steadily from a negative phase to a positive phase over the course of the simulation, and it would appear therefore that this is in fact just the drift in global temperature of the control climate over the 200 years. It is not surprising that this drift would be the dominant 'variability'

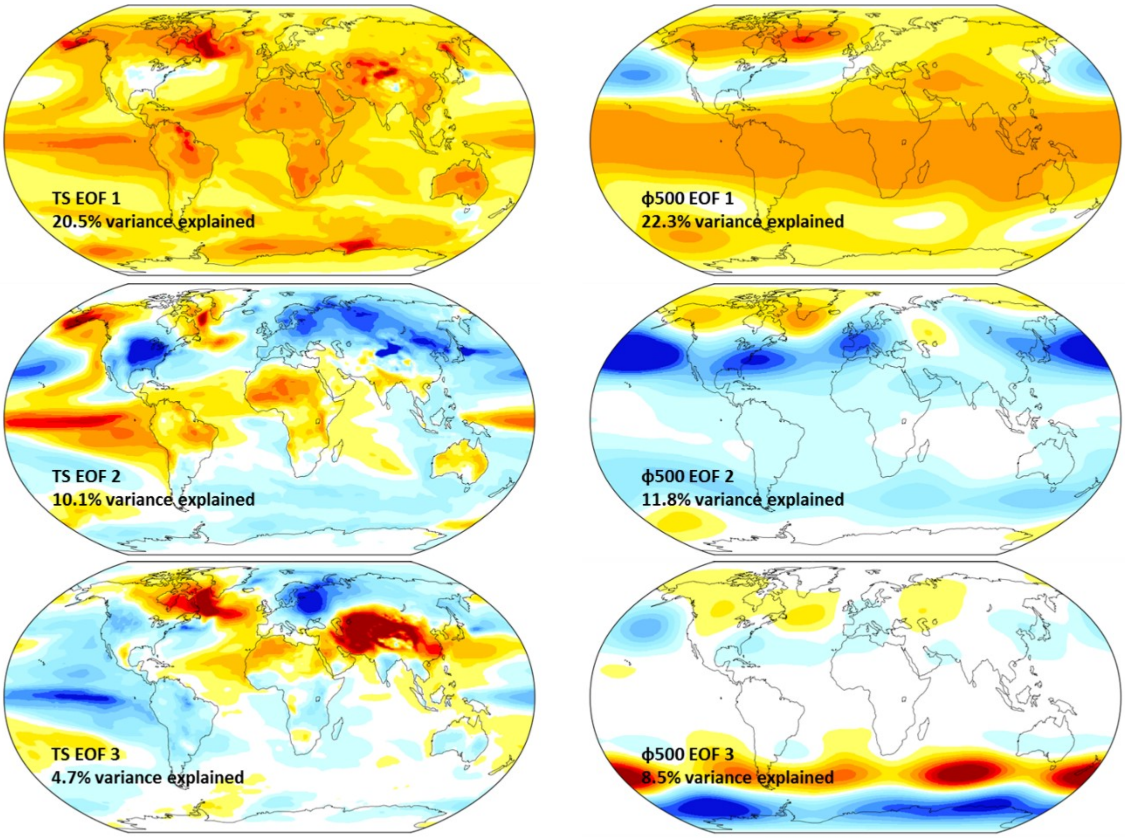

Figure 5-16: *Leading empirical orthogonal functions (EOFs) in HadGEM3-GA4 for global annual mean surface temperature (TS, left column) and global annual mean geopotential height at 500 hPa (φ500, right column). EOFs are computed from all 200 years of the coupled control simulation. No scale is shown because the absolute magnitude and sign of the EOF patterns is arbitrary.*

over the 200 year course of the simulation, and so this first EOF is probably not particularly revealing, and is not truly an intrinsic mode of variability.

The second EOF modes of both surface temperature and geopotential height are particularly interesting, however. Ignoring the ENSO-like pattern in the Pacific, the second surface temperature EOF is dominated by a pattern in the northern hemisphere which includes same-sign changes over North America, north-east Europe and Russia, and in the western Pacific extending out from Japan, which bear a distinct spatial resemblance to the patterns of temperature change in the three boxed regions identified in Figure 5-12. The second geopotential height mode is also dominated by an anomaly over North America and the Atlantic which is very similar to that seen in the geopotential height changes in Figure 5-13, although over Europe and Russia it is less similar. This US/North Atlantic pattern is also seen somewhat convolved with the third temperature and geopotential height EOFs, although the third geopotential height EOF is mostly seen to pick out a Southern Annual Mode behaviour.

The implication though is that these patterns already existed in the control simulation, as spatial patterns of natural internal variability in the simulated climate. It would therefore appear that the response to regional forcing in the northern hemisphere to some extent projects onto this existing mode, or modes, of variability in the climate, resulting in a response that looks somewhat like one phase of this pattern of variability. It has been suggested before, for example by Ring and Plumb (2008) and Shepherd (2014), that the regional climate responses to a forcing – which are controlled strongly by dynamics – will project onto existing modes of variability in the climate system. Such a phenomenon appears to be seen in my results, such that the spatial pattern of the dynamical and temperature responses is not particularly sensitive to the zonal position of the forcing, so long as the resultant heating from it is strong enough to influence the pattern of mid-latitude variability seen in the second EOF modes in Figure 5-16. This potentially could also explain why the US perturbation resulted in the strongest response per unit forcing, if the location of this forcing intersects more with the pattern of variability that is being excited over North America and the Atlantic.

If this explains the behaviour of the model, then whether or not the simulated patterns of remote response are plausible hinges on whether the modes of variability seen in the control simulation are actually representative of the real climate system. To explore this, Figure 5-17 reproduces the three leading EOF modes of reconstructed annual global temperatures from 1902 to 1980, reported by Mann et al. (1998). As discussed, the leading mode of variability in my simulations is likely dominated by the drift in global mean temperatures, but focusing again on the second and third modes there is an encouraging similarity with the corresponding modes in Mann et al. (1998). In particular, the second observed EOF displays the same anomaly connecting North America and Europe, with other features such as opposite sign anomalies over Alaska and the eastern Pacific also present in both model and observations. The third observed EOF in Figure 5-17 also displays almost identical patterns over the North Atlantic and Europe, with the (arbitrary) sign reversed from the simulated EOF in Figure 5-16. This lends considerable confidence that the patterns of variability identified above are indeed present in the real climate, and in turn suggests that the correct spatial patterns of response to regional forcings can be captured by the model, if, as suggested, they project onto these existing modes.

EOF no.1

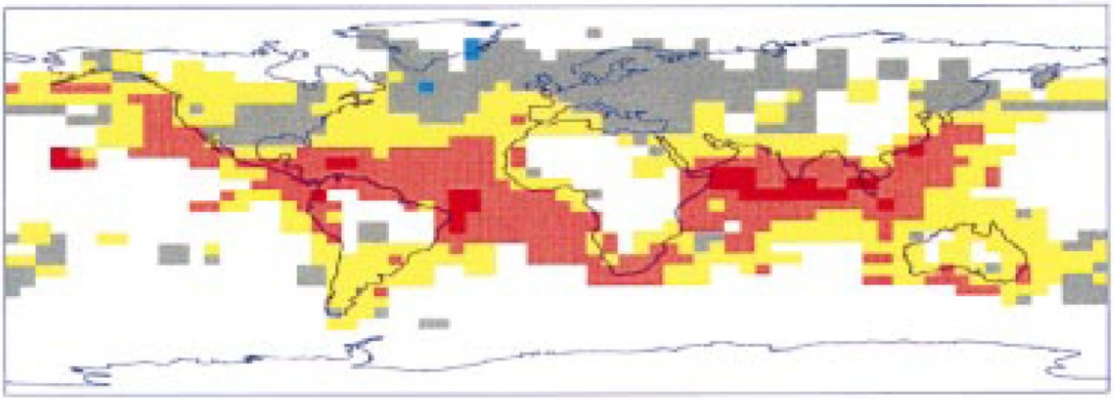

EOF no.2

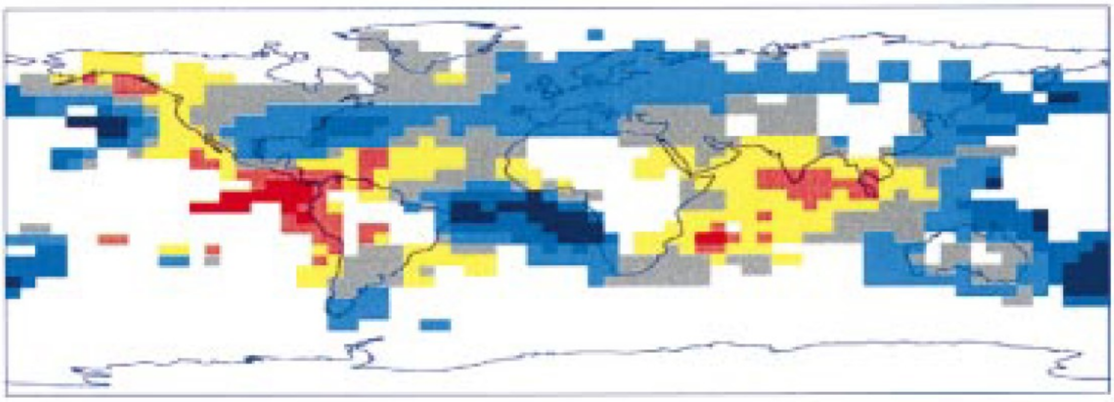

EOF no.3

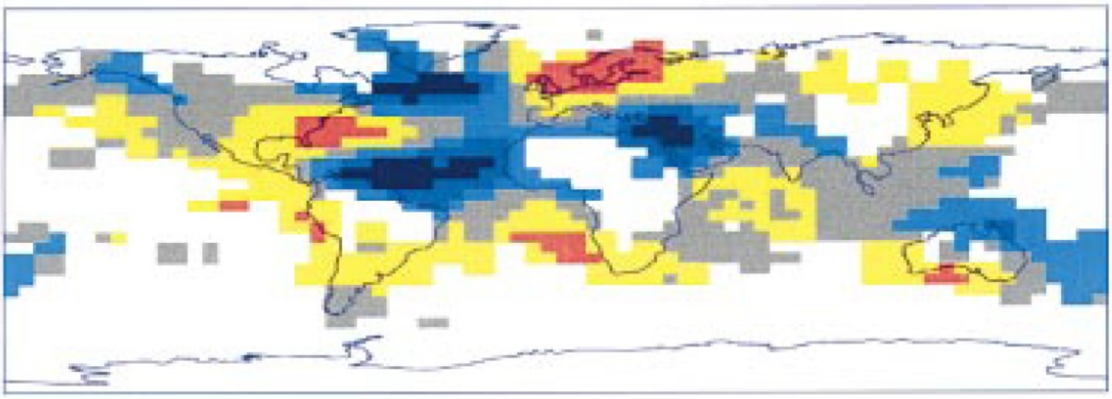

Figure 5-17: *Reproduction of first, second, and third panels in Figure 2 of Mann et al. (1998), showing the three leading EOFs of reconstructed 1902-1980 global temperature data.*

5.5 Comparison with CESM1

The results presented above are still only for one model, HadGEM3-GA4, and the results of Chapter 4 demonstrated that the magnitude of the climate response to regional SO_2 emissions can vary hugely between different models. HadGEM3-GA4 has been shown to have a particularly strong sulfate forcing both in Chapter 4 of this thesis, and in the multi-model comparison study of Samset et al. (2016) where large global perturbations were applied in a greater range of models. As a result, the magnitude of the climate responses seen here is likely an upper bound. However, it was noted in Chapter 4 that although HadGEM3-GA4 and CESM1 disagreed on the absolute magnitude of the surface temperature response to perturbing Chinese emissions, there was some indication that the simulated pattern of response was more robust between the two models. The comprehensive range of different regional perturbations that I have presented here has not been replicated with any other models. However, a US SO_2 removal experiment was also pursued with CESM1 alongside the China SO_2 removal experiment discussed in Chapter 4, and it is interesting to compare the responses to emissions from just these two different regions here. As before, I am grateful to Jean-Francois Lamarque at the National Center for Atmospheric Research for performing the simulations with CESM1 and providing the model output data.

The 150-year mean surface temperature changes due to removing SO_2 emissions from either the US or China is shown in Figure 5-18. The comparison is very interesting – both show a remarkably similar pattern of temperature change over Eurasia and the western Pacific, much as the US and East Asia perturbations (and China perturbation in the previous chapter) with HadGEM-GA4 did. The exception, however, is that the CESM1 China SO_2 removal shows no particular response over North America, whereas this was the region with the most consistently similar response in HadGEM3-GA4.

Comparing the CESM1 US perturbation with the equivalent HadGEM3-GA4 noSO2_US response (Figure 5-8), the picture is very much the same as was seen for the Chinese emissions perturbation in Chapter 4, i.e. CESM1 has a somewhat weaker surface temperature response, however qualitatively there are again strong similarities in the distribution of warming. Consequently, the conclusion in Chapter 4 that there were qualitative similarities in the response to Chinese SO_2 clearly extends to the US perturbation as well – if anything, more so, since the responses over North America were different between the two models for the Chinese

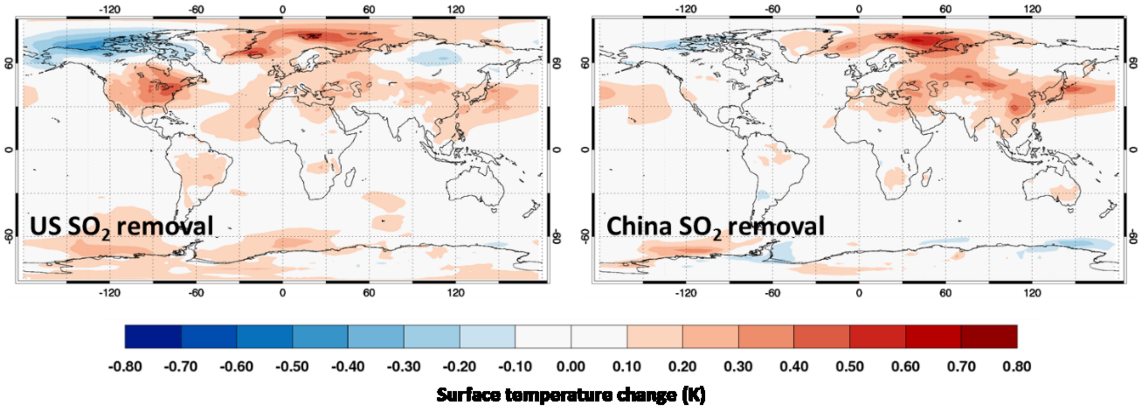

Figure 5-18: *Annual mean surface temperature changes in the CESM1 model due to removing SO_2 emissions from either the US (left), or from China (right). Temperature differences are from 150-year means of coupled perturbation simulations minus a control simulation. CESM1 setup and China removal is the same as described in Chapter 4, US removal is the same as used for HadGEM3-GA4 in this Chapter.*

emissions removal in Chapter 4 (as mentioned above), but are in fact very similar between these two models for the US perturbation here.

Both models appear to somewhat agree on a preferred pattern of response over Eurasia to distant regional forcings, though disagree on whether this also extends to North America. Unfortunately, additional variables like geopotential height were not available for CESM1 to test whether these surface temperature responses are also related to similar dynamical responses. However, one other interesting finding that both models also agree on is that the efficacy of US SO_2 emissions is greater than China SO_2 emissions: the global mean temperature change due to removing US emissions in CESM1 is 0.067 K, whereas for China it was 0.054 K. As in HadGEM3-GA4, this is associated with larger changes in global mean SW flux for the US perturbation than for the China perturbation – 0.214 W m^{-2} rather than 0.186 W m^{-2} (noting that for CESM1 the changes in SW flux were diagnosed from coupled simulations and do not technically represent radiative forcing). The CESM1 simulations were forced with the same emissions inventory, and the same perturbation, as my HadGEM3-GA4 simulations, and so the noSO2_US perturbation similarly equates to a smaller emissions change in CESM1. This lends support that this is in fact a robust finding: US SO_2 emissions have a larger global climate effect than SO_2 emissions from China, per unit emission change, because US sulfate appears to result in a greater radiative forcing, most likely due to stronger local cloud interactions. As with HadGEM3-GA4 though, CESM1 also predicts that the temperature change in China itself is larger when Chinese emissions are removed, indicating again that the local temperature response is still most strongly influenced by the local emissions, within these regions.

5.6 Conclusions

In this Chapter I have investigated a systematic series of perturbations to fossil-fuel black carbon and sulphur dioxide emissions from four different localised northern hemisphere regions – the US, Europe, East Asia, and India – as well as a broader northern hemisphere mid-latitude (NHML) region.

Unlike in many previous studies (e.g. Shindell and Faluvegi, 2009; Shindell et al., 2012; Teng et al., 2012; Samset et al., 2016) which have scaled up aerosol concentrations by large factors to obtain a clear response, I have perturbed emissions within each region by removing them, resulting in a somewhat more realistic perturbation in terms of what could be achieved with future emission control policies, and also, to the extent possible with a single model, a better indication of the actual contribution of these regional emissions (rather than zonal forcings) individually to present-day climate disruption.

In the first instance, the climate responses to fossil-fuel BC emission reductions proved to be almost negligible, even for an emissions removal across the whole northern mid-latitude band. Temperature changes were particularly small, and overwhelmed by natural variability both globally and regionally. Potentially, there was a small global precipitation increase due to removing FFBC emissions for the largest perturbations (noBC_NHML, noBC_EA, and noBC_IND), despite the mostly negligible temperature responses, associated with the change in atmospheric heating (although these precipitation changes were still of similar magnitude to the unforced variability). The finding that FFBC forcing is too small to result in significant global climate responses unless perturbed by unrealistically large amounts is consistent with an emerging understanding in the literature from recent multi-model studies using fully coupled climate models and going beyond radiative forcing to study climate response (e.g. Baker et al., 2015; Samset et al., 2016). It has been reported recently by Myhre and Samset (2015) that current climate model radiation codes are likely to underestimate black carbon radiative forcing, but only by about 10%, and so even if accounted for this would be unlikely to change these findings.

Removing SO_2 emissions regionally resulted in much stronger and clearer responses globally and regionally for both temperature and precipitation due to the resulting sulfate aerosol changes – although as was seen in Chapter 4, the strength of such effects may be somewhat model-dependent. Surface temperature changes were dominated by broad warming across most of the northern hemisphere, with stronger sensitivity in the Arctic and also preferential warming across particular mid-latitude regions: North America and the western Atlantic, central and northern Russia, and the western Pacific. These regions of preferential response show a qualitative similarly to existing patterns of variability in the control climate, suggesting that on a regional scale the pattern of response to a given forcing may be modulated by the excitation of natural modes.

In all cases, the local temperature responses outweighed the responses to remote forcings, indicating that, at least over the fairly broad and highly polluting regions investigated here, the climate of a particular region is most strongly influenced by the emissions within the region itself. However, globally and in regions outside the immediate vicinity of the aerosol forcing, the sensitivity of the surface temperature response is greater for US or European emissions, despite East Asia being the largest SO_2 emissions source globally. This is found to be primarily due to a greater radiative forcing per unit emission change for the US and Europe, associated with larger aerosol-cloud interactions. The treatment of aerosol-cloud interactions is known to vary considerably between models; however, a comparison with identical US and China SO_2 removal simulations in the CESM1 model reveals that the sensitivity to US emissions is greater in this model as well, and lends support that this may be a robust result, and not due to peculiarities of the cloud behaviour in HadGEM3-GA4. Consequently, the effectiveness of a given short-lived emission change at altering the climate appears to be quite region-dependent, even if the spatial pattern of response to a given forcing might not be. CESM1 did not simulate the same preferential pattern of warming over North America, however, but it did produce very similar patterns of response over Eurasia to either US or China SO_2 perturbations. Exactly which regions show a consistent pattern of warming may therefore be partly model-dependent, perhaps due to differing patterns of internal variability between the models, although this hypothesis could not be tested here.

Precipitation response features were dominated by shifts in tropical rainfall, mainly over oceanic regions, consistent with a large-scale contrast between the magnitude of temperature responses in the northern and southern hemispheres. Globally averaged, precipitation change also scales closely with global temperature change, although the magnitude of warming around the nearby regions is still important for individual precipitation features like the South Asian monsoon. The particularly strong warming in the NHML SO_2 removal also resulted in regions of significant precipitation change in both the northern and southern mid-latitudes, mainly wettening, though also with a shift and/or decrease above the Atlantic and Pacific western boundary currents, suggesting weaker storm activity in these regions. The large-scale shift in tropical precipitation, and the extra-tropical wettening in the NHML case, are very much dependent on the (magnitude of the) broad warming of the northern hemisphere, and as a result are only seen in the long-term coupled response, where sea-surface temperatures have been allowed to adjust. Fast temperature and precipitation responses in the atmosphere-only experiments are fairly noisy and show very little of the consistent large-scale responses that are seen in the coupled simulations, although there is some suggestion that higher in the troposphere the dynamical anomalies found to be excited in the coupled responses are already present in the fast atmosphere-only responses.

6 Summary and conclusions

Aerosols are a significant driver of the climate system, and they are particularly interesting to study as climate forcers because of their short lifetimes. This means that their radiative forcing is very inhomogeneous, possibly with different effects on the climate depending on the source region, and it also means that policy decisions have the potential to change aerosol forcing very quickly. As described in the introduction, numerous previous studies have investigated the impacts that historical aerosol changes have had on the climate, but these are not an ideal guide to for policy because future emission changes are unlikely to exactly mirror historical trajectories everywhere. They are also not ideal for understanding the behaviour of the climate system when driven by localised forcings, because in that way the effect of different historical emissions from different locations cannot be disentangled.

Very few studies, by comparison, have attempted to systematically investigate the sensitivity of the climate to different forcing distributions. None have previously investigated the responses to emissions from different regions within a single modelling framework, or the responses to emissions from a localised region in multiple models. The work presented represents a first attempt at addressing this.

I have evaluated the regional performance at modelling sulfate in three different state-of-the-art composition-climate models, which I have then used to investigate the response to a realistic (~100%) regionally-localised emission perturbation – the first time such an experiment has been explored with multiple complex models. This provided an important, if sobering, conclusion: even in present-generation models, there is a very large uncertainty in the climate response to a realistic emissions perturbation. This comes about because of uncertainty in the translation of precursor emission to aerosol, and aerosol to radiative forcing, as well as radiative forcing to climate response. Moreover, validation of aerosol-related fields with currently available observations can only provide loose constraints, because aerosol radiative forcing is not directly measured in the real climate system.

Nonetheless, the indications are that the HadGEM3-GA4 model performs well in reproducing aerosol optical depths, at least over continental regions, which are also the areas of major anthropogenic sources. It seems likely though that HadGEM3-GA4 slightly overestimates AOD in general, and also is on the upper end of the present modelling spectrum in its response to sulfate perturbations - both from Chapters 3 and 4 of this study, and also from the recent PDRMIP multi-model intercomparison (Samset et al., 2016), to which I contributed additional simulations with HadGEM3-GA4.

Bearing this in mind, I have addressed the key need identified at the outset – for a systematic study of responses to aerosol emissions from different regions – with an extensive series of simulations with the HadGEM3-GA4 model. In both coupled atmosphere-ocean and fixed-SST setups, I simulated the response to removing either fossil-fuel BC or SO_2 emissions from each of five regions – the Northern Hemisphere mid-latitudes, the United States, Europe, East Asia, and India. Some particular conclusions, and caveats, that can be drawn are (for more detailed conclusions, please see the end of each chapter):

- The large-scale climate response to realistic black carbon emissions is likely small, and not remarkable from natural variability. This conclusion is also supported by other recent multi-model studies (Baker et al., 2015; Samset et al., 2016), which focused on global BC perturbations rather than the regional approach pursued in the current study. Here, I have only investigated large-scale, annual mean climate responses, however, so this does not imply that individual BC pollution events cannot have significant short-term effects on regional climate, nor that policy measures to reduce black carbon emissions are not still pertinent for the separate reason of providing regional air quality improvements.
- Sulfur dioxide emissions from any of the major industrialised northern-hemisphere regions (the US, Europe, China/East Asia, and India) likely affect temperature significantly across the whole hemisphere, regardless of the emission region. By affecting temperature across the hemisphere, emissions from any of these regions also affect tropical precipitation, through symmetric shifts of the intertropical convergence zone.
- The spatial pattern of temperature response to regionally-localised forcings is not uniform, but shows a preferred pattern. This pattern of remote response is relatively insensitive to the location of the forcing, within the same hemisphere, although there is typically also a strong local response, which is specific to the forcing location. The structure of the response is tied to existing modes of internal model variability which may be partially model-dependent, but some features appear robust across at least two models.

- Although the pattern of remote temperature and precipitation responses is not sensitive to the location of the perturbation, the absolute magnitude is. The global response per unit SO_2 emission is relatively lower for emissions from China/East Asia than for emissions from the US and Europe, and possibly India. The greater efficacy of US SO_2 is robust across at least two models. However, local climate is still most strongly sensitive to local emissions, at least among these regions examined here.
- Although the response per unit SO_2 emission is stronger for emissions from some regions than others, combinations of regions appear roughly additive: the response to northern mid-latitude sulfate per unit emission is roughly the mean of the responses per unit emission for the regions contained within it. If this result is robust, it would imply that the sensitivities calculated from regional SO_2 removal simulations could be used to estimate the response to any combination and magnitude of emission perturbations from the different regions investigated.

These are findings which could not have been revealed without a systematic study of the unique scope presented here. However, there is still considerable scope to expand further with future studies in this area. In particular, the majority of regional emission perturbations were only performed with one model, and yet I showed that current models do not converge in their magnitude of responses to SO_2 emission reductions from at least two major regions. Studies of this nature, including the previous Shindell and Faluvegi (2009) and Shindell et al. (2012) studies, have been isolated due to the considerable computational costs of performing the large number of necessary simulations – the simulations presented in this thesis, for instance, total more than 4,300 years of simulation time.

Although the magnitudes of response to regional aerosol emissions do not seem well constrained, the suggestion that different regions may force similar responses, or that certain regions are more efficient at forcing the climate than others, would alone represent remarkable insights into the behaviour of the climate system if they are proved robust, and so there is a clear and pressing need for additional modelling centres to perform studies of this nature. Ideally, simulations with localised regional perturbations would become a standard experiment of large multi-model intercomparison projects in addition to the usual global forcings like $2xCO_2$, since the results appear to provide valuable additional insight into the forcing-response behaviour of the climate system, and have implications for international climate policy. It would also be particularly valuable to investigate further the potential additivity of responses to different regions, both across different models, and by looking at different combinations of regions within the same model, to test further the extent to which this finding holds. If it is robust, this could allow responses to future emissions scenarios to be estimated without performing additional full simulations.

There are also a number of possible avenues for future work to isolate the particular processes that lead to the model diversity seen here in more detail; for instance studies imposing the aerosol field from one model into others would remove the diversity introduced by translating emissions into aerosol concentrations, while imposing surface temperatures and meteorology from one model into others could remove the diversity introduced by different background climatologies and climate sensitivities. Simulations with prescribed meteorology would also allow a cleaner and more quantitative disentanglement of aerosol-cloud radiative interactions from dynamical cloud feedbacks. Such experiments could allow a better isolation of the processes where uncertainty originates than has been possible here, which would be useful in order to target further experimental work to constrain model parameterisations. A thorough assay of the range of parameter choices and formulae used in the aerosol schemes of various models could also help reveal where assumed aerosol properties diverge. However, without stronger observational constraints on aerosol radiative forcing, it is not clear that this alone could help make models more realistic. In particular, it seems that being able to better constrain the column-integrated sulfate burden, the AOD per sulfate burden, and the radiative forcing per unit AOD, would all also be needed. This represents a considerable observational challenge, and until it is possible, the considerable current model diversity may be irreducible.

One ambition of this study has been to provide results which are relevant to policy applications, through isolating responses to emissions from geographically connected regions. However, there is also scope to enhance this relevance further still. The legacy of this study is a considerable dataset of simulations, and there is the potential for future analysis just with this dataset to explore many further characteristics of the responses to the different regional emission perturbations that were simulated. The analysis presented here focused on responses that were large-scale, both spatially and temporally. However, there are also regionally and seasonally very specific climate features which are extremely important for the economy and society – for instance, the South Asian monsoon, which is known to be susceptible to disruption by aerosol forcing (e.g. Bollasina et al., 2011; Guo et al., 2015). The data from these simulations is therefore also being used in another ongoing study (Shawki and et al., in preparation) to understand the influence of different emission regions specifically on the very localised South Asian monsoon system. Other possible aspects that could be analysed in the future could include the behaviour of other short-timescale or localised responses such as climate extremes, or air quality metrics, both of which are also highly policy relevant because of their implications for human health and security.

To summarise the current study though: analysis of long-term mean changes indicates that remote responses to large localised sulfate forcings are surprisingly consistent. The forcing due to a given emissions change is, however, highly variable – across emission regions, but even more so across models. Computational constraints notwithstanding, a greater modelling effort to explore the robustness of these results is needed. Encouragingly, some multi-model projects now being pursued, such as the Precipitation Driver Response Model Intercomparison Project (Samset et al., 2016; Myhre et al., 2016), are starting to partly incorporate regional experiments with short-lived species and are exploring the resulting climate responses, and so this will hopefully prove an exciting area to watch.

References

Adler, R. F., Huffman, G. J., Chang, A., Ferraro, R., Xie, P.-P., Janowiak, J., Rudolf, B., Schneider, U., Curtis, S., and Bolvin, D.: The version-2 global precipitation climatology project (GPCP) monthly precipitation analysis (1979-present), Journal of hydrometeorology, 4, 1147-1167, 2003.

Allen, R. J., Sherwood, S. C., Norris, J. R., and Zender, C. S.: Recent Northern Hemisphere tropical expansion primarily driven by black carbon and tropospheric ozone, Nature, 485, 350-354, 10.1038/nature11097, 2012.

Andreae, M. O., and Crutzen, P. J.: Atmospheric Aerosols: Biogeochemical Sources and Role in Atmospheric Chemistry, Science, 276, 1052-1058, 10.1126/science.276.5315.1052, 1997.

Andreae, M. O., Rosenfeld, D., Artaxo, P., Costa, A. A., Frank, G. P., Longo, K. M., and Silva-Dias, M. A.: Smoking rain clouds over the Amazon, Science, 303, 1337-1342, 10.1126/science.1092779, 2004.

Andres, R. J., and Kasgnoc, A. D.: A time-averaged inventory of subaerial volcanic sulfur emissions, Journal of Geophysical Research: Atmospheres, 103, 25251-25261, 10.1029/98jd02091, 1998.

Andrews, T., Forster, P. M., Boucher, O., Bellouin, N., and Jones, A.: Precipitation, radiative forcing and global temperature change, Geophysical Research Letters, 37, n/a-n/a, 10.1029/2010gl043991, 2010.

Andrews, T., Ringer, M. A., Doutriaux-Boucher, M., Webb, M. J., and Collins, W. J.: Sensitivity of an Earth system climate model to idealized radiative forcing, Geophysical Research Letters, 39, L10702, 10.1029/2012gl051942, 2012.

Baker, L. H., Collins, W. J., Olivié, D. J. L., Cherian, R., Hodnebrog, Oslash, Myhre, G., and Quaas, J.: Climate responses to anthropogenic emissions of short-lived climate pollutants, Atmospheric Chemistry and Physics, 15, 8201-8216, 10.5194/acp-15-8201-2015, 2015.

Bauer, S. E., Koch, D., Unger, N., Metzger, S. M., Shindell, D. T., and Streets, D. G.: Nitrate aerosols today and in 2030: a global simulation including aerosols and tropospheric ozone, Atmospheric Chemistry and Physics, 7, 5043-5059, 10.5194/acp-7-5043-2007, 2007.

Bellouin, N., Boucher, O., Haywood, J., Johnson, C., Jones, A., Rae, J., and Woodward, S.: Improved representation of aerosols for HadGEM2, Technical Note 73, Hadley Centre, Met Office, Exeter, UK, 2007.

Bellouin, N., Rae, J., Jones, A., Johnson, C., Haywood, J., and Boucher, O.: Aerosol forcing in the Climate Model Intercomparison Project (CMIP5) simulations by HadGEM2-ES and the role of ammonium nitrate, Journal of Geophysical Research, 116, 10.1029/2011jd016074, 2011.

Bodas-Salcedo, A., Williams, K. D., Field, P. R., and Lock, A. P.: The Surface Downwelling Solar Radiation Surplus over the Southern Ocean in the Met Office Model: The Role of Midlatitude Cyclone Clouds, Journal of Climate, 25, 7467-7486, 10.1175/jcli-d-11-00702.1, 2012.

Bollasina, M. A., Ming, Y., and Ramaswamy, V.: Anthropogenic aerosols and the weakening of the South Asian summer monsoon, Science, 334, 502-505, 10.1126/science.1204994, 2011.

Booth, B. B., Dunstone, N. J., Halloran, P. R., Andrews, T., and Bellouin, N.: Aerosols implicated as a prime driver of twentieth-century North Atlantic climate variability, Nature, 484, 228-232, 10.1038/nature10946, 2012.

Boucher, O., Randall, D., Artaxo, P., Bretherton, C., Feingold, G., Forster, P., Kerminen, V.-M., Kondo, Y., Liao, H., Lohmann, U., Rasch, P., Satheesh, S. K., Sherwood, S., Stevens, B., and Zhang, X. Y.: Clouds and Aerosols, in: Climate Change 2013: The Physical Science Basis. Contribution of Working Group I to the Fifth Assessment Report of the Intergovernmental Panel on Climate Change, edited by: Stocker, T. F., Qin, D., Plattner, G.-K., Tignor, M., Allen, S. K., Boschung, J., Nauels, A., Xia, Y., Bex, V., and Midgley, P. M., Cambridge University Press, Cambridge, United Kingdom and New York, NY, USA, 2013.

Carslaw, K. S., Lee, L. A., Reddington, C. L., Pringle, K. J., Rap, A., Forster, P. M., Mann, G. W., Spracklen, D. V., Woodhouse, M. T., Regayre, L. A., and Pierce, J. R.: Large contribution of natural aerosols to uncertainty in indirect forcing, Nature, 503, 67-71, 10.1038/nature12674, 2013.

Ceppi, P., Hwang, Y.-T., Liu, X., Frierson, D. M. W., and Hartmann, D. L.: The relationship between the ITCZ and the Southern Hemispheric eddy-driven jet, J. Geophys. Res. Atmos., 118, 5136–5146, doi:10.1002/jgrd.50461, 2013.

Chand, D., Wood, R., Anderson, T. L., Satheesh, S. K., and Charlson, R. J.: Satellite-derived direct radiative effect of aerosols dependent on cloud cover, Nature Geoscience, 2, 181-184, 10.1038/ngeo437, 2009.

Chang, E. K. M., Guo, Y., and Xia, X.: CMIP5 multimodel ensemble projection of storm track change under global warming, Journal of Geophysical Research: Atmospheres, 117, n/a-n/a, 10.1029/2012jd018578, 2012.

Chýlek, P., and Coakley, J. A.: Aerosols and climate, Science, 183, 75-77, 1974.

Cione, J. J., Raman, S., and Pietrafesa, L. J.: The effect of Gulf Stream-induced baroclinicity on US East Coast winter cyclones, Monthly weather review, 121, 421-430, 1993.

Cionni, I., Eyring, V., Lamarque, J. F., Randel, W. J., Stevenson, D. S., Wu, F., Bodeker, G. E., Shepherd, T. G., Shindell, D. T., and Waugh, D. W.: Ozone database in support of CMIP5 simulations: results and corresponding radiative forcing, Atmospheric Chemistry and Physics, 11, 11267-11292, 10.5194/acp-11-11267-2011, 2011.

Clough, S., Shephard, M., Mlawer, E., Delamere, J., Iacono, M., Cady-Pereira, K., Boukabara, S., and Brown, P.: Atmospheric radiative transfer modeling: a summary of the AER codes, Journal of Quantitative Spectroscopy and Radiative Transfer, 91, 233-244, 2005.

Collins, M., Knutti, R., Arblaster, J., Dufresne, J.-L., Fichefet, T., Friedlingstein, P., Gao, X., Gutowski, W. J., Johns, T., Krinner, G., Shongwe, M., Tebaldi, C., Weaver, A. J., and Wehner, M.: Long-term Climate Change: Projections, Commitments and Irreversibility. In: Climate Change 2013: The Physical Science Basis. Contribution of Working Group I to the Fifth Assessment Report of the Intergovernmental Panel on Climate Change [Stocker, T.F., Qin, D., Plattner, G.-K., Tignor, M., Allen, S. K., Boschung, J., Nauels, A., Xia, Y., Bex, V., and Midgley, P. M. (eds.)]. Cambridge University Press, Cambridge, United Kingdom and New York, NY, USA, 2013.

Collins, W. J., Fry, M. M., Yu, H., Fuglestvedt, J. S., Shindell, D. T., and West, J. J.: Global and regional temperature-change potentials for near-term climate forcers, Atmospheric Chemistry and Physics, 13, 2471-2485, 10.5194/acp-13-2471-2013, 2013.

Curry, J. A., Schramm, J. L., and Ebert, E. E.: Sea ice-albedo climate feedback mechanism, Journal of Climate, 8, 240-247, 1995.

Derwent, R., Collins, W., Jenkin, M., Johnson, C., and Stevenson, D.: The global distribution of secondary particulate matter in a 3-D Lagrangian chemistry transport model, Journal of atmospheric chemistry, 44, 57-95, 2003.

Dong, B., Sutton, R. T., Highwood, E., and Wilcox, L.: The Impacts of European and Asian Anthropogenic Sulfur Dioxide Emissions on Sahel Rainfall, Journal of Climate, 27, 7000-7017, 10.1175/jcli-d-13-00769.1, 2014.

Edwards, J., and Slingo, A.: Studies with a flexible new radiation code. I: Choosing a configuration for a large-scale model, Quarterly Journal of the Royal Meteorological Society, 122, 689-719, 1996.

Evan, A. T., Kossin, J. P., Chung, C. E., and Ramanathan, V.: Arabian Sea tropical cyclones intensified by emissions of black carbon and other aerosols, Nature, 479, 94-97, 10.1038/nature10552, 2011.

Fan, J., Rosenfeld, D., Ding, Y., Leung, L. R., and Li, Z.: Potential aerosol indirect effects on atmospheric circulation and radiative forcing through deep convection, Geophysical Research Letters, 39, n/a-n/a, 10.1029/2012gl051851, 2012.

Flato, G., Marotzke, J., Abiodun, B., Braconnot, P., Chou, S. C., Collins, W., Cox, P., Driouech, F., Emori, S., Eyring, V., Forest, C., Gleckler, P., Guilyardi, E., Jakob, C., Kattsov, V., Reason, C., and Rummukainen, M.: Evaluation of Climate Models, in: Climate Change 2013: The Physical Science Basis. Contribution of Working Group I to the Fifth Assessment Report of the Intergovernmental Panel on Climate Change, edited by: Stocker, T. F., Qin, D., Plattner, G.-K., Tignor, M., Allen, S. K., Boschung, J., Nauels, A., Xia, Y., Bex, V., and Midgley, P. M., Cambridge Univeristy Press, Cambridge, United Kingdom and New York, NY, USA, 2013.

Goto, D., Nakajima, T., Dai, T., Takemura, T., Kajino, M., Matsui, H., Takami, A., Hatakeyama, S., Sugimoto, N., Shimizu, A., and Ohara, T.: An evaluation of simulated particulate sulfate over East Asia through global model intercomparison, Journal of Geophysical Research: Atmospheres, 120, 6247-6270, 10.1002/2014jd021693, 2015.

Graversen, R. G., and Wang, M.: Polar amplification in a coupled climate model with locked albedo, Climate Dynamics, 33, 629-643, 10.1007/s00382-009-0535-6, 2009.

Gregory, J. M., Ingram, W. J., Palmer, M. A., Jones, G. S., Stott, P. A., Thorpe, R. B., Lowe, J. A., Johns, T. C., and Williams, K. D.: A new method for diagnosing radiative forcing and climate sensitivity, Geophysical Research Letters, 31, L03205, 10.1029/2003gl018747, 2004.

Guo, L., Highwood, E. J., Shaffrey, L. C., and Turner, A. G.: The effect of regional changes in anthropogenic aerosols on rainfall of the East Asian Summer Monsoon, Atmospheric Chemistry and Physics, 13, 1521-1534, 10.5194/acp-13-1521-2013, 2013.

Guo, L., Turner, A. G., and Highwood, E. J.: Impacts of 20th century aerosol emissions on the South Asian monsoon in the CMIP5 models, Atmospheric Chemistry and Physics, 15, 6367-6378, 10.5194/acp-15-6367-2015, 2015.

Hansen, J., Russell, G., Rind, D., Stone, P., Lacis, A., Lebedeff, S., Ruedy, R., and Travis, L.: Efficient three-dimensional global models for climate studies: Models I and II, Monthly Weather Review, 111, 609-662, 1983.

Hansen, J., Sato, M., Ruedy, R., Nazarenko, L., Lacis, A., Schmidt, G. A., Russell, G. L., Aleinov, I., Bauer, M., Bauer, S., Bell, N., Cairns, B., Canuto, V., Chandler, M., Cheng, Y., Del Genio, A., Faluvegi, G., Fleming, E., Friend, A., Hall, T., Jackman, C., Kelley, M., Kiang, N., Koch, D., Lean, J., Lerner, J., Lo, K., Menon, S., Miller, R., Minnis, P., Novakov, T., Oinas, V., Perlwitz, J., Perlwitz, J., Rind, D., Romanou, A., Shindell, D., Stone, P., Sun, S., Tausnev, N., Thresher, D., Wielicki, B., Wong, T., Yao, M. S., and Zhang, S.: Efficacy of climate forcings, Journal of Geophysical Research, 110, 10.1029/2005jd005776, 2005.

Hawkins, E., and Sutton, R.: The Potential to Narrow Uncertainty in Regional Climate Predictions, Bulletin of the American Meteorological Society, 90, 1095-1107, 10.1175/2009bams2607.1, 2009.

Haywood, J., and Boucher, O.: Estimates of the direct and indirect radiative forcing due to tropospheric aerosols: A review, Reviews of Geophysics, 38, 513-543, 10.1029/1999rg000078, 2000.

Haywood, J. M., Jones, A., Bellouin, N., and Stephenson, D.: Asymmetric forcing from stratospheric aerosols impacts Sahelian rainfall, Nature Climate Change, 3, 660-665, 10.1038/nclimate1857, 2013.

Haywood, J. M., Jones, A., Dunstone, N., Milton, S., Vellinga, M., Bodas-Salcedo, A., Hawcroft, M., Kravitz, B., Cole, J., and Watanabe, S.: The impact of equilibrating hemispheric albedos on tropical performance in the HadGEM2-ES coupled climate model, Geophysical Research Letters, 2016.

Held, I. M., and Soden, B. J.: Robust responses of the hydrological cycle to global warming, Journal of Climate, 19, 5686-5699, 2006.

Held, I. M., Lyons, S. W., and Nigam, S.: Transients and the Extratropical Response to El Niño, Journal of the Atmospheric Sciences, 46(1), 163-174, 1989.

Hemispheric Transport of Air Pollution (HTAP): Hemispheric Transport of Air Pollution 2010. Part A: Ozone and Particulate Matter, Air Pollution Studies No. 17, New York, NY, USA, 2010.

Holben, B. N., Tanré, D., Smirnov, A., Eck, T. F., Slutsker, I., Abuhassan, N., Newcomb, W. W., Schafer, J. S., Chatenet, B., Lavenu, F., Kaufman, Y. J., Castle, J. V., Setzer, A., Markham, B., Clark, D., Frouin, R., Halthore, R., Karneli, A., O'Neill, N. T., Pietras, C., Pinker, R. T., Voss, K., and Zibordi, G.: An emerging ground-based aerosol climatology: Aerosol optical depth from AERONET, Journal of Geophysical Research: Atmospheres, 106, 12067-12097, 10.1029/2001JD900014, 2001.

Hoskins, B. J., and Karoly, D. J.: The Steady Linear Response of a Spherical Atmosphere to Thermal and Orographic Forcing, Journal of the Atmospheric Sciences, 38, 1179-1196, 1981.

Huang, Y., Dickinson, R. E., and Chameides, W. L.: Impact of aerosol indirect effect on surface temperature over East Asia, Proceedings of the National Academy of Sciences of the United States of America, 103, 4371-4376, 2006.

Hunke, E. C., and Lipscombe, W. H.: CICE: the Los Alamos sea ice model documentation and software user's manual, Version 4.0, Los Alamos National Laboratory, New MexicoLA-CC-06-012, 2008.

Hwang, Y.-T., Frierson, D. M. W., and Kang, S. M.: Anthropogenic sulfate aerosol and the southward shift of tropical precipitation in the late 20th century, Geophysical Research Letters, 40, 2845-2850, 10.1002/grl.50502, 2013.

Jacob, D. J.: Introduction to Atmospheric Chemistry, Princeton University Press, Princeton, NJ, USA, 1999.

Jimenez, J. L., Canagaratna, M. R., Donahue, N. M., Prevot, A. S. H., Zhang, Q., Kroll, J. H., DeCarlo, P. F., Allan, J. D., Coe, H., Ng, N. L., Aiken, A. C., Docherty, K. S., Ulbrich, I. M., Grieshop, A. P., Robinson, A. L., Duplissy, J., Smith, J. D., Wilson, K. R., Lanz, V. A., Hueglin, C., Sun, Y. L., Tian, J., Laaksonen, A., Raatikainen, T., Rautiainen, J., Vaattovaara, P., Ehn, M., Kulmala, M., Tomlinson, J. M., Collins, D. R., Cubison, M. J., Dunlea, E. J., Huffman, J. A., Onasch, T. B., Alfarra, M. R., Williams, P. I., Bower, K., Kondo, Y., Schneider, J., Drewnick, F., Borrmann, S., Weimer, S., Demerjian, K., Salcedo, D., Cottrell, L., Griffin, R., Takami, A., Miyoshi, T., Hatakeyama, S., Shimono, A., Sun, J. Y., Zhang, Y. M., Dzepina, K., Kimmel, J. R., Sueper, D., Jayne, J. T., Herndon, S. C., Trimborn, A. M., Williams, L. R., Wood, E. C., Middlebrook, A. M., Kolb, C. E., Baltensperger, U., and Worsnop, D. R.: Evolution of organic aerosols in the atmosphere, Science, 326, 1525-1529, 10.1126/science.1180353, 2009.

Jin, F., and Hoskins, B. J.: The direct Response to Tropical Heating in a Baroclinic Atmosphere, Journal of the Atmospheric Sciences, 52(3), 307-319, 1995.

Johnson, B. T., Haywood, J. M., Langridge, J. M., Darbyshire, E., Morgan, W. T., Szpek, K., Brooke, J., Marenco, F., Coe, H., Artaxo, P., Longo, K. M., Mulcahy, J., Mann, G., Dalvi, M., and Bellouin, N.: Evaluation of biomass burning aerosols in the HadGEM3 climate model with observations from the SAMBBA field campaign, Atmos. Chem. Phys. Discuss., doi:10.5194/acp-2016-442, in review, 2016.

Jones, A., Roberts, D. L., Woodage, M. J., and Johnson, C. E.: Indirect sulphate aerosol forcing in a climate model with an interactive sulphur cycle, Journal of Geophysical Research: Atmospheres, 106, 20293-20310, 10.1029/2000jd000089, 2001.

Jones, A., Haywood, J. M., and Boucher, O.: Aerosol forcing, climate response and climate sensitivity in the Hadley Centre climate model, Journal of Geophysical Research, 112, 10.1029/2007jd008688, 2007.

Kahn, R. A., Gaitley, B. J., Garay, M. J., Diner, D. J., Eck, T. F., Smirnov, A., and Holben, B. N.: Multiangle Imaging SpectroRadiometer global aerosol product assessment by comparison with the Aerosol Robotic Network, Journal of Geophysical Research: Atmospheres, 115, D23209, 10.1029/2010JD014601, 2010.

Kawase, H., Takemura, T., and Nozawa, T.: Impact of carbonaceous aerosols on precipitation in tropical Africa during the austral summer in the twentieth century, Journal of Geophysical Research, 116, 10.1029/2011jd015933, 2011.

Keil, A., and Haywood, J. M.: Solar radiative forcing by biomass burning aerosol particles during SAFARI 2000: A case study based on measured aerosol and cloud properties, Journal of Geophysical Research: Atmospheres, 108, D13, 8467, 10.1029/2002jd002315, 2003.

Kinne, S., Schulz, M., Textor, C., Guibert, S., Balkanski, Y., Bauer, S. E., Berntsen, T., Berglen, T. F., Boucher, O., Chin, M., Collins, W., Dentener, F., Diehl, T., Easter, R., Feichter, J., Fillmore, D., Ghan, S., Ginoux, P., Gong, S., Grini, A., Hendricks, J., Herzog, M., Horowitz, L., Isaksen, I., Iversen, T., Kirkevåg, A., Kloster, S., Koch, D., Kristjansson, J. E., Krol, M., Lauer, A., Lamarque, J. F., Lesins, G., Liu, X., Lohmann, U., Montanaro, V., Myhre, G., Penner, J., Pitari, G., Reddy, S., Seland, O., Stier, P., Takemura, T., and Tie, X.: An AeroCom initial assessment – optical properties in aerosol component modules of global models, Atmos. Chem. Phys., 6, 1815-1834, 10.5194/acp-6-1815-2006, 2006.

Koch, D., Schmidt, G. A., and Field, C. V.: Sulfur, sea salt, and radionuclide aerosols in GISS ModelE, Journal of Geophysical Research, 111, D06206, 10.1029/2004jd005550, 2006.

Koch, D., Bond, T. C., Streets, D., Unger, N., and van der Werf, G. R.: Global impacts of aerosols from particular source regions and sectors, Journal of Geophysical Research, 112, 10.1029/2005jd007024, 2007.

Koch, D., Bauer, S. E., Del Genio, A., Faluvegi, G., McConnell, J. R., Menon, S., Miller, R. L., Rind, D., Ruedy, R., Schmidt, G. A., and Shindell, D.: Coupled Aerosol-Chemistry–Climate Twentieth-Century Transient Model Investigation: Trends in Short-Lived Species and Climate Responses, Journal of Climate, 24, 2693-2714, 10.1175/2011jcli3582.1, 2011.

Krotkov, N. A., McLinden, C. A., Li, C., Lamsal, L. N., Celarier, E. A., Marchenko, S. V., Swartz, W. H., Bucsela, E. J., Joiner, J., Duncan, B. N., Boersma, K. F., Veefkind, J. P., Levelt, P. F., Fioletov, V. E., Dickerson, R. R., He, H., Lu, Z., and Streets, D. G.: Aura OMI observations of regional SO_2 and NO_2 pollution changes from 2005 to 2015, Atmospheric Chemistry and Physics, 16, 4605-4629, 10.5194/acp-16-4605-2016, 2016.

Lamarque, J. F., Bond, T. C., Eyring, V., Granier, C., Heil, A., Klimont, Z., Lee, D., Liousse, C., Mieville, A., Owen, B., Schultz, M. G., Shindell, D., Smith, S. J., Stehfest, E., Van Aardenne, J., Cooper, O. R., Kainuma, M., Mahowald, N., McConnell, J. R., Naik, V., Riahi, K., and van Vuuren, D. P.: Historical (1850–2000) gridded anthropogenic and biomass burning emissions of reactive gases and aerosols: methodology and application, Atmospheric Chemistry and Physics, 10, 7017-7039, 10.5194/acp-10-7017-2010, 2010.

Lau, N.-C.: Interactions between Global SST Anomalies and the Midlatitude Atmospheric Circulation, Bulletin of the American Meteorological Society, 78(1), 21-33, 1997.

Lawrence, D. M., Oleson, K. W., Flanner, M. G., Thornton, P. E., Swenson, S. C., Lawrence, P. J., Zeng, X., Yang, Z.-L., Levis, S., Sakaguchi, K., Bonan, G. B., and Slater, A. G.: Parameterization improvements and functional and structural advances in Version 4 of the Community Land Model, Journal of Advances in Modeling Earth Systems, 3, M03001, 10.1029/2011MS000045, 2011.

Levy, R. C., Mattoo, S., Munchak, L. A., Remer, L. A., Sayer, A. M., Patadia, F., and Hsu, N. C.: The Collection 6 MODIS aerosol products over land and ocean, Atmos. Meas. Tech., 6, 2989-3034, 10.5194/amt-6-2989-2013, 2013.

Liu, X., Easter, R. C., Ghan, S. J., Zaveri, R., Rasch, P., Shi, X., Lamarque, J. F., Gettelman, A., Morrison, H., Vitt, F., Conley, A., Park, S., Neale, R., Hannay, C., Ekman, A. M. L., Hess, P., Mahowald, N., Collins, W., Iacono, M. J., Bretherton, C. S., Flanner, M. G., and Mitchell, D.: Toward a minimal representation of aerosols in climate models: description and evaluation in the Community Atmosphere Model CAM5, Geoscientific Model Development, 5, 709-739, 10.5194/gmd-5-709-2012, 2012.

Lorenz, D. J., and DeWeaver, E. T.: Tropopause height and zonal wind response to global warming in the IPCC scenario integrations, J. Geophys. Res., 112, D10119, doi:10.1029/2006JD008087, 2007.

Madec, G.: NEMO ocean engine, No. 27, Institut Piere-Simon Laplace (IPSL), FranceISSN No. 1288-1619, 2008.

Malm, W. C., Sisler, J. F., Huffman, D., Eldred, R. A., and Cahill, T. A.: Spatial and seasonal trends in particle concentration and optical extinction in the United States, Journal of Geophysical Research: Atmospheres, 99, 1347-1370, 1994.

Mann, M. E., Bradley, R. S., and Hughes, M. K.: Global-scale temperature patterns and climate forcing over the past six centuries, Nature, 392, 779-787, 10.1038/33859, 1998.

Mann, G. W., Carslaw, K. S., Spracklen, D. V., Ridley, D. A., Manktelow, P. T., Chipperfield, M. P., Pickering, S. J., and Johnson, C. E.: Description and evaluation of GLOMAP-mode: a modal global aerosol microphysics model for the UKCA composition-climate model, Geosci. Model Dev., 3, 519–551, doi:10.5194/gmd-3-519-2010, 2010.

Meehl, G. A., Washington, W. M., Arblaster, J. M., Hu, A., Teng, H., Kay, J. E., Gettelman, A., Lawrence, D. M., Sanderson, B. M., and Strand, W. G.: Climate Change Projections in

CESM1(CAM5) Compared to CCSM4, Journal of Climate, 26, 6287-6308, 10.1175/jcli-d-12-00572.1, 2013.

Meinshausen, M., Smith, S. J., Calvin, K., Daniel, J. S., Kainuma, M. L. T., Lamarque, J. F., Matsumoto, K., Montzka, S. A., Raper, S. C. B., Riahi, K., Thomson, A., Velders, G. J. M., and van Vuuren, D. P. P.: The RCP greenhouse gas concentrations and their extensions from 1765 to 2300, Climatic Change, 109, 213-241, 10.1007/s10584-011-0156-z, 2011.

Menon, S., Koch, D., Beig, G., Sahu, S., Fasullo, J., and Orlikowski, D.: Black carbon aerosols and the third polar ice cap, Atmospheric Chemistry and Physics, 10, 4559-4571, 2010.

Miller, R. L., Schmidt, G. A., Nazarenko, L. S., Tausnev, N., Bauer, S. E., DelGenio, A. D., Kelley, M., Lo, K. K., Ruedy, R., Shindell, D. T., Aleinov, I., Bauer, M., Bleck, R., Canuto, V., Chen, Y., Cheng, Y., Clune, T. L., Faluvegi, G., Hansen, J. E., Healy, R. J., Kiang, N. Y., Koch, D., Lacis, A. A., LeGrande, A. N., Lerner, J., Menon, S., Oinas, V., Pérez García-Pando, C., Perlwitz, J. P., Puma, M. J., Rind, D., Romanou, A., Russell, G. L., Sato, M., Sun, S., Tsigaridis, K., Unger, N., Voulgarakis, A., Yao, M.-S., and Zhang, J.: CMIP5 historical simulations (1850–2012) with GISS ModelE2, Journal of Advances in Modeling Earth Systems, 6, 441-477, 10.1002/2013MS000266, 2014.

Ming, Y., Ramaswamy, V., and Persad, G.: Two opposing effects of absorbing aerosols on global-mean precipitation, Geophysical Research Letters, 37, L13701, 10.1029/2010gl042895, 2010.

Ming, Y., Ramaswamy, V., and Chen, G.: A model Investigation of Aerosol-Induced Changes in Boreal Winter Extratropical Circulation, Journal of Climate, 24, 6077-6091, 10.1175/2011JCLI4111.1, 2011.

Morice, C. P., Kennedy, J. J., Rayner, N. A., and Jones, P. D.: Quantifying uncertainties in global and regional temperature change using an ensemble of observational estimates: The HadCRUT4 data set, Journal of Geophysical Research: Atmospheres, 117, D08101, 10.1029/2011jd017187, 2012.

Myhre, G., Samset, B. H., Schulz, M., Balkanski, Y., Bauer, S., Berntsen, T. K., Bian, H., Bellouin, N., Chin, M., Diehl, T., Easter, R. C., Feichter, J., Ghan, S. J., Hauglustaine, D., Iversen, T., Kinne, S., Kirkevåg, A., Lamarque, J. F., Lin, G., Liu, X., Lund, M. T., Luo, G., Ma, X., van Noije, T., Penner, J. E., Rasch, P. J., Ruiz, A., Seland, Ø., Skeie, R. B., Stier, P., Takemura, T., Tsigaridis, K., Wang, P., Wang, Z., Xu, L., Yu, H., Yu, F., Yoon, J. H., Zhang, K., Zhang, H., and Zhou, C.: Radiative forcing of the direct aerosol effect from AeroCom Phase II simulations, Atmospheric Chemistry and Physics, 13, 1853-1877, 10.5194/acp-13-1853-2013, 2013a.

Myhre, G., Shindell, D., Bréon, F.-M., Collins, W., Fuglestvedt, J., Huang, J., Koch, D., Lamarque, J.-F., Lee, D., Mendoza, B., Nakajima, T., Robock, A., Stephens, G., Takemura, T., and Zhang, H.: Anthropogenic and Natural Radiative Forcing, in: Climate Change 2013: The Physical Science Basis. Contribution of Working Group I to the Fifth Assessment Report of the Intergovernmental Panel on Climate Change, edited by: Stocker, T. F., Qin, D., Plattner, G.-K., Tignor, M., Allen, S. K., Boschung, J., Nauels, A., Xia, Y., Bex, V., and Midgley, P. M., Cambrigde University Press, Cambridge, United Kingdom and New York, NY, USA, 2013b.

Myhre, G., and Samset, B. H.: Standard climate models radiation codes underestimate black carbon radiative forcing, Atmospheric Chemistry and Physics, 15, 2883-2888, 10.5194/acp-15-2883-2015, 2015.

Myhre, G., Forster, P., Samset, B., Hodnebrog, Ø., Sillmann, J., Andrews, T., Boucher, O., Faluvegi, G., Fläschner, D., Iversen, T., Kharin, S., Kasoar, M., Kirkevåg, A., Lamarque, J.-F., Olivié, D., Richardson, T., Shindell, D., Shine, K., Stjern, C., Takemura, T., Voulgarakis, A., and Zwiers, F. W.: PDRMIP: A Precipitation Driver and Response Model Intercomparison Project, Protocol and preliminary results, Submitted to Bull. Am. Meteorol. Soc., 2016.

Neale, R. B., Chen, C.-C., Gettleman, A., Lauritzen, P. H., Park, S., Williamson, D. L., Conley, A. J., Garcia, R., Kinnison, D., Lamarque, J.-F., Marsh, D., Mills, M., Smith, A. K., Tilmes, S., Vitt, F., Morrison, H., Cameron-Smith, P., Collins, W. D., Iacono, M. J., Easter, R. C., Ghan, S. J., Liu, X., Rasch, P. J., and Taylor, M. A.: Description of the NCAR Community Atmosphere Model (CAM 5.0), NCAR Technical Note TN-486+STR, National Center for Atmospheric Research, Boulder, Colorado, USA, 2012.

Oman, L., Robock, A., Stenchikov, G. L., and Thordarson, T.: High-latitude eruptions cast shadow over the African monsoon and the flow of the Nile, Geophysical Research Letters, 33, L18711, 10.1029/2006GL027665, 2006

Pan, X., Chin, M., Gautam, R., Bian, H., Kim, D., Colarco, P. R., Diehl, T. L., Takemura, T., Pozzoli, L., Tsigaridis, K., Bauer, S., and Bellouin, N.: A multi-model evaluation of aerosols over South Asia: common problems and possible causes, Atmos. Chem. Phys., 15, 5903-5928, doi:10.5194/acp-15-5903-2015, 2015.

Pithan, F., and Mauritsen, T.: Arctic amplification dominated by temperature feedbacks in contemporary climate models, Nature Geoscience, 7, 181-184, 10.1038/ngeo2071, 2014.

Polson, D., Bollasina, M., Hegerl, G. C., and Wilcox, L. J.: Decreased monsoon precipitation in the Northern Hemisphere due to anthropogenic aerosols, Geophysical Research Letters, 41, 6023-6029, 10.1002/2014gl060811, 2014.

Polvani, L. M., Waugh, D. W., Correa, G. J. P., and Son, S.-W.: Stratospheric Ozone Depletion: The Main Driver of Twentieth-Century Atmospheric Circulation Changes in the Southern Hemisphere, Journal of Climate, 24, 795-812, 10.1175/2010jcli3772.1, 2011.

Poschl, U., Martin, S. T., Sinha, B., Chen, Q., Gunthe, S. S., Huffman, J. A., Borrmann, S., Farmer, D. K., Garland, R. M., Helas, G., Jimenez, J. L., King, S. M., Manzi, A., Mikhailov, E., Pauliquevis, T., Petters, M. D., Prenni, A. J., Roldin, P., Rose, D., Schneider, J., Su, H., Zorn, S. R., Artaxo, P., and Andreae, M. O.: Rainforest aerosols as biogenic nuclei of clouds and precipitation in the Amazon, Science, 329, 1513-1516, 10.1126/science.1191056, 2010.

Ramanathan, V., Crutzen, P. J., Kiehl, J. T., and Rosenfeld, D.: Aerosols, climate, and the hydrological cycle, Science, 294, 2119-2124, 10.1126/science.1064034, 2001.

Ring, M. J., and Plumb, R. A.: Forced annular mode patterns in a simple atmospheric general circulation model. J. Atmos. Sci., 64, 3611–3626, 2007.

Ring, M. J., and Plumb, R. A.: The Response of a Simplified GCM to Axisymmetric Forcings: Applicability of the Fluctuation–Dissipation Theorem, Journal of the Atmospheric Sciences, 65, 3880-3898, 10.1175/2008jas2773.1, 2008.

Rosenfeld, D.: TRMM observed first direct evidence of smoke from forest fires inhibiting rainfall, Geophysical Research Letters, 26, 3105-3108, 10.1029/1999gl006066, 1999.

Rosenfeld, D.: Suppression of Rain and Snow by Urban and Industrial Air Pollution, Science, 287, 1793-1796, 10.1126/science.287.5459.1793, 2000.

Rosenfeld, D., Lohmann, U., Raga, G. B., O'Dowd, C. D., Kulmala, M., Fuzzi, S., Reissell, A., and Andreae, M. O.: Flood or drought: how do aerosols affect precipitation?, Science, 321, 1309-1313, 10.1126/science.1160606, 2008.

Rosenfeld, D., Clavner, M., and Nirel, R.: Pollution and dust aerosols modulating tropical cyclones intensities, Atmospheric Research, 102, 66-76, 10.1016/j.atmosres.2011.06.006, 2011.

Rotstayn, L. D., Collier, M. A., Jeffrey, S. J., Kidston, J., Syktus, J. I., and Wong, K. K.: Anthropogenic effects on the subtropical jet in the Southern Hemisphere: aerosols versus long-lived greenhouse gases, Environ. Res. Lett., 8, 014030, 10.1088/1748-9326/8/1/014030, 2013.

Rotstayn, L. D., Plymin, E. L., Collier, M. A., Boucher, O., Dufresne, J.-L., Luo, J.-J., von Salzen, K., Jeffrey, S. J., Foujols, M.-A., Ming, Y., and Horowitz, L. W.: Declining Aerosols in CMIP5 Projections: Effects on Atmospheric Temperature Structure and Midlatitude Jets, Journal of Climate, 27, 6960-6977, 10.1175/jcli-d-14-00258.1, 2014.

Russell, G. L., Miller, J. R., and Rind, D.: A coupled atmosphere-ocean model for transient climate change studies, Atmosphere-ocean, 33, 683-730, 1995.

Samset, B., and Myhre, G.: Climate response to externally mixed black carbon as a function of altitude, Journal of Geophysical Research: Atmospheres, 120, 2913-2927, 2015.

Samset, B. H., Myhre, G., Schulz, M., Balkanski, Y., Bauer, S., Berntsen, T. K., Bian, H., Bellouin, N., Diehl, T., Easter, R. C., Ghan, S. J., Iversen, T., Kinne, S., Kirkevåg, A., Lamarque, J. F., Lin, G., Liu, X., Penner, J. E., Seland, Ø., Skeie, R. B., Stier, P., Takemura, T., Tsigaridis, K., and Zhang, K.: Black carbon vertical profiles strongly affect its radiative forcing uncertainty, Atmospheric Chemistry and Physics, 13, 2423-2434, 10.5194/acp-13-2423-2013, 2013.

Samset, B. H., Myhre, G., Forster, P. M., Hodnebrog, Ø., Andrews, T., Faluvegi, G., Fläschner, D., Kasoar, M., Kharin, V., Kirkevåg, A., Lamarque, J. F., Olivié, D., Richardson, T., Shindell, D., Shine, K. P., Takemura, T., and Voulgarakis, A.: Fast and slow precipitation responses to individual climate forcers: A PDRMIP multimodel study, Geophysical Research Letters, 43, 2782-2791, 10.1002/2016GL068064, 2016.

Schmidt, G. A., Ruedy, R., Hansen, J. E., Aleinov, I., Bell, N., Bauer, M., Bauer, S., Cairns, B., Canuto, V., Cheng, Y., Del Genio, A., Faluvegi, G., Friend, A. D., Hall, T. M., Hu, Y., Kelley, M., Kiang, N. Y., Koch, D., Lacis, A. A., Lerner, J., Lo, K. K., Miller, R. L., Nazarenko, L., Oinas, V., Perlwitz, J., Perlwitz, J., Rind, D., Romanou, A., Russell, G. L., Sato, M., Shindell, D. T., Stone, P. H., Sun, S., Tausnev, N., Thresher, D., and Yao, M.-S.: Present-Day Atmospheric Simulations Using GISS ModelE: Comparison to In Situ, Satellite, and Reanalysis Data, Journal of Climate, 19, 153-192, 10.1175/jcli3612.1, 2006.

Schmidt, G. A., Kelley, M., Nazarenko, L., Ruedy, R., Russell, G. L., Aleinov, I., Bauer, M., Bauer, S. E., Bhat, M. K., Bleck, R., Canuto, V., Chen, Y.-H., Cheng, Y., Clune, T. L., Del Genio, A., de

Fainchtein, R., Faluvegi, G., Hansen, J. E., Healy, R. J., Kiang, N. Y., Koch, D., Lacis, A. A., LeGrande, A. N., Lerner, J., Lo, K. K., Matthews, E. E., Menon, S., Miller, R. L., Oinas, V., Oloso, A. O., Perlwitz, J. P., Puma, M. J., Putman, W. M., Rind, D., Romanou, A., Sato, M., Shindell, D. T., Sun, S., Syed, R. A., Tausnev, N., Tsigaridis, K., Unger, N., Voulgarakis, A., Yao, M.-S., and Zhang, J.: Configuration and assessment of the GISS ModelE2 contributions to the CMIP5 archive, Journal of Advances in Modeling Earth Systems, 6, 141-184, 10.1002/2013MS000265, 2014.

Schulz, M., Textor, C., Kinne, S., Balkanski, Y., Bauer, S., Berntsen, T., Berglen, T., Boucher, O., Dentener, F., Guibert, S., Isaksen, I. S. A., Iversen, T., Koch, D., Kirkevåg, A., Liu, X., Montanaro, V., Myhre, G., Penner, J. E., Pitari, G., Reddy, S., Seland, Ø., Stier, P., and Takemura, T.: Radiative forcing by aerosols as derived from the AeroCom present-day and pre-industrial simulations, Atmos. Chem. Phys., 6, 5225-5246, 10.5194/acp-6-5225-2006, 2006.

Screen, J. A., and Simmonds, I.: The central role of diminishing sea ice in recent Arctic temperature amplification, Nature, 464, 1334-1337, 10.1038/nature09051, 2010.

Shawki, D., and et al.: South Asian climate responses to local and remote sulphur dioxide emissions, In preparation.

Shepherd, T. G.: Atmospheric circulation as a source of uncertainty in climate change projections, Nature Geoscience, 7, 703-708, 10.1038/ngeo2253, 2014.

Shindell, D., and Faluvegi, G.: Climate response to regional radiative forcing during the twentieth century, Nature Geoscience, 2, 294-300, 10.1038/ngeo473, 2009.

Shindell, D., Schulz, M., Ming, Y., Takemura, T., Faluvegi, G., and Ramaswamy, V.: Spatial scales of climate response to inhomogeneous radiative forcing, Journal of Geophysical Research, 115, 10.1029/2010jd014108, 2010.

Shindell, D. T.: Evaluation of the absolute regional temperature potential, Atmospheric Chemistry and Physics, 12, 7955-7960, 10.5194/acp-12-7955-2012, 2012.

Shindell, D. T., Voulgarakis, A., Faluvegi, G., and Milly, G.: Precipitation response to regional radiative forcing, Atmospheric Chemistry and Physics, 12, 6969-6982, 10.5194/acp-12-6969-2012, 2012.

Shindell, D. T., Lamarque, J. F., Schulz, M., Flanner, M., Jiao, C., Chin, M., Young, P. J., Lee, Y. H., Rotstayn, L., Mahowald, N., Milly, G., Faluvegi, G., Balkanski, Y., Collins, W. J., Conley, A. J., Dalsoren, S., Easter, R., Ghan, S., Horowitz, L., Liu, X., Myhre, G., Nagashima, T., Naik, V., Rumbold, S. T., Skeie, R., Sudo, K., Szopa, S., Takemura, T., Voulgarakis, A., Yoon, J. H., and Lo, F.: Radiative forcing in the ACCMIP historical and future climate simulations, Atmospheric Chemistry and Physics, 13, 2939-2974, 10.5194/acp-13-2939-2013, 2013a.

Shindell, D. T., Pechony, O., Voulgarakis, A., Faluvegi, G., Nazarenko, L., Lamarque, J. F., Bowman, K., Milly, G., Kovari, B., Ruedy, R., and Schmidt, G. A.: Interactive ozone and methane chemistry in GISS-E2 historical and future climate simulations, Atmos. Chem. Phys., 13, 2653-2689, 10.5194/acp-13-2653-2013, 2013b.

Shindell, D. T.: Inhomogeneous forcing and transient climate sensitivity, Nature Climate Change, 4, 274-277, 10.1038/nclimate2136, 2014.

Shindell, D. T., Faluvegi, G., Rotstayn, L., and Milly, G.: Spatial patterns of radiative forcing and surface temperature response, Journal of Geophysical Research: Atmospheres, 120, 5385-5403, 10.1002/2014jd022752, 2015.

Smith, S. J., Aardenne, J. v., Klimont, Z., Andres, R. J., Volke, A., and Delgado Arias, S.: Anthropogenic sulfur dioxide emissions: 1850–2005, Atmospheric Chemistry and Physics, 11, 1101-1116, 2011.

Stier, P., Schutgens, N. A. J., Bellouin, N., Bian, H., Boucher, O., Chin, M., Ghan, S., Huneeus, N., Kinne, S., Lin, G., Ma, X., Myhre, G., Penner, J. E., Randles, C. A., Samset, B., Schulz, M., Takemura, T., Yu, F., Yu, H., and Zhou, C.: Host model uncertainties in aerosol radiative forcing estimates: results from the AeroCom Prescribed intercomparison study, Atmos. Chem. Phys., 13, 3245-3270, doi:10.5194/acp-13-3245-2013, 2013.

Teng, H., Washington, W. M., Branstator, G., Meehl, G. A., and Lamarque, J.-F.: Potential impacts of Asian carbon aerosols on future US warming, Geophysical Research Letters, 39, L11703, 10.1029/2012gl051723, 2012.

Textor, C., Schulz, M., Guibert, S., Kinne, S., Balkanski, Y., Bauer, S., Berntsen, T., Berglen, T., Boucher, O., Chin, M., Dentener, F., Diehl, T., Easter, R., Feichter, H., Fillmore, D., Ghan, S., Ginoux, P., Gong, S., Grini, A., Hendricks, J., Horowitz, L., Huang, P., Isaksen, I., Iversen, I., Kloster, S., Koch, D., Kirkevåg, A., Kristjansson, J. E., Krol, M., Lauer, A., Lamarque, J. F., Liu, X., Montanaro, V., Myhre, G., Penner, J., Pitari, G., Reddy, S., Seland, Ø., Stier, P., Takemura, T., and Tie, X.: Analysis and quantification of the diversities of aerosol life cycles within AeroCom, Atmos. Chem. Phys., 6, 1777-1813, 10.5194/acp-6-1777-2006, 2006.

Tilmes, S., Lamarque, J. F., Emmons, L. K., Kinnison, D. E., Ma, P. L., Liu, X., Ghan, S., Bardeen, C., Arnold, S., Deeter, M., Vitt, F., Ryerson, T., Elkins, J. W., Moore, F., Spackman, J. R., and Val Martin, M.: Description and evaluation of tropospheric chemistry and aerosols in the Community Earth System Model (CESM1.2), Geoscientific Model Development, 8, 1395-1426, 10.5194/gmd-8-1395-2015, 2015.

Trenberth, K. E., and Dai., A.: Effects of Mount Pinatubo volcanic eruption on the hydrological cycle as an analogue of geoengineering, Geophysical Research Letters, 34, L15702, 10.1029/2007GL030524, 2007

Tsigaridis, K., Daskalakis, N., Kanakidou, M., Adams, P. J., Artaxo, P., Bahadur, R., Balkanski, Y., Bauer, S. E., Bellouin, N., Benedetti, A., Bergman, T., Berntsen, T. K., Beukes, J. P., Bian, H., Carslaw, K. S., Chin, M., Curci, G., Diehl, T., Easter, R. C., Ghan, S. J., Gong, S. L., Hodzic, A., Hoyle, C. R., Iversen, T., Jathar, S., Jimenez, J. L., Kaiser, J. W., Kirkevåg, A., Koch, D., Kokkola, H., Lee, Y. H., Lin, G., Liu, X., Luo, G., Ma, X., Mann, G. W., Mihalopoulos, N., Morcrette, J. J., Müller, J. F., Myhre, G., Myriokefalitakis, S., Ng, N. L., O'Donnell, D., Penner, J. E., Pozzoli, L., Pringle, K. J., Russell, L. M., Schulz, M., Sciare, J., Seland, Ø., Shindell, D. T., Sillman, S., Skeie, R. B., Spracklen, D., Stavrakou, T., Steenrod, S. D., Takemura, T., Tiitta, P., Tilmes, S., Tost, H., van Noije, T., van Zyl, P. G., von Salzen, K., Yu, F., Wang, Z., Wang, Z., Zaveri, R. A., Zhang, H., Zhang, K., Zhang, Q., and Zhang, X.: The AeroCom evaluation and intercomparison of organic aerosol in global models, Atmospheric Chemistry and Physics, 14, 10845-10895, 10.5194/acp-14-10845-2014, 2014.

Twomey, S.: The influence of pollution on the shortwave albedo of clouds, Journal of the atmospheric sciences, 34, 1149-1152, 1977.

Verheggen, B., Cozic, J., Weingartner, E., Bower, K., Mertes, S., Connolly, P., Gallagher, M., Flynn, M., Choularton, T., and Baltensperger, U.: Aerosol partitioning between the interstitial and the condensed phase in mixed-phase clouds, Journal of Geophysical Research, 112, 10.1029/2007jd008714, 2007.

Vet, R., Artz, R. S., Carou, S., Shaw, M., Ro, C.-U., Aas, W., Baker, A., Bowersox, V. C., Dentener, F., Galy-Lacaux, C., Hou, A., Pienaar, J. J., Gillett, R., Forti, M. C., Gromov, S., Hara, H., Khodzher, T., Mahowald, N. M., Nickovic, S., Rao, P. S. P., and Reid, N. W.: A global assessment of precipitation chemistry and deposition of sulfur, nitrogen, sea salt, base cations, organic acids, acidity and pH, and phosphorus, Atmospheric Environment, 93, 3-100, 10.1016/j.atmosenv.2013.10.060, 2014.

Voulgarakis, A., and Shindell, D. T.: Constraining the Sensitivity of Regional Climate with the Use of Historical Observations, Journal of Climate, 23, 6068-6073, 10.1175/2010jcli3623.1, 2010.

Walters, D. N., Williams, K. D., Boutle, I. A., Bushell, A. C., Edwards, J. M., Field, P. R., Lock, A. P., Morcrette, C. J., Stratton, R. A., Wilkinson, J. M., Willett, M. R., Bellouin, N., Bodas-Salcedo, A., Brooks, M. E., Copsey, D., Earnshaw, P. D., Hardiman, S. C., Harris, C. M., Levine, R. C., MacLachlan, C., Manners, J. C., Martin, G. M., Milton, S. F., Palmer, M. D., Roberts, M. J., Rodríguez, J. M., Tennant, W. J., and Vidale, P. L.: The Met Office Unified Model Global Atmosphere 4.0 and JULES Global Land 4.0 configurations, Geoscientific Model Development, 7, 361-386, 10.5194/gmd-7-361-2014, 2014.

Warner, J., and Twomey, S.: The production of cloud nuclei by cane fires and the effect on cloud droplet concentration, Journal of the atmospheric sciences, 24, 704-706, 1967.

Warner, J.: A reduction in rainfall associated with smoke from sugar-cane fires-An inadvertent weather modification?, Journal of Applied Meteorology, 7, 247-251, 1968.

Wayne, R. P.: Chemistry of Atmospheres, Third ed., Oxford Univeristy Press, Oxford, United Kingdom, 2000.

Wilcox, L. J., Highwood, E. J., and Dunstone, N. J.: The influence of anthropogenic aerosol on multi-decadal variations of historical global climate, Environmental Research Letters, 8, 024033, 10.1088/1748-9326/8/2/024033, 2013.

Wilcox, L. J., Highwood, E. J., Booth, B. B. B., and Carslaw, K. S.: Quantifying sources of inter-model diversity in the cloud albedo effect, Geophysical Research Letters, 42, 1568-1575, 10.1002/2015gl063301, 2015.

Williams, K., Harris, C., Bodas-Salcedo, A., Camp, J., Comer, R., Copsey, D., Fereday, D., Graham, T., Hill, R., and Hinton, T.: The Met Office global coupled model 2.0 (GC2) configuration, Geoscientific Model Development, 8, 1509-1524, 2015.

Yu, H., Chin, M., West, J. J., Atherton, C. S., Bellouin, N., Bergmann, D., Bey, I., Bian, H., Diehl, T., Forberth, G., Hess, P., Schulz, M., Shindell, D., Takemura, T., and Tan, Q.: A multimodel assessment of the influence of regional anthropogenic emission reductions on aerosol direct radiative forcing and the role of intercontinental transport, Journal of Geophysical Research: Atmospheres, 118, 700-720, 10.1029/2012jd018148, 2013.

Zhang, X. Y., Wang, Y. Q., Niu, T., Zhang, X. C., Gong, S. L., Zhang, Y. M., and Sun, J. Y.: Atmospheric aerosol compositions in China: spatial/temporal variability, chemical signature, regional haze distribution and comparisons with global aerosols, Atmospheric Chemistry and Physics, 12, 779-799, 10.5194/acp-12-779-2012, 2012.